A NUMERICAL AND EXPERIMENTAL STUDY OF NEAR SURFACE GROUND ENERGY SYSTEMS INCLUDING THE USE OF ADAPTABLE INSULATION LAYER

Hassanein Jawad Mobarek

Geoenvironmental Research Centre
School of Engineering
Cardiff University

Thesis submitted in candidature for the degree of

Doctor of Philosophy at Cardiff University

October 2017

DECLARATIONS

This work has not been submitted in substance for any other degree or award at this or any other university or place of learning, nor is being submitted concurrently in candidature for any degree or other award.

Signed ---------- (Hassanein Mobarek)

Date ----------

STATEMENT 1

This thesis is being submitted in partial fulfilment of the requirements for the degree of PhD.

Signed ---------- (Hassanein Mobarek)

Date ----------

STATEMENT 2

This thesis is the result of my own independent work/investigation, except where otherwise stated, and the thesis has not been edited by a third party beyond what is permitted by Cardiff University's Policy on the Use of Third Party Editors by Research Degree Students. Other sources are acknowledged by explicit references. The views expressed are my own.

Signed ---------- (Hassanein Mobarek)

Date ----------

STATEMENT 3

I hereby give consent for my thesis, if accepted, to be available online in the University's Open Access repository and for inter-library loan, and for the title and summary to be made available to outside organisations.

Signed ---------- (Hassanein Mobarek)

Date ----------

Acknowledgments

I would like to express deep and sincere gratitude to my supervisor Dr. Peter Cleall for his invaluable academic guidance that helped me upgrading my knowledge during the course of study. I would like also to thank Dr. Steve Rees, Dr. Snehasis Tripathy. The continuous help, encouragement and endless patience of my supervisory team led to made possible the completion of this thesis. Their sincere support and trust have inspired me to give my very best throughout the duration of research.

I would like to acknowledge the help provided by Dr. Jose Javier Muñoz Criollo, for guiding me through his work and for his genuine and kind support throughout the study period.

During the PhD study course, several people have helped me one way or another for the achievement of my objectives. In particular, I would like to thank the staff at the Research Office at the School of Engineering of Cardiff University for their continuous guidance and efforts to unravel the messed thoughts of a PhD student.

In addition, I would like to express my deep gratitude to the technicians from the School of Engineering of Cardiff University Mr. Harry Lane and Mr. Steffan Jones for their kind help in the experimental aspects of this investigation.

Thanks is deserved to the staff in charge of ARCCA in Cardiff University for technical assistance in the numerical aspects of this research. Their always-accessible attitude have facilitated the journey through the learning curve that represents the use of advanced computing equipment.

Also, special thanks is deserver to University of Kufa for sponsoring this study, and to the Transport Research Laboratory (TRL) for supplying and allowing the use of the data published in (Carder, *et al.* 2008)[1] for the purposes of this thesis.

To all of my friends, just for being there and having an endless hours of random (really random and lateral) talks that in some way have kept me sane I really thank you all for that. Special thanks is deserved to the three musketeers: Amjad, Alaa and Saif for bailing me out and helping me achieving this dream and made it a reality.

Finally, very special thanks is deserved to my mother for her consistent, continuous praying; and for helping me becoming the person I am now; to my brothers Mohammed and Moez; to my lovely wife for her saint like patience and endless cheering; and lastly to my beautiful children, for illuminating and enriching my life; without you all being there I would have cracked a long time ago.

Thanks to all of you ..... Hassanein Mobarek

[1] Carder, D. R., Barker, K. J., Hewitt, M. G., Ritter, D. and Kiff, A. 2008. Performance of an interseasonal heat transfer facility for collection, storage, and re-use of solar heat from the road surface. Transport Research Laboratory.

Abstract

Unfortunately, the global conventional fuels in reserves are running out while the world energy consumption is increasing unruly. Therefore, innovative methods for providing sustainable heating and cooling through thermal energy storage (TES) have gained increasing attention. This study presents a numerical and experimental investigation of near surface ground energy systems including the use of adaptable insulation layers. The experimental set up involves the development of an innovative technique that is proposed to regulate the transfer of heat energy to the storage regions of the soil mass. Furthermore, a theoretical framework to represent the transient processes of such systems was developed and 1D and 2D numerical models were established to simulate ground energy system behaviour. The finite element method was utilised for spatial discretization and the finite difference method for time-stepping. The resulting model took into account conductive and convective heat transfer between the fluid inside pipe heat exchangers and the surrounding soil. Key additions were introduced to the recent model work which allowed it to take into account surface snow and ground freezing presence in the system, the amount of thermal energy available in the system and the ability to represent porous layer thermal properties of a multi layered system through considering its components (i.e. air, water and solids particles).

The proposed new experimental setup was used to investigate the practical implementation of adaptable insulation layers with the experimental data then used to validate the numerical model. Further validation of the modelling of the surface snow and ground freezing was achieved via comparison against an experimental case study performed by others. In the analysis performed, particular attention was given to the energy balance at the soil surface and its impact on the performance of thermal energy storage devices in shallow regions of the ground. Additionally, the developed models were applied to explore the use of the adaptable insulation layer in different systems in comparison to typical designs. Three case scenarios were chosen to represent different type of systems, a comparisons analysis was then introduced which shows the potential effectiveness of using the adaptable insulation layer.

Table of Contents

List of Figures

List of Tables

List of Symbols

A_i	Pipe internal area	m^2
$\boldsymbol{A_V}$	Laplace matrix for heat flow	
$\boldsymbol{A_W}$	Laplace matrix for heat advection	
b_0, b_1, b_2	Parameters used to predict scaler roughness	dimensionless
C_e	Coefficient of evaporation for fully dense canopies	dimensionless
c_f	Transfer coefficient for aerodynamic resistance	dimensionless
C_{fc}	Coefficient for forced convection	dimensionless
C_{nc}	Coefficient for natural convection	dimensionless
c_a	Specific heat capacity at constant pressure of soil air particles	J/kgK
c_b	Soil bulk specific heat capacity at constant pressure	J/kgK
$H_{c,b}$	Soil bulk volumetric heat capacity at constant pressure	J/m^3K
c_s	Specific heat capacity at constant pressure of soil solid particles	J/kgK
c_w	Specific heat capacity at constant pressure of soil water particles	J/kgK
C_{sh}	Coefficient of sheltering	dimensionless
D_{sh}	Shading factor	dimensionless
D_w	Unsaturated diffusivity	m^2/s
e_a	Atmospheric vapour pressure	kPa
$e_{a,sat}$	Atmospheric saturation vapour pressure	kPa
$e_{ss,sat}$	Soil surface saturation vapour pressure	kPa
E_i	Total bulk volumetric energy	J/m^3
$e_{c,sat}$	Saturated vapour pressure of canopy cover	kPa
e_s	Surface vapour pressure	kPa
E_s	Thermal energy stored in column of soil	J/m^2
f	Friction factor	dimensionless
f_i	Boundary condition i	
F_{12}	View factor between surface 1 and 2	dimensionless
F_i	Initial condition	
$\boldsymbol{F_V}$	Load vector for heat flow	
$\boldsymbol{F_W}$	Load vector for heat advection	
H_a	Relative humidity	%
h_C	Convective heat transfer coefficient	W/m^2K
$h_{C,c}$	Convective heat transfer coefficient of canopy cover	W/m^2K
h_{LE}	Evaporative heat transfer coefficient	W/m^2K
$h_{LE,c}$	Evaporative heat transfer coefficient of canopy cover	W/m^2K
h_C	Convective heat transfer coefficient of pipe wall	W/m^2K
L_c	Characteristic length of pipe	m
L	Monin-Obukhov length	m
L_s	Depth of column of soil	m

L_p	Length of pipe	m
L_v	Latent heat of evaporation for water	J/kg
$\boldsymbol{M_U}$	Mass matrix for heat flow	
$\boldsymbol{M_V}$	Mass matrix for heat advection	
N_u	Nusselt number	
Pr	Prandtl number	
q_C	Convective heat flux per unit area	W/m^2
q_{LE}	Latent heat flux per unit area	W/m^2
Q_f	Pipe internal heat generation	W/m^3
q_G	Conductive heat flux per unit area	W/m^2
q_T	Thermal energy flux per unit area	W/m^2
q_L	Longwave radiation per unit area	W/m^2
$Q_{L,1}$	Longwave heat flux rate from surface 1	W
$q_{L,1}$	Longwave heat flux rate per unit area from surface 1	W/m^2
$Q_{L,2}$	Longwave heat flux rate from surface 2	W
$q_{L,2}$	Longwave heat flux rate per unit area from surface 2	W/m^2
$q_{L,in}$	Incoming longwave radiation per unit area	W/m^2
Q_{max}	Maximum possible heat transfer rate on pipe	W
Q_p	Heat flux rate through pipe wall	W
q_p	Pipe heat transfer per unit area	W/m^2
Q_{real}	Actual heat transfer rate on pipe	W
q_S	Shortwave radiation per unit area	W/m^2
q_{sh}	Solar radiation reaching the surface after taking into account a shade factor	W/m^2
$q_{s,in}$	Total amount of energy reaching the soil surface per unit of area	W/m^2
$q_{s,out}$	Total amount of energy leaving the soil surface per unit of area	W/m^2
q_{C0}	Surface kinematic heat flux	W/m^2
u_*	Friction velocity	m/s
r	radius	m
R	Global shortwave radiation per unit area	W/m^2
R_0	Radius of soil particles	m
R_w	Gas constant	J/kgK
r_a	Aerodynamic resistance	s/m
r_e	External pipe radius	m
R_e	Reynolds number	dimensionless
Re_*	Roughness Reynolds number	dimensionless
r_i	Internal pipe radius	m
r_s	Stomata resistance	s/m
T	Temperature	K
t	Time	s
a, b, κ	Empirical parameters	
e	Void ratio	Dimensionless
n	Porosity	Dimensionless
T_a	Air temperature	K
$T_{a,K}$	Absolute air temperature	K

$T_{sky,K}$	Absolute sky temperature	K
T_{ss}	Temperature of the soil surface	K
$T_{ss,K}$	Absolute temperature of the soil surface	K
T_c	Temperature of canopy cover	°C
T_f	Temperature of fluid inside pipe	°C
T_{pw}	Temperature of pipe wall	°C
T_{ss}	Soil surface temperature	°C
T_v	Virtual temperature	°C
u_f	Velocity of fluid inside pipe	m/s
U_p	Pipe overall heat transfer coefficient	W/m^{2}K
u_s	Wind speed	m/s
V	Volume	m^3
V	Volume occupied by constituent i	m^3
x, y, z	Cartesian coordinates	m
z_0	Soil surface roughness length	m
z_T	Soil surface roughness for sensible heat transfer	m
z_Q	Soil surface roughness for humidity	m
z_m	Soil surface roughness for momentum	m
z_u	Reference high at which wind speed is measured	m
h_{ss}	Pressure head at the soil surface	m
R_{max}	Maximum noon solar radiation	dimensionless
Ri_B	Bulk Richardson number	dimensionless

Greek symbols

α	Coefficient for the estimation of vapour pressure at the soil surface	dimensionless
α_a	Normalized air thermal conductivity	dimensionless
α_w	Normalized water thermal conductivity	dimensionless
α_b	Soil bulk thermal diffusivity	m/s^2
α_C	Solar albedo for canopy cover	dimensionless
α_S	Solar albedo	dimensionless
β	Coefficient for the estimation of vapour pressure at the soil surface	dimensionless
ξ	Soil geometric parameter	
Γ	Finite element spatial boundary	
ε_s	Surface emissivity	dimensionless
ε_c	Canopy cover infrared emissivity	dimensionless
ε_{sky}	Sky infrared emissivity	dimensionless
ε_{ss}	Soil surface infrared emissivity	dimensionless
η	Parameter for time discretization	
θ_w	Water content	dimensionless
θ_{wp}	Wilting point	dimensionless
θ_s	Sun's zenith angle	dimensionless
c_f	Transfer coefficient	dimensionless
λ	Thermal conductivity	W/mK

λ_r	Soil normalized thermal conductivity	W/mK
λ_b	Soil bulk thermal conductivity	W/mK
λ_i	Thermal conductivity of constituent i	W/mK
λ_f	Thermal conductivity of fluid inside pipe	W/mK
λ_{pw}	Thermal conductivity of pipe wall	W/mK
λ_{sat}	Saturated soil thermal conductivity	W/mK
λ_{dry}	Dry soil thermal conductivity	W/mK
n	Porosity	dimensionless
e	Void ratio	dimensionless
S_r	Degree of saturation	dimensionless
i	Soil texture effect	dimensionless
ν	Density of canopy cover	dimensionless
ϑ	Cell structure parameter	dimensionless
α_w	Normalized thermal conductivity	dimensionless
α_a	Normalized thermal conductivity	dimensionless
ρ_a	Density of air	kg/m^3
ρ_b	Soil bulk density	kg/m^3
ρ_f	Density of fluid inside pipe	kg/m^3
ρ_s	Density of soil solid particles	kg/m^3
ρ_w	Density of water	kg/m^3
ρ_r	Thermal resistivity	mK/W
ς	Size of mesh element	
ϕ	Finite element test function	
χ_a	Fraction of air	dimensionless
χ_w	Fraction of water	dimensionless
χ_s	Fraction of solid particles	dimensionless
χ_i	Fraction of constituents i	dimensionless
ψ_h	Empirical stability parameter for temperature	dimensionless
ψ_m	Empirical stability parameter for momentum	dimensionless
ϕ_h	Empirical gradient parameter for temperature	dimensionless
ϕ_m	Empirical gradient parameter for momentum	dimensionless
Ω	Finite element domain	

Constants

g	Acceleration due to gravity	9.81 m/s^2
R_c	Solar constant	1.362 W/m^2
R_w	Gas constant for water vapour	461.5 J/kgK
k	von Kármán constant	0.41
σ	Steffan-Boltzmann constant	5.6704x10^{-8} W/m^{2}K^4
Pa	Atmospheric pressure	101.325 kPa

Mathematical operators

Δ	Difference operator
∇	Vector differential operator
∂	Partial derivative
$\hat{n}$	Normal unitary vector
$\prod$	Product of multiple terms
$\sum$	Summation of multiple terms

Superscripts

n	At previous time step
$n+1$	At current time step

Subscripts

i, j	Counters

Chapter 1: Introduction

1.1 Motivation

Amongst the major global problems lie the problems of excessive consumption of fossil resources, oil shortages, rapidly increasing greenhouse gas (GHG) emissions and global warming (Letcher 2016). Many modern industrial and commercial buildings have high heating and/or cooling loads that may cause potential, environmental impact. Therefore, there is a strong pressure to obtain the necessary energy from renewable sources. In response to that, the renewable energy agenda has received an increasing attention, studies and goals. The UK government for example set an initial target for renewable sources to reach 30-45 % of all energy consumed in the UK by 2030 (UK Department of Business Energy & Industrial Strategy 2016 ; UK Department of Energy and Climate Change 2011).

One of the possibilities is to use the ground itself as a source of renewable energy. Thermal energy can be extracted from the ground at greater depth (geothermal energy). Another possibility that the ground may be used to store heat or cold in one season and to liberate this energy in another season. Such energy can be stored in subsoil sand layers (aquifers) or in soil/rock using boreholes. By providing cold energy storage, it is possible to provide cooling in summer months by means of winter cold. Conversely, the seasonal storage of heat in subsoil offers the opportunity of space heating with summer heat in winter.

A crucial aspect of the challenge is to effectively store excess energy and bridge the gap between energy generation and consumption. Among recent and effective technique lies in the use of the inter-seasonal storage systems. Typically inter-seasonal storage systems store thermal energy in regions of soil close to the surface by means of engineering thermal devices utilizing the heat capacity of the ground (or other suitable medium) to store the surplus thermal energy from one season to be used at another time. The relatively high specific heat capacity and low thermal conductivity of many soils allows the usage of the stored energy to be delayed in time with only

relatively small energy losses. In general, the storage process is carried out in the summer months when there is high solar energy or heat waste (from various heating and ventilation systems) while the cycle reverse in winter months when energy demand increases.

Applications of inter-seasonal heat storage systems include: heating for buildings, ice-prevention in highway pavements or aircraft runways, and winter thermal maintenance of aircraft stands (Morita and Tago 2000). Sources of solar thermal energy for these systems are, for example, road surfaces (Bobes-Jesus *et al.* 2013) and roof solar collectors (Kroll and Ziegler 2011). The preferred surfaces to be used for an inter-seasonal system is the former, as it comprises large areas of our infrastructure including roads, pedestrian pathways, and parking areas. Given their dark colour, asphalt pavements can get heated up to 70 °C due to solar irradiation in summertime because of their excellent heat-absorbing properties (Chen *et al.* 2009). If the road surface system is to be used, the operation of the system would be highly affected by the interactions between the atmosphere and the ground surface. Which is why, a correct understanding of the energy fluxes at that area is of high importance for correct representation. Moreover, it will provide aid in performance assessment, decision making, design and implementation.

Inter-seasonal heat storage can be viewed as a sub-topic of the wider area of research, namely Thermal Energy Storage (TES) when classified according to the storage period. TES can also be broadly subdivided into three main categories according to the technology used:

- Sensible heat storage, which is based on the specific heat of a storage medium and has the lowest energy density and it requires large volumes for its implementation. Despite these shortcomings, this technology is commonly used due to its relatively inexpensive cost, especially in applications with a low number of storage cycles as is the case of inter-seasonal heat storage (UK Department of Business Energy & Industrial Strategy 2016 ; International Renewable Energy Agency and International Energy Agency 2013).

- Latent heat storage, which involves a phase change from liquid to solid of a suitable material. The main advantages of this process are simply related to the fact that it stores high energy in a smaller volume (Pomianowski *et al.* 2013).
- Thermo-chemical energy storage, which uses reversible chemical reactions to store thermal energy in chemical bonds. The chemical compound is dissociated into its components under the influence of a heat supply, and it can be stored separately. When these components are put in contact the chemical compound is restored with a heat release. With this process, thermal energy can be stored with negligible losses since heat is not kept in sensible or latent form but as a chemical compound (N'Tsoukpoe *et al.* 2009).

The concept of inter-seasonal heat storage is usually based on sensible heat technology due to the limited amount of cycles (one cycle per year) that are achieved in the lifetime of the system and the relatively low construction costs. These systems, due to the large volume usually required, are typically placed in the ground and are commonly referred as Underground Thermal Energy Storage (UTES) systems. They are implemented in four main ways: aquifers, boreholes, caverns and water tanks/pits (Xu *et al.* 2014). Further details on these systems will be presented later in Chapter 2.

1.2 Aims and objectives

The overall aim of this research is to focus on methods and factors affecting the performance of an inter-seasonal thermal system (e.g. snow surface and ground freezing presence). Possibilities of improving the performance of such system was explored both experimentally and numerically with an exploration provided for the use of the proposed method on other systems. In accordance with that, the main objectives of this study are:

1) To provide a state-of-the-art review of the research related to near surface ground energy storage systems.

2) To develop a general transient three-dimensional theoretical framework of the transient processes of storage and extraction of thermal energy from the ground and extend it to incorporate snow/ice cover and general freezing.
3) To develop a numerical solution of the above theoretical framework using the finite element method for spatial discretization and a finite difference time-stepping method with the aid of a program scripted in C++ language.
4) To measure and compare key material properties where necessary.
5) To develop and build a new experimental device that will involve practical implementation of adaptable thermal insulation.
6) To identify the impact that relevant factors occurring on the soil surface (e.g. surface snow presence) have on the potential thermal energy stored in the ground.
7) To investigate the impact of ground freezing on the potential thermal energy stored in the ground and validate the numerical model against an experimental case study.
8) To investigate the impact of snow accumulation at the soil surface has on the potential thermal energy stored in the ground and validate the numerical model against an experimental case study.
9) To explore the use of the novel proposed system of controlling thermal properties on different system performances.

1.3 Scope and limitations of the study

In this thesis, a numerical model is proposed to study the transient behaviour of buried engineering devices for storage and extraction of thermal energy in shallow regions. The model was constructed using the finite element method and can solve the transient heat transfer equation in soil. The model takes into account the presence of heat exchange devices buried in the ground and the transport of heat inside them, and, between them and the soil. Moreover, the impact of surface snow cover and ground freezing on the system performance was also explored.

The main scope of the study is limited primarily to the interactions of thermal energy at the boundaries between the soil/snow surface with the atmosphere and between the soil with buried heat exchangers and their impact on the amount of energy stored in the ground. The model was validated using experimental data reported by (Transport Research Laboratory TRL) Carder *et al.* (2008), while, the use of adaptable insulation layer was investigated in this study and verified against the novel laboratory experimental test series.

1.4 Contents summary

The structure of the thesis and the summary of each chapter is summarized as follows:

- Chapter 2: Seeks to present targeted reviews of the main approaches used to estimate soil thermal properties, theoretical representation of solar collectors on highways and pavements, with special focus on the transfer of heat between horizontal pipes and soil, representation of heat transfer process at the soil/snow surface, heat transfer processes in the soil, analytical and numerical methods used in the estimation of soil temperature profiles, general freezing within soil and the study of thermal devices buried in the ground.
- Chapter 3: Presents the governing equations that describe the transfer of heat in soil and the flow of heat within pipe systems. The key assumptions made in the development of these equations are also introduced. The main heat transfer approaches considered at the soil/snow surface are fully described.
- Chapter 4: Presents the numerical solution of the partial differential equations that describe the heat transfer within soils and the advection of heat by a fluid using the finite element method. The general numerical implementation of different kinds of boundary conditions is also presented. Since the particular method of discretization adopted allows changes in mesh refinement between time steps in transient simulations, an algorithm for the selection of elements based on the gradient of the independent variable (e.g. temperature) is also presented.

- Chapter 5: Presents the experimental design and methodology of a new device to test an adaptable insulation layer. Results obtained using the design are presented in this chapter alongside the results obtained from the developed numerical model.
- Chapter 6: Shows the validation of the numerical model in 2D which was based on the work of Muñoz-Criollo (2014) and experimental results from full-scale test presented and reported by UK's Transport Research Laboratory (TRL) Carder *et al.* (2008) who performed an experimental study about the feasibility of implementing an inter-seasonal heat storage system. This experiment which was done under the auspices of the British Highways Agency, aimed to provide maintenance to road surfaces by preventing the formation of frost that otherwise would be hazardous to road users. The main objectives of this chapter are to assess the impact of the ground freezing and surface snow availability on the system.
- Chapter 7: Provides an exploration of use for the developed and validated numerical model on certain case studies which demonstrate the effectiveness of the proposed novel system.
- Chapter 8: Presents the overall conclusions of the study and discuss possible future work.
- Appendix A: Presents thermal properties of a fluid commonly used in thermal engineering applications: water-ethylene-glycol mixtures.
- Appendix B: Explores the impact of varying fluid temperature and mean velocities on the convective heat transfer coefficient between the walls of a pipe and the fluid flowing inside it.

1.5 References

Bobes-Jesus, V., Pascual-Muñoz, P., Castro-Fresno, D. and Rodriguez-Hernandez, J. 2013. Asphalt solar collectors: a literature review. *Applied Energy.* 102, pp. 962-970. DOI: 10.1016/j.apenergy.2012.08.050.

Carder, D. R., Barker, K. J., Hewitt, M. G., Ritter, D. and Kiff, A. 2008. *Performance of an interseasonal heat transfer facility for collection, storage, and re-use of solar heat from the road surface*. Transport Research Laboratory.

Chen, M. Z., Wei, W. and Wu, S. P. 2009. On cold materials of pavement and high-temperature performance of asphalt concrete. *Materials Science Forum.* 620-622, pp. 379-382. DOI: 10.4028/www.scientific.net/MSF.620-622.379.

International Renewable Energy Agency and International Energy Agency. 2013. *Thermal Energy Storage - Technology Brief E17. IRENA-IEA-ETSAP* [Online]. Available at:http://www.irena.org/DocumentDownloads/Publications/IRENA-ETSAP%20Tech%20Brief%20E17%20Thermal%20Energy%20Storage.pdf [Accessed: 01/01/2018].

Kroll, J. A. and Ziegler, F. 2011. The use of ground heat storages and evacuated tube solar collectors for meeting the annual heating demand of family-sized houses. *Solar Energy.* 85(11), pp. 2611-2621. DOI: 10.1016/j.solener.2011.08.001.

Letcher, T. M. 2016. *Storing energy: with special reference to renewable energy sources*. Elsevier Science.

Morita, K. and Tago, M. 2000. Operational characteristics of the gaia snow-melting system in Ninohe, Iwate, Japan. *Geo-Heat Center.* 21(4), pp. 5-11. DOI.

Muñoz-Criollo, J. J. 2014. *An investigation of inter-seasonal near-surface ground heat transfer and storage.* Ph.D. thesis, Cardiff University, http://orca.cf.ac.uk/73226/.

N'Tsoukpoe, K. E., Liu, H., Le Pierrès, N. and Luo, L. 2009. A review on long-term sorption solar energy storage. *Renewable and Sustainable Energy Reviews.* 13(9), pp. 2385-2396. DOI: 10.1016/j.rser.2009.05.008.

Pomianowski, M., Heiselberg, P. and Zhang, Y. 2013. Review of thermal energy storage technologies based on PCM application in buildings. *Energy and Buildings.* 67(Supplement C), pp. 56-69. DOI: 10.1016/j.enbuild.2013.08.006.

UK Department of Business Energy & Industrial Strategy. 2016. *Evidence Gathering: Thermal Energy Storage (TES) Technologies* [Online]. https://www.gov.uk/. Available at:https://www.gov.uk/government/uploads/system/uploads/attachment_data/file/545249/DELTA_EE_DECC_TES_Final_1_.pdf [Accessed: 05/02/2018].

UK Department of Energy and Climate Change. 2011. *UK renewable energy roadmap* [Online].https://www.decc.gov.uk/. Available at: https://www.gov.uk/government/uploads/system/uploads/attachment_data/file/48128/2167-uk-renewable-energy_-roadmap.pdf [Accessed: 01/01/2018].

Xu, J., Wang, R. Z. and Li, Y. 2014. A review of available technologies for seasonal thermal energy storage. *Solar Energy.* 103(Supplement C), pp. 610-638. DOI: 10.1016/j.solener.2013.06.006.

Chapter 2: Literature Review

2.1 Introduction

The topics of heat transfer and thermal and hydraulic properties of soils have been subjected to many studies and publications due to their importance, with significant contributions provided by many authors. Hillel (2003), Arya (2001) and Koorevaar *et al.* (1983) discuss in detail both the transfer of thermal energy in soils and how to estimate temperature profiles without taking moisture movement into account. Deb *et al.* (2011), Vasco (2010), Grifoll *et al.* (2005), Fredlund and Rahardjo (1993), Winterkorn (1962) and de Vries (1958) provide useful contributions on the transport of moisture under non-isothermal conditions. Furthermore, Zhang and Wang (2017), Alrtimi *et al.* (2016), Pielke (2013), Reeves *et al.* (2006), Hillel (2005), Farouki (1981) and de Vries (1963) study both the thermal and hydraulic properties of soils. In many cases, the authors provide thorough reviews of the thermal properties of soil as a function of moisture content and/or degree of saturation. Other authors provide the fundamental theoretical framework for moisture movement for unsaturated soil (Grant 2005 ; Haverkamp *et al.* 1998 ; Fredlund and Rahardjo 1993 ; Maidment 1993).

Singh *et al.* (2011) provide an encyclopaedia that thoroughly reviews in detail a broad spectrum of topics in various aspects of snow, ice and glacier. The physical and surface properties are covered among other subjects in the context of this book.

In light of the extensive coverage offered in the literature the aim of this chapter is to present a targeted review for the following subjects which have particular relevance to the present study:
(i) approaches to estimate soil thermal properties and the main factors that affect heat transfer, (ii) theoretical representation of solar collectors for pavements and highways, with a particular focus on the heat transfer between horizontal pipes and soil, (iii) representation of the process of heat transfer at the soil surface, (iv) heat transfer process in soils, and (v) analytical and numerical methods applied in the

estimation of soil temperature profiles alongside the study of thermal devices buried in the ground (which are used for thermal energy storage and extraction).

This chapter is subdivided into the following sections:

- Section 2.2 discusses the heat transfer in soils and the factors affecting it, heat transfer processes are discussed in this section alongside soil thermal properties with a special attention for the specific heat capacity and thermal conductivities, the major methods of calculating thermal conductivity are presented in here as well.
- Section 2.3 discusses the types of thermal energy storage systems with a detailed description for the underground thermal energy storage system. Variable methods for controlling energy flow into ground were discussed as well.
- Section 2.4 deals with the energy balance interaction between the soil and atmosphere, different scenarios of surface cover are discussed, the convective and evaporative coefficients are presented for turbulent and non-turbulent conditions and longwave heat transfer coefficient is discussed as well.
- Section 2.5 is dedicated to discuss the impact of freezing on heat transfer in soils.
- Predicting temperature variations in soil profile using the analytical or numerical methods are presented in Section 2.6
- Section 2.7 is allocated for chapter conclusion remarks.
- Section 2.8 summarizes the chapter references.

2.2 Heat transfer in soils and factors affecting it

Thermal energy transfer in a porous medium occurs via the main processes of; heat conduction, radiation, heat of wetting, latent heat transferred by vapour movement and heat convection.

- Conduction is considered the most common method of transmitting energy, and occurs regularly in nature. This transfer occurs at the molecular level (from one

body to another) when heat energy is absorbed by a surface and causes the molecules of that surface to move more quickly. In the process, they bump into their neighbours and transfer the energy to them, this process will continue as long as heat is still being added. The process of heat conduction depends on four basic factors: the temperature gradient, the cross section of the materials involved, their path length, and the properties of those materials.

- Thermal radiation, is a process by which energy, in the form of electromagnetic radiation, is emitted by a heated surface in all directions and travels directly to its point of absorption at the speed of light (i.e. it does not require an intervening medium to carry it). Thermal radiation wavelength ranges from the longest infrared rays through the visible-light spectrum to the shortest ultraviolet rays. The intensity and distribution of radiant energy within this range is governed by the temperature of the emitting surface.
- Latent heat is the required quantity of heat absorbed or released by a substance undergoing a change of state, for example ice changing to water or water to gas. It happens in soil when the available moisture undergoes a phase change due to changes in temperature. Its effect has an important relevance in some cases (e.g. for vapour-dominated flow mechanisms) like in semi-arid and arid regions where soils dry rapidly (Feddes *et al.* 1988). Another important example relates to soil freeze-thaw behaviour where it can have a considerable influence on the thermal response of the soil (thermal conductivities assumed constant in frozen, frozen fringe and unfrozen zone) (Thomas *et al.* 2009).
- Heat of wetting, is the heat released by a unit mass of initially dry soil when mixed with water and it is related to the soil's specific surface (i.e. the content and composition of the clay fraction) (Gliński *et al.* 2011).
- Heat convection is associated with soil's air or moisture movement without phase change. It is induced either by thermal, mechanical or pressure gradients. In most cases, its value is neglected as it is usually very small except under very humid conditions (de Vries 1958).

Many authors assume that the dominant heat transfer process within soils is conduction and the relative importance of the others could vary depending on the

problem specific conditions and the moisture movement within which. Other authors neglect the moisture effects on the thermal distribution and heat transfer in the soil (Grant 2005 ; Romero *et al.* 2001 ; Nobre and Thomson 1993).

The soil mixture composes of three main constituents, mainly solids, water and air and the thermal properties of soil are dependent on the soil moisture content. Pielke (2013), Sellers (1965) and Marshall *et al.* (1996) have studied the variation of thermal diffusivity (it is the ratio of the thermal conductivity to the volumetric heat capacity) and thermal conductivity of soils with moisture content. Garratt (1994) on the other hand, offered a summary of their studies and provides a list of representative values for bulk thermal conductivity (λ_b), bulk specific heat capacity (c_b), bulk density (ρ_b) and bulk thermal diffusivity α_b for various types of soil at three water contents that cover the range from saturated to dry conditions.

Table (2.1) shows values taken from Garratt (1994) for clay soils. It is easily noticed that the variations of density and specific heat capacity are mostly linear, while the variations in bulk thermal conductivity and bulk thermal diffusivity are non-linear having the strongest changes close to the dry range of moisture content (Rees *et al.* 2000).

$\boldsymbol{\theta_w}$	$\boldsymbol{\lambda_b}$ (W/mK)	$\boldsymbol{c_b}$ (J/kgK)	$\boldsymbol{\rho_b}$ (kg/m^3)	$\boldsymbol{\alpha_b}$ (m^2/s)
0	0.25	890	1600	0.18
0.2	1.1	1170	1800	0.52
0.4	1.6	1550	2000	0.52

Table (2.1) Variation of thermal properties with WC for clay soils (Garratt 1994)

As presented earlier, heat transfer in soil is affected by the relative presence of soil constituents (i.e. solid, liquid and gaseous phases) as they in-turn impact the soil density, specific heat capacity and thermal conductivity. The next sections present common relations used to estimate the specific heat capacity and thermal conductivity of soils while relationships for soil density can be found in basic literature sources (e.g. Fredlund and Rahardjo 1993).

2.2.1 Thermal conductivity

Zhang and Wang (2017), Alrtimi *et al.* (2016), Barry-Macaulay *et al.* (2015), Pielke (2013), Reeves *et al.* (2006), Hillel (2005), Abu-Hamdeh (2003), Rees *et al.* (2000) and Farouki (1981) provide reviews and descriptions of the main approaches to estimate thermal conductivity in soils. In general, they agree (as stated before) that conduction is the dominant thermal process within soils and that is commonly used in thermal energy balances at the soil surface to represent thermal energy transferred between the atmosphere and the ground.

The study performed by Zhang and Wang (2017) provide a recommendation for using three main equations to predict soil thermal conductivity presented by Zhang *et al.* (2015), Haigh (2012) and Chen (2008) which would be discussed later amongst others. On the other hand, Alrtimi *et al.* (2016) investigate the effect of porosity and degree of saturation on the thermal conductivity of a sandy soil through conducting 20 thermal experiments at different porosity and saturation values. Their results have shown that the thermal conductivity increases as the degree of saturation increases especially at low degree of saturations' ratio (less than 10 %).

Barry-Macaulay *et al.* (2015) evaluate four thermal conductivity methods by comparing their performance against experimental results obtained from 27 different soils prepared at a range of saturation levels and densities. The study recommends using Côté and Konrad (2005) (discussed later) method for predicting thermal conductivity value for coarse grained soil.

Rees *et al.* (2000) suggest the possibility of defining a bulk thermal conductivity through averaging the thermal conductivities of the mixed elements available in the soil. The calculation of thermal conductivity is comparable to calculating the electrical conductivity when more than one resistance is present.

The thermal conductivity would depend on the arrangement of the constituents besides their relative presence. Three scenarios can be summarized following this idea:

First scenario is when the soil constituents can be assumed to have a distribution that is parallel to heat flow, the soil bulk thermal conductivity can be expressed as a weighted arithmetic mean (Woodside and Messmer 1961):

$$\lambda_b = \sum_i \chi_i \lambda_i \tag{2.1}$$

where χ_i and λ_i (W/mK) are the volume fraction and thermal conductivity of constituent i and λ_b is the resulting average bulk thermal conductivity of soil. The volume fraction of constituent i is given by:

$$\chi_i = \frac{V_i}{V} \tag{2.2}$$

where V_i (m^3) is the volume occupied by constituent i and V (m^3) is the total volume of soil.

Second scenario is when the constituents can be assumed to follow a series distribution with respect to the direction of heat flow, the thermal conductivity of the soil is given as a harmonic mean (Woodside and Messmer 1961):

$$\lambda_b = \frac{\prod_i \lambda_i}{\sum_i \chi_i \lambda_i} \tag{2.3}$$

where Π and Σ are symbols to represent product and sum of multiple terms.
Woodside and Messmer (1961) concluded that equations (2.1) and (2.3) tend to over-estimate and under-estimate, respectively, the soil thermal conductivity. The possible explanation of this deviation might be related to the fact that the soil constituents are more likely to be randomly distributed rather than following a perfect series or parallel distribution.

Woodside and Messmer (1961) found an alternative approach (third scenario) that offers an intermediate result between the arithmetic and geometric approaches which is shown as:

$$\lambda_b = \Pi \lambda_i^{\chi_i} \quad (2.4)$$

The following paragraphs are covering some of the main equations used to predict the thermal conductivity of soils with varying degree of saturations and dry densities.

- Johansen (1975) proposed a mathematical expression to predict the thermal conductivity for saturated soils is as follows:

$$\lambda_{sat} = \lambda_s^{1-n} \lambda_w^n \quad (2.5)$$

where λ_s and λ_w (W/mK) are soil solids and water thermal conductivity respectively and n is the porosity of soils. Johansen (1975) also proposed an equation to predict thermal conductivity of dry soils

$$\lambda_{dry} = \frac{0.137\rho_d + 64.7}{2650 - 0.947\rho_d} \quad (2.6)$$

where ρ_d (kg/m^3) is the dry density of soils and the density of soil solids is 2650 kg/m^3.

Johansen's model was the first model to introduce the concept of normalized thermal conductivity (or what also known as Kersten number) and correlated it with the degree of saturation. The effect of soil type, moisture content, porosity and mineralogy on thermal conductivity can be reflected on this relationship which is expressed as:

$$\lambda_r = \frac{\lambda - \lambda_{dry}}{\lambda_{sat} - \lambda_{dry}} \quad (2.7)$$

where λ_{sat} and λ_{dry} (W/mK) are the soil thermal conductivities under fully saturation and dry condition respectively. It is obvious from equation (2.7) that when the soil is totally dry $\lambda_r = 0$ while $\lambda_r = \lambda_{sat}$ for fully saturated condition.

Furthermore, Johansen (1975) obtained several $\lambda_r - S_r$ relationships through fitting experimental data done by Kersten (1949), for a sandy soil it is:

$$\lambda_r = 0.7 \log S_r + 1 \quad (2.8)$$

Finally, using the equations presented earlier, the model thermal conductivity could be expressed as:

$$\lambda = \left(\lambda_w^n \lambda_s^{1-n} - \frac{0.137\rho_d + 64.7}{2650 - 0.947\rho_d}\right)(0.7\ log\, S_r + 1) + \frac{0.137\rho_d + 64.7}{2650 - 0.947\rho_d} \qquad (2.9)$$

It is important to note that this equation is valid only for saturation ratios above 5 %, as below this level it can predict negative thermal conductivities.

- Donazzi (1977) used the following exponential function based on laboratory experiments to express the relationship of thermal resistivity ρ_r (the inverse function of thermal conductivity), with porosity n and degree of saturation S_r

$$\rho_r = \left(\frac{1}{\lambda_w}\right)^n \left(\frac{1}{\lambda_s}\right)^{1-n} exp[3.08n(1 - S_r)^2] \qquad (2.10)$$

where λ_w (W/mK) is the thermal conductivity of still water with a value of 0.588, λ_s (W/mK) is the thermal conductivity of solid grains.

It should be noted that Donazzi (1977) quote the thermal conductivity of sand grains as being 4 (W/mK) rather than the value of 7.5 (W/mK) used by Chen (2008).

- Côté and Konrad (2005) modified the Johansen (1975) model in order to eliminate the logarithmic dependence on saturation ratio, that causes the distorted predictions at low degrees of saturation. Their proposed modified formula is:

$$\lambda = (\lambda_w^n \lambda_s^{1-n} - \chi 10^{-\eta n})\left[\frac{iS_r}{1 + (i-1)S_r}\right] + \chi 10^{-\eta n} \qquad (2.11)$$

where χ (W/mK) and η account for particle shape effects, and i accounts for soil texture effects. They suggested different values for these three parameters depending on the soil type. For a fine and medium sands consisting of crushed rock particles the values are 3.55 for i, 1.7 for χ and 1.8 for η.

- Lu *et al.* (2007) also proposed a modification of Johansen (1975) model and uses the following equation for the estimation of the thermal conductivity of sandy soils:

$$\lambda = [(\lambda_w)^n (\lambda_s)^{1-n} - (b - an)]exp\left[\kappa\left(1 - {S_r}^{\kappa - 1.33}\right)\right] + (b - an) \quad (2.12)$$

where a, b and κ are empirical parameters and the suggested values for sandy soils are 0.56, 0.51 and 0.96, respectively.

- Based on laboratory investigation of sandy soil, Chen (2008) proposed an empirical equation of thermal conductivity expressed as a function of porosity and degree of saturation where he performed 80 needle-probe experimental tests on four types of sandy soils with different degrees of saturation at different porosities. He proposed the following equation:

$$\lambda = (\lambda_w)^n (\lambda_s)^{1-n}[(1 - 0.0022)S_r + 0.0022]^{0.78n} \quad (2.13)$$

- Haigh (2012) proposed an analytical model based on unidirectional heat flow through a three-phase soil element. The model analyses the one-dimensional heat flow between equally sized spherical soil particles of radius R, arranged in different dell structure. According to this procedure, the overall thermal conductivity can be expressed as the following:

$$\frac{\lambda_b}{\vartheta\lambda_s} = 2(1+\xi)^2\left[\frac{\alpha_w}{(1-\alpha_w)^2} ln\frac{(1+\xi)+(\alpha_w-1)}{\xi+\alpha_w}\right.$$

$$\left. + \frac{\alpha_a}{(1-\alpha_a)}\ln\frac{(1+\xi)}{(1+\xi)+(\alpha_a-1)x}\right] \quad (2.14)$$

$$+ \frac{2(1+\xi)}{(1-\alpha_w)+(1-\alpha_a)}[(\alpha_w-\alpha_a)x-(1-\alpha_a)\alpha_w]$$

where ϑ is cell structure parameter and equals 1 for simple cubic cell and 1.58 for face centred ones, ξ, α and x are given by:

$$\xi = \frac{2e - 1}{3} \tag{2.15}$$

$$\alpha_w = \frac{\lambda_w}{\lambda_s} \tag{2.16}$$

$$\alpha_a = \frac{\lambda_a}{\lambda_s} \tag{2.17}$$

$$x = \frac{(1 + \xi)}{2}\left(1 + cos\,\theta - \sqrt{3}\,sin\,\theta\right) \tag{2.18}$$

and θ is given by:

$$cos\,3\theta = \frac{2(1 + 3\xi)(1 - S_r) - (1 + \xi)^3}{(1 + \xi)^3} \tag{2.19}$$

where α_w and α_a are the thermal conductivities, normalized by that of the soil solids, of water and air respectively, as found in equation (2.16) and (2.17).

Finally, the degree of saturation defined as:

$$S_r = \frac{2x^3 - 3(1 + \xi)x^2 + 3\xi + 1}{1 + 3\xi} \tag{2.20}$$

- Zhang *et al.* (2015) modified Côté and Konrad (2005) model for sand with extremely high quartz content by fitting the experimental data obtained by the thermo-TDR probe method. Their suggested values of x, χ and η are 6.0, 8.12, 3.28, respectively. Figure (2.1) shows the graphical comparisons of the previously listed methods.

In the model prediction, thermal conductivities of solid, water and air are assumed to be 8.79 (W/mK), 0.57 (W/mK) and 0.025 (W/mK), respectively (Rees *et al.* 2000). It should be noted that Johansen (1975), and Lu *et al.* (2007) models cannot be applied to dry soils and that Haigh (2012) model is based on analytical solutions which may cause the differences relative to other models.

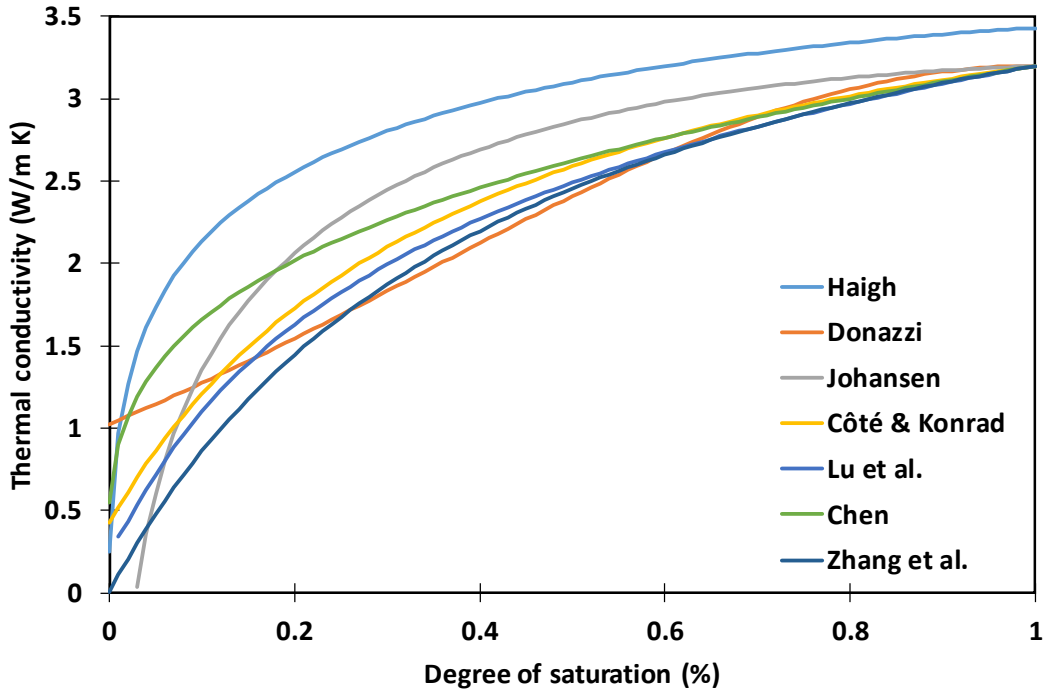

Figure (2.1) Predicted thermal conductivity of sands using different degree of saturations at ($n = 36.9\ \%$)

2.2.2 Specific heat capacity

The specific heat capacity of a material c_p (J/kgK), is defined as: the amount of thermal energy required to change by 1 K the temperature of 1 kg of the material at constant pressure (Çengel 2007). At a constant pressure it is possible to introduce an associated quantity that is the volumetric heat capacity, H_c (J/m^{3}K), which is defined as: the amount of thermal energy required to change the temperature by 1 K of one unit of volume of material (m^3) (Çengel 2007).

Different authors (Hillel 2005 ; Garratt 1994 ; Fredlund and Rahardjo 1993) provides a similar expression to estimate the soil volumetric heat capacity at constant pressure based on the specific heat capacities of the soil constituents weighted by their corresponding densities, and it is expressed as:

$$H_c = \chi_s c_s \rho_s + \chi_w c_w \rho_w + \chi_a c_a \rho_a \qquad (2.21)$$

where χ, ρ and c represent the volume fractions (Equation(2.22)), density (kg/m^3) and specific heat capacity (J/kgK) respectively; while the subscript s, w and a stand for solid, water and air respectively.

The volume fractions are defined as follow:

$$\chi_i = \frac{V_i}{V} \tag{2.22}$$

where V_i (m^3) is the volume occupied by the constituent (i) and V (m^3) is the total volume. Equation (2.21) shows that the volumetric heat capacity is related to the degree of saturation of the soil because of the inclusion of the volume fraction of water χ_w.

Alternatively, if an experimental means being used (e.g. the bulk specific heat capacity suggested by ASTM (2008)) then the volumetric heat capacity can be expressed as:

$$H_{c,b} = \rho_b c_b \tag{2.23}$$

where ρ_b (kg/m^3) is the soil bulk density and c_b (J/kgK) is the soil bulk specific heat capacity.

2.3 Thermal Energy Storage (TES) systems

Thermal energy storage (TES) systems are considered amongst the most effective as they effectively addresses the mismatch problem between the supply and demand of energy (Cabeza 2014). The main two types of TES systems, sensible (e.g., water and rock), latent (e.g., water/ice and salt hydrates) and thermo-chemical as described below. The selection of a TES system would mainly depend on the required storage period (whether it was for diurnal or seasonal application) and the operating conditions. Examples of TES systems are: (i) storage of solar energy for night and weekend use, (ii) storage of summer heat for winter space heating, and (iii) ice based storage from winter for space cooling in summer. TES deals with the storage of energy through different manner such as: cooling, heating, melting, freezing a material. The

effectiveness of TES depends majorly on the material properties. Sensible storage systems commonly use rocks, ground, or water as the storage medium, and the thermal energy is stored by increasing the medium temperature (UK Department of Energy and Climate Change 2011). On the other hand, latent heat storage systems store energy in phase change materials (PCMs), with the thermal energy stored when the material changes phases (usually from a solid to a liquid). The specific heat of solidification/fusion or vaporization and the temperature at which the phase change occurs are of importance in terms of system design (Cabeza 2014). The thermo-chemical storage systems uses reversible chemical reactions to store thermal energy in chemical bonds. Under the influence of a heat supply, a chemical compound is dissociated into its components which can be then stored separately. When these components are put in contact, the chemical compound is restored with a heat release. With this process, thermal energy can be stored with negligible losses since heat is not kept in sensible or latent form but as a chemical compound (N'Tsoukpoe *et al.* 2009). Furthermore, Letcher and Reay (2016) discusses the available storing methods with special reference to renewable energy sources.

2.3.1 Underground Thermal Energy Storage (UTES)

Underground thermal energy storage (UTES) uses the ground to store heat and cold. There are different types of storage systems such as, ATES (aquifer TES), BTES (boreholes TES) which are named after the type of storage system. In ATES systems, groundwater is used to move thermal energy to and from an aquifer, using water wells and storing the heat in the groundwater and in the solid mass around it (Andersson 2007). On the other hand, BTES systems have several closely spaced boreholes that ranges between 50 and 200 m deep where they act as heat exchangers to the underground, usually in U-pipe form (Andersson 2007). Another UTES system is the energy piles, where the use of the building foundations as ground heat exchangers is implemented (de Moel *et al.* 2010 ; Nagano 2007). This approach is widely used in Japan (Nagano 2007) and Australia (de Moel *et al.* 2010) and has been found to provide cost reduction in the construction of the ground heat exchangers. Another

important soil storage system which transfer heat between pipes that is embedded under highways and pavements.

An additional way of implementing UTES is via using horizontal heat exchangers at shallower depths. Kupiec *et al.* (2015) analysed heat transfer in a horizontal ground heat exchanger through providing a 1D mathematical model of transient heat conduction equation with an internal source of heat that describes the operation of a horizontal heat exchanger at a depth of 1.14 m and validated the results against the experimental results obtained by Wu *et al.* (2010). Wu *et al.* (2010) monitored the performance of a horizontal-coupled slinky ground source heat pump (GSHP) installed in the UK and used measured results to validate a Computational Fluid Dynamics (CFD) model. Their prediction showed the larger the diameter of coil, the higher the heat extraction per meter length of soil, while the heat extraction per meter length of soil decreased with the increase of coil central interval distance. In order to compare the impact of different pipe distributions in the performance of horizontal ground heat exchangers Congedo *et al.* (2012) performed a simulation study using the CFD code Fluent which covered one year of system operation, both in summer and winter for typical climate conditions of the South of Italy. They concluded that the slinky configurations offer advantages over the traditional straight arrangements and that the depth of installation of the horizontal ground heat exchangers did not play an important role on the system performance.

Liu *et al.* (2011) present an in-depth investigation of the role of ground heat transfer within the context of the urban heat island phenomenon through using numerical and experimental investigations. Shi *et al.* (2012) performed a year long experiment in China where the impact of the heat island effect on the average soil temperature and moisture content in shallow regions of the soil (<3 m) was studied. They revealed an obvious heat island effect in urban soil with average intensity of 2.02 °C over 1 year period. In order to avoid that phenomenon, Santamouris (2013) proposed two techniques namely passive and active. Those techniques harvest thermal energy through horizontal heat exchangers located under paved surfaces with the active techniques being more effective in harvesting.

Bobes-Jesus *et al.* (2013) provided an extensive review of the existing research on asphalt solar collectors and reported findings on asphalt solar collectors by identifying the main mechanisms involved in the solar energy collection process. They summarised the most important parameters and variables and focused on the thermal behaviour studies and different methodologies employed by other authors.

Using BTES, Zhou *et al.* (2015) built a small-scale pilot project with an automatic data acquisitions system to study the effectiveness of a pavement solar energy system. The system operated continuously in summer for 69 days (1656 hours) and in winter for 104 days (2496 hours). Their conclusion was that the amount of electrical energy required to circulate the water through the system was minimal compared to the thermal energy harvested. Also, it was possible to reduce the pavement surface temperature in summer, which helped to eliminate rutting of the pavement, while in winter the asphalt pavement absorbs heat from underground soil which effectively increases its temperature, cutting 32 % days of surface temperature below the freezing point. To increase this proportion, they suggest to only operate the system in times of snowy weather winter and only when freezing conditions appear on the surface instead of a continuous 24 hours' operation.

For heating or cooling applications, liquid or gas flow within pipes or ducts is generally used to transport heat energy, where the fluid is forced to flow by a fan or pump through a long tube to accomplish the desired heat transfer (Çengel 2007). General physical descriptions of internal flow (within a pipe for example) can be found in textbooks such as Holman (2010), Çengel (2007) and Roberson and Crowe (1989).

It is important to take note about an important variable that is usually associated with this process which is the heat convection coefficient that is defined as: the amount of thermal energy transferred between a surface and a moving fluid at a different temperature (Çengel 2007). Svec and Palmer (1989) and Svec *et al.* (1983) discusses the application of the theory of fluid flow in pipes in real ground heat exchangers for water based heat exchangers, whilst Krarti and Kreider (1996) deal with an air based heat exchanger. Soni *et al.* (2015) provide a detailed review for the experimental and modelling studies carried out on ground heat exchanger systems. The reviewed

literature focuses on performance of both types of GHE systems and brings out their pros and cons.

2.3.2 Methods to control energy flow into ground

It is of potential advantage in certain scenarios to control the thermal properties of system in hand in order to prevent problematic effects due to thermal changes. A good example is infrastructure built in permafrost regions which, as some studies predict, could be subjected to widespread collapse due to climate change impacts on thermal conditions in the soil (Perreault and Shur 2016).

Amongst studies investigating available techniques to preserve thermal properties is the numerical study proposed by Perreault and Shur (2016). The study focused on minimizing heat gains in permafrost regions through applying a thermal insulation layer placed on the soil surface in Spring and removed in Autumn to restrict Summer heat flow into the ground, their main intention was to keep the soil cooler and thus prevent any thawing effects disturbing the foundations in those regions. The same principle was reported by Duan and Naterer (2009) but using a phase change material to create thermal barrier that effectively reduces the temperature variation amplitude in the foundation, thereby alleviating the seasonal freezing and thawing cycles.

Vasiliev *et al.* (2017) discuss the use of a two-phase closed thermosyphons which represents a hermetic one-piece welded structure that is compound of a thin-walled tubular casing. The tubular casing cavity is partially filled with a working fluid (ammonia, propane, CO2, etc.) and its length can be from several to hundred meters and the diameter ranges from 20 to 300 mm. Thermosyphons are fabricated from carbon steel, stainless steel, aluminium allows. They concluded that thermosyphons applications could be extendable to more comprehensive applications.

Yu *et al.* (2016) discuss in detail the use of the two-phase thermosyphons method to prevent permafrost layers from degrading, and consequently ensure the stabilities of engineering constructions in those regions via studying road sections of Qinghai-Tibet

highway before and after installing the system, in particular they provide recommendations for better design of this system.

Another possibility to control the heat gain and to minimise the heat loss from the underground application via using a variable thermal conductivity layer inside the system. Those systems, however, are often considered as impractical or uneconomic for many underground applications were the systems are not easily accessible and/or are subjected to mechanical strains (Clark *et al.* 2013 ; Alderman 2003 ; Goodrich 1993).

Furthermore, the use of hydrophobic materials can prevent the water from penetrating into the soil stratum which in turn can affect the thermal properties through affecting the water content of the soil. Hydrophobic soils are created when hydrocarbon residue is created after organic material is burnt and soaks into empty pore spaces in the soils, making it impervious to water (e.g. wild fire)(Zheng *et al.* 2017).

Finally, Faizal *et al.* (2016) discuss methods available to enhance the heat exchange between the heat carrier fluid and the ground for geothermal energy piles. The suggested methods includes (i) reducing the total pile thermal resistance through geometrical optimization of the number of pipes and their arrangement, (ii) using Nanofluids as the heat carrier fluid to enhance the fluid conductive and convective heat transfer, (iii) highly thermally conductive fillers can be mixed with the pipe material to enhance its thermal conductivity and (iv) enhance the thermal properties of the concrete by adding highly thermo-conductive materials to the concrete mixture.

2.4 Energy balance at the soil/atmosphere interface

The analysis of the energy balance at the soil surface is an important and in some cases critical aspect in understanding and analysing for the process of inter-seasonal heat storage systems as it relates to determining how much thermal energy is transferred into the soil and is thus available for any thermal engineering

application. It would also determine how much energy will be lost between seasons to the atmosphere until the stored thermal energy is required.

According to Sauer and Horton (2005), the thermal energy balance at the soil surface can be expressed as:

$$q_G = q_S + q_L + q_C + q_{LE} \tag{2.24}$$

where q_G (W/m^2) is the energy transferred into the ground by thermal conduction. As mentioned in Section 2.2 thermal conduction is the main process by which thermal energy is transferred into the soil and its magnitude is defined by the balance of the other four heat transfer processes: shortwave radiation (q_S) (W/m^2), longwave radiation (q_L) (W/m^2), air convection (q_C) (W/m^2) and latent heat (q_{LE}) (W/m^2).

The solar radiation term is defined according to Duffie and Beckman (2013) as:

$$q_S = R(1 - \alpha_S) \tag{2.25}$$

where α_S is the solar albedo of the surface and R (W/m^2) is the global radiation which is a measurement commonly reported by meteorological stations (National Meteorological Library and Archive 2014) and is composed of direct and diffuse solar radiation. On the other hand, albedo is a dimensionless number that defines the ratio of reflected radiation to incident radiation and is a function of the optical properties of the surface (mainly the colour and roughness) (Çengel 2007).

Duffie and Beckman (2013) suggest that the surface can be considered as a relatively small surface that is enclosed by a larger surface (e.g. the sky) and provide an expression for this scenario of longwave radiation:

$$q_L = \varepsilon_s \sigma \left(T_{sky,K}^4 - T_{s,K}^4\right) \tag{2.26}$$

where ε_s is the longwave emissivity of the surface and σ is the Stefan-Boltzmann constant (equals to 5.6704x10^{-8} W/m^{2}K^4). $T_{s,K}$ (K) is the absolute temperature of the

surface. $T_{sky,K}$ (K) is the theoretical absolute temperature of the sky considered as a black surface.

Iziomon *et al.* (2003) propose the following relationship to relate the absolute sky temperature to the absolute air temperature:

$$T_{sky,K}^4 = \varepsilon_{sky} T_{a,K}^4 \tag{2.27}$$

where ε_{sky} is the longwave emissivity of the theoretical atmospheric surface and $T_{a,K}$ (K) is the absolute temperature of air (a summary of different expressions proposed for ε_{sky} are presented later in Section 2.4.3).

Edinger *et al.* (1968) and Penman (1948) showed that theoretical formulations for thermal convection and evaporation share a similar form, as thermal convection is driven by the temperature difference between the temperature of the surface and the air above ground, while evaporation is driven by the gradient of vapour pressures between the surface and the atmospheric air. They can be mathematically expressed as:

$$q_C = h_C(T_a - T_s) \tag{2.28}$$

$$q_{LE} = h_{LE}\left(e_{a,sat} - e_s\right) \tag{2.29}$$

where h_C (W/m^{2}K) and h_{LE} (W/m^{2}kPa) are convective and evaporative heat transfer coefficients respectively, $e_{a,sat}$ (kPa) is the atmospheric saturation vapour pressure and e_s (kPa) is the water vapour pressure at the saturated surface.

Two possible formulations for these coefficients depending on the assumptions made for the atmospheric boundary layer are presented later in Section 2.4.2.

2.4.1 Influence of surface cover

Soil surface characteristics directly impacts certain aspects of the process of heat transfer between the soil and the atmosphere. The optical properties of the

surface influence the solar and infrared heat transfers while its roughness and moisture content influence convective and latent heat transfers. In addition, all these processes are affected by the presence of vegetation or snow surfaces (Duffie and Beckman 2013). The representation of four different surface scenarios relevant for the problems studied in this work are reviewed in the following subsections. These are: bare soil, soil covered by asphalt, soil covered with vegetation and soil covered by snow.

2.4.1.1 Bare Soil

Many authors have studied the process of heat transfer between bare soils and the atmosphere, among which Bittelli *et al.* (2008), Hillel (2003), Alvenäs and Jansson (1997) and Penman (1948). If the soil surface is not covered by any layer, the characteristics of the material that compose the soil would play an important role in the surface heat balance formulation (e.g. roughness).

Garratt (1994) provided values for the solar and infrared optical properties used in equations (2.25) and equation (2.26) for wet and dry surface conditions. The solar albedo for a soil composed of clay which is given by:

$$\alpha_S = 0.2 - 0.35 \text{ (dry clay)} \tag{2.30}$$

$$\alpha_S = 0.1 - 0.2 \text{ (wet clay)} \tag{2.31}$$

Herb *et al.* (2008) suggest a similar value for soil:

$$\alpha_S = 0.15 \tag{2.32}$$

On the other hand, for longwave optical properties Garratt (1994) and Herb *et al.* (2008) proposed the following values:

$$\varepsilon_{ss} = 0.95 \text{ (dry clay)} \tag{2.33}$$

$$\varepsilon_{ss} = 0.97 \text{ (wet clay)} \tag{2.34}$$

For saturated conditions, Penman (1948) offered an analysis for the case of the evaporative heat transfer process by suggesting a combination between two theoretical approaches in order to make theoretical estimates of evaporation rates out from standard meteorological data. Philip and de Vries (1957) modified this method to consider the possibility of unsaturated soil surface conditions through modifying the term corresponding to the surface vapour pressure (assumed saturated by Penman) in the following way:

$$e_{ss} = exp\left(-\frac{h_{ss}g}{R_w T_{ss,K}}\right) e_{ss,sat}(T_{ss}) \tag{2.35}$$

where h_{ss} (m) is the pressure head at the soil surface, g (9.81 m/s^2) is the acceleration due to gravity, R_w (461.5 J/kgK) is the gas constant for water vapour, $e_{ss,sat}$ (kPa) is the saturation vapour pressure at the soil surface and T_{ss} (K), $T_{ss,K}$ (K) are the temperature and absolute temperature of the soil surface.

Boast and Simmons (2005) and Alvenäs and Jansson (1997) point out the importance to estimate the moisture availability at the surface in relation to the evaporative heat transfer process with the latter study focuses on the unsaturated surfaces.

Mahfouf and Noilhan (1991) provide a comparison between two main expressions, that is classical bulk aerodynamic method α-method and threshold formulation method β-method and test them both against in situ data. The α-method is given by:

$$e_{ss} = \alpha e_{ss,sat}(T_{ss}) \tag{2.36}$$

where the coefficient α represents the relative humidity of air at the surface.

In the β-method the whole process of evaporation is described from the water level to the atmosphere. In this method equation (2.29) can be expressed as:

$$q_{LE} = h_{LE}\beta(e_a - e_{ss}) \tag{2.37}$$

Both coefficients α and β are functions of soil water content that compensate for the changes in soil surface humidity during drying.

Another parameter that influences the amount of evaporation and convection are the convective and latent heat transfer coefficients h_C and h_{LE} presented earlier in equations (2.28) and (2.29) (defined later in this section). A theoretical formulation presented by Garratt (1994) shows how these parameters are a function of the dynamic roughness of the soil z_0 (m), the momentum roughness, z_m (m) and the roughness lengths for sensible heat and vapour transfer, z_T (m).

The dynamic roughness z_0 is a measure of the surface irregularities while the momentum roughness, z_m, represents the height at which the wind speed considered to be zero (assuming that the wind follows a logarithmic profile with height) and it depends on the conditions at the lower atmospheric boundary layer and how it interact with the surface roughness.

Garratt (1994) offers different values of surface roughness lengths for a range of natural surfaces of four sites which are as follows:

$$z_0 = 0.001 - 0.01 \tag{2.38}$$

Garratt (1994) mentions that the value of z_m, for relatively rough surfaces (most of earth's surfaces been considered in this category including bare soil surfaces), can be assumed equal to the surface roughness:

$$z_m = z_0 \tag{2.39}$$

While regarding the roughness lengths for sensible heat, z_T, ASCE Hydrology Handbook (1996) recommended that for most agricultural surfaces, their values can be considered to be proportional to z_m:

$$z_T = 0.1 z_m \tag{2.40}$$

This value lies between those related to smooth surfaces and permeable-rough (vegetated) surfaces and it agrees well with experiments carried out by Kubota and Sugita (1994) in a pasture field during a growing. Using a radiometric determination, he shows that the scalar roughness for sensible heat flux may vary over a range of 10^{-1} to 10^{-7} (m) both diurnally and seasonally.

Recent studies performed by (Muñoz-Criollo *et al.* 2016b) dealt with this case alongside others using a numerical approach and compare the results to a large-scale experiment. The main finding was that correct representation of the heat transfer processes occurring at the soil surface is of critical importance.

2.4.1.2 Pavement/Bituminous Cover

Jansson *et al.* (2006) provide solar optical properties for dry and wet paved surfaces. The solar albedo used by them is given by:

$$\alpha_S = 0.1 \quad \text{(dry pavement)} \tag{2.41}$$

$$\alpha_S = 0.1 - 0.2 \quad \text{(wet pavement)} \tag{2.42}$$

Herb *et al.* (2008) on the other hand, offer a general value without specifying if the surface is wet or dry:

$$\alpha_S = 0.12 \tag{2.43}$$

In relation to infrared optical properties Jansson *et al.* (2006) assumes the paved surface as perfect black body:

$$\varepsilon_s = 1 \tag{2.44}$$

while Herb *et al.* (2008) offers a slightly lower value:

$$\varepsilon_s = 0.94 \tag{2.45}$$

Scholz and Grabowiecki (2007) suggest that the type of pavement should be taken into consideration whether it is impermeable, porous or permeable pavements in order to correctly address the evaporation from the pavement. The asphalt could be considered as porous surface with a moisture content of 5 % (Jansson *et al.* 2006) while Herb *et al.* (2008) assumes that it is impervious surface and neglect evaporation except during rainfall events (during which the surface is assumed to be saturated).

Chen *et al.* (1999) provide values for the aerodynamic characteristics of pavements for momentum roughness (z_m) and heat roughness (z_T) as follows:

$$z_m = 5 \times 10^{-4} \quad (2.46)$$

$$z_T = 1 \times 10^{-4} \quad (2.47)$$

2.4.1.3 Soil with Vegetation Cover (Grass, Tall Grass, Crops)

Another scenario for the soil surface occurs when it is covered partially by vegetation, often the approach taken is to adopt Herb *et al.* (2008) which in turns based on the works of Deardorff (1978) and Best (1998), however, the work of Herb *et al.* (2008) is a frequently cited example of this.

The Deardorff model includes a separate heat balance equation for the plant canopy, a canopy temperature, and a distinct air temperature and humidity within the canopy. The canopy model is similar to the model used by Best (1998), which is a simplified version of the Deardorff model. The convective and evaporative heat flux components between the ground and the canopy are assumed to be negligible to eliminate the need to calculate a separate air temperature and humidity within the plant canopy.

Deardorff (1978) assumes the presence of a single layer of vegetation with negligible heat capacity on top of soil. The density of the cover is characterized by the average area shielding factor, ν which varies from 0 to 1. If ν=0 then the soil is completely exposed with no vegetation cover while if the value is 1 then it will indicate that the soil is completely covered by vegetation as it corresponds to a leaf area index of

approximately 7 (Deardorff 1978). It is obvious that ν is a function of the type of vegetation present on top of the soil.

Geiger (1950) provides an estimation for the values of ν for different plant types based on the measurement of Ångström (1925). These measurements indicate that the vegetation density (thus, the amount of solar radiation that reaches the ground) varies seasonally due to the natural process of seasonal grow and decay (or sow and harvest) of most types of vegetation.

Vogel *et al.* (1995) provide a comparison of heat transfer canopy models including the model of Deardorff (1978). Their conclusion was that the model has the best relative performance for sensible heat plus it considers the radiative transfers (short and long) and turbulent transfers of heat and moisture between the vegetation canopy-soil-atmosphere system and the thermal energy transferred to the ground by conduction. However, that indicates the need for more details regarding the structure and properties of the vegetation.

Best (1998) produced a simplified version of Deardorff (1978) model. The main characteristics of Best (1998) model that it neglects the turbulent heat transfer interactions between the soil surface and the canopy cover for a relatively dense vegetation and also, unlike Deardorff (1978) model he considers the heat capacity of the canopy layer even though he assumes it as a very small value (Herb *et al.* 2008).

The suggested model of Herb *et al.* (2008) accepted the simplification proposed by Best (1998) but neglects the heat capacity of the canopy layer as suggested by Deardorff (1978).

Herb *et al.* (2008) model is developed via two equations one to predict the magnitude of the radiative, convective, conductive and latent heat fluxes at a dry or wet surface, using standard climate data as input while the other one is to model the effect of plant canopies for vegetated land surfaces.

The equation for the canopy cover is given by:

$$(1-\alpha_c)\nu R + \nu\sigma\left(\varepsilon_{ss}\varepsilon_{sky}T_{a,K}^4 - 2\varepsilon_c T_{c,K}^4 + \varepsilon_{ss}T_{ss,K}^4\right) + h_{LE,c}\left(e_a - e_{c,sat}(T_v)\right) + h_{C,c}(T_a - T_c) = 0 \quad (2.48)$$

where α_c, ε_s, T_c (˚C) and $T_{c,K}$ (˚C) are the solar albedo, infrared emissivity, temperature and absolute temperature of the canopy cover respectively.

$h_{C,c}$ (W/m^{2}K) and $h_{LE,c}$ (W/m^{2}kPa) are the convective and evaporative heat transfer coefficients between the canopy cover and the atmosphere. The convective and evaporative interactions between the canopy layer and the atmosphere are assumed to be turbulent (these coefficients are presented later in Section 2.4.2) and inversely proportional to an aerodynamic resistance r_a (s/m), similarly to the coefficients corresponding to bare soil and pavement formulations, and to a stomata resistance r_s (s/m). Herb *et al.* (2008) provided expressions for these resistances:

$$r_a = \frac{1}{c_f u_s} \quad (2.49)$$

$$r_s = 200\left[\frac{R_{max}}{R + 0.03R_{max}} + \left(\frac{\theta_{wp}}{\theta_w}\right)^2\right] \quad (2.50)$$

where u_s (m/s) is wind speed, R_{max} is the maximum noon solar radiation that can be achieved, θ_w is the soil moisture content, θ_{wp} is the wilting point moisture content and c_f is a transfer coefficient given by:

$$c_f = 0.01 + \left(1 + \frac{0.3}{u_s}\right) \quad (2.51)$$

According to Deardorff (1978), the stomata resistance given by (2.50) takes into account the fact that many types of leaves transpire only from the underside, and that older leaves transpire less than newer ones.

The balance equation for the soil surface is given by:

$$-\lambda_b \frac{dT_{ss}}{dx} = (1-\alpha_S)(1-\nu)R + \sigma\varepsilon_{ss}\left[(1-\nu)\varepsilon_{sky}T_{a,K}^4 - T_{ss,K}^4\right] + \nu\varepsilon_c\sigma T_{c,K}^4 + (1-C_e\nu)[\,h_{LE}(e_a - e_{ss}) + h_C(T_a - T_{ss})] \quad (2.52)$$

where C_e is a constant that establishes the level of soil evaporation for fully dense canopies, for example setting C_e< 1 gives non-zero soil evaporation for the full canopy case. Deardorff (1978) suggest solving equation (2.48) using Newton's method as a nonlinear relation with T_c. The calculated canopy temperature can then be used to calculate the ground surface heat flux using equation (2.52).

2.4.1.4 Snow Surface Condition

Another scenario for the soil surface happens when it is covered by snow, a detailed coverage of the relevant processes and how they can be represented is given by Armstrong and Brun (2008) and Singh *et al.* (2011). A summary of the key topics covered by Singh *et al.* (2011) and others is given below.

The heat exchange between the atmosphere and a surface snow layer includes: solar shortwave and thermal longwave radiation, as well as turbulent fluxes of sensible and latent heat. The surface heat balance and exchange of momentum is directly affected by the changes in the snow surface properties, while changes in the atmospheric water content affect the radiative transfer, convection, condensation, and precipitation (Armstrong and Brun 2008). The momentum exchange happens due to the wind stress (which depends on the aerodynamic characteristics of the snow surface and the thermal stratification) over the snow surface. The presence of seasonal snow cover during the cold season of the annual air temperature cycle has significant influence on the ground thermal regime in cold regions Singh *et al.* (2011). Snow has high albedo and emissivity, that cool the snow surface, high absorptivity, that tends to warm the snow surface, low thermal conductivity so that the snow layer acts as an insulator, and high latent heat (if snowmelt is considered) due to snowmelt. The overall impact of snow cover on the ground thermal regime depends on many

factors such as the timing, duration, accumulation, density, structure, and thickness of seasonal snow cover, and interactions of snow cover with micrometeorological conditions (vegetation). In the continuous permafrost regions, impact of seasonal snow cover can result in an increase of the mean annual ground and permafrost surface temperature by several degrees, whereas in discontinuous and sporadic permafrost regions the absence of seasonal snow cover may be a key factor for permafrost development Singh *et al.* (2011).

Compared to other material (e.g. soil surface), snow has a low thermal conductivity value (0.025-0.12 W/mK) meaning that the snow surface temperature rapidly adapts to changes in the atmosphere (Riche and Schneebeli 2013). Also, the snow thickness and density can vary a lot both spatially and temporally implying that the conductive heat flux and the response of the surface temperature to atmospheric forcing would change in time and space.

A surface balance equation to represent the heat balance on the snow surface is given by Timo (2011) as:

$$-\lambda_b \frac{dT_s}{d\hat{n}} = (1-\alpha_S)R + \sigma\varepsilon_s\left[\varepsilon_{sky}T_{a,K}^4 - T_{s,K}^4\right] + h_{LE}(e_a - e_s) + h_C(T_a - T_s) \quad (2.53)$$

This is a general form of the equation and the particular values of the coefficients will change to take into consideration the specific nature of the snow surface, (i.e. surface roughness length and albedo of short wave radiation). Stull (2000) provide values for surface roughness for different surface condition, for vegetation canopy the surface roughness equals to:

$$z_0 = 0.03 \quad (2.54)$$

While for a paved area or snow covered flat plane, it is equal to:

$$z_0 = 0.0002 \quad (2.55)$$

On the other hand, Serreze and Barry (2005) provide snow albedo values for a fresh snow condition as:

$$\alpha = 0.7 - 0.9 \tag{2.56}$$

While for a melting snow, the values would be:

$$\alpha = 0.5 - 0.6 \tag{2.57}$$

2.4.2 Convective and evaporative coefficients under turbulent and non-turbulent conditions

This section reviews reported studies of the representation of convective and evaporative heat transfer and the formulation of suitable coefficients for use in equations (2.28) and (2.29).

The main approaches commonly available in the literature are: turbulent atmospheric conditions, non-turbulent conditions and evaporation and convection through a layer of vegetation.

Jansson (2012) describe evaporation and convection from bare soils in the development of the model "*CoupModel"*. This is a physically based model that simulates water and heat flux through a one-dimensional soil profile using a combination of the Richards and Fourier equation. It comprises a substantial range of sub-models, such as infiltration, evapotranspiration, heat storage, soil frost and crop growth.

This approach of simulating soil water and heat processes in many types of soil (including bare soils or soils covered by vegetation) is known as the turbulent approach which is applicable when the rates of transfer and mixing are several orders of magnitude greater than the rate of molecular diffusion and it is based on the theory of atmospheric boundary layer behaviour (Garratt 1994). Under these conditions the convective and evaporative heat transfer coefficients are defined as:

$$h_C = \frac{\rho_a c_a}{r_{a,C}} \tag{2.58}$$

$$h_{LE} = \frac{\rho_a c_a}{r_{a,LE}\gamma} \tag{2.59}$$

where ρ_a (kg/m^3) and c_a (J/kgK) are the density and specific heat capacity of air, γ (kPa/K) is the psychrometric constant and r_a (s/m) is the aerodynamic resistance of the soil surface and is inversely proportional to the wind speed. Andreas (2002) offer the following expression for $r_{a,C}$ and $r_{a,LE}$:

$$r_{a,C} = \frac{1}{k^2 u_s^2 [ln(z/z_0) - \psi_m(\zeta)][ln(z/z_T) - \psi_h(\zeta)]} \tag{2.60}$$

$$r_{a,LE} = \frac{1}{k^2 u_s^2 [ln(z/z_0) - \psi_m(\zeta)]\left[ln(z/z_Q) - \psi_h(\zeta)\right]} \tag{2.61}$$

where z_Q (m) is the roughness length for humidity, z_T (m) is the roughness lengths for heat, k is the von Kármán constant (a dimensionless number used in the description of the logarithmic velocity profile of a turbulent fluid flow near a boundary with no-slip condition). Its value is commonly accepted to be 0.41 (Garratt 1994), L (m) is the Monin-Obukhov length and is used to describe the effects of buoyancy on turbulent flows, particularly in the lower tenth of the atmospheric boundary layer and ψ_m, ψ_T are the empirical stability functions which are a measure of the deviation of the atmospheric wind and temperature profile from the standard logarithmic law.

In order to successfully capture the aerodynamic air resistance of the surface knowing the functional forms for ψ_m and ψ_m is important and to be able to find those factors, authors suggest introducing the gradient function $\phi_m(\zeta)$ and $\phi_h(\zeta)$ and use them instead.

These gradient functions are related to the surface-layer profiles of potential temperature, wind speed, and specific humidity and could be calculated, the expression that links the ψ and ϕ functions (e.g., Panofsky (1963)):

$$\psi(\zeta) = \int_0^{\zeta} \frac{1-\phi(\zeta)}{\zeta} d\zeta \tag{2.62}$$

A host of ϕ_m and ϕ_h functions for stable and unstable stratification have been suggested. Several authors (Andreas 2002 ; Launiainen 1995 ; Vihma 1995) review available hosts functions and came to recommendations to use Holtslag and De Bruin (1988) expressions for ϕ_m and ϕ_h that are specially adapted for very stable stratification where the usual assumption of $\psi_m = \psi_h$ is applied. However, Arya (2001) recommend using a generally accepted form of $\phi_h(\zeta)$ and $\phi_m(\zeta)$ is expressed as:

$$\phi_m(\zeta) = \begin{cases} (1-\gamma_1\zeta)^{-1/4} & for\ \zeta < 0 \quad (unstable) \\ 1+\varsigma\zeta & for\ \zeta \geq 0 \quad (stable) \end{cases} \tag{2.63}$$

$$\phi_h(\zeta) = \begin{cases} \varphi(1-\gamma_2\zeta)^{-1/2} & for\ \zeta < 0 \quad (unstable) \\ \varphi+\varsigma\zeta & for\ \zeta \geq 0 \quad (stable) \end{cases} \tag{2.64}$$

where $\varphi = 0.74$, $\varsigma = 4.7$, $\gamma_1 = 15$ and $\gamma_2 = 9$

Finally, to calculate z_T and z_Q in order to find latent and sensible heat coefficients, Andreas (1987) built on the surface-renewal models of Brutsaert (1975) and Liu *et al.* (1979) to produce theoretically based model that specifically predicts z_T over snow-covered surfaces. The model's basic result is an equation that predicts the scalar roughness z_s from the roughness Reynolds number as:

$$ln(z_S/z_0) = b_0 + b_1\, ln(Re_*) + b_2(ln(Re_*))^2 \tag{2.65}$$

where z_S is either z_T or z_Q, the polynomial coefficients b_0, b_1 and b_2 are presents in Table (2.2) and Re_* is the roughness Reynolds number defined as:

$$Re_* = u_* z_0/\upsilon \tag{2.66}$$

where υ is the kinematic viscosity of air.

	$\boldsymbol{Re_*} \leq 0.135$	$0.135 < \boldsymbol{Re_*} < 2.5$	$2.5 \leq \boldsymbol{Re_*} \leq 1000$
Temperature $\boldsymbol{z_T/z_0}$			
$\boldsymbol{b_0}$	1.250	0.149	0.317
$\boldsymbol{b_1}$	0	-0.550	-0.565
$\boldsymbol{b_2}$	0	0	-0.183
Humidity $\boldsymbol{z_Q/z_0}$			
$\boldsymbol{b_0}$	1.610	0.351	0.396
$\boldsymbol{b_1}$	0	-0.628	-0.512
$\boldsymbol{b_2}$	0	0	-0.180

Table (2.2) Values of the coefficients to use in equation (2.65) to estimates the scalar roughness lengths in the three aerodynamic regimes after (Andreas 1987).

Herb *et al.* (2008), Adams *et al.* (1990) and Ryan *et al.* (1974) adopt another approach which will referred to as "non-turbulent" to distinguish it from the previously presented model (turbulent atmospheric conditions).

The non-turbulent approach is characterized by the inclusion of terms that take into account natural convective processes on the soil surface that were neglected in turbulent scenarios. Herb *et al.* (2008) proposed the following expressions for the convective and evaporative heat transfer coefficients based on the work of Ryan *et al.* (1974):

$$h_C = \rho_a c_a \left(C_{fc} C_{sh} u_s + C_{nc} T_v^{0.33}\right) \tag{2.67}$$

$$h_{LE} = \rho_a L_v \left(C_{fc} C_{sh} u_s + C_{nc} T_v^{0.33}\right) \tag{2.68}$$

where L_v (J/kg) is the latent heat of evaporation, C_{fc}, C_{nc} (m/sK1/3) and C_{sh} are coefficients that weight the contribution of forced convection, natural convection and sheltering respectively and take value between 0 and 1, T_v (K) is the difference in virtual temperature between the air and the soil surface. Best (1998) and Deardorff (1978) propose canopy cover heat transfer coefficients for convection and evaporation which are defined as follows:

$$h_{LE,c} = \frac{\rho_a L_v \nu}{r_{a,LE} + r_s} \tag{2.69}$$

$$h_{C,c} = \frac{\rho_a c_a \nu}{r_{a,C}} \tag{2.70}$$

2.4.3 Longwave heat transfer coefficient

Available relationships representing sky emissivity (as used in equation (2.27)) are reviewed in this section. Many authors treated the atmosphere as a surface (as if it were a dome) that surrounds the soil (Duffie and Beckman 2013 ; Iziomon *et al.* 2003 ; Berdahl and Martin 1984). The atmosphere, however, is actually composed of several layers of gas, each one of them having different temperatures and chemical compositions that are continuously changing.

The atmosphere absorbs much of the longwave terrestrial radiation and a significant part of the solar radiation and an important aspect of the atmospheric radiation is that absorption and emission of radiation by various gases occur in a series of discrete wavelengths or bands of wavelengths, rather than continuously across the spectrum (Arya 2001). Tomasi (1978) shows how the water vapour availability and its radiative properties define an atmospheric window between 8 µm and 14 µm. In this window, the atmosphere is basically transparent to infrared radiation, and in contrast to that outside this window the infrared radiation is mostly absorbed. In conjunction, these properties determine the net incoming long wave radiation from the sky.

For modelling purpose Duffie and Beckman (2013) explain that the sky is usually treated as a black body at an equivalent sky temperature $T_{sky,K}$. Few relations that accounts for all atmospheric complexities mentioned before having been proposed to relate $T_{sky,K}$ to measured meteorological variables (e.g. vapour pressure and air temperature). In general, they adopt the same form of equation (2.26) and are summarized in Table (2.3).

Table (2.3) and (2.4) present relations for longwave radiation under clear sky conditions while Table (2.5) take into considerations the cloud presence despite its difficulties. The reason for distinguishing the cloud effects is related to the fact that the water vapour absorbs energy in atmospheric window and re-emits it to the ground.

Brunt (1932)	$q_{L,in} = (a_1 + b_1 e_a^{0.5})\sigma T_{a,K}^4$	$a_1 = 0.55$ $b_1 = 0.0065$ kPa$^{-1/2}$
Monteith (1961)	$q_{L,in} = (a_2 + b_2 e_a^{0.5})\sigma T_{a,K}^4$	$a_2 = 0.53$ $b_2 = 0.0065$ kPa$^{-1/2}$
Berdahl and Martin (1984)	$q_{L,in} = (a_3 + b_3 e_a^{0.5})\sigma T_{a,K}^4$	$a_3 = 0.56$ $b_3 = 0.0059$ kPa$^{-1/2}$
Iziomon *et al.* (2003)(1)	$q_{L,in} = (a_4 + b_4 e_a^{0.5})\sigma T_{a,K}^4$	$a_4 = 0.50$ $b_4 = 0.0066$ kPa$^{-1/2}$
Swinbank (1963)(1)	$q_{L,in} = (a_5 + b_5 e_a^{0.5})\sigma T_{a,K}^4$	$a_5 = 0.64$ $b_5 = 0.0037$ kPa$^{-1/2}$
Fund and Ångström (1915) (1)	$q_{L,in} = (a_6 + b_6 10^{-c_6 e_a})\sigma T_{a,K}^4$	$a_6 = 0.82$ $b_6 = 0.25$ $c_6 = 0.0094$ kPa$^{-1/2}$
Fund and Ångström (1915) (2)	$q_{L,in} = (a_7 + b_7 10^{-c_7 e_a})\sigma T_{a,K}^4$	$a_7 = 1.017$ $b_7 = 0.331$ $c_7 = 0.002$ kPa$^{-1/2}$
Iziomon *et al.* (2003) (2)	$q_{L,in} = \left[1 - a_8 exp\left(\frac{-b_8 e_a}{T_{a,K}}\right)\right]\sigma T_{a,K}^4$	$a_8 = 0.35$ $b_8 = 1$ kPa$^{-1/2}$

Table (2.3) Expressions dependent on atmospheric vapour pressure, e_a (kPa), and absolute air temperature $T_{a,K}$ (K) for clear sky incoming infrared radiation

Swinbank (1963) [2]	$q_{L,in} = \left(a_9 T_{a,K}^2\right)\sigma T_{a,K}^4$	$a_9 = 9.34 \times 10^{-6}\text{k}^{-2}$
(Idso and Jackson 1969)	$q_{L,in} = \left(1 - a_{10} exp\left[-b_{10}\left(273 - T_{a,K}^2\right)^2\right]\right)\sigma T_{a,K}^4$	$a_{10} = 0.261$ $b_{10} = 7.77 \times 10^{-4}\text{k}^{-2}$

Table (2.4) Expressions dependent on the absolute air temperature $T_{a,K}$ (K) only for clear sky incoming radiation

Edinger *et al.* (1968)	$q_{L,in} = \left[N + a_{11}\left(1 - N e_a^{b_{11}}\right)\right]\sigma T_{a,K}^4$	$a_{11} = 0.067\ \text{kPa}^{-1}$ $b_{11} = 0.08$
Iziomon *et al.* (2003)	$q_{L,in} = \left[1 - a_{12} exp\left(\frac{-b_{12} e_a}{T_{a,K}}\right)\right](1 + 64 c_{12} N^2)\sigma T_{a,K}^4$	$a_{10} = 0.261$ $b_{10} = 7.77 \times 10^{-4}\text{k}^{-2}$

Table (2.5) Expressions for cloud-covered sky incoming infrared radiation
N is the cover factor being 0 for clear sky and 1 for completely cloudy

As in the convective heat transfer process, h_{LE} depends on the specific conditions of the fluid and the surface characteristics. The atmospheric water vapour pressure, e_a, (the same equation can be applied for $e_{ss,sat}$) can be calculated according to North and Erukhimova (2009) as follows:

$$e_a = \left(\frac{H_a}{100}\right) e_a(0) exp\left[\frac{L_v}{R_w}\left(\frac{1}{273.15K} - \frac{1}{T_{a,K}}\right)\right] \quad (2.71)$$

where H_a (%) is the relative humidity, $e_a(0)$ is the atmospheric vapour pressure at 0°C.

Sky emissivity equations that are shown in Table (2.3) are plotted in Figure (2.2) and Figure (2.3). In Figure (2.2) air vapour pressure is calculated through keeping air temperature constant at $T_{a,K}$ = 282.67 K and varying relative humidity from 50 % to 100 % which corresponds to an air vapour pressure range from approximately 600 Pa to 1200 Pa. In Figure (2.3) the air vapour pressure is calculated by holding the relative

humidity value constant at H_a= 80 % and varying air temperature from 273.15 K to 323.15 K, which in turn corresponds to an air vapour pressure range from approximately 500 Pa to 10000 Pa.

It can be observed that air temperature has the strongest impact on the value of air vapour pressure and that the different sky emissivity models behave linearly in the range of air vapour pressures obtained with variations in relative humidity. In contrast, the models behave nonlinearly in the wider range of air vapour pressures obtained with the variations in air temperature which is an indication of the high level of uncertainty in the calculation of this term. Due to the higher amount of water molecules present in the atmosphere at higher vapour pressure values, the sky emissivity increases with the increase of water pressure as the molecules absorb and reemit the infrared radiation to the ground. Figure (2.4) shows two of the equations presented in Table (2.4) which depends on air temperature. Their main advantage is to lower the meteorological variables required to estimate the value of sky emissivity even if this can reduce its accuracy.

As a comparison, Figure (2.3) shows that equations that use vapour pressure in addition to air temperature tend to approach asymptotically to 1 at higher values of vapour pressure which means that equations presented in in Table (2.4) underestimate the sky emissivity at higher temperatures (and higher vapour pressure values). However, the inherent uncertainty among different models makes this possibility less important when compared with the advantages of requiring fewer meteorological input data.

Figure (2.5) shows equations (that corresponds to cloudy skies) presented in Table (2.5) using constant values of air temperature (282.67 K) and relative humidity (80 %). It can be seen that whenever the cloud cover factor increases, the value of sky emissivity increases as well, however, there could be a difference of up to 0.1 between the two models which is relates to the fact that these models are based on experimental observations of meteorological stations. Nevertheless, as they consider clouds presence, it is expected to also offer more realistic values especially on regions with a high level of cloudiness as is the UK.

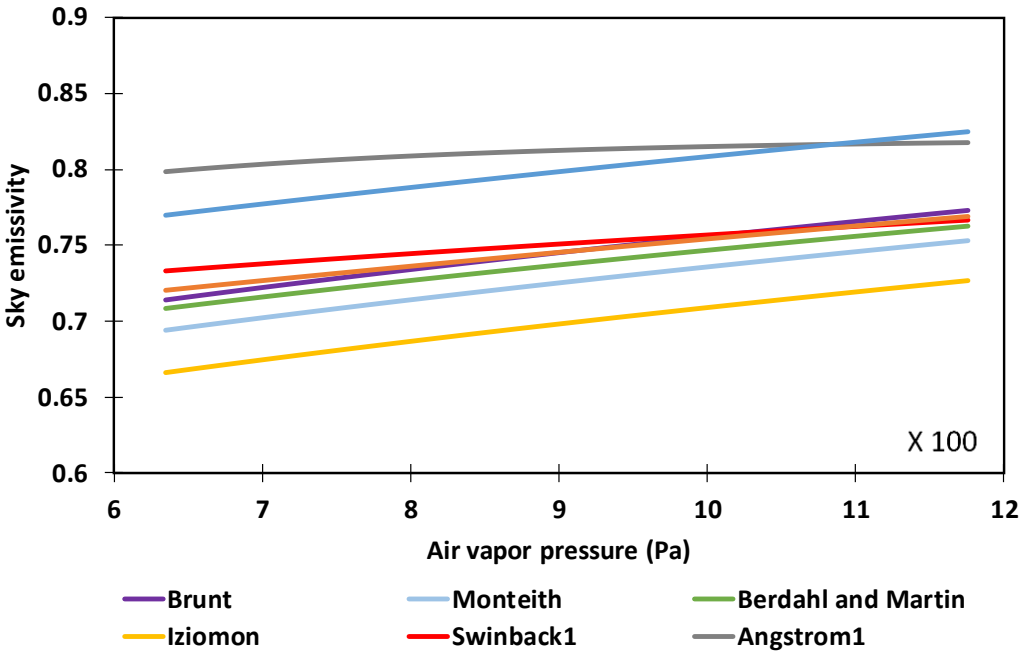

Figure (2.2) Sky emissivity's for clear skies based on equations shown in Table (2.3); air vapour pressure is calculated keeping air temperature constant at 282.67 K and varying the relative humidity from 50 % to 100 %

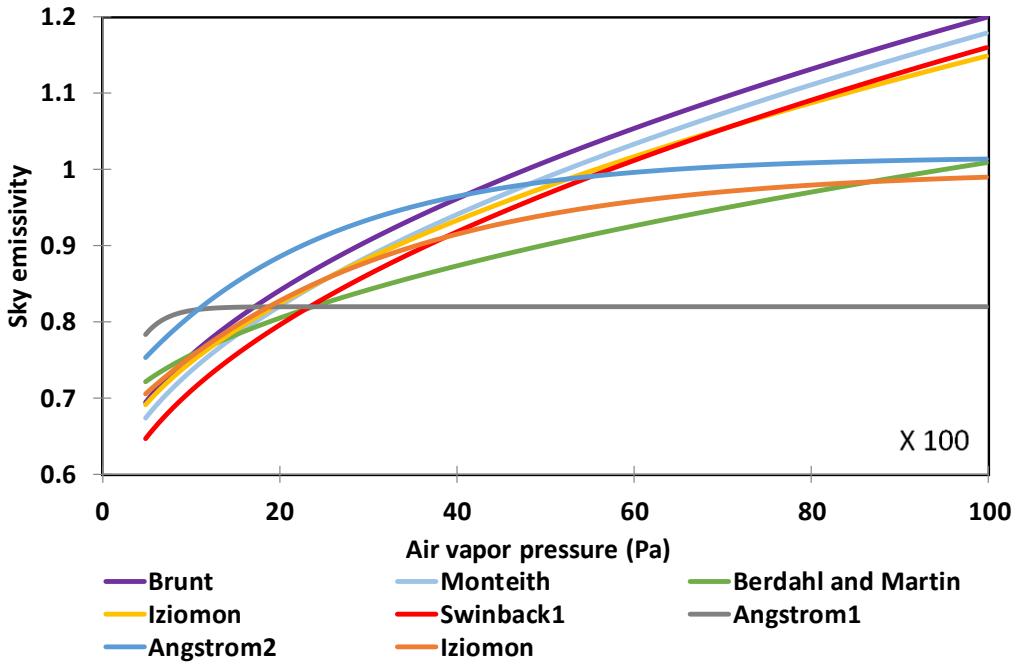

Figure (2.3) Sky emissivity's for clear skies based on equations shown in Table (2.3); air vapour pressure is calculated keeping relative humidity constant at 80 % and varying the air temperature from 273.15 K to 323.15 K

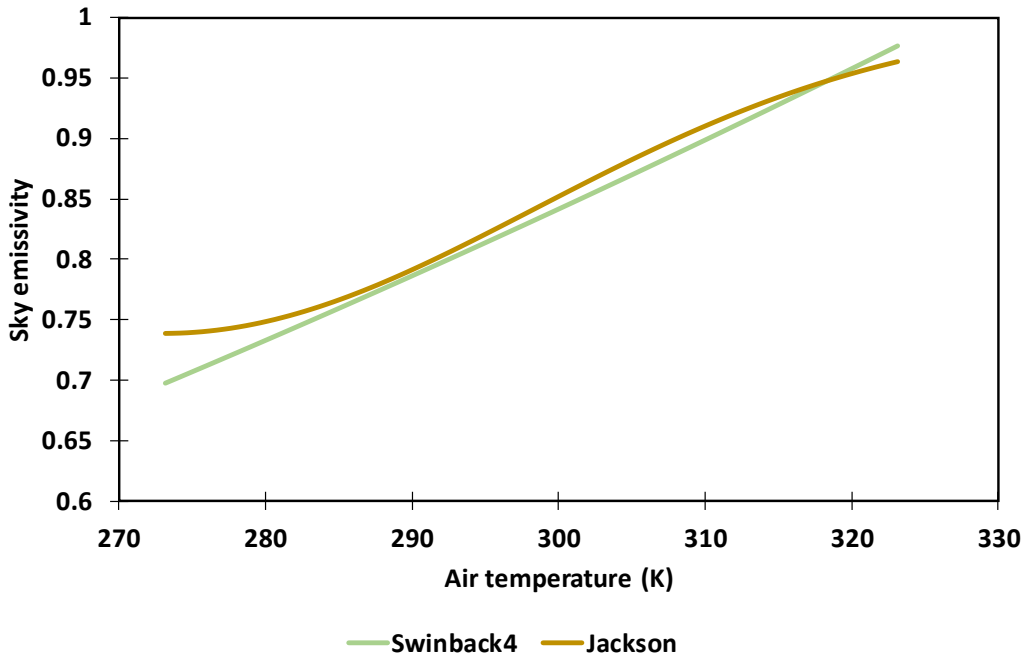

Figure (2.4) Sky emissivity's for clear skies from two equations shown in Table (2.4); these relations are only dependent on-air temperature.

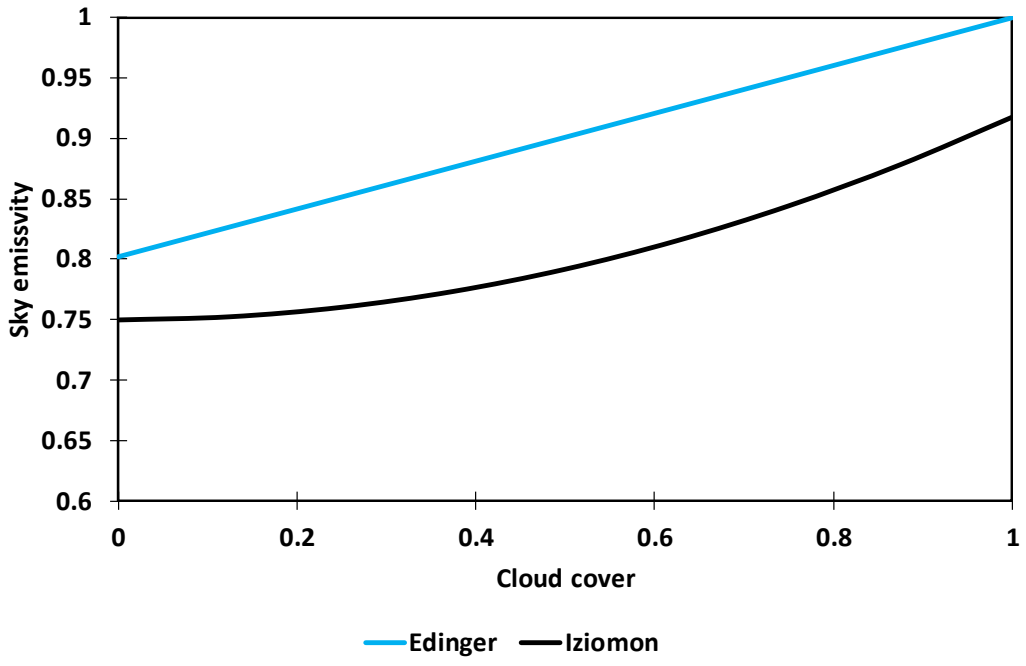

Figure (2.5) Sky emissivity's for cloudy skies from equations shown in Table (2.5); value of '0' for cloud cover corresponds to a clear sky while '1' corresponds to a completely cloud-covered sky

2.5 Impact of freezing on heat transfer in soils

Freezing the soil affects the heat transfer in soil, not only through the release and adsorption of the latent heat of fusion, but also through changes in the thermal and hydraulic properties. The thermal conductivity of frozen soil can be more or less than that of unfrozen soil, depending on the moisture content (Kersten 1949). One of the most obvious effects of freezing on the moisture transfer is the moisture's immobility (in the case of completely frozen state). The not-so-obvious effect though is the non-isothermal phase change; in fact, a very small amount of liquid water remains even at temperatures near liquid nitrogen (Harlan 1973). Depending on the soil type, most of the liquid-to-solid occurs between 0.0 °C and -0.2 °C (Horiguchi and Miller 1983). The remaining unfrozen water content exists in thin films that is adsorbed on the soil grains. The solutes presence lowers the freezing point and can cause pockets of unfrozen moisture as the solute becomes concentrated ahead of the freezing front (Kay and Perfect 1983).

Another obvious effect relates to the permeability and soil structure that would be changed due to freezing and thawing. Freezing and thawing caused a reduction in void ratio and an increase in vertical permeability. The increase in permeability is attributed to the formation of polygonal shrinkage cracks and/or to the reduction of the volume of fines in the pores of the coarse fraction (Chamberlain and Gow 1979).

Dagesse (2013) discusses the soil structural stability following the winter months. His study objective was to establish the separate effects of the freezing, freeze-thaw and freeze-drying processes in defining soil structural stability following the over-winter period. The main findings suggest that the freezing-induced desiccation process improves aggregate stability, while the addition of a thaw component following freezing, with the attendant liquid water, is responsible for degradation of aggregate stability. Clay content and initial water content are important factors governing the magnitude of this process.

Furthermore, Soil freezing also affects the potential release of carbon and nutrients from soil microbial cells that have been lysed by freeze-thaw transitions which have

significant impacts on the overall carbon balance of ecosystems, and therefore on atmospheric CO_2 concentrations (Kumar *et al.* 2013).

2.6 Predicting temperature variations in the soil profile

A summary of analytical and numerical methods used in the estimation of soil temperature profiles and the study of thermal devices buried in the ground are presented in the following sections.

2.6.1 Analytical methods

Applications of analytical methods to solve the diffusion equation and diffusion-convection equation in various fields has often been used to estimate the soil temperature profile. Some studies related to the interaction of soil-building heat diffusion problem such as, Hollmuller and Lachal (2014), Hagentoft (1996a, 1996b) and Jacovides *et al.* (1996) while others dealt with the contaminants diffusion in porous media that is composed of two or more layers, for example, Li and Cleall (2010) and Chen *et al.* (2009).

Few analytical solutions are available for convection and diffusion in relation to water infiltration (Wang *et al.* 2012 ; Gao *et al.* 2008 ; Gao *et al.* 2003 ; Shao *et al.* 1998). Li and Cleall (2011) focussed on the general solute transport in porous media under various boundary conditions while Huang and Wu (2012) derived steady-state solutions for horizontal and vertical infiltration of water in unsaturated soils. Approximate analytical solutions proposed by Kurylyk *et al.* (2014) for predicting soil thawing subject to conduction, advection and phase change (thawing).

Three main types of boundary conditions are considered in each of these approaches which are: first type (which is also known as *Dirichlet type*), which specifies the value of the variable at the boundary; second type boundary conditions (also known as *Neumann type*) which specify the value of the derivative of a variable at the boundary; and third type boundary conditions (also known as *Robin type*), these specify both (as a linear combination) the value of the variable and its derivative at the boundary.

Typically, the analytical solutions result from the simplification of real life problem which limits the solutions to those simplified aspects. A good example of that is the approaches proposed by Michopoulos *et al.* (2010), Mihalakakou *et al.* (1997) to estimate the ground temperature and the coupled heat diffusion and water infiltration based on the assumptions of fixed boundary conditions (constant or periodic) presented by Shao *et al.* (1998). Similar assumption was used by Chuangchid and Krarti (2001) to determine the temperature field within the ground medium and within the concrete slab-on-grade floor. Recent studies tried to include more details for the problem of mass and energy transfer interactions at the soil surface, Wang (2012) and Wang and Bou-Zeid (2012) is a good example of those because of the inclusion of the second type time dependent boundary conditions, while others like Cleall and Li (2011) have taken into consideration an even more descriptive boundary condition by using the third type. On the other hand, the boundary condition at the bottom of the domain commonly either assumed fixed at an estimated temperature or insulated (no heat flux, i.e. any geothermal heat flux coming from the deepest layers of the ground would be neglected (Davies 2013)). However, the inclusion of a constant heat flux at the bottom of the domain is not difficult if the assumption cannot be made.

2.6.1.1 Analytical equations for meteorological variables

dos Santos and Mendes (2006) ; Frouin *et al.* (1989) ; Cinquemani *et al.* (1979) ; Lumb (1964) provides analytical relations to directly model the diurnal variations of solar radiation that can be applied to different fields (including the estimation of soil temperatures).

Lumb (1964) proposed the following equation for the solar radiation:

$$R = R_c \cos\theta_s \, (a + b \, cos \, \theta_s) \tag{2.72}$$

where θ_s is the sun's zenith angle, which is the angle measured from directly overhead to the geometric centre of the sun's disc, R_c (1.362 kW/m^2) is the solar constant, defined as the amount of electromagnetic radiation per unit area that would-be

incident on a plane that is perpendicular to the rays at a distant of one astronomical unit from the sun, and a and b are coefficients that need to be adjusted depending on the required location of interest.

While the solar relation presented by dos Santos and Mendes (2006) have the following form:

$$R(t) = 300 + 100 \sin\left(\pi + \frac{\pi t}{31536000}\right) sin\left(\frac{3\pi}{2} + \frac{\pi t}{43200}\right) \quad (2.73)$$

where t is the time in seconds.

The value for total solar radiation given by (2.73) is valid between 6:00 am and 6:00 pm with highest values at noon, and, elsewhere it equals to zero.

Hillel (2003) presented an analytical model to represent the annual variations of air temperature which is given by:

$$T_a(t) = T_{a,ave} + T_{a,amp} \sin\left(\frac{2\pi t}{86400}\right) \quad (2.74)$$

where $T_{a,ave}$ (˚C) is the average ambient temperature and $T_{a,amp}$ (˚C) is the diurnal amplitude.

dos Santos and Mendes (2006) suggested the use of the following equations for air temperature:

$$T_a(t) = 20 + 0.5\, sin\left(\pi + \frac{\pi t}{3153600}\right) + 5 \sin\left(\pi + \frac{\pi t}{43200}\right) \quad (2.75)$$

Furthermore, dos Santos and Mendes (2006) provide an analytical description for a relative humidity despite the fact the difficulties in describing this challenging meteorological variable:

$$H_a(t) = 0.6 - 0.1 \sin\left(\pi + \frac{\pi t}{43200}\right) \quad (2.76)$$

Recent studies provided by Cleall *et al.* (2015) provide analytical solutions to estimate the soil temperature with depth and stored energy. The boundary conditions used are of the second kind (Neumann) at the bottom of the domain and of the third kind (Robin) based on a heat balance at the soil surface. The presented analytical solutions used to investigate a case-study problem based upon results of a field experiment. Predicted soil temperature profiles and stored energy transients have been compared against experimental recordings for over 1 year and the predicted meteorological data compared against widely available public records and against data recorded on site.

2.6.2 Numerical methods

Numerical modelling has been shown to be a useful tool for engineering design and analysis. It is based on the process of solving physical problems by appropriate simplification and approximation of the governing equations involved. The use of numerical methods can also be applied for 1D, 2D or 3D conditions, where it can more readily accommodate complex geometries or non-linear material properties and transient processes and in this case numerical modelling used for the optimization and design of thermal energy storage systems.

Qin *et al.* (2002) presented a detailed description of surface energy balance in 2D and 3D models that couples soil temperature change with soil moisture movement for estimation of soil and latent heat fluxes. The numerical solution of the model involves the estimation of the dynamics of heat fluxes and many useful soil-water and meteorological parameters required for different applications. Yumrutaş *et al.* (2005) developed a computational model for determining annual periodic performance of a cooling system utilizing a ground coupled chiller and a spherical underground thermal energy storage tank. An analytical solution for the transient heat transfer problem outside the storage tank was obtained to estimate the heat flux between the storage system and the surrounding soils with the initial condition of soil temperature assumed to be constant, with no (or reduced) heat flux interaction with the

atmosphere because of the assumed position of the tank. A similar approach was used by Kong *et al.* (2017) who investigated the thermal performance of ground heat exchanger with a set of designed U-tubes by using experimental measurements and computational fluid dynamics (CFD) simulation. Nabi and Al-Khoury (2012) used the same approach to perform the numerical analysis of U-tube heat exchangers for ground heat storage devices buried at relatively high depths into the ground (~100m). Same approach was used by Shang *et al.* (2011) who developed 3D model to study the geo-temperature recovery using ground-source heat pumps under intermittent operation and validated the simulation in comparison with experiment that carried out on the mode of heating. The initial, bottom and distant (far-field) boundary conditions in these works are considered constant and equal to the annual average soil temperature while the surface boundary condition is usually simplified. For the numerical treatment of shallower heat storage devices, for example, Kroll and Ziegler (2011) concluded that the thermal energy interactions at the soil surface can be simplified or assumed negligible (if it is well insulated).

Wu *et al.* (2010) numerically solved the 3D transient heat transfer equation using a commercial CFD package software (FLUENT) without considering the moisture movement in the domain of a horizontal slinky ground-source heat exchanger. The model input data and the initial conditions was based on the experimental data a 2 month experimental measurement system placed near the soil surface (1-2 m depth) at a site near Oxfordshire, UK with a mixture of water and ethylene glycol at 30 % was used as a heat carrier. Esen *et al.* (2007) and İnallı and Esen (2004) performed a yearlong experimental measurement for two heat exchanger system buried 1 m and 2 m in the ground, and developed a numerical model to solve the transient heat transfer equation, without considering the moisture movement in the domain simulations that was intended to evaluate the thermal performance of shallow horizontal ground-source heat pump systems. The heat carrier fluid mixture composed of water and ethylene glycol at 25 %. Congedo *et al.* (2012) performed a set of 3D numerical simulations in a cubic domain of 2 m per side where he compared the different pipe distributions with the performance of horizontal ground heat exchangers using constant thermal properties. The bottom boundary was fixed

depending on experimentally measured data while the top boundary condition was defined based on meteorological data that has been recorded on site. Similar numerical models to study the behaviour of ground-source heat pump systems have been developed and used by others (Hollmuller and Lachal 2014 ; Bittelli *et al.* 2010 ; Nam *et al.* 2008).

Using the finite element method Muñoz-Criollo (2014) presented a numerical study for the inter-seasonal heat transfer processes in soils where he focuses on the energy balance at the soil surface and its impact on the performance of thermal energy storage devices in shallow regions of the ground. The model takes into account conductive and convective heat transfer between the fluid inside pipe heat exchangers and the surrounding soil. Even though the study provides a 1D, 2D and 3D models but did not consider many surface conditions with some parameters being simplified. Muñoz-Criollo *et al.* (2016a) investigated the influence of surface boundary conditions, varying climatic conditions and engineering material parameters on the collection performance of near surface inter-seasonal ground energy collection and storage systems using numerical model. Amongst their main findings it was reported that a higher storage layer thermal conductivity would increase storage of thermal energy and lower peak temperatures and that the performance of insulation layers would strongly influence the system heat losses and it is highly critical to use the correct surface boundary conditions in modelling the dynamics of these systems.

In terms of building sciences, Tariku *et al.* (2010) developed a transient heat, air and moisture transfer model on basic conservation of mass and energy equations and verified the results with experimental results obtained by Maref *et al.* (2002). The governing partial-differential equations (PDEs) of the three transport phenomena are coupled and solved simultaneously for temperature, relative humidity and pressure. However, the model was not coupled with an indoor model to create a whole-building hygrothermal model. dos Santos and Mendes (2006) presents a 3D numerical analysis using the finite volume method of the energy interactions of a building's envelope with the soil underneath where they consider the simultaneous heat and moisture transfer within the soil. The soil domain size was 10 m×10 m with 4 m for the depth

(the z direction). Two different sets of boundary conditions were used at the top of the soil surface, one for the interaction between the soil and building while the other one was for the interaction between the soil and atmosphere. Other soil domain surfaces were considered impermeable and adiabatic and in order to correctly estimate the temperature and moisture content profiles, a pre-simulation period of several years was recommended for the correct estimation of temperature and moisture content profile. Unlike Tariku *et al.* (2010) model this one considers the moisture effects on indoor air analysis, dos Santos and Mendes (2006) showed that a very slight difference exists in terms of room air temperature between the purely conductive model for the ground and the moisture model. However, a significant difference of 15 % was noticed on the room air humidity ratio, even for the high infiltration rate case. Therefore, higher energy consumption could be expected when an air conditioning system is used. Rees *et al.* (2007) provided a 2D numerical simulation based on the finite element method for a full-scale experiment that dealt with the energy interactions of a building's envelope and the ground which last for a year-long. The moisture movement was not considered in the domain since the accuracy offered by standard uncoupled methods was considered enough for that application. The domain dimension was 12.95 m in the x-direction and 14.626 m in the z-direction (depth) and the vertical boundary conditions were considered as adiabatic while the bottom boundary fixed to a suitable temperature. A four year-long pre-conditioning analysis was considered enough to have a suitable initial condition for the problem. However, the climate conditions were basically covered in this work especially the frozen soil effect.

On the other hand Rees *et al.* (2013) explored soil freezing and snow cover effects by inclusion of soil freezing within the simulation of heat flow from a building to the neighbouring foundation soils. However, non-linear thermal conductivity and heat capacity relations that account for the effect of soil freezing are presented in their work and in addition, it considers latent heat generated by phase change occurring due to the soil water temperature reduces and the ice forms. Their results provide a first indication of the potential significance of the inclusion of ground freezing within the context of modelling heat transfer.

2.7 Conclusions

This chapter has presented a literature review of factors related to the thermal energy storage in soils using shallow heat exchangers.

The main physical properties governing the heat and moisture transfer in the ground have been described. The thermal conductivity and specific heat capacity and how they relate to the moisture content has been explained as well with a special attention for the thermal conductivities' derivation relations.

Special attention has been given to the description of four main formulations describing the energy interactions at the soil surface for different cover scenarios (bare soil, pavement, vegetation and snow covered). Heat transfer coefficients have been offered for the typical heat flux processes at the surface of the soil: shortwave and longwave radiation, air convection and latent heat.

Also, the effect of freezing on soil have been discussed in the previous sections. The freezing can affect the soil in a multi levels such as, the heat transfer in soil, not only through the release and adsorption of the latent heat of fusion, but also through changes in the thermal and hydraulic properties. Furthermore, it can affect the permeability and soil structure that would be changed due to freezing and thawing cycle. Furthermore, Soil freezing also affects the potential release of carbon and nutrients from soil microbial cells which have significant impacts on the overall carbon balance of ecosystems, and therefore on atmospheric CO_2 concentrations.

Analytical methods for soil temperature profile estimation have also been discussed. The importance to have these profiles arises as it provides details about the physical processes happening in the problem even though they are for limited scenarios. The numerical models and their benefits have been discussed with an overview of some numerical simulations regarding the treatment of buried thermal devices has been offered. Although different numerical methods are available (finite differences, finite elements or finite volumes) embedded in different software packages (FLUENT, COMSOL, etc.) or even in purpose-built in languages (FORTRAN, C, C++, MATLAB), but

it has been shown that (in general) they share similar assumptions regarding the treatment of boundary conditions and the physical processes related with the transfer of heat in soils (usually neglecting moisture transfer).

This chapter's objectives were covered via providing a detailed background for the problem in hand and different possibilities to enhance the performance or parameters affecting it, alongside possible methods suggested for calculating them. The details of which method or equation to be used in the developed model will be presented in the next theoretical framework chapter.

2.8 References

Abu-Hamdeh, N. H. 2003. Thermal properties of soils as affected by density and water content. *Biosystems Engineering.* 86(1), pp. 97-102. DOI: 10.1016/S1537-5110(03)00112-0.

Adams, E. E., Cosler, D. J. and Helfrich, K. R. 1990. Evaporation from heated water bodies: predicting combined forced plus free convection. *Water Resources Research.* 26(3), pp. 425-435. DOI: 10.1029/WR026i003p00425.

Alderman, R. 2003. Insulation system having a variable R-value. *Google Patents*. Alderman R. J.

Alrtimi, A., Rouainia, M. and Haigh, S. 2016. Thermal conductivity of a sandy soil. *Applied Thermal Engineering.* 106, pp. 551-560. DOI: 10.1016/j.applthermaleng.2016.06.012.

Alvenäs, G. and Jansson, P. 1997. Model for evaporation, moisture and temperature of bare soil: calibration and sensitivity analysis. *Agricultural and Forest Meteorology.* 88(1), pp. 47-56. DOI: 10.1016/S0168-1923(97)00052-X.

Andersson, O. 2007. Aquifer thermal energy storage (ATES). In: Paksoy, H.O. ed. *Thermal energy storage for sustainable energy consumption: fundamentals, case studies and design*. Vol. 234. Dordrecht: Springer Netherlands, pp. 155-176.

Andreas, E. L. 1987. A theory for the scalar roughness and the scalar transfer coefficients over snow and sea ice. *Boundary-Layer Meteorology.* 38(1), pp. 159-184. DOI: 10.1007/bf00121562.

Andreas, E. L. 2002. Parameterizing scalar transfer over snow and ice: a review. *Journal of Hydrometeorology.* 3(4), pp. 417-432. DOI: 10.1175/1525-7541(2002)003 <0417:pstosa>2.0.co;2.

Ångström, A. 1925. The albedo of various surfaces of ground. *Geografiska Annaler.* 7, pp. 323-342. DOI: 10.2307/519495.

Armstrong, R. L. and Brun, E. 2008. *Snow and climate: physical processes, surface energy exchange and modeling*. Cambridge University Press.

Arya, S. P. 2001. *Introduction to micrometeorology*. Academic Press.

ASCE Hydrology Handbook. 1996. *Hydrology handbook*.

ASTM. 2008. Test method for specific heat of rock and soil. ASTM International.

Barry-Macaulay, D., Bouazza, A., Wang, B. and Singh, R. M. 2015. Evaluation of soil thermal conductivity models. *Canadian Geotechnical Journal.* 52(11), pp. 1892-1900. DOI: 10.1139/cgj-2014-0518.

Berdahl, P. and Martin, M. 1984. Emissivity of clear skies. *Solar Energy.* 32(5), pp. 663-664. DOI: 10.1016/0038-092X(84)90144-0.

Best, M. J. 1998. A model to predict surface temperatures. *Boundary-Layer Meteorology.* 88(2), pp. 279-306. DOI: 10.1023/A:1001151927113.

Bittelli, M., Tomei, F., Pistocchi, A., Flury, M., Boll, J., Brooks, E. S. and Antolini, G. 2010. Development and testing of a physically based, three-dimensional model of surface and subsurface hydrology. *Advances in Water Resources.* 33(1), pp. 106-122. DOI: 10.1016/j.advwatres.2009.10.013.

Bittelli, M., Ventura, F., Campbell, G. S., Snyder, R. L., Gallegati, F. and Pisa, P. R. 2008. Coupling of heat, water vapor, and liquid water fluxes to compute evaporation in bare soils. *Journal of Hydrology.* 362(3–4), pp. 191-205. DOI: 10.1016/j.jhydrol. 2008.08.014.

Boast, C. W. and Simmons, F. W. 2005. Evaportation of water from bare soil.*Encyclopedia of Soils in the Environment*. 10.1016/B0-12-348530-4/00358-1 Oxford: Elsevier, pp. 494-502.

Bobes-Jesus, V., Pascual-Muñoz, P., Castro-Fresno, D. and Rodriguez-Hernandez, J. 2013. Asphalt solar collectors: a literature review. *Applied Energy.* 102, pp. 962-970. DOI: 10.1016/j.apenergy.2012.08.050.

Brutsaert, W. 1975. A theory for local evaporation (or heat transfer) from rough and smooth surfaces at ground level. *Water Resources Research.* 11(4), pp. 543-550. DOI: 10.1029/WR011i004p00543.

Cabeza, L. F. 2014. *Advances in thermal energy storage systems: methods and applications*. Elsevier Science.

Çengel, Y. A. 2007. *Heat and mass transfer: a practical approach*. Mcgraw-Hill.

Chamberlain, E. J. and Gow, A. J. 1979. Effect of freezing and thawing on the permeability and structure of soils. *Engineering Geology.* 13(1), pp. 73-92. DOI: 10.1016/0013-7952(79)90022-X.

Chen, D., Gustavsson, T. and Bogren, J. 1999. The applicability of similarity theory to a road surface. *Meteorological Applications.* 6(1), pp. 81-88. DOI: 10.1017/ S1350482799001036.

Chen, S. X. 2008. Thermal conductivity of sands. *Heat and Mass Transfer.* 44(10), p. 1241. DOI: 10.1007/s00231-007-0357-1.

Chen, Y., Xie, H., Ke, H. and Chen, R. 2009. An analytical solution for one-dimensional contaminant diffusion through multi-layered system and its applications. *Environmental Geology.* 58(5), pp. 1083-1094. DOI: 10.1007/s00254-008-1587-3.

Chuangchid, P. and Krarti, M. 2001. Foundation heat loss from heated concrete slab-on-grade floors. *Building and Environment.* 36(5), pp. 637-655. DOI: 10.1016/S0360-1323(00)00040-8.

Cinquemani, V., Owenby, J. R. and Baldwin, R. G. 1979. *Input data for solar systems*. National Climatic Center.

Clark, W. W., Schaefer, L. A., Knotts, W. A., Mo, C. and Kimber, M. 2013. Variable thermal insulation. In: Pittsburgh, U.o. ed. *Google Patents*. University of Pittsburgh.

Cleall, P. J. and Li, Y.-C. 2011. Analytical solution for diffusion of VOCs through composite landfill liners. *Journal of Geotechnical and Geoenvironmental Engineering.* 137(9). DOI: 10.1061/(ASCE)GT.1943-5606.0000506.

Cleall, P. J., Muñoz-Criollo, J. J. and Rees, S. W. 2015. Analytical solutions for ground temperature profiles and stored energy using meteorological data. *Transport in Porous Media.* 106(1), pp. 181-199. DOI: 10.1007/s11242-014-0395-3.

Congedo, P. M., Colangelo, G. and Starace, G. 2012. CFD simulations of horizontal ground heat exchangers: a comparison among different configurations. *Applied Thermal Engineering.* 33–34, pp. 24-32. DOI: 10.1016/j.applthermaleng.2011.09.005.

Côté, J. and Konrad, J.-M. 2005. A generalized thermal conductivity model for soils and construction materials. *Canadian Geotechnical Journal.* 42(2), pp. 443-458. DOI: 10.1139/t04-106.

Dagesse, D. F. 2013. Freezing cycle effects on water stability of soil aggregates. *Canadian Journal of Soil Science.* 93(4), pp. 473-483. DOI: 10.4141/cjss2012-046.

Davies, J. H. 2013. Global map of solid earth surface heat flow. *Geochemistry, Geophysics, Geosystems.* 14(10), pp. 4608-4622. DOI: 10.1002/ggge.20271.

de Moel, M., Bach, P. M., Bouazza, A., Singh, R. M. and Sun, J. O. 2010. Technological advances and applications of geothermal energy pile foundations and their feasibility in Australia. *Renewable and Sustainable Energy Reviews.* 14(9), pp. 2683-2696. DOI: 10.1016/j.rser.2010.07.027.

de Vries, D. A. 1958. Simultaneous transfer of heat and moisture in porous media. *Eos, Transactions American Geophysical Union.* 39(5), pp. 909-916. DOI: 10.1029/TR039i005p00909.

de Vries, D. A. 1963. *Thermal properties of soils In W.R. van Wijk (ed.) physics of plant environment*. Amsterdam: North-Holland Publishing Company.

Deardorff, J. W. 1978. Efficient prediction of ground surface temperature and moisture, with inclusion of a layer of vegetation. *Journal of Geophysical Research: Oceans.* 83(C4), pp. 1889-1903. DOI: 10.1029/JC083iC04p01889.

Deb, S. K., Shukla, M. K., Sharma, P. and Mexal, J. G. 2011. Coupled liquid water, water vapor, and heat transport simulations in an unsaturated zone of a sandy loam field. *Soil Science.* 176(8), pp. 387-398. DOI: 10.1097/SS.0b013e318221f132.

Donazzi, F. ed. 1977. *Soil thermal and hydrological characteristics in designing underground cables*. Proceedings of the Institution of Electrical Engineers.

dos Santos, G. H. and Mendes, N. 2006. Simultaneous heat and moisture transfer in soils combined with building simulation. *Energy and Buildings.* 38(4), pp. 303-314. DOI: 10.1016/j.enbuild.2005.06.011.

Duan, X. and Naterer, G. F. 2009. Thermal protection of a ground layer with phase change materials. *Journal of Heat Transfer.* 132(1), pp. 011301-011301-011309. DOI: 10.1115/1.3194764.

Duffie, J. A. and Beckman, W. A. 2013. *Solar engineering of thermal processes*. Wiley.

Edinger, J. E., Duttweiler, D. W. and Geyer, J. C. 1968. The response of water temperatures to meteorological conditions. *Water Resources Research.* 4(5), pp. 1137-1143. DOI: 10.1029/WR004i005p01137.

Esen, H., Inalli, M. and Esen, M. 2007. Numerical and experimental analysis of a horizontal ground-coupled heat pump system. *Building and Environment.* 42(3), pp. 1126-1134. DOI: 10.1016/j.buildenv.2005.11.027.

Faizal, M., Bouazza, A. and Singh, R. M. 2016. Heat transfer enhancement of geothermal energy piles. *Renewable and Sustainable Energy Reviews.* 57, pp. 16-33. DOI: 10.1016/j.rser.2015.12.065.

Farouki, O. T. 1981. *Thermal properties of soils*. U.S. Army Corps of Engineers, Cold Regions Research and Engineering Laboratory.

Feddes, R. A., Kabat, P., Van Bakel, P. J. T., Bronswijk, J. J. B. and Halbertsma, J. 1988. Modelling soil water dynamics in the unsaturated zone - State of the art. *Journal of Hydrology.* 100(1), pp. 69-111. DOI: 10.1016/0022-1694(88)90182-5.

Fredlund, D. G. and Rahardjo, H. 1993. *Soil mechanics for unsaturated soils*. Wiley.

Frouin, R., Lingner, D. W., Gautier, C., Baker, K. S. and Smith, R. C. 1989. A simple analytical formula to compute clear sky total and photosynthetically available solar irradiance at the ocean surface. *Journal of Geophysical Research: Oceans.* 94(C7), pp. 9731-9742. DOI: 10.1029/JC094iC07p09731.

Gao, Z., Fan, X. and Bian, L. 2003. An analytical solution to one-dimensional thermal conduction-convection in soil. *Soil Science.* 168(2), pp. 99-107. DOI.

Gao, Z., Lenschow, D. H., Horton, R., Zhou, M., Wang, L. and Wen, J. 2008. Comparison of two soil temperature algorithms for a bare ground site on the Loess Plateau in China. *Journal of Geophysical Research: Atmospheres.* 113(D18), pp. n/a-n/a. DOI: 10.1029/2008JD010285.

Garratt, J. R. 1994. *The atmospheric boundary layer*. Cambridge University Press.

Geiger, R. 1950. *The climate near the ground*. Cambridge, Massachusetts Harvard University Press.

Gliński, J., Horabik, J. and Lipiec, J. 2011. Heat of wetting.*Encyclopedia of agrophysics*. 10.1007/978-90-481-3585-1_675 Dordrecht: Springer Netherlands, pp. 364-364.

Goodrich, L. E. 1993. Variable conductivity trafficked surface for permafrost regions. French: Google Patents.

Grant, S. A. 2005. Hydraulic properties, temperature effects.*Encyclopedia of Soils in the Environment*. 10.1016/B0-12-348530-4/00379-9 Oxford: Elsevier, pp. 207-211.

Grifoll, J., Gastó, J. M. and Cohen, Y. 2005. Non-isothermal soil water transport and evaporation. *Advances in Water Resources.* 28(11), pp. 1254-1266. DOI: 10.1016/j.advwatres.2005.04.008.

Hagentoft, C.-E. 1996a. Heat losses and temperature in the ground under a building with and without ground water flow - I. Infinite ground water flow rate. *Building and Environment.* 31(1), pp. 3-11. DOI: 10.1016/0360-1323(95)00028-3.

Hagentoft, C.-E. 1996b. Heat losses and temperature in the ground under a building with and without ground water flow - II. Finite ground water flow rate. *Building and Environment.* 31(1), pp. 13-19. DOI: 10.1016/0360-1323(95)00029-1.

Haigh, S. K. 2012. Thermal conductivity of sands. *Géotechnique.* 62(7), pp. 617-625. DOI: 10.1680/geot.11.P.043.

Harlan, R. L. 1973. Analysis of coupled heat-fluid transport in partially frozen soil. *Water Resources Research.* 9(5), pp. 1314-1323. DOI: 10.1029/WR009i005p01314.

Haverkamp, R., Bouraoui, F., Zammit, C. and Angulo-Jaramillo, R. 1998. Soil properties and moisture movement in the unsaturated zone.*The Handbook of Groundwater Engineering*. 10.1201/9781420048582.ch5 CRC Press.

Herb, W. R., Janke, B., Mohseni, O. and Stefan, H. G. 2008. Ground surface temperature simulation for different land covers. *Journal of Hydrology.* 356(3–4), pp. 327-343. DOI: 10.1016/j.jhydrol.2008.04.020.

Hillel, D. 2003. 12 - Soil Temperature and Heat Flow.*Introduction to Environmental Soil Physics (First)*. 10.1016/B978-012348655-4/50013-7 Burlington: Academic Press, pp. 215-233.

Hillel, D. 2005. Thermal properties and processes.*Encyclopedia of Soils in the Environment*. 10.1016/B0-12-348530-4/00523-3 Oxford: Elsevier, pp. 156-163.

Hollmuller, P. and Lachal, B. 2014. Air–soil heat exchangers for heating and cooling of buildings: design guidelines, potentials and constraints, system integration and global energy balance. *Applied Energy.* 119, pp. 476-487. DOI: 10.1016/j.apenergy.2014.01.042.

Holman, J. P. 2010. *Heat transfer*. McGraw Hill Higher Education.

Holtslag, A. A. M. and De Bruin, H. A. R. 1988. Applied modeling of the nighttime surface energy balance over land. *Journal of Applied Meteorology.* 27(6), pp. 689-704. DOI: 10.1175/1520-0450(1988)027<0689:amotns>2.0.co;2.

Horiguchi, K. and Miller, R. D. eds. 1983. *Hydraulic conductivity functions of frozen materials*. Permafrost: Fourth International Conference Proceedings. Washington, D.C. National Academy Press.

Huang, R. Q. and Wu, L. Z. 2012. Analytical solutions to 1-D horizontal and vertical water infiltration in saturated/unsaturated soils considering time-varying rainfall. *Computers and Geotechnics.* 39, pp. 66-72. DOI: 10.1016/j.compgeo.2011.08.008.

Idso, S. B. and Jackson, R. D. 1969. Thermal radiation from the atmosphere. *Journal of Geophysical Research.* 74(23), pp. 5397-5403. DOI: 10.1029/JC074i023p05397.

İnallı, M. and Esen, H. 2004. Experimental thermal performance evaluation of a horizontal ground-source heat pump system. *Applied Thermal Engineering.* 24(14–15), pp. 2219-2232. DOI: 10.1016/j.applthermaleng.2004.01.005.

Iziomon, M. G., Mayer, H. and Matzarakis, A. 2003. Downward atmospheric longwave irradiance under clear and cloudy skies: Measurement and parameterization. *Journal of Atmospheric and Solar-Terrestrial Physics.* 65(10), pp. 1107-1116. DOI: 10.1016/j.jastp.2003.07.007.

Jacovides, C. P., Mihalakakou, G., Santamouris, M. and Lewis, J. O. 1996. On the ground temperature profile for passive cooling applications in buildings. *Solar Energy.* 57(3), pp. 167-175. DOI: 10.1016/S0038-092X(96)00072-2.

Jansson, C., Almkvist, E. and Jansson, P. E. 2006. Heat balance of an asphalt surface: observations and physically-based simulations. *Meteorological Applications.* 13(2), pp. 203-212. DOI: 10.1017/S1350482706002179.

Jansson, P.-E. 2012. CoupModel: model use, calibration, and validation. 55(4), p. 1337. DOI: 10.13031/2013.42245.

Johansen, O. 1975. *Thermal conductivity of soils.* Ph.D. thesis, University of Trondheim, Norway.

Kay, B. D. and Perfect, E. eds. 1983. *State of the art: heat and mass transfer in freezing soils*. 5th International Symposium on Ground Freezing. Nottingham-England.

Kersten, M. S. 1949. *Thermal properties of soils*. Bulletin 1949 [No. 28. Minneapolis, MN: University of Minnesota Engineering Experiment Station].

Kong, X.-R., Deng, Y., Li, L., Gong, W.-S. and Cao, S.-J. 2017. Experimental and numerical study on the thermal performance of ground source heat pump with a set of designed buried pipes. *Applied Thermal Engineering.* 114, pp. 110-117. DOI: 10.1016/j.applthermaleng.2016.11.176.

Koorevaar, P., Menelik, G. and Dirksen, C. 1983. Heat transport in soil.*Developments in soil science*. Vol. 13. Elsevier, pp. 193-207.

Krarti, M. and Kreider, J. F. 1996. Analytical model for heat transfer in an underground air tunnel. *Energy Conversion and Management.* 37(10), pp. 1561-1574. DOI: 10.1016/0196-8904(95)00208-1.

Kroll, J. A. and Ziegler, F. 2011. The use of ground heat storages and evacuated tube solar collectors for meeting the annual heating demand of family-sized houses. *Solar Energy.* 85(11), pp. 2611-2621. DOI: 10.1016/j.solener.2011.08.001.

Kubota, A. and Sugita, M. 1994. Radiometrically determined skin temperature and scalar roughness to estimate surface heat flux. part I: parameterization of radiometric scalar roughness. *Boundary-Layer Meteorology.* 69(4), pp. 397-416. DOI: 10.1007/bf00718127.

Kumar, N., Grogan, P., Chu, H., Christiansen, C. T. and Walker, V. K. 2013. The effect of freeze-thaw conditions on arctic soil bacterial communities. *Biology.* 2(1), pp. 356-377. DOI: 10.3390/biology2010356.

Kupiec, K., Larwa, B. and Gwadera, M. 2015. Heat transfer in horizontal ground heat exchangers. *Applied Thermal Engineering.* 75, pp. 270-276. DOI: 10.1016/j.applthermaleng.2014.10.003.

Kurylyk, B. L., McKenzie, J. M., MacQuarrie, K. T. B. and Voss, C. I. 2014. Analytical solutions for benchmarking cold regions subsurface water flow and energy transport models: one-dimensional soil thaw with conduction and advection. *Advances in Water Resources.* 70, pp. 172-184. DOI: 10.1016/j.advwatres.2014.05.005.

Launiainen, J. 1995. Derivation of the relationship between the Obukhov stability parameter and the bulk Richardson number for flux-profile studies. *Boundary-Layer Meteorology.* 76(1), pp. 165-179. DOI: 10.1007/bf00710895.

Letcher, T. M. and Reay, D. 2016. *Storing energy: with special reference to renewable energy sources*. Elsevier Science & Technology Books.

Li, Y.-C. and Cleall, P. J. 2010. Analytical solutions for contaminant diffusion in double-layered porous media. *Journal of Geotechnical and Geoenvironmental Engineering.* 136(11), pp. 1542-1554. DOI: 10.1061/(ASCE)GT.1943-5606.0000365.

Li, Y.-C. and Cleall, P. J. 2011. Analytical solutions for advective–dispersive solute transport in double-layered finite porous media. *International Journal for Numerical and Analytical Methods in Geomechanics.* 35(4), pp. 438-460. DOI: 10.1002/nag.903.

Liu, C., Shi, B., Tang, C. and Gao, L. 2011. A numerical and field investigation of underground temperatures under urban heat island. *Building and Environment.* 46(5), pp. 1205-1210. DOI: 10.1016/j.buildenv.2010.12.015.

Liu, W. T., Katsaros, K. B. and Businger, J. A. 1979. Bulk parameterization of air-sea exchanges of heat and water vapor including the molecular constraints at the interface. *Journal of Atmospheric Sciences.* 36(9), pp. 1722-1735. DOI.

Lu, S., Ren, T., Gong, Y. and Horton, R. 2007. An improved model for predicting soil thermal conductivity from water content at room temperature. *Soil Science Society of America Journal.* 71(1), pp. 8-14. DOI: 10.2136/sssaj2006.0041.

Lumb, F. E. 1964. The influence of cloud on hourly amounts of total solar radiation at the sea surface. *Quarterly Journal of the Royal Meteorological Society.* 90(383), pp. 43-56. DOI: 10.1002/qj.49709038305.

Mahfouf, J. F. and Noilhan, J. 1991. Comparative study of various formulations of evaporations from bare soil using in situ data. *Journal of Applied Meteorology.* 30(9), pp. 1354-1365. DOI: 10.1175/1520-0450(1991)030<1354:csovfo>2.0.co;2.

Maidment, D. R. 1993. *Handbook of hydrology*. McGraw-Hill.

Maref, W., Lacasse, M. A. and Booth, D. G. 2002. *Benchmarking of IRC's Advanced Hygrothermal Model - hygIRC Using Mid- and Large-Scale Experiments*. National Research Council Canada.

Marshall, T. J., Holmes, J. W. and Rose, C. W. 1996. *Soil physics*. Cambridge University Press.

Michopoulos, A., Papakostas, K. T., Mavrommatis, T. and Kyriakis, N. 2010. Comparative assessment of eight models predicting the ground temperature. *JP Journal of Heat and Mass Transfer.* 4(2), pp. 119-135. DOI.

Mihalakakou, G., Santamouris, M., Lewis, J. O. and Asimakopoulos, D. N. 1997. On the application of the energy balance equation to predict ground temperature profiles. *Solar Energy.* 60((s 3–4)), pp. 181–190. DOI: 10.1016/S0038-092X(97)00012-1.

Muñoz-Criollo, J. J. 2014. *An investigation of inter-seasonal near-surface ground heat transfer and storage.* Ph.D. thesis, Cardiff University, http://orca.cf.ac.uk/73226/.

Muñoz-Criollo, J. J., Cleall, P. J. and Rees, S. W. 2016a. Factors influencing collection performance of near surface interseasonal ground energy collection and storage systems. *Geomechanics for Energy and the Environment.* 6, pp. 45-57. DOI: 10.1016/j.gete.2016.04.001.

Muñoz-Criollo, J. J., Cleall, P. J. and Rees, S. W. 2016b. Modelling thermal fluxes at the soil surface. *Environmental Geotechnics.* 0(0), pp. 1-1. DOI: 10.1680/jenge.15.00075.

N'Tsoukpoe, K. E., Liu, H., Le Pierrès, N. and Luo, L. 2009. A review on long-term sorption solar energy storage. *Renewable and Sustainable Energy Reviews.* 13(9), pp. 2385-2396. DOI: 10.1016/j.rser.2009.05.008.

Nabi, M. and Al-Khoury, R. 2012. An efficient finite volume model for shallow geothermal systems - Part II: verification, validation and grid convergence. *Computers & Geosciences.* 49, pp. 297-307. DOI: 10.1016/j.cageo.2012.03.023.

Nagano, K. 2007. Energy pile system in new building of Sapporo City University. In: Paksoy, H.O. ed. *Thermal energy storage for sustainable energy consumption: fundamentals, case studies and design*. Vol. 234. Dordrecht: Springer Netherlands, pp. 245-253.

Nam, Y., Ooka, R. and Hwang, S. 2008. Development of a numerical model to predict heat exchange rates for a ground-source heat pump system. *Energy and Buildings.* 40(12), pp. 2133-2140. DOI: 10.1016/j.enbuild.2008.06.004.

National Meteorological Library and Archive. 2014. *Observations: weather observations over land. fact sheet 17 version 01.*

Nobre, R. C. M. and Thomson, N. R. 1993. The effects of transient temperature gradients on soil moisture dynamics. *Journal of Hydrology.* 152(1), pp. 57-101. DOI: 10.1016/0022-1694(93)90141-U.

North, G. R. and Erukhimova, T. L. 2009. *Atmospheric thermodynamics: elementary physics and chemistry*. Cambridge University Press.

Panofsky, H. A. 1963. Determination of stress from wind and temperature measurements. *Quarterly Journal of the Royal Meteorological Society.* 89(379), pp. 85-94. DOI: 10.1002/qj.49708937906.

Penman, H. L. 1948. Natural evaporation from open water, bare soil and grass. *Proceedings of the Royal Society of London. Series A. Mathematical and Physical Sciences.* 193(1032), pp. 120-145. DOI: 10.1098/rspa.1948.0037.

Perreault, P. and Shur, Y. 2016. Seasonal thermal insulation to mitigate climate change impacts on foundations in permafrost regions. *Cold Regions Science and Technology.* 132, pp. 7-18. DOI: 10.1016/j.coldregions.2016.09.008.

Philip, J. R. and de Vries, D. A. 1957. Moisture movement in porous materials under temperature gradients. *Eos, Transactions American Geophysical Union.* 38(2), pp. 222-232. DOI: 10.1029/TR038i002p00222.

Pielke, R. A. 2013. *Mesoscale meteorological modeling*. Elsevier.

Qin, Z., Berliner, P. and Karnieli, A. 2002. Numerical solution of a complete surface energy balance model for simulation of heat fluxes and surface temperature under bare soil environment. *Applied Mathematics and Computation.* 130(1), pp. 171-200. DOI: 10.1016/S0096-3003(01)00089-3.

Rees, S. W., Adjali, M. H., Zhou, Z., Davies, M. and Thomas, H. R. 2000. Ground heat transfer effects on the thermal performance of earth-contact structures. *Renewable & sustainable energy reviews.* 4(3), pp. 213-265. DOI: 10.1016/S1364-0321(99)00018-0.

Rees, S. W., Cleall, P. J., Li, Y.-C. and Shao, K. 2013. Freezing soil effects on earth-contact heat transfer. *Building Services Engineering Research and Technology.* 34(3), pp. 259-274. DOI: 10.1177/0143624412441616.

Rees, S. W., Zhou, Z. and Thomas, H. R. 2007. Ground heat transfer: a numerical simulation of a full-scale experiment. *Building and Environment.* 42(3), pp. 1478-1488. DOI: 10.1016/j.buildenv.2005.12.022.

Reeves, G. M., Sims, I., Cripps, J. C. and Geological Society of London. 2006. *Clay materials used in construction*. Geological Society.

Riche, F. and Schneebeli, M. 2013. Thermal conductivity of snow measured by three independent methods and anisotropy considerations. *The Cryosphere.* 7(1), pp. 217-227. DOI: 10.5194/tc-7-217-2013.

Roberson, J. A. and Crowe, C. T. 1989. *Engineering fluid mechanics*. Houghton Mifflin.

Romero, E., Gens, A. and Lloret, A. 2001. Temperature effects on the hydraulic behaviour of an unsaturated clay. *Geotechnical & Geological Engineering.* 19(3), pp. 311-332. DOI: 10.1023/a:1013133809333.

Ryan, P. J., Harleman, D. R. F. and Stolzenbach, K. D. 1974. Surface heat loss from cooling ponds. *Water Resources Research.* 10(5), pp. 930-938. DOI: 10.1029/WR010i005p00930.

Santamouris, M. 2013. Using cool pavements as a mitigation strategy to fight urban heat island—A review of the actual developments. *Renewable and Sustainable Energy Reviews.* 26, pp. 224-240. DOI: 10.1016/j.rser.2013.05.047.

Sauer, T. J. and Horton, R. 2005. Soil heat flux. *U.S. Department of Agriculture: Agricultural Research Service, Lincoln, Nebraska.* DOI.

Scholz, M. and Grabowiecki, P. 2007. Review of permeable pavement systems. *Building and Environment.* 42(11), pp. 3830-3836. DOI: 10.1016/j.buildenv.2006.11.016.

Sellers, W. D. 1965. *Physical climatology*. University of Chicago Press.

Serreze, M. C. and Barry, R. G. 2005. *The arctic climate system*. Cambridge University Press.

Shang, Y., Li, S. and Li, H. 2011. Analysis of geo-temperature recovery under intermittent operation of ground-source heat pump. *Energy and Buildings.* 43(4), pp. 935-943. DOI: 10.1016/j.enbuild.2010.12.017.

Shao, M., Horton, R. and Jaynes, D. B. 1998. Analytical solution for one-dimensional heat conduction-convection equation. *Soil Science Society of America Journal.* 62(1), pp. 123-128. DOI: 10.2136/sssaj1998.03615995006200010016x.

Shi, B., Tang, C. S., Gao, L., Liu, C. and Wang, B. J. 2012. Observation and analysis of the urban heat island effect on soil in Nanjing, China. *Environmental Earth Sciences.* 67(1), pp. 215-229. DOI: 10.1007/s12665-011-1501-2.

Singh, V. P., Singh, P., Bishop, M. P., Björnsson, H., Haritashya, U. K., Haeberli, W., Oerlemans, J., Shroder, J. F. and Tranter, M. 2011. *Encyclopedia of snow, ice and glaciers*. Springer Netherlands.

Soni, S. K., Pandey, M. and Bartaria, V. N. 2015. Ground coupled heat exchangers: A review and applications. *Renewable and Sustainable Energy Reviews.* 47, pp. 83-92. DOI: 10.1016/j.rser.2015.03.014.

Stull, R. B. 2000. *Meteorology for scientists and engineers*. Brooks/Cole.

Svec, O. J., Goodrich, L. E. and Palmer, J. H. L. 1983. Heat transfer characteristics of in-ground heat exchangers. *International Journal of Energy Research.* 7(3), pp. 265-278. DOI: 10.1002/er.4440070307.

Svec, O. J. and Palmer, J. H. L. 1989. Performance of a spiral ground heat exchanger for heat pump application. *International Journal of Energy Research.* 13(5), pp. 503-510. DOI: 10.1002/er.4440130502.

Tariku, F., Kumaran, K. and Fazio, P. 2010. Transient model for coupled heat, air and moisture transfer through multilayered porous media. *International Journal of Heat and Mass Transfer.* 53(15), pp. 3035-3044. DOI: 10.1016/j.ijheatmasstransfer.2010.03.024.

Thomas, H. R., Cleall, P. J., Li, Y.-C., Harris, C. and Kern-Luetschg, M. 2009. Modelling of cryogenic processes in permafrost and seasonally frozen soils. *Géotechnique.* 59(3), pp. 173-184. DOI: 10.1680/geot.2009.59.3.173.

Timo, V. 2011. *Atmospher-snow/ice interations*. Finnish Meteorological Institute, Helsinki, Finland: Springer Netherlands.

Tomasi, C. 1978. On the water vapour absorption in the 8–13 μm spectral region for different atmospheric conditions. *pure and applied geophysics.* 116(6), pp. 1063-1076. DOI: 10.1007/bf00874671.

UK Department of Energy and Climate Change. 2011. *UK renewable energy roadmap* [Online]. https://www.decc.gov.uk/. Available at: https://www.gov.uk/government/uploads/system/uploads/attachment_data/file/48128/2167-uk-renewable-energy_-roadmap.pdf [Accessed: 01/01/2018].

Vasco, D. W. 2010. On fluid flow in a heterogeneous medium under nonisothermal conditions. *Water Resources Research.* 46(12). DOI: 10.1029/2010WR009571.

Vasiliev, L. L., Grakovich, L. P., Rabetsky, M. I., Vassiliev, L. L., Jr. and Zhuravlyov, A. S. 2017. Thermosyphons with innovative technologies. *Applied Thermal Engineering.* 111, pp. 1647-1654. DOI: 10.1016/j.applthermaleng.2016.07.101.

Vihma, T. 1995. Subgrid parameterization of surface heat and momentum fluxes over polar oceans. *Journal of Geophysical Research: Oceans.* 100(C11), pp. 22625-22646. DOI: 10.1029/95JC02498.

Vogel, C. A., Baldocchi, D. D., Luhar, A. K. and Rao, K. S. 1995. A comparison of a hierarchy of models for determining energy balance components over vegetation canopies. *Journal of Applied Meteorology.* 34(10), pp. 2182–2196. DOI: 10.1175/1520-0450(1995)034<2182:ACOAHO>2.0.CO;2.

Wang, L., Gao, Z., Horton, R., Lenschow, D. H., Meng, K. and Jaynes, D. B. 2012. An analytical solution to the one-dimensional heat conduction–convection equation in soil. *Soil Science Society of America Journal.* 76(6), pp. 1978-1986. DOI: 10.2136/sssaj2012.0023N.

Wang, Z. 2012. Reconstruction of soil thermal field from a single depth measurement. *Journal of Hydrology.* 464, pp. 541-549. DOI: 10.1016/j.jhydrol.2012.07.047.

Wang, Z. and Bou-Zeid, E. 2012. A novel approach for the estimation of soil ground heat flux. *Agricultural and Forest Meteorology.* 154–155, pp. 214-221. DOI: 10.1016/ j.agrformet.2011.12.001.

Winterkorn, H. F. 1962. Behavior of moist soils in thermal energy field.*Clays and Clay Minerals*. 10.1016/B978-1-4831-9842-2.50009-2 Pergamon, pp. 85-103.

Woodside, W. and Messmer, J. H. 1961. Thermal conductivity of porous media. I. Unconsolidated sands. *Journal of Applied Physics.* 32(9), pp. 1688-1699. DOI: 10.1063/1.1728419.

Wu, Y., Gan, G., Verhoef, A., Vidale, P. L. and Gonzalez, R. G. 2010. Experimental measurement and numerical simulation of horizontal-coupled slinky ground source heat exchangers. *Applied Thermal Engineering.* 30(16), pp. 2574-2583. DOI: 10.1016/j.applthermaleng.2010.07.008.

Yu, F., Qi, J., Zhang, M., Lai, Y., Yao, X., Liu, Y. and Wu, G. 2016. Cooling performance of two-phase closed thermosyphons installed at a highway embankment in permafrost regions. *Applied Thermal Engineering.* 98, pp. 220-227. DOI: 10.1016/j.applthermaleng.2015.11.102.

Yumrutaş, R., Kanoğlu, M., Bolatturk, A. and Bedir, M. Ş. 2005. Computational model for a ground coupled space cooling system with an underground energy storage tank. *Energy and Buildings.* 37(4), pp. 353-360. DOI: 10.1016/j.enbuild.2004.07.004.

Zhang, N. and Wang, Z. 2017. Review of soil thermal conductivity and predictive models. *International Journal of Thermal Sciences.* 117, pp. 172-183. DOI: 10.1016/ j.ijthermalsci.2017.03.013.

Zhang, N., Yu, X., Pradhan, A. and Puppala, A. J. 2015. Thermal conductivity of quartz sands by thermo-time domain reflectometry probe and model prediction. *Journal of Materials in Civil Engineering.* 27(12). DOI: 10.1061/(ASCE)MT.1943-5533.0001332.

Zheng, S., Lourenço, S. D. N., Cleall, P. J., Millis, S. W., Ng, A. K. Y. and Chui, T. F. M. 2017. Synthetic water repellent soils for slope stabilization. In: Mikoš, M. and Arbanas, Ž. and Yin, Y. and Sassa, K. eds. *Advancing Culture of Living with Landslides: Volume 3 Advances in Landslide Technology*. 10.1007/978-3-319-53487-9_61 Cham: Springer International Publishing, pp. 523-528.

Zhou, Z., Wang, X., Zhang, X., Chen, G., Zuo, J. and Pullen, S. 2015. Effectiveness of pavement-solar energy system - An experimental study. *Applied Energy.* 138, pp. 1-10. DOI: 10.1016/j.apenergy.2014.10.045.

Chapter 3: Theoretical Framework

3.1 Introduction

This chapter presents governing equations that describe the transfer of heat in soil and includes consideration of surface fluxes, the impact of snow on the ground surface, ground freezing and also interaction with the heat flow within a pipe system.

This chapter is subdivided in several sections which cover the following aspects:

- The main assumptions the theoretical model is based on, are presented in Section 3.2.
- The law of conservation used to produce the governing equation for heat flow is discussed in Section 3.3.
- Fourier's law is described in Section 3.4.
- Section 3.5 discusses heat diffusion in soils including the effects of soil freezing.
- Heat advection within fluid carrying pipes and heat transfer between the fluid and surrounding soil through the pipe is considered in Section 3.6.
- Surface energy balances with its different components are discussed in Section 3.7.
- The overall surface balance equation for different conditions at the soil surface are presented in Section 3.8.
- Section 3.9 discusses the boundary conditions at the bottom and far field of the domain.
- Conclusions and summarizing remarks are given in Section 3.10.
- Section 3.11 summarizes the chapter references.

3.2 Assumptions

The main assumptions used in the theoretical framework presented in the next sections are summarized as follows:

- Local thermal equilibrium is assumed inside the soil, i.e. the local temperature is the same for soil solid, pore water and ice.
- The soil is assumed to be non-deformable material with no variation of moisture content considered.
- On the soil surface, the effect of moisture mass transfer associated with precipitation, condensation and evaporation is neglected over surfaces, meaning there is no mass transfer to be included in the surface modelling.
- Inward heat fluxes normal to the soil surface are considered positive.

3.3 Conservation laws

The conservation laws are considered to be the fundamental laws of nature with broad application in physics as well as in other fields such as chemistry, biology, geology, and engineering.

The law of conservation of energy, also known as first law of thermodynamics, is useful to describe the variation of temperature on a given region over time. It states that heat is a form of energy, and thermodynamic processes are therefore subject to the principle of conservation of energy. This means that heat energy cannot be created or destroyed, but it can, however, be transferred from one location to another and converted to and from other forms of energy.

This law states that the total internal energy of the system E_i (J/m^3) during a process is equal to the thermal energy q_h (W/m^2) entering or leaving the system during that process which can be expressed, in a one-dimensional system as:

$$\frac{\partial E_i}{\partial t} = -\frac{q_h(x+\Delta x) - q_h(x)}{\Delta x} + Q \tag{3.1}$$

By taking the limit of $\Delta x \to 0$ yields the heat equation:

$$\frac{\partial E_i}{\partial t} = -\frac{\partial q_h}{\partial x} + Q \tag{3.2}$$

This can be written for a three-dimensional system as:

$$\frac{\partial E_i}{\partial t} = -\nabla . q_h + Q \tag{3.3}$$

where Q refers to the sink/source term while ∇ is the differential operator that is given by:

$$\nabla = \frac{\partial}{\partial x} + \frac{\partial}{\partial y} + \frac{\partial}{\partial z} \tag{3.4}$$

The expressions that define the heat flow rates depend on the specific characteristics of the problem and the physical process involved, for example Fourier's law (discussed later) describes heat conduction in solids but if there are more processes involved (e.g. internal heat generation, advection, convection) they would need to be considered in the right-hand side of equation (3.3).

An important application of the energy conservation principle arises in the consideration of surface energy balances. A surface does not have a volume nor mass, and thus, has no energy, but it can be viewed as a fictitious system which energy content remains constant during a process (Çengel 2007). According to this assumption it is possible to keep track of the energy interactions at a surface when energy is transferred from one medium to another. The energy balance for a surface (e.g. the soil surface) can be expressed as:

$$q_{s,in} = q_{s,out} \tag{3.5}$$

where $q_{s,in}$ (W/m^2) is the net amount of energy reaching the surface and on the other hand $q_{s,out}$ (W/m^2) is the net amount of energy leaving it.

3.4 Fourier's law

Fourier's law describes the transfer of thermal energy within a body by conduction. It states that the ratio of thermal energy transfer through a material is proportional to the temperature gradient and to the area through which the thermal energy flows. In its differential expression (per unit area), it is given by Holman (2010):

$$q_h = -\lambda_b \nabla T \quad (3.6)$$

where T (K) is the temperature of the material, λ_b (W/mK) is the bulk thermal conductivity of the material which is a material property of the medium through which the thermal energy transfers.

3.5 Governing differential equation for heat transfer of frozen / unfrozen Soil

The previous sections discussed conservation principles used to describe the transport of heat within soils. Heat movement implies non-isothermal conditions in the soil that could cause changes in the pore pressure equilibrium of water (Fredlund and Rahardjo 1993). For example, a change in the temperature of the pore air could change the amount of water vapour that it can hold (this could be represented via consideration of the partial pressure of water vapour). The condensation or evaporation of water would modify the pore water pressure while at the same time extracts or delivers energy to the soil, thereby changing its temperature.

These coupled changes in temperature and potentials could result in moisture, air and water vapour migration and heat transfer within the soil. In principle, the thermal properties of water are, dependent on temperature, moisture content and/or pore-pressure (Rees *et al.* 2000). Hence, the change in soil moisture content driven by moisture migration can have an impact on the overall thermal properties of the soil. However, the relative strength of these coupled interdependencies is not the same, for example the variations found in the thermal properties because of the changes in the moisture content are more significant than the changes in hydraulic properties due to thermal gradients (Rees *et al.* 2000).

The approach adopted here is based on the thermal model for frozen soils presented by Rees *et al.* (2013) which is a simplified version from the coupled thermo-hydro-mechanical model presented by Thomas *et al.* (2009). The model presented by Rees *et al.* (2013) considers only the thermal field and was extended to consider

unsaturated conditions. The model assumes the soil to be a partially saturated medium consisting of solid grains, pore air, pore water and pore ice within which the pore water is either fully frozen, partially frozen or unfrozen.

The law of conservation of energy for heat flow for soil dictates that the temporal derivative of heat content, Φ, is equal to the spatial derivative of the heat flux q.

$$\frac{\partial(\Phi dV)}{\partial t} + \nabla q dV = 0 \tag{3.7}$$

where Φ refers to the heat content of soil per unit volume and is defined as:

$$\Phi = H_c(T - T_r) - L_f n S_r S_i \rho_i \tag{3.8}$$

where H_c (J/m^{3}K) is the volumetric heat capacity, T_r (K) is a reference temperature, L_f (J/kg) is the latent heat of fusion, ρ_i (kg/m^3) is the density of ice, S_r is the degree of moisture saturation, n is the porosity, S_i is the degree of moisture in the ice phase and can be represented by a power function of the temperature as (Rees *et al.* 2013):

$$S_i = 1 - [1 - (T - T_0)]^a \qquad T \leq T_0 \tag{3.9}$$

where T_0 is the freezing point of pore water and a is a parameter which is dependent on pore size, if variations of the chemical composition of the pore liquid are not considered. Figure (3.1) present a relationship of S_i and $T - T_0$ with a ranging from -10 to -1.

The heat flux per unit volume q, which includes conduction is defined using Fourier's law where the thermal conductivity of the soil will vary with degree of moisture saturation and degree of moisture in the ice phase. Finally, the governing equation of heat transfer can be written as:

$$\left(H_c + [(S_r \rho_i c_i - S_r \rho_l c_l)(T - T_r) - S_r \rho_i L] n \frac{\partial S_i}{\partial T}\right) \frac{\partial T}{\partial t} = \nabla(\lambda_b \nabla T) \tag{3.10}$$

This approach takes into consideration (a) conduction, (b) latent heat of fusion on freezing and (c) impact of partial saturation and freezing on thermal conductivity and heat capacity.

For an unfrozen soil equation (3.10) reduces to:

$$H_c \frac{\partial T}{\partial t} = \nabla(\lambda_b \nabla T) \tag{3.11}$$

It is assumed that heat is transferred in the soil only by conduction, as it is thought to be the dominant heat transfer process in soils, this approach is commonly used to study the heat transfer interactions between the soils and buried thermal devices whenever no significant advection processes are expected to happen in the soil's domain (Rees *et al.* 2007) .

Moreover, since the soil's bulk thermal conductivity λ_b is dependent on the soil water content and due to the derivation with respect to time the use of absolute temperature is no longer needed.

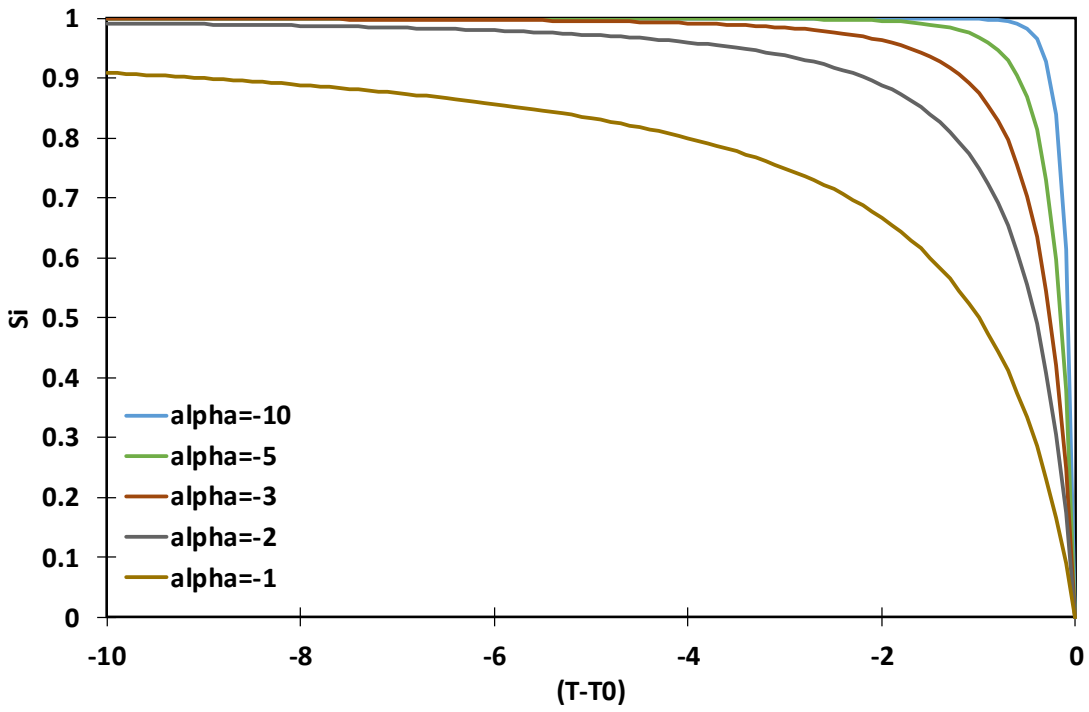

Figure (3.1) Relationship between degree of moisture in the ice phase and temperature presented in equation (3.9) (Thomas *et al.* 2009)

Among the most important parameters that affect the heat transfer governing differential equation are the specific heat capacity and these are considered in the next sections.

3.5.1 Volumetric heat capacity of frozen / unfrozen soils

The major thermal properties that affects heat transfer and of real interest are the thermal conductivity (discussed later in Section 3.5.2) and the thermal capacity. While it is possible to determine the latter with fairly good accuracy either analytically or experimentally, numerous problems are encountered in the determination of thermal conductivity (Alrtimi *et al.* 2016).

The volumetric heat capacity of the soil has been defined by de Vries (1963) as:

$$H_c = (1 - S_i)S_r n\rho_l c_l + nS_r S_i \rho_i c_i + n(1 - S_r)\rho_a c_a + (1 - n)\rho_s c_s \qquad (3.12)$$

where c_l, c_i, c_a and c_s (J/kgK) are the specific heat capacities of pore water, pore ice, pore air and the solid particles, respectively; ρ_l, ρ_a and ρ_s (kg/m^3) are the density of pore water, pore air and the solid particles, respectively.

3.5.2 Thermal conductivity of frozen / unfrozen soils

In general, soils are either two or three phase materials that consist of mineral particles, organic matter, and pores that contain water, air or a combination of both. The soils thermal conductivity had been found to be a function of several parameters including temperature, dry density, mineralogy, water content, particle size, particle shape and the volumetric proportions of the soil constituents (Alrtimi *et al.* 2016).

In the following sections, some of the proposed approaches and their equations that were used to predict the thermal conductivity of soils with varying saturation and dry density are presented.

3.5.2.1 Donazzi method

Donazzi (1977) used the following exponential function to express the relationship of thermal resistivity ρ_r (the inverse function of thermal conductivity), with porosity n and degree of saturation S_r

$$\rho_r = \rho_{r,w}^{n}\, \rho_{r,s}^{1-n} exp(3.08(1 - S_r)n) \tag{3.13}$$

where $\rho_{r,w}$ (mK/W) is the thermal resistivity of water with a value of 1.70, $\rho_{r,s}$ (mK/W) is the thermal resistivity of soil grains with a value of 0.25 for sandy soils (Chen 2008).

3.5.2.2 Haigh method

Haigh (2012) proposed an analytical model based on unidirectional heat flow through a three-phase soil element. The model analyses the one-dimensional heat flow between two equally sized spherical soil particles of radius R_0. According to this procedure, the overall thermal conductivity can be expressed as the following:

$$\begin{aligned}\frac{\lambda_b}{1.58\lambda_s} = 2(1+\xi)^2 \Bigg[& \frac{\alpha_w}{(1-\alpha_w)^2} \ln \frac{(1+\xi) + (\alpha_w - 1)x}{\xi + \alpha_w} \\ & + \frac{\alpha_a}{(1-\alpha_a)^2} \ln \frac{(1+\xi)}{(1+\xi) + (\alpha_a - 1)x} \Bigg] \\ & + \frac{2(1+\xi)}{(1-\alpha_w) + (1-\alpha_a)} [(\alpha_w - \alpha_a)x - (1-\alpha_a)\alpha_w]\end{aligned} \tag{3.14}$$

where ξ, α and x are given by:

$$\xi = \frac{2e-1}{3} \tag{3.15}$$

$$\alpha = \frac{\lambda_{fluid}}{\lambda_{soil}} \tag{3.16}$$

$$x = \frac{(1+\xi)}{2}\left(1 + \cos\theta - \sqrt{3}\sin\theta\right) \tag{3.17}$$

and θ is given by:

$$\cos 3\theta = \frac{2(1+3\xi)(1-S_r)-(1+\xi)^3}{(1+\xi)^3} \tag{3.18}$$

where α_w and α_a are the thermal conductivities, normalized by that of the soil solids, of water and air respectively, as found in equation (3.16).

Finally, the degree of saturation is defined as:

$$S_r = \frac{2x^3 - 3(1+\xi)x^2 + 3\xi + 1}{1+3\xi} \tag{3.19}$$

Figure (3.2) shows the thermal conductivity variations using the two approaches discussed earlier of Donazzi and Haigh with n = 0.344 and e = 0.523 for a fully saturated soil. The difference between the two methods is obvious which is mainly related to the reasoning of deriving those equations as Donazzi's method is derived from an empirical equation while Haigh method is derived from an analytical solution.

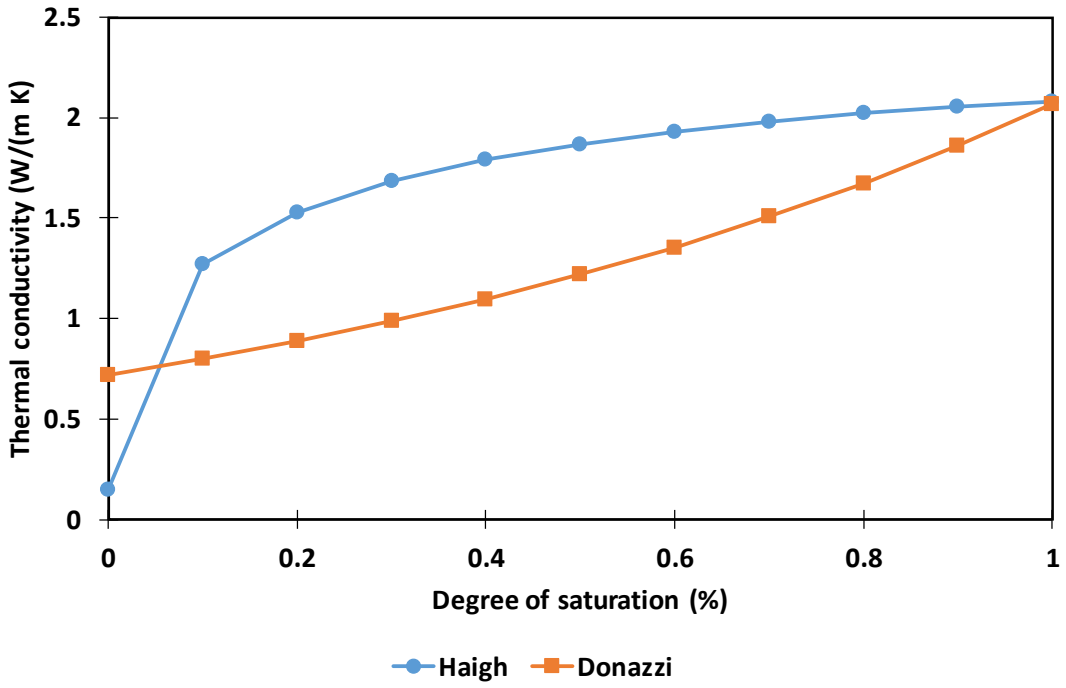

Figure (3.2) Thermal conductivity of soil using two different approaches.

3.5.2.3 Snow thermal conductivity

Snow insulates surfaces from the cold atmosphere and limits ground freezing and permafrost extent (Zhang 2005). Therefore, the thermal conductivity of snow, λ_{snow}, is an essential parameter in problems where surface snow layers are considered.

Snow thermal conductivity is very strongly dependent on snow structure, because diffusive thermal transport mostly takes place through the network of interconnected ice crystals (Sturm *et al.* 1997). Thermal conductivity of fresh snow can be as low as 0.025 (W/mK), that is, more insulating than many materials (e.g. styrofoam), while very hard wind packs or melt-freeze layers have high values as much as 0.65 (W/mK) (Sturm *et al.* 1997), which is similar to light concrete. Different values of λ_{snow} presented by Domine *et al.* (2008) for different snow types are shown in Table (3.1).

Physical Variable	Fresh snow	Decomposing particles	Rounded grain, ET metamorp-hism	Rounded grain, windpack	Faceted crystals	Depth hoar	Melt-freeze layer
Thermal conductivity (W/mK)	0.025-0.12	0.06-0.2	0.08-0.3	0.2-0.6	0.08	0.035-0.15	0.1-0.6

Table (3.1) Typical range of values of thermal conductivity for the most frequent snow crystal types in snow surface (Domine *et al.* 2008)

3.6 Heat advection within pipes

The previous sections have discussed the process of heat transport within soils, in this section the interaction between soil and buried thermal devices which utilise the advection of heat within pipe networks will be considered. Advection is defined as the physical process whereby energy (e.g. heat) or substances (dissolved ions) are transported by means of the bulk motion of a carrier fluid. Typical examples of advection are the transport of pollutants in rivers or heat in pipes (when the fluid is being pumped by an external agent).

The reason for considering this physical process in this study is to describe the transport of thermal energy between a heat exchanger (usually composed by a set of pipes with a carrier fluid running inside) buried in the ground and an external application such as road pavements. The variation of temperature in a given region due to the advection of thermal energy by movement of a fluid (in one dimension) can be expressed as (Pérez Guerrero *et al.* 2009 ; Carslaw and Jaeger 1986):

$$\rho_f c_{p,f} \left[\frac{\partial T_f}{\partial t} + u_f \frac{\partial T_f}{\partial x} \right] = Q_f \tag{3.20}$$

where u_f (m/s) is the velocity vector field that describes the fluid's motion, T_f(K), ρ_f (kg/m^3) and $c_{p,f}$ (J/kgK) are its temperature, density and specific heat capacity. Q_f (W/m^3) takes into account heat generation inside the pipes.

It is important to note that the advection process is assumed to occur only within the pipes constituting a buried heat exchanger while the thermal interaction between these pipes and ground is treated as a boundary condition (for the soil domain) using the transport equations for heat presented earlier in Section 3.5. For the pipe domain, this thermal interaction can be treated as an internal heat source using the term Q_f to represent the energy transferred through the external pipe' surface (W/m^2), integrated over the area of the pipe element that is in contact with the soil domain and then distributed on its corresponding volume (W/m^3). This approach is applicable if the relative size between the soil and pipe domains allows the latter to be considered as a one-dimensional. The thermal properties of the fluid inside the pipe are in general a function of temperature and, together with the fluid's velocity, will affect the amount of thermal energy transferred with the surrounding domain through the pipes boundaries.

Appendix A offers an analysis of the temperature dependence of the physical properties of a common fluid used in thermal engineering applications.

3.6.1 Heat transfer between fluid and solid

In Figure (3.3), the main variables involved in the heat transfer between the fluid inside the pipes and the surrounding soil are shown:

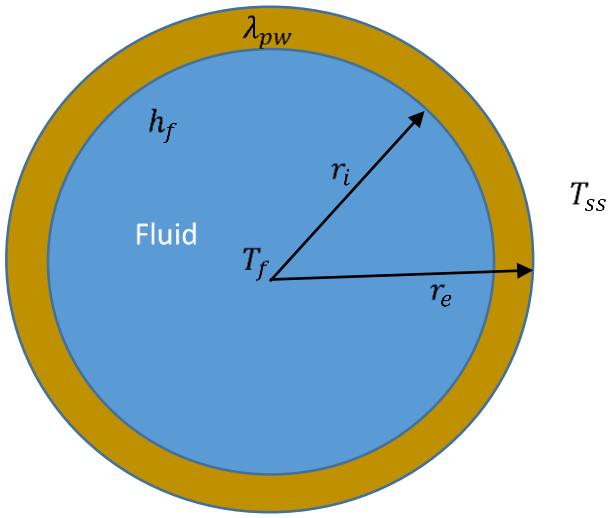

Figure (3.3) Cross-section of one pipe illustrating the main variables involved in heat transfer between surrounding soil and interior fluid

where r_i (m) is the internal pipe radius, r_e (m) is the external pipe radius, λ_{pw} (W/mK) is the thermal conductivity of the pipe wall, h_f (W/m^{2}K) is the convective heat transfer coefficient between the fluid inside the pipe and the pipe's wall, T_f (K) is the fluid temperature at the cross-section and T_{ss} (K) is the temperature of the soil directly in contact with the pipes which is assumed to be equal to the temperature of the exterior pipe walls. The heat Q_p (W) that is transferred across the wall of a pipe that has a length of L_p (m) is driven only by conduction (the temperature at the external surface of the wall is assumed to be known and equal to the temperature of the soil directly that is in contact with it) and is given by Çengel (2007) as:

$$Q_p = 2\pi L_p \lambda_{pw} \frac{T_{ss} - T_{pw}(r_i)}{\ln\left(r_e/r_i\right)} \tag{3.21}$$

where T_{pw} (K) is the temperature of the pipe wall.

Equation (3.21) is obtained from integrating the Fourier heat equation in cylindrical coordinates across the cylindrical layer of the pipe's wall, that is:

$$Q_p = 2\pi r L_p \lambda_{pw} \frac{dT_{pw}}{dr} \tag{3.22}$$

$$\frac{Q_p}{2\pi r L_p} = \lambda_{pw} \frac{dT_{pw}}{dr} \tag{3.23}$$

$$\int_{r_i}^{r_e} \frac{Q_p}{2\pi r L_p} dr = \int_{T_{pw(r_i)}}^{T_s} \lambda_{pw}\, dT_{pw} \tag{3.24}$$

The result of the integration of equation (3.24) is shown in equation (3.21). Furthermore, equation (3.21) can be rearranged to resemble Ohm's law for electrical networks as:

$$Q_p = \frac{T_{ss} - T_{pw}(r_i)}{\ln\left({}^{r_e}/_{r_i}\right)/2\pi L_p \lambda_{pw}} \tag{3.25}$$

where the denominator represents a thermal resistance (i.e. a resistance to the flow of thermal energy across the pipe wall).

The heat transferred between the fluid in the interior of the pipe and its wall can be considered as forced convection (as the fluid is considered to be pumped).

The temperature profile at the interior of the pipe is neglected and a constant temperature for the cross-section is assumed (although variable along the pipe). The heat transfer is given by:

$$Q_p = 2\pi r_i L_p h_f (T_{pw}(r_i) - T_f) \tag{3.26}$$

where h_f (W/m^{2}K) is the convective heat transfer coefficient between the fluid and the pipe wall. Equation (3.26) can be rearranged to have the same form as (3.25) such that:

$$Q_p = \frac{(T_{pw}(r_i) - T_f)}{\frac{1}{2\pi r_i L_p h_f}} \tag{3.27}$$

where the denominator in (3.27) has the same meaning (physical) as in (3.25), that is, a resistance to the flux of thermal energy in this case in the interface between the pipe wall and the fluid.

Heat transfer in equation (3.25) and equation (3.27) are expressed using the same symbol Q_p since both equations must have the same value (as there are no thermal sources nor sinks in the pipe wall). Then, following the electrical network analogy, it is possible to obtain a total resistance by summing up the individual resistances in series. This would be the total resistance to the flux of thermal energy from the fluid inside the pipes to the soil surrounding them. That is:

$$Q_p = \frac{(T_{ss} - T_f)}{\left[\frac{\ln\left({}^{r_e}/_{r_i}\right)}{2\pi L_p \lambda_{pw}}\right] + \left[\frac{1}{2\pi r_i L_p h_f}\right]} \tag{3.28}$$

$$Q_p = (T_{ss} - T_f) A_i U_p \tag{3.29}$$

where A_i (m^2) is the pipe internal area defined as $A_i = 2\pi r_i L_p$ and U_p (m^{2}K/ W) is the pipe overall heat transfer coefficient defined as:

$$U_p = \left[\frac{r_i \ln\left({}^{r_e}/_{r_i}\right)}{\lambda_{pw}}\right] + \left[\frac{1}{h_f}\right] \tag{3.30}$$

It is possible to express equation (3.29) per unit area as:

$$q_p = \frac{Q_p}{A_i} = U_p(T_{ss} - T_f) \tag{3.31}$$

All terms in equation (3.31) are known (or assumed to be) except for h_f the convective heat transfer coefficient. This coefficient can be calculated from:

$$N_u = \frac{h_f L_c}{\lambda_f} \tag{3.32}$$

where N_u is the Nusselt number and L_c is the characteristic length of the pipe, in this case, its internal diameter and λ_f (W/mK) is fluid thermal conductivity.

The Nusselt number is a dimensionless convection heat transfer coefficient and it represents (physically) the enhancement of heat transfer through a fluid layer as a result of convection relative to conduction across the same fluid layer. The larger the Nusselt number the more effective the convection is. If this value is known is possible to solve (3.32) for the convective coefficient h_f.

There are several approaches to calculate N_u (Çengel 2007) depending on the type of the fluid flow (i.e. laminar, transitory or turbulent), thus, it is necessary to firstly determine the nature of the flow regime. This is typically found via consideration of the Reynolds number:

$$R_e = \frac{\rho_f v_m L_c}{\mu_f} \tag{3.33}$$

where v_m (m/s), ρ_f (kg/m^3) and μ_f (kg/ms) are the mean velocity, density and dynamic viscosity of the fluid inside the pipes.

It is necessary to describe the criteria used to differentiate where the fluid is laminar, transitional or turbulent. For example, Çengel (2007) suggests that the transitional region is 2300 < R_e < 10000 and that the behaviour for values lower than 2300 is described as laminar while for the values greater than 10000 it is described as turbulent ones. Another suggestion is given by (Roberson and Crowe 1989), they mentioned that although it is possible to maintain laminar regimes at high Reynolds numbers, those regimes would be unstable and subjected to become turbulent when vibrations are present. In general, most engineering applications would involve vibrations (e.g. highways), so it is expected the transitional region to be narrower. For this reason, the limits offered by Roberson and Crowe (1989) have been adopted, they define the transitional region as 2000 < R_e < 4000 for smooth pipes (smooth pipe is

defined by Çengel (2007) as a pipe where the size of the irregularities on the internal surface relative to the diameter of the pipe is less than 0.00001).

If the fluid is subjected to a laminar flow regime, the Nusselt number is constant provided that either constant heat flux (N_u=4.36) or constant temperature (N_u=3.66) can be assumed at the pipe wall (Çengel 2007). If the fluid is undergoing a turbulent regime the Gnielinski modified equation is suitable to calculate the Nusselt number (Çengel 2007):

$$N_u = \frac{\left(\frac{f}{8}\right)(Re - 1000)Pr}{1 + 12.7\left(\frac{f}{8}\right)^{0.5}(Pr^{0.66} - 1)} \qquad \begin{pmatrix} 0.5 \leq Pr \leq 2000 \\ 3\text{X}10^3 < Re < 5\text{X}10^6 \end{pmatrix} \qquad (3.34)$$

where Pr is Prandtl number (a dimensionless number to describes the relative thickness of the velocity and the thermal boundary layers) and f is the friction factor that relates the molecular diffusivity of momentum and the molecular diffusivity of heat and is given by Abu-Hamdeh (2003):

$$Pr = \frac{\mu_f c_{p,f}}{\lambda_f} \qquad (3.35)$$

where $c_{p,f}$ (J/kgK) is the specific heat capacity of the fluid, the friction factor f in equation (3.34) depends on the regime of the fluid and (in case of turbulent regimes) on the level of roughness of the surface in contact with the fluid (Çengel 2007). The expression for f in the laminar regime is given by:

$$f = \frac{64}{Re} \qquad Re < 2000 \qquad (3.36)$$

whilst in turbulent regimes (for smooth surfaces) is given by Çengel (2007):

$$f = (0.79\ln(Re) - 1.64)^{-2} \qquad Re > 4000 \qquad (3.37)$$

The transitional regime is more complicated and there is no clearly defined expression for the friction factor, and the behaviour in this region can be assumed to be linear (Roberson and Crowe 1989), so it is possible to calculate a linear expression based on

the equations for the friction factor on the limits of this region. This expression has the form:

$$f = \frac{\frac{64}{Re} - (0.79\ln(Re) - 1.64)^{-2}}{2000 - 4000}(Re - 2000) + \frac{64}{Re} \tag{3.38}$$

Equations (3.31) to (3.33) covered all possible regimes for the fluids inside the pipe.

Finally, with the formulation presented in this section it is possible to solve equation (3.32) and obtain the convective heat transfer coefficient h_f. Appendix B presents a summary of h_f results for typical temperatures and mean velocities.

3.6.2 Heat exchange efficiency

In geoenvironmental and geotechnical applications, heat exchangers are devices that ease or facilitate the exchange of heat between a fluid and the surrounding soil. The process of heat transfer that is involved in heat exchangers is, convection for the fluid flowing through a pipe or duct and conduction through the wall separating the fluid from the surrounding soil. In the analysis of heat exchangers, it is convenient to work with an overall heat transfer coefficient U_p (given by equation (3.30)) which accounts for the contribution of these effects to the heat transfer. The heat transfer rate between the fluid and the soil at a location in the pipes comprising the heat exchanger would depend on the magnitude of the temperature difference at that location (which varies along the pipe).

To analyse the heat exchangers there are two main approaches which are defined as follows: the logarithmic mean temperature difference (LMTD), which is an equivalent mean temperature difference between the fluid and the surrounding environment for the entire heat exchanger, it is used to dimension the heat exchanger when the desired inlet and outlet temperatures are known. The other method which is effectiveness–NTU method, which allows analysis of heat exchangers when the outlet temperature of the fluid is not known (i.e. the effectiveness-NTU method enables the determination of the heat transfer rate without knowing the outlet temperature of

the fluid and it depends on the geometry of the heat exchanger as well as the flow arrangement). Therefore, different types of heat exchangers have different effectiveness relations. The heat transfer effectiveness is defined as:

$$\varepsilon_p = \frac{Q_{real}}{Q_{max}} \tag{3.39}$$

where Q_{max} (W) is the maximum possible heat transfer rate and Q_{real} (W) is the actual heat transfer rate and it can be determined from a heat balance on the pipe:

$$Q_{real} = c_{p,f}\dot{m}_f\left(T_{f,0} - T_{f,i}\right) \tag{3.40}$$

where is the $\dot{m}_f$ (kg/s) is the mass flow rate of the fluid flowing through the pipe, Q_{real} will be positive if the fluid is being heated. $T_{f,i}$ (K) and $T_{f,o}$ (K) are the temperatures at the inlet and outlet of the pipe respectively.

The maximum possible heat transfer rate, Q_{max} on the other hand, is proportional to the maximum temperature difference in the heat exchanger. According to the context of geoenvironmental thermal applications, the heat exchanger pipes are commonly in contact with soil and if the temperature of soil that is in contact with a pipe can be considered to remain constant along the direction of the flow in a time step in a transient analysis, then Q_{max} can be expressed as:

$$Q_{max} = c_{p,f}\dot{m}_f\left(T_{ss} - T_{f,i}\right) \tag{3.41}$$

As it can be seen in equation (3.40) to determine Q_{max} requires the availability of the inlet pipe temperature and its mass flow rate.

Next, it is necessary to estimate the amount of energy transferred from a differential section of the pipe. This is proportional to the change in temperature in the differential section:

$$dQ_p = c_{p,f}\dot{m}_f dT_f \tag{3.42}$$

An alternative way to estimate this is by using equation (3.29) as:

$$dQ_p = U_p(T_s - T_f)dA_i \tag{3.43}$$

Substituting equation (3.43) into equation (3.42) and integrating dT_f between the pipe inlet and outlet:

$$\ln\frac{(T_{ss} - T_{f,o})}{(T_{ss} - T_{f,i})} = -\frac{U_p\, A_i}{c_{p,f}\dot{m}_f} \tag{3.44}$$

Solving equation (3.40) for $T_{f,o}$ and substituting into equation (3.44) we get:

$$\frac{T_{ss} - T_{f,i} - \frac{Q_{real}}{c_{p,f}\dot{m}_f}}{T_{ss} - T_{f,i}} = exp\left(-\frac{U_p\, A_i}{c_{p,f}\dot{m}_f}\right) \tag{3.45}$$

By using the definition of Q_{max} in equation (3.41) and equation (3.39) it is possible to obtain an expression for the heat transfer effectiveness:

$$\varepsilon_p = 1 - exp\left(-\frac{U_p\, A_i}{c_{p,f}\dot{m}_f}\right) \tag{3.46}$$

Finally, using equation (3.46) it is possible to calculate the pipe heat transfer (per square meter) and the outlet temperature from equation (3.43) and equation (3.41) as follows:

$$q_p = \varepsilon_p c_{p,f}\dot{m}_f(T_{ss} - T_{f,i}) \tag{3.47}$$

$$T_{f,o} = \frac{q_p}{c_{p,f}\dot{m}_f} + T_{f,i} \tag{3.48}$$

3.7 Energy balance at soil surfaces

The flux of energy or mass in a given direction is defined as its amount per unit time passing through a unit area that is normal to that direction. The following sections are concerned with fluxes of various forms of heat energy at or near the surface, the units of energy flux are (J/s m^2 or W/m^2).

The surface considered here is assumed as relatively smooth, horizontal, homogenous, extensive and opaque to radiation and most importantly the energy budget of such surface is considerably simplified in that only the vertical fluxes of energy need to be considered.

The next sections introduce the general relations that describe thermal energy interactions at the surface of the soil and act as boundary conditions for the heat transfer equations presented earlier. Approaches that deal with different surface conditions be considered.

The essential types of energy flux at an ideal surface can be listed as: the net radiation to or from the surface, the sensible (direct) and latent (indirect) heat fluxes to or from the atmosphere.

3.7.1 Short wave radiation

The sun emits radiation in several regions of the electromagnetic spectrum and the term short wave radiation "solar radiation" is commonly referred to as the radiation located in the visible range (0.4 μm-0.7 μm) (Duffie and Beckman 2013). There are two parts of the radiation in this region, the first one is the solar radiation that reaches the Earth and arrives to a surface directly which is also known as "beam radiation". The other part is the one that arrives after being scattered by the atmosphere or by other surfaces and is called "diffuse radiation". The sum of these two types gives the total short radiation or global radiation R (W/m^2) which is typically reported in meteorological measurements (Duffie and Beckman 2013). The amount of this radiation that effectively contributes to the energy balance of a surface is defined by:

$$q_S = R(1 - \alpha_S) \tag{3.49}$$

where α_S is the solar albedo of the soil surface and R (W/m^2) is the global radiation (a measurement commonly reported by meteorological stations National Meteorological Library and Archive (2014)) composed of direct and diffuse solar radiation.

If an object is placed in the proximity of a surface in such a way that they have the possibility to block the solar radiation reaching the surface, they cast a shadow and reduce the received amount of thermal energy. In general, such a shadow will be moving during the day so its size and location will vary through the year due to the seasonal diurnal and seasonal variation of the position of the sun in the sky (Duffie and Beckman 2013). A recent study by Muñoz-Criollo (2014) proposed a simplified method to take into account the shadow cast by near objects. This method is expected to be applicable in situations where the detailed seasonal evolution of the shading is not essential. The method involves weighting of the solar radiation calculated with equation (3.49) by a suitable factor:

$$q_{sh} = q_S D_{sh} \tag{3.50}$$

where q_{sh} (W/m^2) is the solar radiation reaching the surface after being blocked (completely or partially) by the object and D_{sh} is the shading factor that takes values between 1 for a complete transparent object and 0 for a fully opaque object.

3.7.2 Long wave radiation

Also occurring in the electromagnetic spectrum, infrared radiation is generated by the vibration of molecules present in a body (thermal energy), in this way it is a volumetric radiation, but in general the radiation generated by molecules inside the body are quickly absorbed by the body itself, and so, infrared radiation can be described as a surface phenomenon (Duffie and Beckman 2013). It is proportional to the fourth power of the absolute temperature of the surface, the Stefan-Boltzmann constant, σ (W/m^{2}K^4) and equal to 5.67x10^{-8}, and an emissivity factor, ε, which depends on the material and defines the ability of the surface to emit infrared radiation. This process of heat transfer takes place between two or more surfaces each one with its own optical properties. The amount of radiation that reaches each surface depends on the view factor, which is a geometrical factor that defines the amount of radiation that can reach a surface in any given arrangement. Beckman (1971) gives a relation to define the net heat transfer, Q_L (W), for any surface in any N-surface arrangement, but practically speaking, many heat transfer problems involve radiation

between two surfaces, and for this particular case, the heat transfer process can be defined as (Duffie and Beckman 2013):

$$Q_{L1} = -Q_{L2} = \frac{\sigma\left(T_{2,K}^4 - T_{1,K}^4\right)}{\frac{1-\varepsilon_1}{\varepsilon_1 A_1} + \frac{1}{A_1 F_{12}} + \frac{1-\varepsilon_2}{\varepsilon_2 A_2}} \tag{3.51}$$

where Q_{L1} (W) is the heat transferred from surface 1, Q_{L2} (W) is the heat transferred from surface 2, F_{12} is the total view factor between surfaces 1 and 2 and takes into account the radiation exchange between the surfaces directly and by all possible specular reflections, A_1 and A_2 (m^2) are the respective areas of the two surfaces.

A particular case of equation (3.51) of interest in the context of this work is when a relatively small convex object (surface one) is surrounded by a large enclosure which is surface two. In this work, this case will represent the heat transfer process between the soil or the snow (surface 1) and the atmosphere (or sky, surface 2) where under these conditions, the area ratio A_1/A_2 approaches zero, the view factor F_{12} is unity and equation (3.51) can be expressed as:

$$q_L = \varepsilon_s \sigma\left(T_{sky,K}^4 - T_{s,K}^4\right) \tag{3.52}$$

where ε_s is the emissivity of the soil's (or snow) surface, $T_{s,K}$ (K) and $T_{sky,K}$ (K) are the absolute temperatures of the surface and sky respectively.

The atmosphere is commonly treated as a surface that surrounds the soil (as if it were a dome) whereas the atmosphere is actually composed of several layers of gas and each one of them has different temperatures and chemical composition and are in continuous movement. These attributes define the radiative characteristics of the atmosphere, in particular the infrared absorption bands of water vapour result in what is termed as 'atmospheric window' that is between 8 and 14 µm (Duffie and Beckman 2013 ; Tomasi 1978). Inside this window, the atmosphere is transparent to infrared radiation, while outside it the infrared radiation is mostly absorbed. In conjunction, these properties determine the net incoming long wave radiation from the sky.

The atmosphere is usually treated as a black body surface with an equivalent sky temperature $T_{sky,K}$, this model in turn is commonly transformed to a grey surface model (with emissivity different from 1 and possibly wavelength and directionally dependent), where the temperature of the atmosphere is assumed to be equal to a temperature measured at ground level (usually taken as air temperature), and with an equivalent emissivity ε_{sky} that takes into account the previously mentioned atmospheric complexities. Several relations have been proposed to relate $T_{sky,K}$ to measured meteorological variables for example vapour pressure and air temperature (Iziomon *et al.* 2003 ; Berdahl and Martin 1984 ; Swinbank 1963 ; Monteith 1961 ; Brunt 1932 ; Ångström 1915). In general, these relations adopt the following form:

$$T_{sky,K} = \varepsilon_{sky} T_{a,K}^4 \tag{3.53}$$

where $T_{a,K}$ (K) is the absolute air temperature.

Equation (3.52) depends on the fourth power of the absolute temperature of the surface and its computational implementation would be difficult without using specialized solvers to handle non-linear equations. However, to retain the simplicity of linear equations, a linearization procedure is proposed by Duffie and Beckman (2013). In this procedure equation (3.52) can be expressed as:

$$\begin{aligned} q_L &= \sigma\varepsilon_s\left(T_{sky,K}^4 - T_{s,K}^4\right) \\ &= \sigma\varepsilon_s\left(T_{sky,K}^2 + T_{s,K}^2\right)\left(T_{sky,K} + T_{s,K}\right)\left(T_{sky,K} - T_{s,K}\right) \\ &\approx 4\sigma\varepsilon_s\left(\frac{T_{sky,K} + T_{s,K}}{2}\right)^3\left(T_{sky,K} - T_{s,K}\right) \end{aligned} \tag{3.54}$$

where the following equivalence have been performed:

$$\sigma\varepsilon_s\left(T_{sky,K}^2 + T_{s,K}^2\right)\left(T_{sky,K} + T_{s,K}\right) = 4\sigma\varepsilon_s\left(\frac{T_{sky,K} + T_{s,K}}{2}\right)^3 \tag{3.55}$$

Figure (3.4) shows the comparison of the linear coefficient at the left-hand side of the equation (blue line) and the real coefficient at the right-hand side (red line) of

equation (3.55) as a function of the difference in temperature between the sky and the soil surface. It can be seen that both approaches are offer comparable results for differences of up to 50 K under surface temperature of 20 °C.

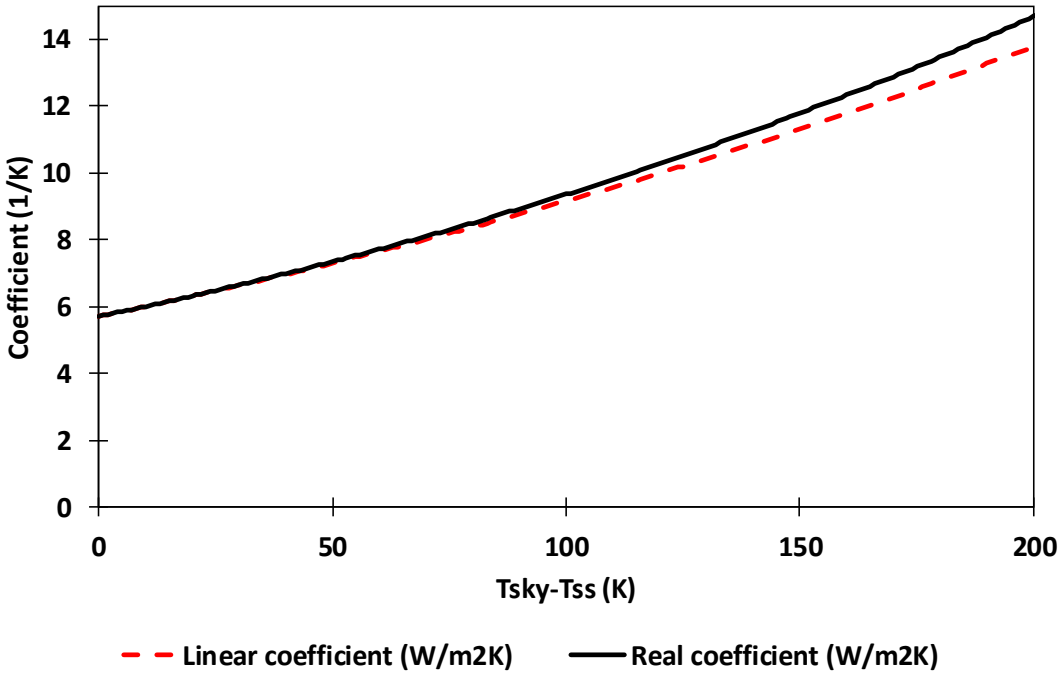

Figure (3.4) Comparison of the linear and real coefficients for the infrared heat transfer process (assuming ε_s=1)

From equation (3.54) it is possible to define an infrared heat transfer coefficient h_L (W/m^{2}K) as:

$$h_L = 4\sigma\varepsilon_s\left(\frac{T_{sky,K} + T_{s,K}}{2}\right)^3 = 4\sigma\varepsilon_s T_*^3 \tag{3.56}$$

where T_* (K) is the average absolute temperature between $T_{sky,K}$ and $T_{s,K}$. It is possible to estimate T_* even without actually knowing both $T_{sky,K}$ and $T_{s,K}$, by using for example the previous time step value in a numerical solution of a transient initial value problem.

3.7.3 Air convection

A convective heat flux from the interaction of a fluid with a solid (in this case atmospheric air with the soil surface) should be considered. The convection mechanism arises in two main ways, the first one is forced convection where the fluid is forced to flow over the surface by external forces; and the other one is natural convection in which the movement of the fluid is driven by thermal gradients. In principle, those two effects should be taken into account when describing the convective heat flux between the atmosphere and the soil whereas the relative importance of each process depends on the fluid conditions (i.e. wind speed) and the surface characteristics (e.g. roughness, temperature).

In general, the convective heat flux between the soil surface and the atmosphere is commonly expressed using Newton's law of cooling (Jansson *et al.* 2006 ; Edinger *et al.* 1974) in which the heat transfer rate per unit area is proportional to the difference between the soil surface temperature and air temperature. Following this approach yields:

$$q_C = h_C(T_s - T_a) \tag{3.57}$$

where q_C (W/m^2) is the convective heat flux, h_C (W/m^{2}K) is the convective heat transfer coefficient that, as discussed above, is dependent on the fluid characteristics and surface conditions, T_s (K) is the surface temperature and T_a (K) is the temperature of the air.

3.7.4 Latent heat flux

The evaporation from a surface into the atmosphere is usually expressed using Dalton's law of partial pressures (Penman 1948). In this approach, the evaporation process is driven by the difference between the water vapour pressure on the (saturated) surface and the atmospheric saturation water vapour pressure. This model was adopted by Penman (1948) who assumed a saturated surface, and later by Philip and de Vries (1957) whom introduced a '*moisture availability factor*' to take into

account the unsaturated condition. This factor is equivalent to a relative humidity for the surface. In general, the heat flow due to evaporation is given by:

$$q_{LE} = h_E(e_a - e_s) \tag{3.58}$$

where q_E (W/m^2) is the heat transfer rate per unit area by evaporation, e_a (kPa) is the atmospheric saturation vapour pressure, h_E (W/m^{2}kPa) is the heat transfer coefficient by evaporation and e_s (kPa) is the water vapour pressure at the saturated surface that is given by Philip and de Vries (1957) as:

$$e_s = exp\left(-\frac{h_s g}{R_w T_{s,K}}\right) e_{s,sat}(T_s) \tag{3.59}$$

where h_s (m) is the pressure head at the surface, g (9.81 m/s^2) is the acceleration due to gravity, R_w (461.5 J/kgK) is the gas constant for water vapour, $e_{s,sat}$ (kPa) is the saturation vapour pressure at the surface. As in the convective heat transfer process, h_{LE} depends on the specific conditions of the fluid and the surface characteristics. The atmospheric saturation water vapour pressure, $e_{s,sat}$ can be calculated according to North and Erukhimova (2009) from the integration of the Clausius-Clapeyron equation (the same equation can be applied for $e_{ss,sat}$):

$$e_{a,sat}(T_a) = e_a(0) exp\left[\frac{L_{vap}}{R_w}\left(\frac{1}{273.15K} - \frac{1}{T_{a,K}}\right)\right] \tag{3.60}$$

where $e_a(0)$ is the water vapour pressure at 0°C (0.611 kPa)(North and Erukhimova 2009), L_{vap} (J/kg) is the latent heat of vaporization of water, R_w (J/kgK) is the gas constant for water vapour.

It can be noted that equation (3.58) is non-linear due to the exponential nature of $e_{a,sat}$ and $e_{s,sat}$ and to linearize $e_{a,sat}$ Deardorff (1978) proposed the following procedure:

$$e_{a,sat}(T_a^{n+1}) = e_{a,sat}(T_a^n) + \left[\frac{\partial e_{a,sat}}{\partial T_a}\right]_{T_a^n} (T_a^{n+1} - T_a^n) \tag{3.61}$$

where the superscripts n and $n+1$ indicate a previous and a new estimate and a similar procedure can be applied to linearize $e_{s,sat}$.

3.7.5 Atmospheric boundary layer coefficient

After showing the main equations for different fluxes, there is a need to identify the coefficients used in them based on different conditions, and it is even more important to discuss the basis of these coefficients firstly in the following section.

3.7.5.1 Monin-Obukhov theory

It has been of considerable interest to meteorologists to find a suitable theoretical or semi empirical framework for a quantitative description of the mean and turbulence structure of the stratified surface layer and the similarity theory of Monin-Obukhov has provided the most suitable and acceptable framework for organizing and presenting meteorological data or even for extrapolating and predicting the data where direct measurement are not available (Arya 2001).

The basic similarity hypothesis first proposed by Monin and Obukhov (1954) is that in a horizontally homogenous surface layer the mean flow and turbulence characteristics depends only on four independent variables that is: height above the surface, the surface drag, the surface kinematic heat flux and the buoyancy variable (which measures the gravitational resistance of an atmosphere to vertical displacements).

The theory implies that the flow is horizontally homogeneous and quasistationary, the turbulent fluxes of momentum and heat are constant (height independent) and the molecular exchange are insignificant in comparison with turbulent exchange.

Because the four independent variables in the Monin and Obukhov theory involves three fundamental dimensions (length, time and temperature), so, according to Buckingham's theorem it can formulate only one independent dimensionless combination out of them which is traditionally chosen in the M-O theory as the buoyancy parameter.

$$\zeta = z/L \tag{3.62}$$

where z (m) are the reference height at which the measurements are taken and L (m) is an important stratification buoyancy length scale parameter known as Obukhov length named after its originator and defined as:

$$L = -\frac{T_v}{g}\frac{u_*^3}{kq_{C0}} \tag{3.63}$$

where k is the von Kármán constant and equals to 0.4.
q_{C0} (mK/s) is the surface kinematic heat flux (which is a converted form of flux due to the difficulty in measuring the dynamic flux form), mathematically speaking it is the sensible heat fluxes between surface and atmosphere divided by density and specific heat capacity of air.

T_v (K) is the mean virtual temperature (it is the temperature that dry air must have to equal the density of moist air at the same pressure) which can defined for saturated (cloudy) air as (Stull 1988):

$$T_v = T(1 + 0.61 * r_{sat} - r_L) \tag{3.64}$$

where r_{sat} is the water vapour saturation mixing ratio of the air parcel and r_L is the liquid water mixing ratio, and for unsaturated air with mixing ratio r:

$$T_v = T(1 + 0.61 * r) \tag{3.65}$$

u_* (m/s) is the friction velocity and is defined according to (Stull 1988) as:

$$u_* = \sqrt{\frac{\tau_{Rynolds}}{\rho_a}} \tag{3.66}$$

where $\tau_{Rynolds}$ is the total vertical flux of horizontal momentum measured near the surface and is defined as the square root for the summation of wind shear near the ground surface.

In magnitude Obukhov length represent the thickness of the layer of dynamic influence near the surface in which shear or friction effects matter the most just like the Richardson number Ri (the generation of turbulence kinetic energy caused by wind shear which is used to show dynamic stability and the formation of turbulence), the negative sign introduced in Obukhov length definition is introduced so that z/L has the same sign as the Richardson number.

It can be noted from equation (3.63) that the values of L could range from $-\infty$ to $+\infty$, the extreme values would be for the limits of heat flux approaching zero from the positive (which is considered unstable) and the negative (stable) side, a more practical range of values for the Obukhov length corresponding to fairly wide ranges of values of u_* and q_C encountered in the atmosphere is shown in Figure (3.5).

In order to overcome the problematic determination of Obukhov length, it would be useful to relate z/L to an easily estimated parameter from known variables. The bulk Richardson number Ri_B provides such a capability and it is defined as follows (Arya 2001):

$$Ri_B = \frac{g}{T_s}\frac{(T_a - T_s)\, z}{u_s^2} \tag{3.67}$$

The bulk Richardson number can also be related to (z/L) by substituting into (3.67) the definition of bulk Richardson number from M-O theory cast in the form of form of $Ri_B = F\left(\frac{z}{z_0}, \frac{z}{L}\right)$ as follows:

$$Ri_B = \frac{z}{L}\left(\frac{\left[\ln\frac{z}{z_0} - \psi_h\left(\frac{z}{L}\right)\right]}{\left[ln\frac{z}{z_0} - \psi_h\left(\frac{z}{L}\right)\right]^2}\right) \tag{3.68}$$

where z_0 (m) is the dynamic roughness of the surface, ψ_m and ψ_h are the stratification corrections factors to the semi logarithmic profiles.

The need of using those stratification factors is due to the fact that many boundary layer measurements are made within the surface layer where wind direction with height is insignificant whereas stratification effects can be deemed important at standard measurement heights of 2 m (for the measurements of temperature and moisture) and 10 m (for winds), so, it is desirable to correct the log-layer profiles for stratification effects.

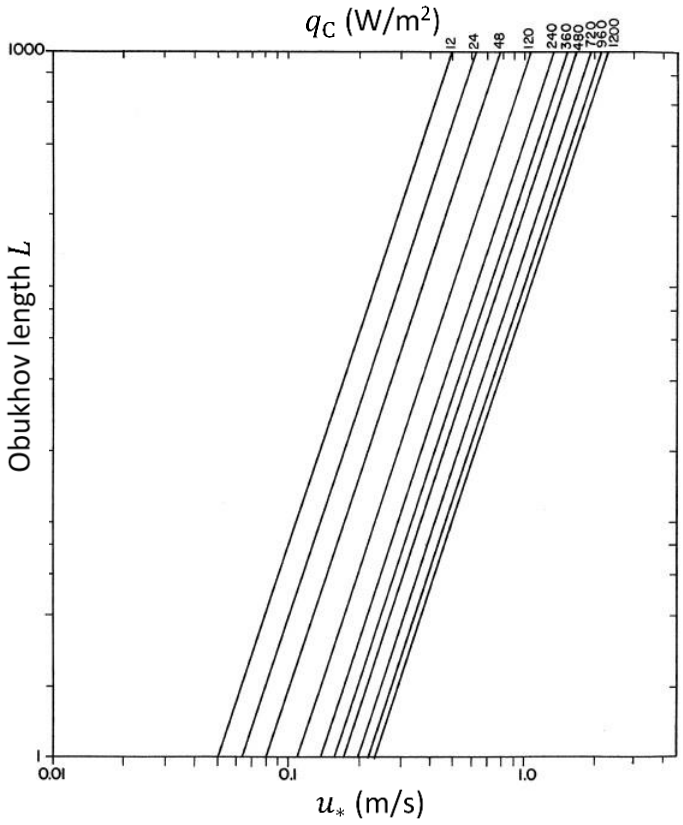

Figure (3.5) Obukhov buoyancy length as a function of the friction velocity and the surface heat flux (Arya 2001)

The inverse of equation (3.68) is often used to determine ζ and, thus, the Obukhov length L for a given value of z/z_0 and Ri_B. A useful graphical representation of equation (3.68) is shown in Figure (3.6) where it shows the variation of surface drag and aerodynamic air resistance of the surface for convective heat flux (discussed later in Section 3.7.5.2) with surface roughness and the bulk Richardson number under stable and unstable condition.

Finally, the surface stress alongside drag coefficient are defined in M-O as:

$$\tau_0 = \rho_a C_D u_s^2 \tag{3.69}$$

$$C_D = \frac{k^2}{\left[ln\frac{z}{z_0} - \psi_m\left(\frac{z}{L}\right)\right]^2} \tag{3.70}$$

where u_s (m/s) is the wind speed.

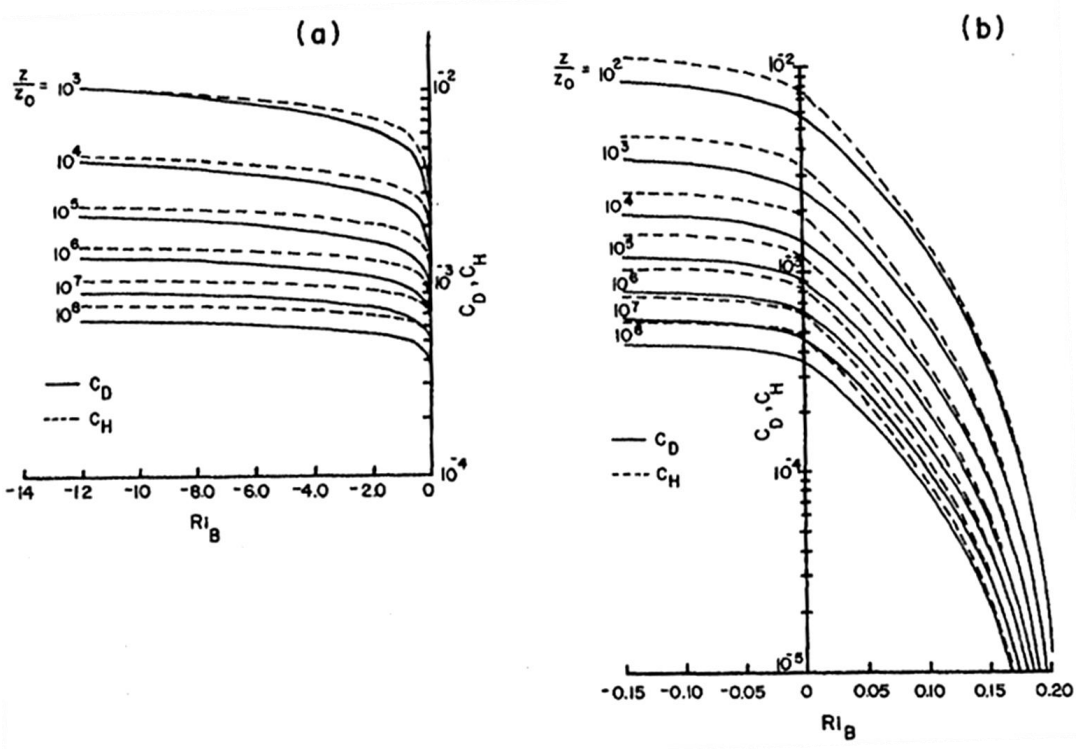

Figure (3.6) variation of surface drag and heat transfer coefficients with surface roughness and Ri_B for (a) unstable condition (b) near neutral and stable condition (Arya 2001)

3.7.5.2 Turbulent coefficient

The turbulent coefficient had been developed from the theory of atmospheric boundary layer and is applicable when the natural convective processes can be neglected due to the characteristics of the flow near the surface of the ground. In this approach, the convective and evaporative heat transfer coefficients are given as:

$$h_C = \frac{\rho_a c_a u^2}{r_{a,C}} \tag{3.71}$$

$$h_{LE} = \frac{\rho_a c_a u^2}{r_{a,LE}\gamma} \tag{3.72}$$

where ρ_a (kg/m^3) and c_a (J/kgK) are the density and specific heat capacity of air, γ (kPa/K) is the psychrometric constant. $r_{a,C}$ and $r_{a,LE}$ (s/m) aerodynamic air resistance of the surface for the convective and latent fluxes at reference height z as (Andreas 2002):

$$r_{a,C} = \frac{k^2}{[\ln(z/z_0) - \psi_m(\zeta)][\ln(z/z_T) - \psi_h(\zeta)]} \tag{3.73}$$

$$r_{a,LE} = \frac{k^2}{[\ln(z/z_0) - \psi_m(\zeta)]\left[\ln(z/z_Q) - \psi_h(\zeta)\right]} \tag{3.74}$$

where z_Q (m) is the roughness length for humidity and z_T (m) is the roughness lengths for heat.

In order to successfully capture the aerodynamic air resistance of the surface knowing the functional forms for ψ_m and ψ_m is important and to be able to find those factors, we would introduce the gradient function $\phi_m(\zeta)$ and $\phi_h(\zeta)$ and use them instead. These gradient functions are related to the surface-layer profiles of potential temperature, wind speed, and specific humidity and could be calculated, the expression that links the ψ and ϕ functions (e.g., Panofsky (1963)):

$$\psi(\zeta) = \int_0^{\zeta} \frac{1 - \phi(\zeta)}{\zeta} d\zeta \tag{3.75}$$

A host of ϕ_m and ϕ_h functions for stable and unstable stratification needs to be suggested. Several authors (Andreas 2002 ; Launiainen 1995 ; Vihma 1995) review available hosts functions and came to recommendations to use Holtslag and De Bruin (1988) expressions for ϕ_m and ϕ_h that are specially adapted for very stable stratification where the usual assumption of $\psi_m = \psi_h$ is applied. However, (Arya

2001) recommend using a generally accepted form of $\phi_h(\zeta)$ and $\phi_m(\zeta)$ which will be adopted in this study and is listed as:

$$\phi_m(\zeta) = \begin{cases} (1-\gamma_1\zeta)^{-1/4} & for\ \zeta < 0 \quad (unstable) \\ 1+\varsigma\zeta & for\ \zeta \geq 0 \quad (stable) \end{cases} \tag{3.76}$$

$$\phi_h(\zeta) = \begin{cases} \varphi(1-\gamma_2\zeta)^{-1/2} & for\ \zeta < 0 \quad (unstable) \\ \varphi+\varsigma\zeta & for\ \zeta \geq 0 \quad (stable) \end{cases} \tag{3.77}$$

where $\varphi = 0.74$, $\varsigma = 4.7$, $\gamma_1 = 15$ and $\gamma_2 = 9$

Finally, we need to be able to calculate z_T and z_Q in order to find latent and sensible heat coefficients, Andreas (1987) built on the surface-renewal models of Brutsaert (1975) and Liu *et al.* (1979) to produce theoretically based model that specifically predicts z_T over snow-covered surfaces. The model's basic result is an equation that predicts the scalar roughness z_s from the roughness Reynolds number as:

$$\ln(z_S/z_0) = b_0 + b_1\ln(Re_*) + b_2(\ln(Re_*))^2 \tag{3.78}$$

where z_S is either z_T or z_Q, the polynomial coefficients b_0, b_1 and b_2 are presents in Table (3.2) and Re_* is the roughness Reynolds number defined as:

$$Re_* = u_* z_0/\upsilon \tag{3.79}$$

where υ is the kinematic viscosity of air.

	$\boldsymbol{Re_*}$ ≤0.135	0.135< $\boldsymbol{Re_*}$ <2.5	2.5≤ $\boldsymbol{Re_*}$ ≤1000
Temperature $\boldsymbol{z_T/z_0}$			
$\boldsymbol{b_0}$	1.250	0.149	0.317
$\boldsymbol{b_1}$	0	-0.550	-0.565
$\boldsymbol{b_2}$	0	0	-0.183
Humidity $\boldsymbol{z_Q/z_0}$			
$\boldsymbol{b_0}$	1.610	0.351	0.396
$\boldsymbol{b_1}$	0	-0.628	-0.512
$\boldsymbol{b_2}$	0	0	-0.180

Table (3.2) Values of the coefficients to use in equation (3.78) to estimates the scalar roughness lengths in the three aerodynamic regimes after Andreas (1987).

3.7.5.3 Non-turbulent coefficient

In this section, the "non-turbulent" nomenclature is used to contrast with the heat transfer coefficients present in the previous sections defined as 'turbulent'. Mainly the difference being the inclusion of a term that takes into account the effects of natural convections neglected by the previous formulation. They are given by:

$$h_C = \rho_a c_a \left(C_{fc} C_{sh} u_s + C_{nc} \Delta\theta_v^{0.33}\right) \tag{3.80}$$

$$h_{LE} = \rho_a L_V \left(C_{fc} C_{sh} u_s + C_{nc} \Delta T_v^{0.33}\right) \tag{3.81}$$

where L_V (J/kg) is the latent heat of evaporation, C_{fc}, C_{nc} (m/sK$^{1/3}$) and C_{sh} are coefficients that weight the contribution of forced convection, natural convection and sheltering respectively and take value between 0 and 1, ΔT_v (K) is the difference in virtual temperature between the air and the surface. The coefficient of sheltering takes into account the presence of nearby objects that could potentially block the flow of wind over the surface of interest.

3.7.5.4 Canopy cover coefficient

The third formulation considered here takes into account the presence of a vegetation layer on top of the soil surface. This formulation requires two sets of heat transfer coefficients for convection and evaporation, one for the soil surface heat balance and a second for the vegetation cover heat balance, and the particular approach adopted here follows that presented by Muñoz-Criollo (2014). The former is identical to the one presented in the previous section and expressed by equation (3.80) and equation (3.81). The latter are given by:

$$h_{C,c} = \frac{\rho_a c_a \nu}{r_{a,c}} \tag{3.82}$$

$$h_{LE,c} = \frac{\rho_a L_v \nu}{r_{a,c} + r_s} \tag{3.83}$$

where $r_{a,c}$ (s/m) is the canopy heat transfer coefficient, and r_s (s/m) is the stomata resistance. ν is the density of the canopy cover and takes values between 0 and 1

(when ν =0 it implies that the soil is completely exposed with no vegetation cover while if ν =1 it means that the soil is completely covered with it). These coefficients are defined as:

$$r_{a,c} = \frac{1}{c_f u_s} \tag{3.84}$$

$$r_s = 200\left(\frac{R_{max}}{R + 0.03R_{max}} + \left(\frac{\theta_{wp}}{\theta_w}\right)^2\right) \tag{3.85}$$

$$c_f = 0.01\left(1 + \frac{0.3}{u_s}\right) \tag{3.86}$$

where c_f is a transfer coefficient, R_{max} is the maximum noon solar radiation that can be achieved, θ_w is the soil moisture content and θ_{wp} is the wilting point moisture content.

3.8 Overall surface balance equation

In order to successfully illustrate all the processes involved in deriving the overall equation a schematic diagram is presented in Figure (3.7).

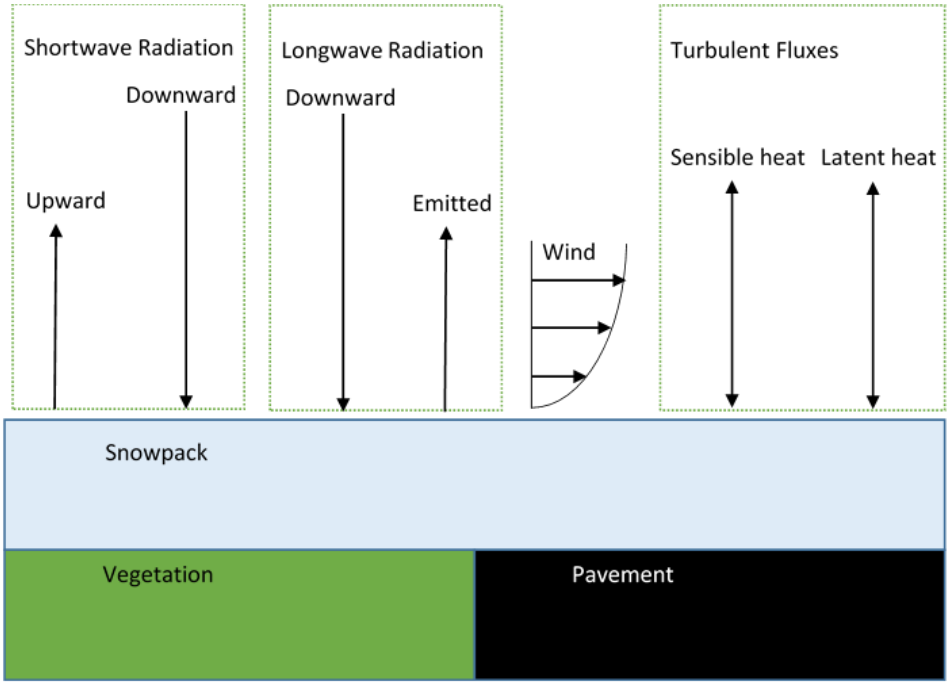

Figure (3.7) Main physical process involved in the model

The bottom surface could be changed from bare soil condition to a canopy one or to the case when everything is fully covered by snow which will represent the three cases discussed below.

3.8.1 Bare soil condition

After discussing the available heat transfer fluxes at the soil surface with its coefficients on the previous sections it is possible now to define a surface energy balance equation. As discussed previously all energy arriving to the surface must leave it in one way or another, since the surface that does not have volume or mass, so energy that is not reflected back into the atmosphere, is transferred into the soil and is further transported following Fourier's law. In general, it is possible to express the energy balance at the soil surface as:

$$\lambda_b \frac{dT_s}{d\hat{n}} = q_S + q_L + q_C + q_{LE} \tag{3.87}$$

where $\hat{n}$ is the unit vector normal to the surface under consideration. The specific formulation of equation (3.87) depends on the conditions of the surface. If the surface under consideration is exposed to the atmosphere, then equation (3.87) can be expressed as:

$$\begin{aligned} \lambda_b \frac{dT_s}{d\hat{n}} &= (1-\alpha_S)R + \sigma\varepsilon_s\left(\varepsilon_{sky}T_{a,K}^4 - T_{s,K}^4\right) \\ &\quad + h_{LE}(e_a - e_s) + h_C(T_a - T_s) \end{aligned} \tag{3.88}$$

3.8.2 Vegetation canopy

If the surface is covered with a layer of vegetation then two heat balances are required, one for the bare soil condition (previous section) surface and one for the vegetation cover. The heat balance for the surface is given by:

$$\lambda_b \frac{dT_s}{d\hat{n}} = (1-\alpha_S)(1-\nu)R + \left[\sigma\varepsilon_s\left((1-\nu)\varepsilon_{sky}T_{a,K}^4 - T_{s,K}^4\right) + \nu\varepsilon_c\sigma T_{c,K}^4\right] + h_{LE}(1-C_e\nu)(e_a - e_s) + h_C(1-C_e\nu)(T_a - T_s) \quad (3.89)$$

where ν, ε_c and $T_{c,K}$ (K) are the density, emissivity and absolute temperature of the canopy cover. C_e is a constant that establishes the level of soil evaporation for fully dense canopies, so setting C_e < 1 gives a non-zero soil evaporation for the full canopy case.

3.8.3 Snow surface condition

Another important case is when the soil or the pavement is covered by a snow layer, the specific formulation values of equation (3.87) would still be the same whereas the coefficients value will change to consider the snow surface, (i.e. surface roughness length and albedo of short wave radiation). For vegetation canopy z_0 = 0.03 and for a paved area or snow covered flat plain it is equal to 0.0002 (Stull 2000). For snow albedo values, it would range from 0.7-0.9 for fresh snow while for melting one it ranges from 0.5-0.6 (Serreze and Barry 2005). Specific details of how a snow layer is considered within a numerical solution are given in the following chapter.

3.9 Boundary conditions at domain base and far field

In many of the analysis of initial and boundary value problems it is necessary to introduce the initial and/or boundary condition. In geoenvironmental problems the bottom boundary condition of the domain would reflect the influence of the strata below the domain on the system, whilst the far field condition represents maximum travelling intensity of the problem (e.g. heat). The common technique is to either fix the temperature on this boundary at an estimated average temperature or assume that there is no heat flux boundary condition (insulated). The implication of the last

assumption would neglect any geothermal heat flux which is typically the case in consideration of the near soil surface (Davies 2013), if this assumption cannot be made, the inclusion of a constant heat flux at the bottom and far field that takes into account this term is not difficult.

When a zero flux is assumed then less information about the soil is required and provided that the thermal energy and mass transfer interactions at the surface are correctly represented, the calculated temperature of the soil at the bottom and sides finally will tend towards a steady state value, which should be representative of the actual temperature. If the temperature at the bottom of the soil is known then this approach can be used to test how well the surface conditions are being represented, under this scenario the heat transfer normal to the domain boundary is set to zero:

$$q_T = 0 \tag{3.90}$$

3.10 Conclusions

This chapter has developed governing equations of heat transfer within soils, heat advection within pipe systems and derived the equations defining the relation between soil and pipes. The Conservation principles for energy and associated flow relationship (Fourier) on which theoretical framework is based were also discussed.

Energy balance equations have been used to define the boundary conditions for selected soil surface cases, bare soil, fully or partially covered by a layer of vegetation and finally dealt with the presence of snow cover.

The implication of ground freezing effects inside the soil and how to capture it was also covered. Boundary conditions applied at the far field of the domain have also been covered. Linearization expressions for the non-linear relations involved in the heat transfer processes at soil surface have been provided as well.

This chapter's objective was covered via providing a detailed theoretical framework that describe the heat transfer within frozen/unfrozen soils using Equations (3.10) and (3.11) respectively. Thermal properties of the soil were calculated using Haigh and

Donazzi methods as shown in Equations (3.13) and (3.14) respectively. The reason for favouring the Donazzi model was due a parametric study over the methods listed in Chapter 2 which shows a very good correlation with the laboratory soil behaviour. On the other hand, Haigh's method was chosen to represent the adaptable insulation layer beads as it was derived from an analytical analysis that assumes a uniformly shaped spherical particle to analyse the soil, which coincides extra well with the problem in hand. Equation (3.12) was used to calculate the volumetric heat capacity and Equation (3.20) for finding the heat advection within the pipes. For defining the heat transfer relation between soil and pipes Equation (3.29) was put in place to capture this behaviour. As there were different boundary condition on the soil surface, different equations were used to represent each one. Equations (3.88) and (3.89) were used to represent the soil surface condition under bare condition and vegetation canopy layer while for snow surface boundary condition Equation (3.88) also was used, however, with a different parameters of roughness length that represents the snow conditions as discussed in Section 3.8.3 (i.e. for vegetation canopy z_0= 0.03 and for a paved area or snow covered flat plain it is equal to 0.0002 while for snow albedo values, it would range from 0.7-0.9 (the average value to be used in the actual implementation).

3.11 References

Abu-Hamdeh, N. H. 2003. Thermal properties of soils as affected by density and water content. *Biosystems Engineering.* 86(1), pp. 97-102. DOI: 10.1016/S1537-5110(03) 00112-0.

Alrtimi, A., Rouainia, M. and Haigh, S. 2016. Thermal conductivity of a sandy soil. *Applied Thermal Engineering.* 106, pp. 551-560. DOI: 10.1016/j.applthermaleng. 2016.06.012.

Andreas, E. L. 1987. A theory for the scalar roughness and the scalar transfer coefficients over snow and sea ice. *Boundary-Layer Meteorology.* 38(1), pp. 159-184. DOI: 10.1007/bf00121562.

Andreas, E. L. 2002. Parameterizing scalar transfer over snow and ice: a review. *Journal of Hydrometeorology.* 3(4), pp. 417-432. DOI: 10.1175/1525-7541(2002)003 <0417:pstosa>2.0.co;2.

Ångström, A. 1915. *A study of the radiation of the atmosphere: based upon observations of the nocturnal radiation during expeditions to algeria and to california*.

Arya, S. P. 2001. *Introduction to micrometeorology*. Academic Press.

Beckman, W. A. 1971. Solution of heat transfer problems on a digital computer. *Solar Energy.* 13(3), pp. 293-300. DOI: 10.1016/0038-092X(71)90012-0.

Berdahl, P. and Martin, M. 1984. Emissivity of clear skies. *Solar Energy.* 32(5), pp. 663-664. DOI: 10.1016/0038-092X(84)90144-0.

Brunt, D. 1932. Notes on radiation in the atmosphere. I. *Quarterly Journal of the Royal Meteorological Society.* 58(247), pp. 389-420. DOI: 10.1002/qj.49705824704.

Brutsaert, W. 1975. A theory for local evaporation (or heat transfer) from rough and smooth surfaces at ground level. *Water Resources Research.* 11(4), pp. 543-550. DOI: 10.1029/WR011i004p00543.

Carslaw, H. S. and Jaeger, J. C. 1986. *Conduction of heat in solids*. Clarendon Press.

Çengel, Y. A. 2007. *Heat and mass transfer: a practical approach*. Mcgraw-Hill.

Chen, S. X. 2008. Thermal conductivity of sands. *Heat and Mass Transfer.* 44(10), p. 1241. DOI: 10.1007/s00231-007-0357-1.

Davies, J. H. 2013. Global map of solid earth surface heat flow. *Geochemistry, Geophysics, Geosystems.* 14(10), pp. 4608-4622. DOI: 10.1002/ggge.20271.

de Vries, D. A. 1963. *Thermal properties of soils In W.R. van Wijk (ed.) physics of plant environment*. Amsterdam: North-Holland Publishing Company.

Deardorff, J. W. 1978. Efficient prediction of ground surface temperature and moisture, with inclusion of a layer of vegetation. *Journal of Geophysical Research: Oceans.* 83(C4), pp. 1889-1903. DOI: 10.1029/JC083iC04p01889.

Domine, F., Albert, M., Huthwelker, T., Jacobi, H. W., Kokhanovsky, A. A., Lehning, M., Picard, G. and Simpson, W. R. 2008. Snow physics as relevant to snow photochemistry. *Atmospheric Chemistry and Physics.* 8(2), pp. 171-208. DOI: 10.5194/acp-8-171-2008.

Donazzi, F. ed. 1977. *Soil thermal and hydrological characteristics in designing underground cables*. Proceedings of the Institution of Electrical Engineers.

Duffie, J. A. and Beckman, W. A. 2013. *Solar engineering of thermal processes*. Wiley.

Edinger, J. E., Brady, D. K. and Electric Power Research Institute. 1974. *Heat exchange and transport in the environment*. John Hopkins University.

Fredlund, D. G. and Rahardjo, H. 1993. *Soil mechanics for unsaturated soils*. Wiley.

Haigh, S. K. 2012. Thermal conductivity of sands. *Géotechnique.* 62(7), pp. 617-625. DOI: 10.1680/geot.11.P.043.

Holman, J. P. 2010. *Heat transfer*. McGraw Hill Higher Education.

Holtslag, A. A. M. and De Bruin, H. A. R. 1988. Applied modeling of the nighttime surface energy balance over land. *Journal of Applied Meteorology.* 27(6), pp. 689-704. DOI: 10.1175/1520-0450(1988)027<0689:amotns>2.0.co;2.

Iziomon, M. G., Mayer, H. and Matzarakis, A. 2003. Downward atmospheric longwave irradiance under clear and cloudy skies: Measurement and parameterization. *Journal of Atmospheric and Solar-Terrestrial Physics.* 65(10), pp. 1107-1116. DOI: 10.1016/ j.jastp.2003.07.007.

Jansson, C., Almkvist, E. and Jansson, P. E. 2006. Heat balance of an asphalt surface: observations and physically-based simulations. *Meteorological Applications.* 13(2), pp. 203-212. DOI: 10.1017/S1350482706002179.

Launiainen, J. 1995. Derivation of the relationship between the Obukhov stability parameter and the bulk Richardson number for flux-profile studies. *Boundary-Layer Meteorology.* 76(1), pp. 165-179. DOI: 10.1007/bf00710895.

Liu, W. T., Katsaros, K. B. and Businger, J. A. 1979. Bulk parameterization of air-sea exchanges of heat and water vapor including the molecular constraints at the interface. *Journal of Atmospheric Sciences.* 36(9), pp. 1722-1735. DOI.

Monin, A. S. and Obukhov, A. 1954. Basic laws of turbulent mixing in the surface layer of the atmosphere. *Contrib. Geophys. Inst. Acad. Sci. USSR.* 151(163), pp. 163-187. DOI: citeulike-article-id:13350567.

Monteith, J. L. 1961. An empirical method for estimating long-wave radiation exchanges in the British Isles. *Quarterly Journal of the Royal Meteorological Society.* 87(372), pp. 171-179. DOI: 10.1002/qj.49708737206.

Muñoz-Criollo, J. J. 2014. *An investigation of inter-seasonal near-surface ground heat transfer and storage.* Ph.D. thesis, Cardiff University, http://orca.cf.ac.uk/73226/.

National Meteorological Library and Archive. 2014. *Observations: weather observations over land. fact sheet 17 version 01.*

North, G. R. and Erukhimova, T. L. 2009. *Atmospheric thermodynamics: elementary physics and chemistry*. Cambridge University Press.

Panofsky, H. A. 1963. Determination of stress from wind and temperature measurements. *Quarterly Journal of the Royal Meteorological Society.* 89(379), pp. 85-94. DOI: 10.1002/qj.49708937906.

Penman, H. L. 1948. Natural evaporation from open water, bare soil and grass. *Proceedings of the Royal Society of London. Series A. Mathematical and Physical Sciences.* 193(1032), pp. 120-145. DOI: 10.1098/rspa.1948.0037.

Pérez Guerrero, J. S., Pimentel, L. C. G., Skaggs, T. H. and van Genuchten, M. T. 2009. Analytical solution of the advection-diffusion transport equation using a change-of-

variable and integral transform technique. *International Journal of Heat and Mass Transfer.* 52(13-14), pp. 3297-3304. DOI: 10.1016/j.ijheatmasstransfer.2009.02.002.

Philip, J. R. and de Vries, D. A. 1957. Moisture movement in porous materials under temperature gradients. *Eos, Transactions American Geophysical Union.* 38(2), pp. 222-232. DOI: 10.1029/TR038i002p00222.

Rees, S. W., Adjali, M. H., Zhou, Z., Davies, M. and Thomas, H. R. 2000. Ground heat transfer effects on the thermal performance of earth-contact structures. *Renewable & sustainable energy reviews.* 4(3), pp. 213-265. DOI: 10.1016/S1364-0321(99)00018-0.

Rees, S. W., Cleall, P. J., Li, Y.-C. and Shao, K. 2013. Freezing soil effects on earth-contact heat transfer. *Building Services Engineering Research and Technology.* 34(3), pp. 259-274. DOI: 10.1177/0143624412441616.

Rees, S. W., Zhou, Z. and Thomas, H. R. 2007. Ground heat transfer: a numerical simulation of a full-scale experiment. *Building and Environment.* 42(3), pp. 1478-1488. DOI: 10.1016/j.buildenv.2005.12.022.

Roberson, J. A. and Crowe, C. T. 1989. *Engineering fluid mechanics*. 4Rev e. edition ed. Houghton Mifflin.

Serreze, M. C. and Barry, R. G. 2005. *The arctic climate system*. Cambridge University Press.

Stull, R. B. 1988. *An Introduction to boundary layer meteorology*. Springer Netherlands.

Stull, R. B. 2000. *Meteorology for scientists and engineers*. Brooks/Cole.

Sturm, M., Holmgren, J., König, M. and Morris, K. 1997. The thermal conductivity of seasonal snow. 43(143), pp. 26-41. DOI: 10.1017/S0022143000002781.

Swinbank, W. C. 1963. Long-wave radiation from clear skies. *Quarterly Journal of the Royal Meteorological Society.* 89(381), pp. 339-348. DOI: 10.1002/qj.49708938105.

Thomas, H. R., Cleall, P., Li, Y. C., Harris, C. and Kern-Luetschg, M. 2009. Modelling of cryogenic processes in permafrost and seasonally frozen soils. *Géotechnique.* 59(3), pp. 173-184. DOI: 10.1680/geot.2009.59.3.173.

Tomasi, C. 1978. On the water vapour absorption in the 8-13 μm spectral region for different atmospheric conditions. *Pure and Applied Geophysics PAGEOPH.* 116(6), pp. 1063-1076. DOI: 10.1007/BF00874671.

Vihma, T. 1995. Subgrid parameterization of surface heat and momentum fluxes over polar oceans. *Journal of Geophysical Research: Oceans.* 100(C11), pp. 22625-22646. DOI: 10.1029/95JC02498.

Zhang, T. 2005. Influence of the seasonal snow cover on the ground thermal regime: an overview. *Reviews of Geophysics.* 43(4). DOI: 10.1029/2004RG000157.

Chapter 4: Numerical Solution

4.1 Introduction

This chapter presents the numerical solution of the partial differential equations that describe heat transfer within soils and the advection of heat by a fluid (as developed in the previous chapter) using different discretization techniques. The implementation of for the temporal discretization achieved using the finite difference method while the spatial ones was done using the finite element method. The general numerical implementation of different kinds of boundary conditions is also presented.

Since the method of discretization adopted here allows changes in mesh refinement between time steps in transient simulations, an algorithm for the selection of elements based on the gradient of the independent variable (temperature) is also presented.

The numerical approaches adopted in this chapter are based on the following references: (Bangerth *et al.* 2013 ; Reddy 2005a ; Baker and Pepper 1991 ; Thomas and Rees 1990 ; Patankar 1980) where the first reference details the Deal.ii library which is used in the implementation of the numerical solution.

4.2 Heat transfer equations

The partial differential equations for heat transfer and for heat advection were presented earlier in Chapter 3 and this section briefly summarizes them.

4.2.1 Heat conduction

Heat conduction in soil was presented in Section 3.5 and expressed as:

$$H_c \frac{\partial T}{\partial t} = \nabla(\lambda_b \nabla T) \tag{4.1}$$

where H_c (J/m^{3}K) is the volumetric heat capacity and λ_b (W/mK) is the thermal conductivity.

4.2.2 Heat advection

The advection of heat by a moving fluid was presented in Section 3.6 and stated as:

$$\rho_f c_{p,f}\left[\frac{\partial T_f}{\partial t} + u_f \frac{\partial T_f}{\partial x}\right] = Q_f \tag{4.2}$$

where u_f (m/s) is the velocity vector field that describes the fluid's motion, T_f(K), ρ_f (kg/m^3) and $c_{p,f}$ (J/kgK) are its temperature, density and specific heat capacity. Q_f (W/m^3) takes into account heat generation inside the pipes.

4.3 Discretization of partial differential equations

The time dependent partial differential equations presented in the previous section are discretized following Rothe's method (Mullineux *et al.* 1969). This method involves discretizing first with respect to time, leading to a stationary PDE at each time step which is then solved using standard finite element techniques. The adopted time discretization approach enables, via a control-parameter, the casting of the solution of the stationary PDE using the implicit, explicit or the Crank-Nicholson schemes depending on the particular equation of interest.

4.3.1 Time discretization

In this section, the temporal finite difference discretization procedure is applied in detail to the heat conduction equation. Then, since the same procedure can be applied in a similar manner to the heat advection equations, only the final discretized form is presented. The time discretization for the heat transport equation of equation (4.1) is given by:

$$\frac{H_c^{n+1/2}(T^{n+1}-T^n)}{\Delta t} = \eta\nabla\left(\lambda_b^{n+1/2}\nabla T^{n+1}\right) + (1-\eta)\nabla(\lambda_b^{n+1/2}\nabla T^n) \tag{4.3}$$

$$H_c^{n+1/2}T^{n+1} - \eta\Delta t\nabla\left(\lambda_b^{n+\frac{1}{2}}\nabla T^{n+1}\right) = H_c^{n+1/2}T^n + (1-\eta)\Delta t\nabla(\lambda_b^{n+1/2}\nabla T^n) \tag{4.4}$$

where η is a control-parameter that dictate the form of finite-difference algorithm to be employed, its values are set between 0 and 1.

If η=0 the temporal discretization obtained is known as the forward or explicit Euler scheme while if η=1 then the backward or implicit Euler method is obtained. A third case would be to set η=0.5 which is known as the Crank-Nicholson method (Crank and Nicolson 1996).

When solving (4.4) initially a first solution for time step $n+1$ is calculated using the solution and physical properties estimated at time step n. Once a first prediction for T^{n+1} is obtained a correction step is formed in which a second approximation of T^{n+1} is calculated using physical properties estimated at time $T^{n+0.5}$. This method is known as a predictor-corrector scheme and is performed for every time step $n+1$.

As mentioned before and by following the same procedure, the time discretization for the heat advection is given by:

$$C_f^{n+1/2}T_f^{n+1} + C_f^{n+1/2}\eta\Delta t u_f\frac{\partial T_f^{n+1}}{\partial x} = C_f^{n+1/2}T_f^n - C_f^{n+1/2}(1-\eta)\Delta t u_f\frac{\partial T_f^n}{\partial x} + \eta\Delta t Q_f^{n+1} + (1-\eta)\Delta t Q_f^n \tag{4.5}$$

4.3.2 Spatial discretization

This section develops the spatial discretization of equation (4.1) and equation (4.2) via the finite element method, specifically the Galerkin weighted residual

method (Reddy 2005b). As before, the method is performed in detail to obtain the spatial discretization of the heat equation while the corresponding spatial discretization for advection equations is summarized.

Using the Galerkin method and multiplying the heat equation by a test function ϕ and integrating over the domain of interest denoted as Ω, it is possible to write the heat equation in the following form:

$$\int_{\Omega} \phi H_c^{n+1/2} T^{n+1}\, d\Omega - \int_{\Omega} \phi \eta \Delta t \nabla\left(\lambda_b^{n+1/2} \nabla T^{n+1}\right) d\Omega = \int_{\Omega} \phi H_c^{n+1/2} T^{n}\, d\Omega + \int_{\Omega} \phi (1-\eta) \Delta t \nabla (\lambda_b^{n+1/2} \nabla T^{n}) d\Omega \tag{4.6}$$

Using the divergence theorem, it is possible to reduce the order of the second spatial derivatives, to yield:

$$\begin{aligned} &\int_{\Omega} H_c^{n+1/2} T^{n+1} \phi d\Omega - \eta \Delta t \int_{\Omega} \lambda_b^{n+1/2} \nabla \phi \nabla T^{n+1} d\Omega \\ &= \int_{\Omega} H_c^{n+1/2} T^{n} \phi d\Omega - (1-\eta) \Delta t \int_{\Omega} \lambda_b^{n+1/2} \nabla \phi \nabla T^{n} d\Omega \\ &+ \eta \Delta t \int_{\Gamma} \phi \left(\lambda_b \frac{\partial T^{n+1}}{\partial \hat{n}}\right) d\Gamma + (1-\eta) \Delta t \int_{\Gamma} \phi \left(\lambda_b \frac{\partial T^{n}}{\partial \hat{n}}\right) d\Gamma \end{aligned} \tag{4.7}$$

where Γ denotes the boundary of the domain and $\hat{n}$ is a unit vector normal to it.

The next step is to find a function T for which (4.6) is true for all test functions ϕ. This cannot be achieved explicitly as a general case, but instead an approximation for T is sought:

$$T_u = \sum_j U_j \phi_j \tag{4.8}$$

where U_j are the unknown expansion coefficients that need to be determined and $\phi_j(x)$ are the finite element shape functions that will be used. The typical finite elements used to describe these shape functions are Lagrange elements that define shape functions by interpolation on support points (the simplest use polynomial degree 1 and are denoted as linear). Note additionally that the shape functions are not necessary the same at different time steps. This allows the adaptation of the mesh depending on the behaviour of the main variables. For this reason, in principle, it is necessary to mark the use to different shape functions for different time steps:

$$T_u^{n+1} = \sum_j {U_j}^{n+1} {\phi_j}^{n+1}(x) \tag{4.9}$$

$$T_u^n = \sum_j {U_j}^n {\phi_j}^n(x) \tag{4.10}$$

Using (4.9) and (4.10), and a set of shape functions ϕ_i, the weak form of the discrete problem defined as:

$$\begin{aligned} &\int_\Omega H_c^{n+1/2}\phi_i^{n+1}\phi_j^{n+1}d\Omega U_j^{n+1} + \eta\Delta t\int_\Omega \lambda_b^{n+1/2}\nabla\phi_i^{n+1}\nabla\phi_j^{n+1}d\Omega U_j^{n+1} \\ &= \int_\Omega H_c^{n+1/2}\phi_i^{n+1}\phi_i^n d\Omega U_j^n - (1-\eta)\Delta t\int_\Omega \lambda_b^{n+1/2}\nabla\phi_i^{n+1}\nabla\phi_j^n d\Omega U_j^n \\ &+ \eta\Delta t\int_\Gamma \phi_i^{n+1}(\lambda_b\frac{\partial T_s^{n+1}}{\partial\hat{n}})d\Gamma + (1-\eta)\Delta t\int_\Gamma \phi_i^{n+1}(\lambda_b\frac{\partial T_s^n}{\partial\hat{n}})d\Gamma \end{aligned} \tag{4.11}$$

Which can be expressed in matrix form as:

$$\begin{aligned} (\boldsymbol{M}_V^{n+1} + \eta\Delta t\boldsymbol{A}_V^{n+1})U^{n+1} &= (\boldsymbol{M}_V^{n+1,n} - (1-\eta)\Delta t\boldsymbol{A}_V^{n+1,n})U^n \\ &+ \eta\Delta t\boldsymbol{F}_V^{n+1} + (1-\eta)\Delta t\boldsymbol{F}_V^n \end{aligned} \tag{4.12}$$

where:

$$\boldsymbol{M}_V^{n+1} = \int_{\Omega} H_c^{n+1/2} \phi_i^{n+1} \phi_j^{n+1} d\Omega$$

$$\boldsymbol{A}_V^{n+1} = \int_{\Omega} \lambda_b^{n+1/2} \nabla \phi_i^{n+1} \nabla \phi_j^{n+1} d\Omega$$

$$\boldsymbol{M}_V^{n+1,n} = \int_{\Omega} H_c^{n+1/2} \phi_i^{n+1} \phi_j^{n} d\Omega$$

$$\boldsymbol{A}_V^{n+1,n} = \int_{\Omega} \lambda_b^{n+1/2} \nabla \phi_i^{n+1} \nabla \phi_j^{n} d\Omega \tag{4.13}$$

$$\boldsymbol{F}_V^{n+1} = \int_{\Gamma} \phi_i^{n+1} (\lambda_b \frac{\partial T_s^{n+1}}{\partial \hat{n}}) d\Gamma$$

$$\boldsymbol{F}_V^{n} = \int_{\Gamma} \phi_i^{n+1} (\lambda_b \frac{\partial T_s^{n}}{\partial \hat{n}}) d\Gamma$$

In the same way, the finite element approximation for the heat advection equation is given by:

$$\begin{aligned}
&\int_{\Omega} \phi_i^{n+1} C_f^{n+1/2} \phi_j^{n+1} d\Omega W_j^{n+1} + \eta u_f \Delta t \int_{\Omega} \phi_i^{n+1} C_f^{n+1/2} \frac{\partial \phi_j^{n+1}}{\partial x} d\Omega W_j^{n+1} \\
&+ \eta u_f \Delta t \int_{\Gamma} \phi_i^{n+1} \phi_j^{n+1} d\Gamma \, W_j^{n+1} = \int_{\Omega} \phi_i^{n+1} C_f^{n+1/2} \phi_i^{n} d\Omega W_j^{n} \\
&- (1-\eta) \Delta t u_f \int_{\Omega} \phi_i^{n+1} C_f^{n+1/2} \frac{\partial \phi_j^{n}}{\partial x} d\Omega W_j^{n} \\
&- (1-\eta) u_f \Delta t \int_{\Gamma} \phi_i^{n+1} \phi_j^{n} d\Gamma W_j^{n} + \eta \Delta t \int_{\Omega} \phi_i^{n+1} Q_f^{n+1} d\Omega \\
&+ \eta \Delta t \int_{\Gamma} \phi_i^{n+1} T_{in} d\Gamma + (1-\eta) \Delta t \int_{\Omega} \phi_i^{n+1} Q_f^{n} d\Omega \\
&+ (1-\eta) \Delta t \int_{\Gamma} \phi_i^{n+1} T_{in} d\Gamma
\end{aligned} \tag{4.14}$$

where W_j are coefficients for the numerical approximation of T_f. Since the boundary condition does not appear naturally in the weak formulation of the heat advection equation, in order to obtain equation (4.14), the following boundary condition (corresponding to an inflow boundary) has been enforced and added to equation (4.5).

$$T_f = T_{in} \text{ (at inflow boundary)} \tag{4.15}$$

In matrix form, equation (4.14) can be expressed as:

$$\begin{aligned}(\boldsymbol{M}_W^{n+1} + \eta\Delta t\boldsymbol{A}_W^{n+1})W^{n+1} = (\boldsymbol{M}_W^{n+1,n} - (1-\eta)\Delta t\boldsymbol{A}_W^{n+1,n})W^n \\ + \eta\Delta t\boldsymbol{F}_W^{n+1} + (1-\eta)\Delta t\boldsymbol{F}_W^n\end{aligned} \tag{4.16}$$

where:

$$\begin{aligned}\boldsymbol{M}_W^{n+1} &= \int_\Omega \phi_i^{n+1} C_f^{n+1/2} \phi_j^{n+1} d\Omega \\ \boldsymbol{A}_W^{n+1} &= u_f \int_\Omega \phi_i^{n+1} C_f^{n+1/2} \frac{\partial \phi_j^{n+1}}{\partial x} d\Omega + u_f \int_\Gamma \phi_i^{n+1} \phi_j^{n+1} d\Gamma \\ \boldsymbol{M}_W^{n+1,n} &= \int_\Omega \phi_i^{n+1} C_f^{n+1/2} \phi_j^{n} d\Omega \\ \boldsymbol{A}_W^{n+1,n} &= u_f \int_\Omega \phi_i^{n+1} C_f^{n+1/2} \frac{\partial \phi_j^{n}}{\partial x} d\Omega + u_f \int_\Gamma \phi_i^{n+1} \phi_j^{n} d\Gamma \\ \boldsymbol{F}_W^{n+1} &= u_f \int_\Omega \phi_i^{n+1} Q_f^{n+1} d\Omega + \int_\Gamma \phi_i^{n+1} T_{in}^{n+1} d\Gamma \\ \boldsymbol{F}_W^{n} &= \int_\Omega \phi_i^{n+1} Q_f^{n} d\Omega + \int_\Gamma \phi_i^{n} T_{in}^{n} d\Gamma\end{aligned} \tag{4.17}$$

4.3.3 Adaptive refinement criteria

In the previous sections, the possibility of changing the mesh refinement from one-time step to the next is taken into account. This action is desirable when the problem involves time-varying localized gradients of the independent variables (e.g. moving fronts, localized and periodic sink/sources and/or cracks/fractures). In order to select appropriate regions where the re-meshing should be performed, a suitable algorithm for the selection of elements needs to be defined. It is known as adaptive refinement because of the possibilities of adapting the mesh to the changing conditions of the independent variables.

The adaptive refinement approach used in this work and implemented in the finite element library of Deal.ii follows the method proposed by Kelly *et al.* (1983). In this method, the error indicator is calculated and prioretizingly sorted (element wise). The higher values of error indicator flagged for further refinement or the lowest values for coarsening. The error indicator itself is calculated by integration of the change of the gradient of the solution along the faces of each element. Mathematically, for element *K*, it is given by Ainsworth and Oden (2000):

$$\vartheta_K^2 = \frac{\varsigma}{24} \int_{\partial K} \left(\frac{\partial u_h}{\partial \hat{n}} \right)^2 d\Omega \tag{4.18}$$

where u_h is the discrete approximation of an independent variable u of interest, ς is the size of the mesh element, Ω is domain and $\hat{n}$ is the respective normal faces of the element K. The term in brackets denotes the jump of the argument at the face.

4.4 Boundary conditions

Typically, three kinds of boundary conditions are encountered in the solution of analytical and numerical problems:

- The independent variable is defined at the boundary which is also known as: *Fixed, Strong, First kind* or *Dirichlet* boundary condition.

- The normal derivative of the independent variable is defined at the boundary and it is also known as: *Free, Natural*, *Second kind* or *Neumann* boundary condition.

- A linear combination of the values of the independent variable and its normal derivative at the boundary is defined which is also known as: *Third kind* or *Robin* boundary condition.

One or more of these boundary condition could be applied to the physical problem under consideration. Their implementation is performed in the boundary terms that arises after the weak form of the discretized equations is obtained. In order to illustrate this, different boundary conditions can be assumed and applied in $\boldsymbol{F_v}$ (evaluated at time step n). This term includes the boundary condition of the heat conduction problem (4.7):

$$\boldsymbol{F}_V^n = \int_\Gamma \phi_i^n (\lambda_b \frac{\partial T_s^n}{\partial \hat{n}}) d\Gamma \tag{4.19}$$

The following sections deal with the specific implementation of each type of boundary condition.

4.4.1 Fixed boundary condition

The implementation of boundary conditions in the finite element method is closely related to the calculus of variations and involves a problem of energy minimization. An energy functional that depends on the independent variable is defined and it needs to be proved that it provides the minimum possible energy for the system for any possible perturbation in the domain including the boundaries. When the value at the boundary is specified, the only possible value for the test function is zero in order to minimize the functional. In this case (4.19) vanishes. This is:

$$\phi_i^n = 0 \tag{4.20}$$

Thus, $\boldsymbol{F_v}$ vanishes as well. Subsequently, after the system has been assembled, the values of the degrees of freedom corresponding to the boundary need to be enforced to the desired fixed value.

4.4.2 Free boundary condition

In the case of the *free* or *Natural* boundary conditions, the flux normal to the boundary is specified (e.g. using Fourier's law):

$$q_h = -\lambda_b \frac{\partial T}{\partial \hat{n}} \tag{4.21}$$

The term represented by (4.21) appears naturally in (4.19) (hence *Natural* boundary condition) and can be replaced directly:

$$\boldsymbol{F}_V^n = -\int_{\Gamma} \phi_i^n q_h d\Gamma \tag{4.22}$$

Equation (4.22) can be added to the right-hand side of (4.11) and the problem solved without further modification.

4.4.3 Robin boundary condition

Robin boundary conditions arise, for example, when the heat flux is dependent on the interaction of the boundary with its environment:

$$\lambda_b \frac{\partial \mathrm{T}}{\partial \hat{n}} = \omega(T_\infty - T) \tag{4.23}$$

where ω is a suitable heat transfer coefficient and T_∞ is the temperature of the surrounding environment. In this case (4.19) is transformed into:

$$\begin{aligned} \boldsymbol{F}_V^n &= -\int_{\Gamma} \phi_i^n \omega (T^n - T_\infty^n) d\Gamma \\ &= -\omega \int_{\Gamma} \phi_i^n T^n d\Gamma + \omega \int_{\Gamma} \phi_i^n T_\infty^n d\Gamma \end{aligned} \tag{4.24}$$

The implementation of this type of boundary condition leads to the inclusion of an extra term that depends on the independent variable (T in this case) that needs to be included in the in the corresponding matrix $\boldsymbol{A}_V$ in (4.13).

4.4.4 Mixed boundary condition

The solution of physical problems by numerical methods usually requires the imposition of more than one kind of boundary condition in the domain. This scenario is known as mixed boundary conditions. If the problem of interest can be represented, for example, with two different boundaries Γ_1 and Γ_2, where a fixed and free boundary conditions are imposed using (4.20) and (4.22) respectively, (4.19) could be rewritten as:

$$\begin{aligned} \boldsymbol{F}_V^n &= \int_{\Gamma_1} \phi_i^n \left(\lambda_b \frac{\partial T^n}{\partial \hat{n}} \right) d\Gamma_1 + \int_{\Gamma 2} \phi_i^n \left(\lambda_b \frac{\partial T^n}{\partial \hat{n}} \right) d\Gamma_2 \\ &= \int_{\Gamma_1} (0) \left(\lambda_b \frac{\partial T^n}{\partial \hat{n}} \right) d\Gamma_1 - \int_{\Gamma 2} \phi_i^n q_T d\Gamma_2 \\ &= -\int_{\Gamma 2} \phi_i^n q_T d\Gamma_2 \end{aligned} \tag{4.25}$$

This method can be applied to include any number of relevant boundary conditions in the domain.

4.4.5 Snow boundary conditions

In the context of this thesis, consideration of a thin layer of snow present on the domain surface for a known period of time is made. The selected periods can be

based on observed data. Two ways are available to introduce the snow surface, based either on a specific timing of snow occurrence or by correlating the system to the air temperatures. The former was chosen as the snow occurrence timing is typically known in modelling of reported / historical system performance or can be arbitrarily assigned in consideration of future performance. The thermal properties of this layer alongside its thickness are assumed to be fixed for the whole interval of occurrence. The analysis of the whole system can be carried based on the theoretical framework presented earlier in Chapter 3 until the time of snow occurrence, when a snow layer is introduced into the system at this point the snow surface temperature would be estimated and fed into the system and by the end of snow occurrence the results would be used by the system as an initial condition for rest of the analysis. The snow surface temperature estimation would be done by assuming a second kind boundary condition where the boundary flux above would be used to estimate the heat transfer between the air and the snow cover. The temperature of the snow would be calculated based on the following equation (Herb *et al.* 2008):

$$T_{snow} = \frac{q_{in} + \left[\left(\frac{\lambda}{\Delta z}\right)_{snow} * T_{s,avrg}\right]}{h_{out} + \left(\frac{\lambda}{\Delta z}\right)_{snow}} \tag{4.26}$$

where T_{snow} (K) is the snow surface temperature, $T_{s,avrg}$ (K) is the surface average temperature, q_{in} (W/m^2) is the inbound heat flux, h_{out} is the outbound convective heat coefficient. It is important to note that as melting is not considered in this study whenever the predicted snow temperature goes above zero it is held at a value of zero to reflect the impact of phase change which would keep the snow temperature at close to zero until all the snow has melted.

4.5 Conclusions

In this chapter, a time and space discretization approach suited for the basic transport equations of interest to this study has been developed. In principle, the approach allows, the use of adaptive mesh refinement. An algorithm for the selection

of elements based on the gradients of the main independent variables has been presented. A general numerical implementation for the relevant boundary conditions present in this work has also been discussed.

4.6 References

Ainsworth, M. and Oden, J. T. 2000. *A posteriori error estimation in finite element analysis*. Wiley.

Baker, A. J. and Pepper, D. W. 1991. *Finite elements 1-2-3*. McGraw-Hill.

Bangerth, B., Heister, T., Heltai, L., Kanschat, G., Kronbichler, M., Maier, M., Turcksin, B. and Young, T. D. 2013. The deal.II Library, Version 8.1. DOI.

Crank, J. and Nicolson, P. 1996. A practical method for numerical evaluation of solutions of partial differential equations of the heat-conduction type. *Advances in Computational Mathematics.* 6(1), pp. 207-226. DOI: 10.1007/BF02127704.

Herb, W. R., Janke, B., Mohseni, O. and Stefan, H. G. 2008. Ground surface temperature simulation for different land covers. *Journal of Hydrology.* 356(3–4), pp. 327-343. DOI: 10.1016/j.jhydrol.2008.04.020.

Kelly, D. W., De S. R. Gago, J. P., Zienkiewicz, O. C. and Babuska, I. 1983. A posteriori error analysis and adaptive processes in the finite element method: Part I - error analysis. *International Journal for Numerical Methods in Engineering.* 19(11), pp. 1593-1619. DOI: 10.1002/nme.1620191103.

Mullineux, N., Reed, J. R., De Kuijper, C. and Hammond, P. 1969. Roth's method for solution of boundary-value problems. *Electrical Engineers, Proceedings of the Institution of.* 116(2), pp. 291-293. DOI: 10.1049/piee.1969.0054.

Patankar, S. 1980. *Numerical heat transfer and fluid flow*. Taylor & Francis.

Reddy, J. 2005a. *An introduction to the finite element method*. McGraw-Hill Education.

Reddy, J. N. 2005b. *An Introduction to the Finite Element Method*. McGraw-Hill Education.

Thomas, H. R. and Rees, S. W. 1990. Modeling field infiltration into unsaturated clay. *Journal of Geotechnical Engineering.* 116(10), pp. 1483-1501. DOI: 10.1061/ (ASCE)0733-9410(1990)116:10(1483).

Chapter 5: Experimental Design, Methodology, Results and Numerical Modelling Validations

5.1 Introduction

This chapter describes the design and construction of a new experimental apparatus. In particular, the approach allows observation of the effect of including materials of adaptable thermal properties within a multi-layered soil system. This work addresses one of the main objectives of the present study, which is *to develop and build a new experimental device that will involve practical implementation of adaptable thermal insulation*.

An inter-seasonal thermal storage system utilizes the heat capacity of the ground (or any other suitable medium) to store the surplus thermal energy for use at a later time. The relatively high specific heat capacity and low thermal conductivity of many soils allows the usage of the stored energy to be delayed in time with only relatively small energy losses. Typically, thermal energy is stored in suitable regions of the soil by means of active engineering thermal devices (e.g. pipe heat exchangers) using a liquid (usually water) to transfer heat. However, this study proposes a new technique that could reduce the dependency or even replace these types of systems. At its core, it involves allowing the heat entering the soil from its surface to be transferred through a layer of adaptable thermal conductivity down to the soil underneath.

Details of the overall design, fabrication and calibration of the new experimental set up are given. Also, the experimental methodology adopted to exploit the new apparatus are discussed. Finally, results from the experimental testing are presented and compared to the numerical simulations from the model presented in Chapter 3 and 4, allowing validation of the model.
This chapter is divided in the following sections:

- Section 5.2 discusses the testing apparatus where the design criteria and description of the apparatus are presented.

- Section 5.3 describes the key accessories used in the system.
- Section 5.4 summarizes the testing methodology, sample preparation and equipment assembly & dismantling.
- Sections 5.5 presents the experimental results.
- Section 5.6 shows the model validation and methods used to improve the predictions and the theory behind them.
- The chapter conclusions are summarized in Section 5.7.
- Section 5.8 summarizes the chapter references.

5.2 Testing apparatus

In order to explore the described novel concept an experimental apparatus was designed and built since no conventional soil testing equipment was available. With this device a set of tests can be defined and carried out at laboratory scale to provide a validation benchmark for the numerical model. The key features of the new apparatus are: i) to automatically apply different boundary conditions on the surface and show the effects of the proposed new technique over a short (intra-day) or long testing period (seasonal replication), ii) to introduce a layer of adaptable thermal properties and iii) to minimize the heat losses at the sides and bottom of the experiments.

A detailed laboratory testing programme has been developed to investigate heat and energy movement in a sandy soil. In particular, a number of tests have been designed and fabricated which apply different thermal boundary conditions to a cylindrical soil sample.

Two sets of boundary conditions were chosen for consideration at the soil surface: i) a time-dependent prescribed surface temperature defined by a sinusoidal function (meant to replicate the annual variation of seasonal weather conditions), ii) a constant fixed temperature. In both cases the bottom end and the sides were insulated and the whole set-up resides in a temperature controlled room.

A number of numerical analyses of the heat movement in the soil column were undertaken prior to the fabrication using the numerical model presented in Chapter 3 and 4 and after multiple runs, the choice of the sample dimensions was settled. Furthermore, radial heat loss was also calculated. Based on those calculations alongside the available budget and ease of handling and application the choice of what materials to be used had been made.

5.2.1 Design criteria of apparatus

The experimental apparatus was designed to satisfy the following criteria so that the measurements of key parameters and control of the experimental conditions could be accomplished:

- The soil sample can be properly inserted into the apparatus so that there is no air gap between the sample and the apparatus walls.
- The apparatus had to be sufficiently strong to withstand the extreme and multiple temperatures created during the test.
- The sample can be subjected to a well-regulated and stable temperature gradient or sinusoidal temperature variation applied at the top of the sample.
- The apparatus must be thermally insulated except for the top surface.
- The apparatus must be both robust and easy to handle, assemble and dismantle.
- The apparatus should accurately capture the radial and central temperature variation on the soil column.
- The apparatus needs to be compatible with existing auxiliary equipment available at the laboratory which is required for this laboratory testing programme.
- The apparatus can be used for future research.

5.2.2 Description of apparatus

The soil column is divided into three layers: A “top layer”, a “middle layer” or “adaptable insulation layer” and a “bottom layer”. The thermal properties of the

adaptable insulation layer are controlled by varying its moisture content as it composes of uniform 5 mm soda lime glass bead. By flooding the adaptable insulation layer with water, it will conduct heat down to the bottom layer allowing it to accumulate thermal energy while by draining it, the layer would minimize the movement of heat.

For the soil in the top layer, the performed tests considered two different initial moisture contents: (i) field capacity and (ii) full saturation. While the soil in the bottom layer is always kept at fully saturated conditions.

An apparatus has been designed to fulfil the design criteria detailed earlier. A schematic diagram of it is shown in Figure (5.1).

The bottom side of the acrylic tube has been closed with a square PVC sheet of 20 mm thickness using a permanent sealant. Except the surface of the column all of it has been wrapped with a 75 mm thickness of Rockwool to insulate the sides and bottom of the tube. The thermal properties of the adaptable insulation layer were controlled via saturating the layer with water to allow it to conduct heat and drain it to act as an insulator.

5.2.3 Testing column

An acrylic tube shown in Figure (5.2) has been used to make the main components of the apparatus. The choice has been made for this material as it has low thermal conductivity of 0.2 (W/mK) and its thermal properties remain relatively the same under high or low temperatures; it has excellent machining, forming and cutting characteristics. The tube has a thickness of 18 mm, length of 610 mm and diameter of 254 mm. Viton® O-rings were used as sealant fitted in a groove at the interfaces of the lower end of the tube to inhibit any moisture escape. The Viton® O-rings are made from a fluoroelastomer and can withstand a range of temperatures from -40 °C to +200 °C and have high chemical resistance with good compressibility.

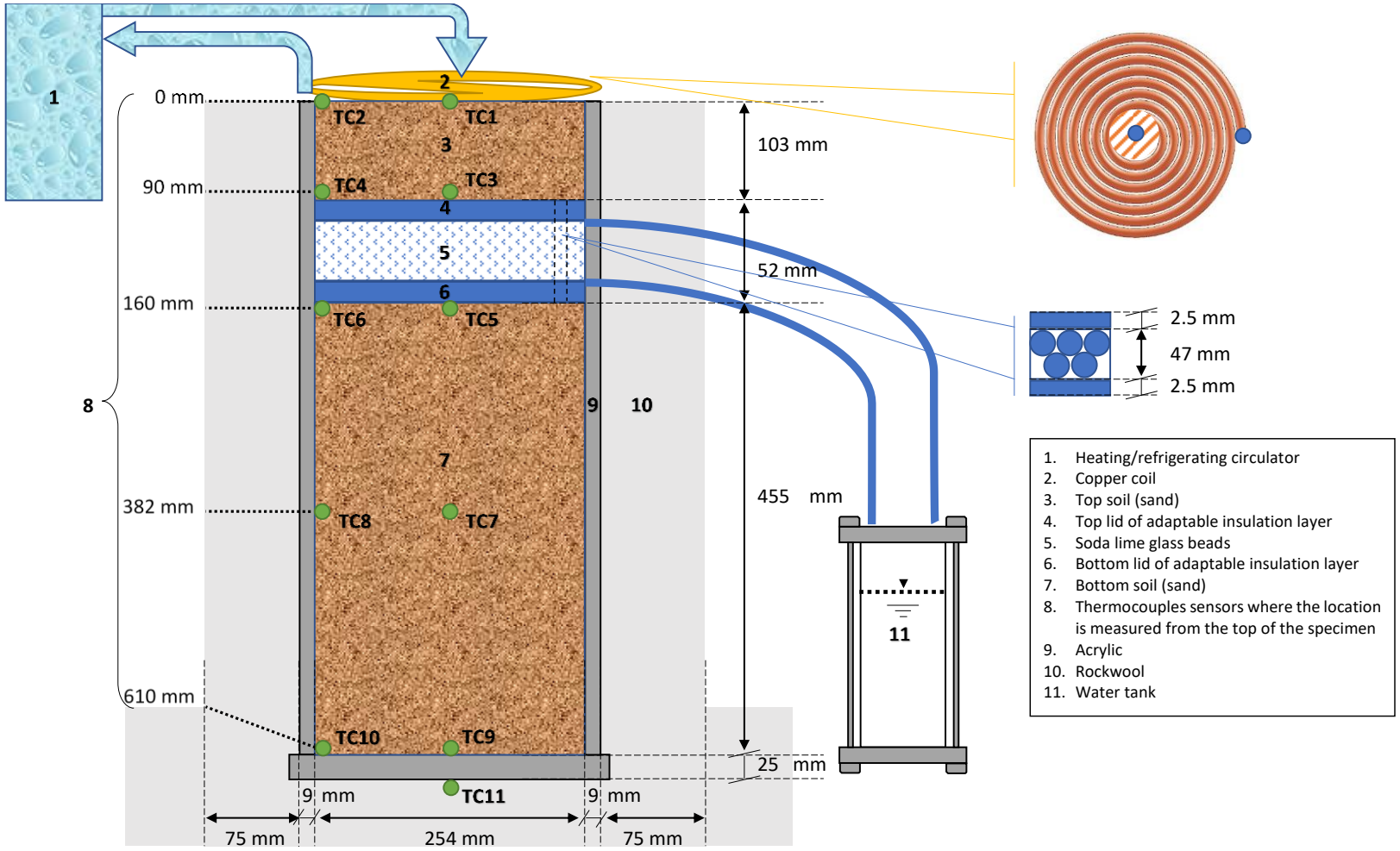

Figure (5.1) Schematic diagram of the experimental setup

5.2.4 Top layer

The thickness of the top layer is 103 mm, two moisture contents for the soil in this layer were used during the different tests performed: field capacity water content and full saturation water content. The soil properties details are listed in Table (5.4). The choice of a field capacity water content was to correlate the moisture content of the experiment with the developed numerical program beside it is a common natural condition while the full saturation moisture content was decided upon later to overcome the uncertainties in the thermal properties of partially saturated soils as most of the empirical or theoretically based thermal conductivity values agrees well for the fully saturated conditions as seen in Figure (2.1).

5.2.5 Adaptable insulation layer

A layer that separates the two soil columns had been introduce, the layer composes of different divisions, and the total thickness of the adaptable insulation layer including two lids is equal to 52 mm. The layer is filled with a unified size of 5 mm soda lime glass beads supplied by Sigma-Aldrich Co Ltd. The plastic lid separators were installed above and below those beads to hold the layer boundary and its designated water content as required, the top separator is a see through 3 mm thickness clear polycarbonate circular sheet while the bottom is a circular grey PVC sheet with a 5 mm thickness. The material parameters of the glass beads are listed in Table (5.3).

Two escape nozzles were inserted in the acrylic cylinder at the very top and bottom of the layer to create inlet and outlet for the water, to allow control of the water content of the layer. The nozzles are connected to one-way flow valves to facilitate the water movement in the required direction only.

5.2.6 Bottom layer

The bottom layer serves as thermal storage medium and is kept at fully saturated conditions. The total thickness of this layer equals to 455 mm and a total of

five thermocouples were inserted in this layer to monitor the heat movement during the experiment. The heat flux was estimated at the tube bottom by placing another thermocouple outside the bottom end of the tube, and using Fourier's law (Section 3.4) to calculate the amount of heat flux.

5.2.7 Insulation

A highly insulative material (Rockwool) is wrapped around the outside of the tube cylinder to minimise radial heat losses. The insulating material used is a Rockwool blanket, supplied by Alliance & Heatshield Engineering Ltd UK.

Typical Feature	Value			Units		
Density	80-100			kg/m^3		
Working temperature	Maximum 250			°C		
Medium thermal conductivity	0.036			W/mK		
Thermal conductivity at different temperatures	50	100	150	200	250	°C
	0.035	0.046	0.056	0.069	0.083	W/mK
Specific heat capacity	840			J/kgK		

Table (5.1) Thermal parameters of Rockwool

Figure (5.2) Acrylic tube before and after applying Rockwool insulation

It has good thermal stability with excellent thermal insulating properties and immune to any thermal shock. Its thermal properties are detailed in Table (5.1). Figure (5.2) shows the acrylic tube before and after applying a 17 mm thick layer of Rockwool insulation.

5.3 Accessories

The soil column needs a range of auxiliary devices related to temperature control and water supply. The following sections provide the detail of them.

5.3.1 Heating/refrigerating circulator

A heating/refrigerating (heater/cooler) water circulator, Thermo Fisher Sceintific® (Advanced Series Heated Immersion Circulators AC200 with A10 bath), was used to control and create the temperature applied at the soil column surface. Water at the required temperature is circulated through an internal copper coil fitted inside the copper plate. The heating/refrigerating circulator is made of high-grade stainless steel and temperature resistant polymer. It has a PID controller and an adjustable over heating or cooling cut-out, the technical specification of the circulator is given in Table (5.2). The user can define the temperature variation in the circulator (e.g. to produce ramp or periodic profiles) by programming up to 30 temperature points at defined time intervals. The circulator temperature range is from -10 °C up to 100 °C. Figure (5.3) shows the circulator front and back panel.

NEScom a software application that was used to control the heating/refrigerating circulator and programme an almost infinite number of steps and relate them to temperature to create a suitable transient temperature profile.

Additional software features include the capability to view and print a temperature and set point chart, configure and log alarms, run and save programs, and view indicators in the form of gauges and meters, all from menu bar selections. The used version of the program is NEScom V.4 courtesy of Thermo Fisher Scientific®.

Specification		Value	Units
Temperature range		-10 to 100	°C
Temperature stability		±0.01	°C
Heater capacity		2000/1200	W
Dimension (H x W x D)		372 x 165 x 199	mm x mm x mm
Pumping capacity	max. flow rate	20	lpm
	max pressure	475	Mbar
	max suction	330	
Connectivity		Remote sensor port, USB port, Multi-function port, RS232/RS485/Ethernet/LAN	

Table (5.2) Circulator technical specification

Figure (5.3) Front and back face of the circulator

5.3.2 Heating/cooling plate

The soil above the adaptable insulation layer was in contact to a heating/cooling plate that has a 6.4 mm annealed copper coil inside which allows water with a controlled temperature (as required) to circulate through.

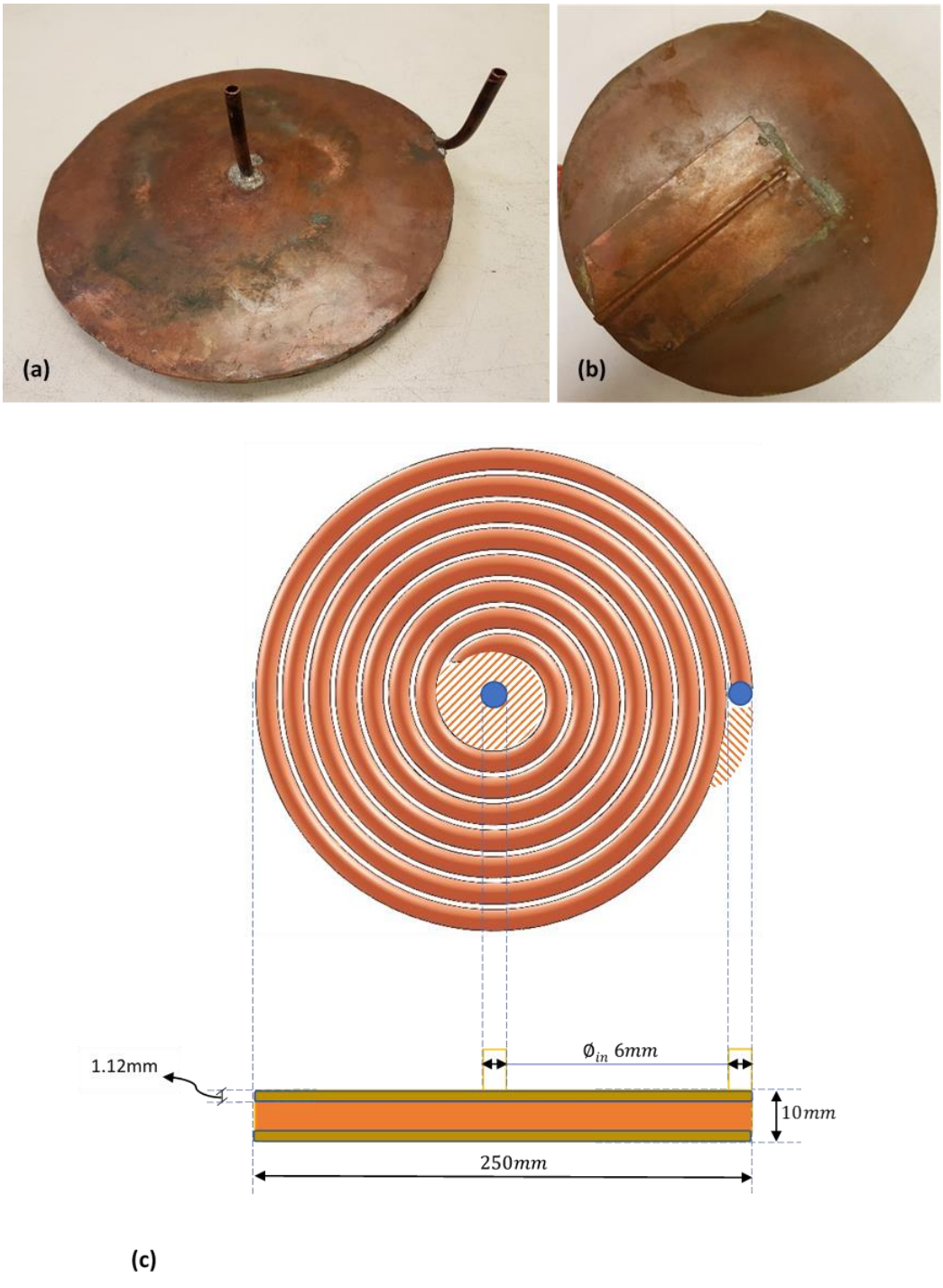

Figure (5.4) (a) Top, (b) bottom and (c) schematic diagram of heating/cooling plate

It was supplied by RS Ltd UK, the coil internal diameter is 6 mm with a maximum operating pressure of 81 bar and the operating temperature ranges between -50 °C to +200 °C. Two elbow fittings were used to create 90° angles for the circulated, twisted and aligned tube as shown in Figure (5.4). Two thin plates of 2 mm thickness were laid and welded above and below the circulated coil and allowing the elbow fittings to penetrate through it.

5.3.3 Temperature sensors

K-type thermocouple temperature sensors were used to measure temperature at several depths in the soil column and at its surface. The thermocouples are placed at 0 mm, 90 mm, 160 mm, 382 mm and 610 mm.

The working method of these thermocouples is based on the principle that when two dissimilar metals (Chromel Ni-Cr alloy and alumel Ni-Al alloy) are joined, a voltage is generated that relates to the difference in temperature between the measuring junction and the reference junction (connected to the measuring device). All the thermocouples were connected to a data logger to measure the transient temperature at various points in the soil sample. The tips of the thermocouple type K are welded, and it has 0.2 mm diameter twisted pair leads insulated with teflon and an operating range of -75 °C to +250 °C.

5.3.4 Data acquisition

As the tests were performed over long periods of time, they produce large quantities of transient data. Therefore, an automated data acquisition system was required. This has been achieved via a Grant Instruments D800 data logging system connected to a desktop computer.

The DT800 data logger has a processor card High Speed Data Acquisition, stand alone and real-time monitoring of up to 42 analogue sensors inputs, 16 digital channels and ATA flash card for removable data storage.

The DT800 must be programmed before it makes any measurements. A program was created by keying it directly into the data logger or on a personal computer using the DT800 data logger support software program “EDLOG”.

5.3.5 Hydrophobic material

A hydrophobic material was used to cover the beads used in the adaptable insulation layer in order to help repelling water from the bead surface and thus help minimizing the overall remaining water which is hard to remove (i.e. it help minimize the thermal bridges). Screwfix Direct Limited supplied a Fabsil© universal protector water repellent, which is a silicone spray that restores water.

5.3.6 Testing of integrity/calibration of thermocouples

Whenever a new apparatus is designed and fabricated, the first step is to test its integrity and calibrate it. The copper coil with its covered plates needed to be checked to see if it could deliver the required amount of heat set out by the user through heating/refrigerating circulator. The thermocouples were numbered and placed around the centre and radius of the copper plate and any difference between the two readings observed. As expected there was a drop in temperature (of approximately 0.3 °C) between the central and radial readings with the maximum temperature occurred at the centre due the heat loss during the circulation of water, to minimize this variation the maximum speed available for the water pump inside the circulator is used.

Dummy tests were then conducted to observe any faults and leaks during operation. During the first trial tests, the circulator temperature was varied on a sinusoidal wave from 16 °C to 28 °C which varied over a period of time (e.g. 24 hour); the circulator controlled the targeted temperature over the soil column with a ~ 1.5 °C margin of error.

The device is equipped with an option that allows the user to apply real-time adjustment for the delivered value (within ±0.1 °C of the required values).

The temperature probe thermocouples were tested and calibrated by subjecting them to direct exposure to a material of know temperature condition (iced and boiling water) to make sure of the data logger and thermocouples functionality and accuracy. Afterwards, the thermocouples were placed alongside other types of thermocouples and temperature probes that were available in the lab in another water filled beaker and left under the room temperature (laboratory controlled room temperature). Figure (5.5) shows the outcomes of this trial experiment.

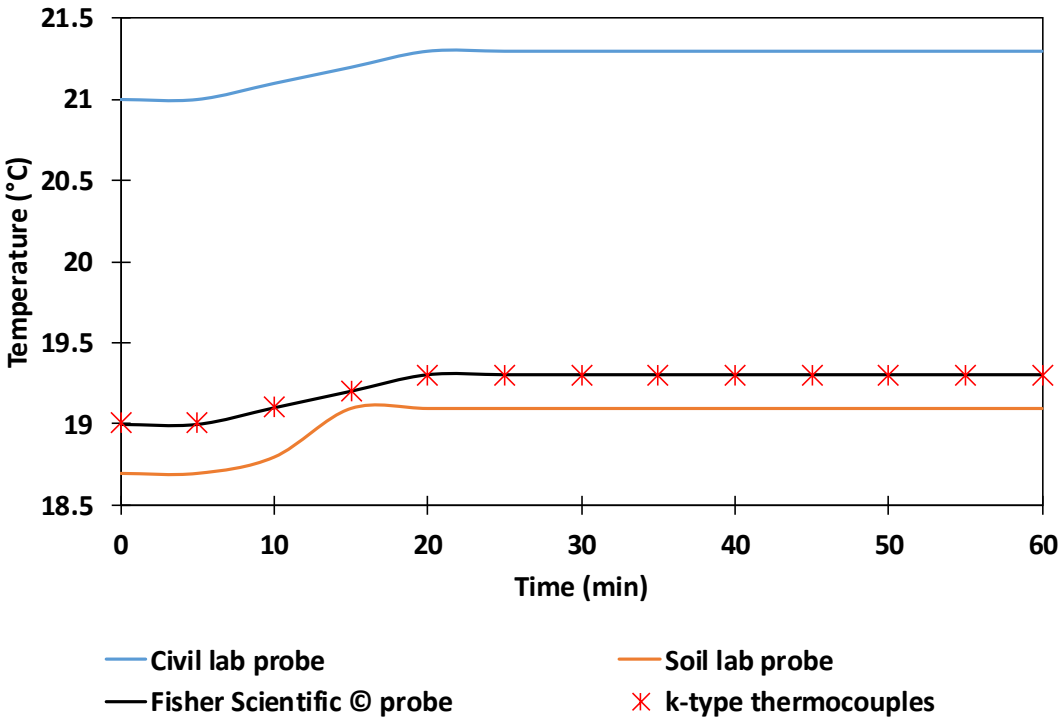

Figure (5.5) Thermocouples calibrations

It can be seen that the k-types thermocouple readings closely coincide with the recorded temperature using the Fisher Scientific © probe (model number 11799735 Fisherbrand™ Traceable™ Digital Thermometers). This led to a satisfactory confidence in using such type of thermocouple.

In general, it was found that new apparatus was working well and meeting all the design criteria stated in Section 5.2.1.

5.4 Testing methodology

An experimental methodology was developed to carry out experiments efficiently. The following section discuss the important steps including sample preparation, assembling and dismantling.

5.4.1 Sample preparation

For the soil above the adaptable insulation layer, firstly, we need to dry the sand for 24 hours in an oven at 105 °C. Then, depending on the required moisture content, water was added and mixed thoroughly with dry soil by using a sprinkling bottle to ensure uniform moisture distribution and the soil was then placed in the column. The achieved dry density of the soil was 1740 kg/m^3. While for the fully saturated condition, mixing was undertaken inside the acrylic tube column itself by adding part of the water first and up to a certain level and then, via wet pluviation, adding the sand gradually to prevent any air gap and likewise up to the top and the same technique was used for the layer below insulation. In all cases, the sand was compacted with a laboratory plate compactor in order to expel air gaps.

5.4.2 Assembling and test setup

The placement of thermocouples at designated locations in the experimental device was performed after the arrangement of the column layers was finished. Small holes are drilled through the acrylic tube surface wide enough to install the temperature probes. Two of the thermocouples wires were inserted in each hole, one placed at approximately the centre of the column while the other was placed near the interior surface of the acrylic tube in order to obtain radial readings. Then a silicon sealant was applied to prevent leakage during the experimental procedures. An important remark is that the central location of the thermocouples is approximate.

After adding the bottom soil layer with its desired water content, the lower lid of the adaptable insulation layer was introduced and pressed onto the saturated soil below it. Silicon sealant was then used to seal the lower lid to the acrylic tube surface to

make sure that there would be no leakage from the adaptable insulation layer. Then, the dry soda lime glass beads were added gradually to achieve the intended number of beads inside, the beads were vibrated and compacted via forcing the upper lid to the required dimension and then it was sealed using silicon sealant. A very small inclination was applied for the upper lid to minimize the presence of any air bubbles. Finally, the upper layer of soil was placed at its designated water content.

The thermocouples were connected to data acquisition system which consisted of the data-logger and the personal computer. Finally, the copper plate which was already connected to the circulator through the temperature probe (alongside water inlet and outlet) was placed and sealed on the top of the soil column.

5.4.3 Dismantling

After finishing the experiment, the layer above insulation was dismantled following the reverse order of assembling the components described above. The data was saved in the hard drive of personal computer.

5.5 Laboratory experimental results

5.5.1 Summary of tests

As described earlier, the laboratory scale experimental setup consists of a sandy soil column with an adaptable insulation layer inserted at some depth. The adaptable insulation layer was created using glass beads and two plastic discs above and below them; the benefits of which was to form the adaptable insulation layer boundaries and allow control of its water content.

The thermal properties of the adaptable insulation layer were modified by the addition or removal of water which in turns regulates the transfer of energy between the soil surface and a storage region within the soil mass.

It is important to note that all the presented results are for central thermocouples (TC1, TC2, TC5, TC 7 and TC9) unless otherwise specified. In practice, a high thermal

conductivity will be used during seasons with high availability of thermal energy (summer) to charge the storage region, while low thermal conductivity will be employed during seasons of lower availability of thermal energy (winter) to minimize heat losses. This is mimicked in the following tests.

- First trial tests: This test used the uncoated glass beads in the adaptable insulation layer and it composes of three different tests.
- Second trial tests: Same as previous test except with the use of hydrophobic material to coat the beads and it involves three tests as well. Both of the trial tests were performed prior to the main seasonal tests, the main objectives of the trial tests are (i) to identify and overcome any technical problems with the testing apparatus, (ii) to provide a validation data set for the numerical model and (iii) to test the instrument limitations and capabilities.
- First seasonal test: This test spanned over a longer period (28 days) in an attempt to represent different seasons. The test also started with conditions representing summer and autumn seasons (charging period) and followed by winter discharging period. In this test, a field capacity degree of saturation (S_r=0.5) was used for the upper soil.
- Second seasonal test: the same as the first seasonal test except a fully saturated soil was used for the upper soil (S_r=1).
- Third seasonal test: This test was allocated for studying the latent heat of fusion ground freezing behaviour in soil.

Finally, before introducing the results, it is worth considering the temperature gradient at base of the apparatus (TC9 and TC11), Figure (5.6) shows the heat flux extracted from first trial sets.

The results show that the gradient is almost negligible and the difference could be attributed to thermocouples sensitivity.

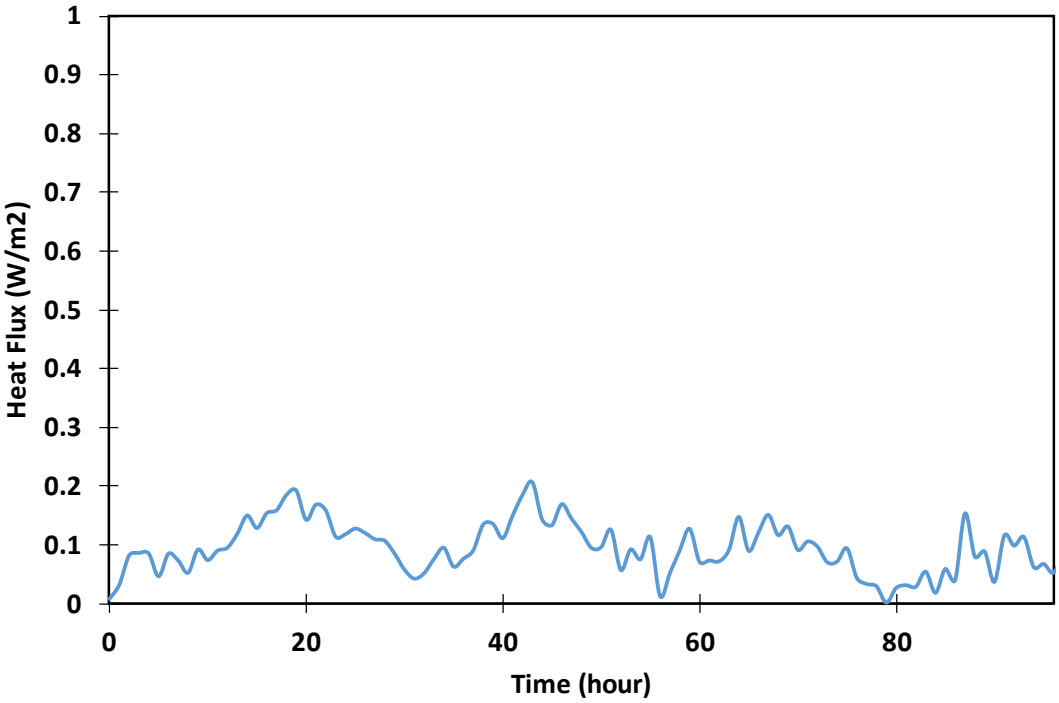

Figure (5.6) Heat flux at base of apparatus 1st trial test

5.5.2 Trial tests

5.5.2.1 First trial tests: preliminary calibration using uncoated bead

Using uncoated glass beads in a condition as supplied in the adaptable insulation layer was the first choice in these initial two sets of dry and saturated conditions. The initial water content for the top soil was set at the field capacity with a degree of saturation of 50 % while the bottom soil was at a fully saturated condition. Each test was undertaken to observe the adaptable insulation layer behaviour and how it reacts under different conditions (i.e. dry or saturated). The dry adaptable insulation layer was created using fully dried bead. The beads were completely dried using a laboratory oven of 105 °C for 24 hours to remove any available water and then the adaptable insulation layer was carefully sealed to ensure a small slope in the upper lid to minimize/prevent trapped air and also to withstand the vacuum pressure applied before filling the layer with water. The temperature applied on the column surface (0 mm) and the results of this test are shown in Figure (5.7).

A fully saturated adaptable insulation layer test was then undertaken after the completion of the previous test, with a rest period observed to allow the soil returning to the original initial temperature of the bottom layer while the top layer is changed with a newer freshly mixed sample.

The adaptable insulation layer was fully saturated with water supplied gradually to prevent any trapped air bubbles under the top lid of the adaptable insulation layer. Figure (5.8) shows the results of this tests.

The adaptable insulation layer was filled with water using a vacuum pump (-5 bar) via using the escape valves placed at top and bottom of the layer in order to extract the excess air and quickly replace it with water.

An empty air tank was connected to the vacuum pump and the other opening to be connected to the upper entrance of the adaptable insulation layer. The lower entrance of the adaptable insulation layer was inserted in a filled water tank.

When it was required to fill the adaptable insulation layer with water, the vacuum pressure would be applied first while the lower valve of the adaptable insulation layer is closed for few minutes in order to expel all of the entrapped air.

After that, the upper valve would be opened and the adaptable insulation layer would be filled with water from bottom to top which would prevent air bubbles to exist while filling with water. The excess water would be ejected through the upper valve when the layer is filled.

For draining the adaptable insulation layer the lower valve was opened and allowed to drain freely its water content and afterwards, pushing a dry air through the upper valve for extra assurance of water removal.

Figure (5.9) provide the results of this test while Figure (5.10) and Figure (5.11) shows the comparison between the three sets for the zones immediately above (TC3) and below (TC5) the adaptable insulation layer.

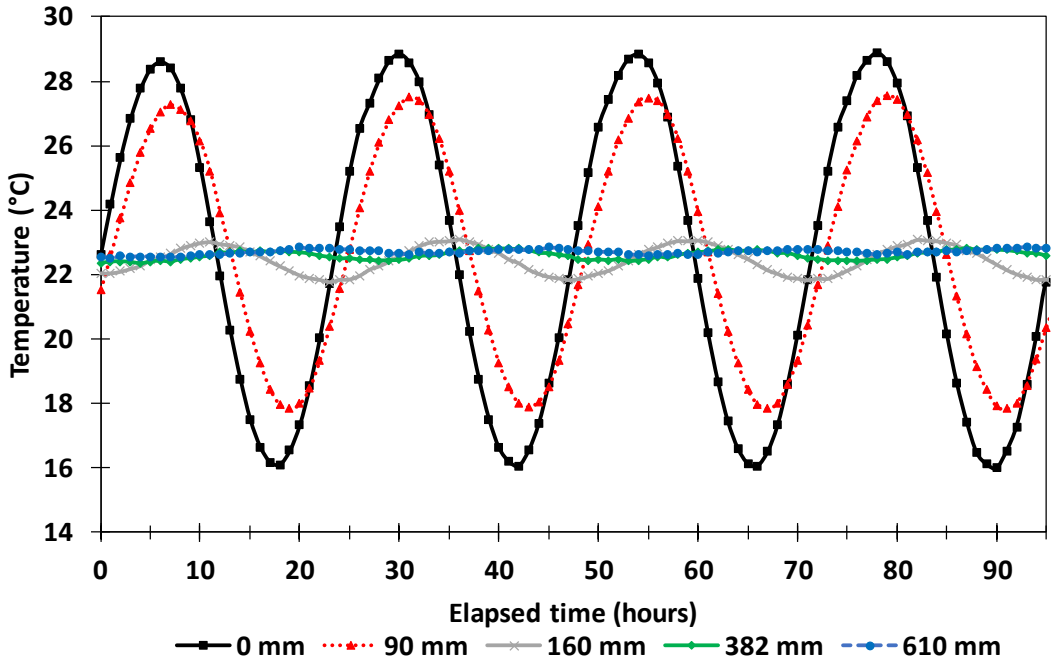

Figure (5.7) Experimental uncoated dry test results

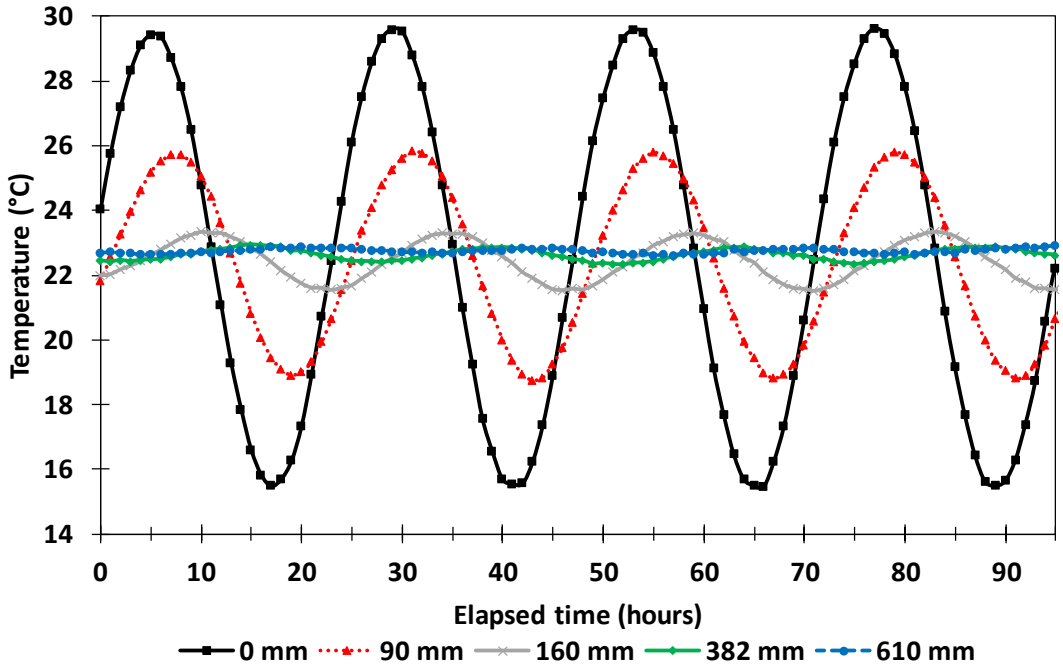

Figure (5.8) Experimental uncoated saturated test results

After finishing the previous test, a third test was followed to investigate the effect of undrained water left in the adaptable insulation layer and whether it creates thermal bridges or not, this is termed the drained test. Drainage was achieved by firstly

allowing the adaptable insulation layer to freely drain and then by circulating dried air through the nozzles for extra assurance of water removal.

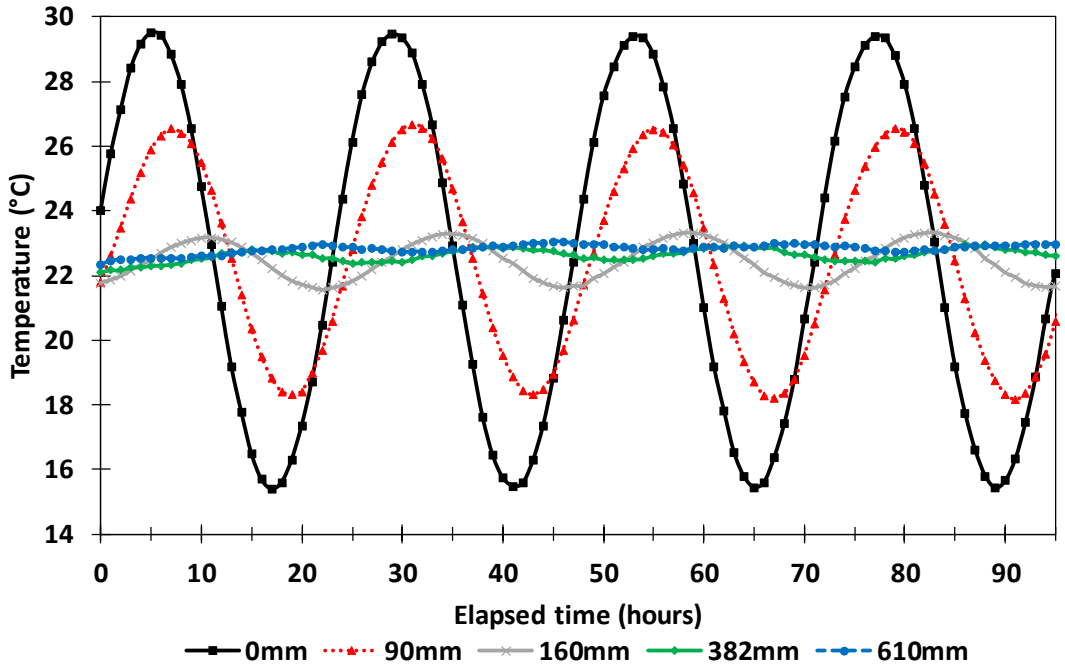

Figure (5.9) Experimental uncoated drained test results

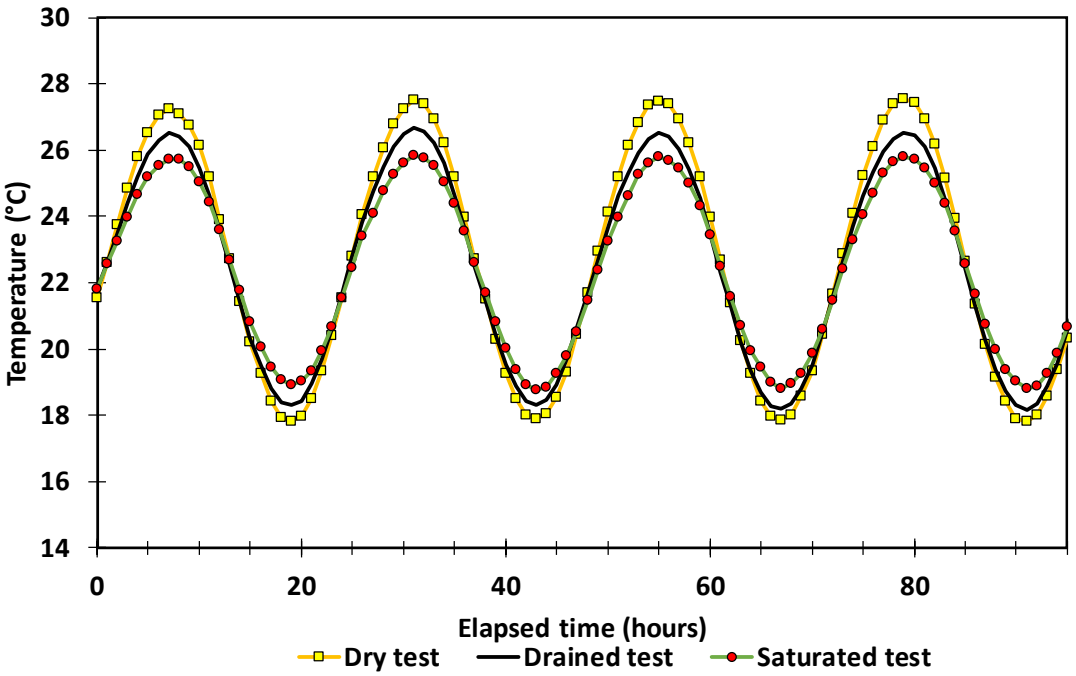

Figure (5.10) Experimental setup comparisons for uncoated bead

(Immediately above adaptable insulation layer at 90 mm)

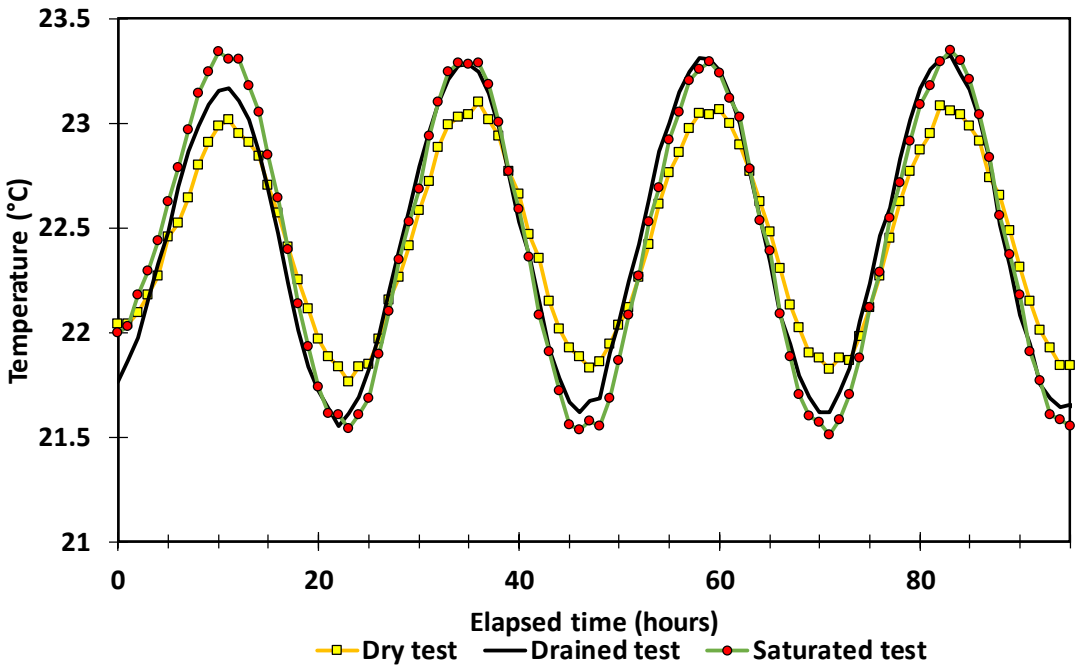

Figure (5.11) Experimental setup comparisons for uncoated bead
(Immediately below adaptable insulation layer at 160 mm)

It is important to note that the temperature applied on the soil surface is not the same between the three tests, which could be related to the instability in room temperature, which in turn could influence the heating/refrigerating circulator. An example of the room temperature variation will be presented later in the following tests. Moreover, the comparisons between the three results shows that there is a thermal bridge created between the beads inside the adaptable insulation layer which will be addressed in the following test in order to make sure it will not affect any following tests.

5.5.2.2 Second trial tests: preliminary calibration using coated bead

The same testing procedures used in the first trials (the adaptable insulation layer draining and filling with water) and initial conditions were applied in these tests except a higher average temperature was applied at the soil surface to test the effectiveness of adaptable insulation layer, and the beads in the adaptable insulation layer were coated with a hydrophobic material (as presented earlier in 5.3.5). The use

of this hydrophobic coating in all subsequent tests was selected to minimize or prevent thermal bridge creation due to water remaining after draining of the adaptable insulation layer. This technique that will be of particular use during the seasonal tests as they will start with a charging period (fully saturated bead) followed by a discharge period (dried bead). As described in the previous section, the first test considers dry adaptable insulation layer whilst the second test considers saturated adaptable insulation layer, Figure (5.12) and Figure (5.13) show the results of the two tests respectively. It can be seen that applying a higher temperature at the soil surface clearly affects the amount of heat penetrating into the soil and also it shows the benefits gained from using the adaptable insulation layer which was the objective of raising the surface temperature compared to the first trial sets. However, even with this temperature the heat slightly affects the base of the soil column which on the other hand confirms the sufficiency of using this tube length for conducting the experiment.

Figure (5.14) shows the results obtained for another test that was conducted following the saturated test where the adaptable insulation layer was drained, the benefit of this test would be to assess the behaviour of the adaptable insulation layer bead after it was subjected to the hydrophobic material.

It should be noted that the temperature profile applied under saturated conditions delivered a lower amount of thermal energy to the soil column as shown in Figure (5.15). The difference in the peak temperature between the temperature profiles applied at the surface in dry and saturated sets of more than 2°C with the higher temperatures applied under dry conditions and it is expected that under identical surface profiles the difference would be expected to be higher.

This difference is attributed to the delivered temperature from the circulator which is affected by many factors (e.g. the fluctuation of room temperature). However, despite the lower surface temperature in the saturated adaptable insulation layer tests, the temperature difference between below the adaptable insulation layer is up to 1.86°C higher temperature which indicates the possibility of it being higher if the same dry surface temperature applied.

Comparisons of Figure (5.16 and 5.16) with Figure (5.10 and 5.10) shows the impact of using the hydrophobic material. The comparisons clearly shows the transients of the drained adaptable insulation layer test approaching the dry adaptable insulation layer rather than the saturated adaptable insulation layer.

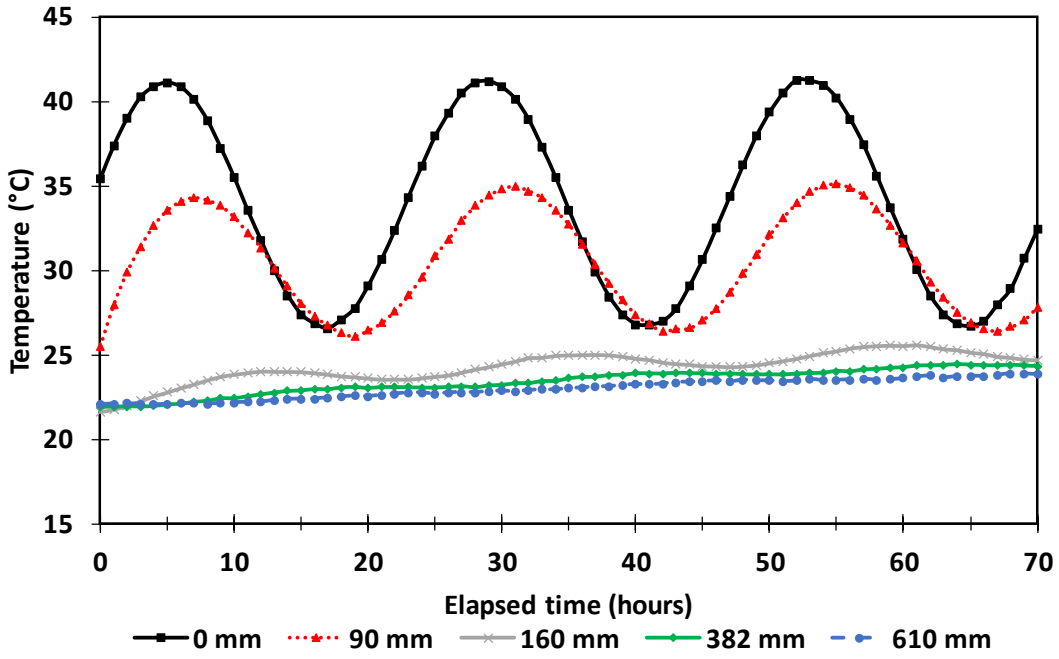

Figure (5.12) Experimental coated dry test results

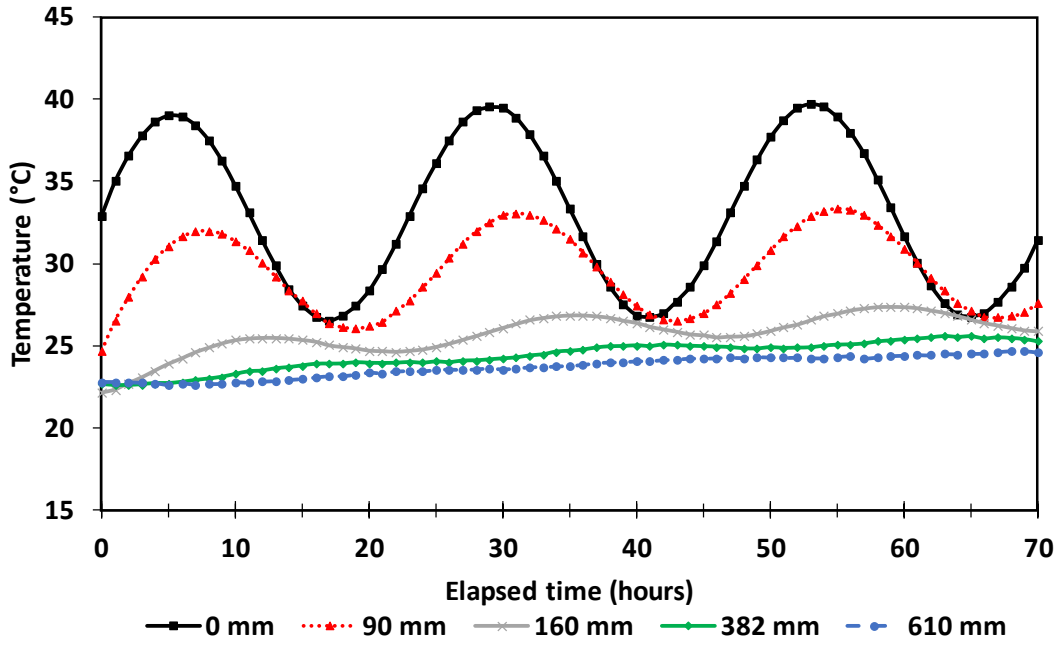

Figure (5.13) Experimental coated saturated test results

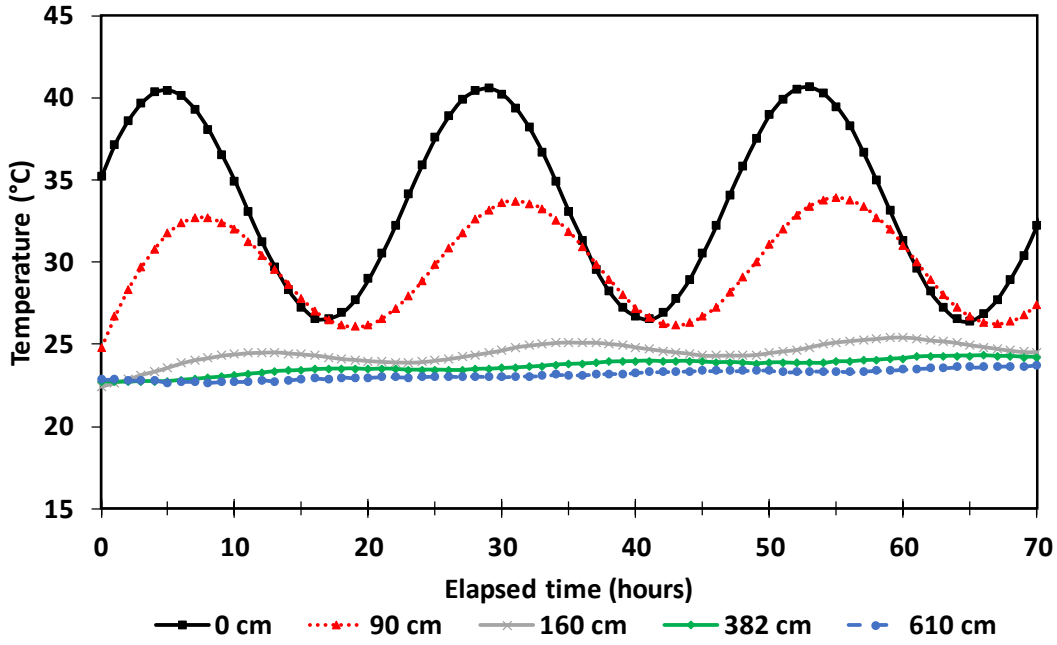

Figure (5.14) Experimental coated drained test results

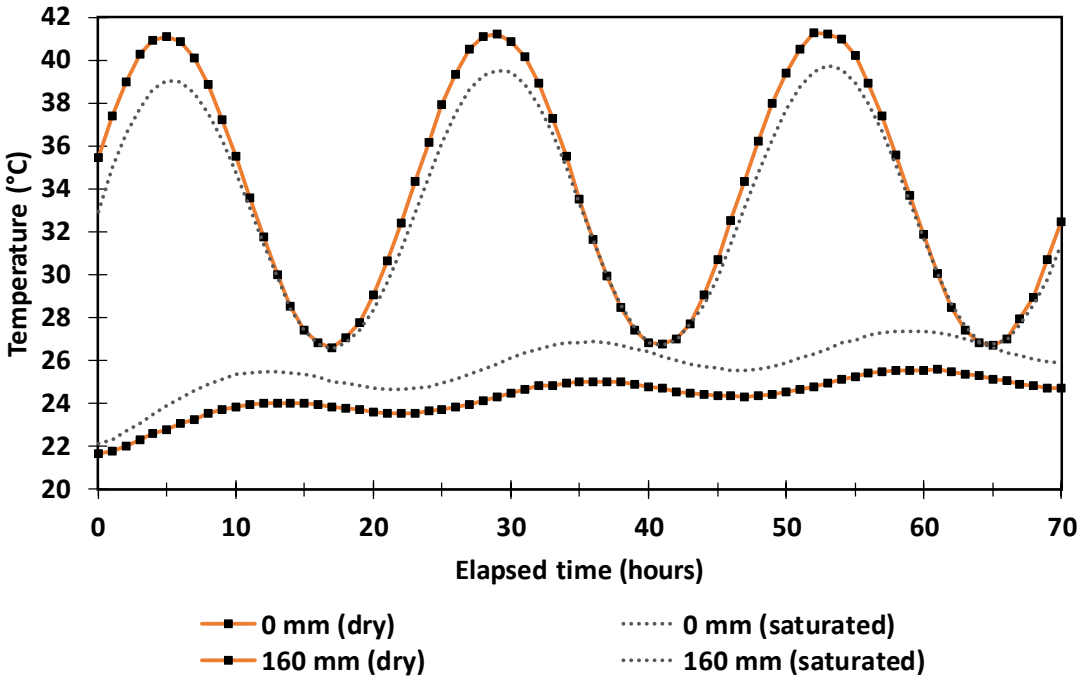

Figure (5.15) Comparisons of experimental temperature variation from trial tests

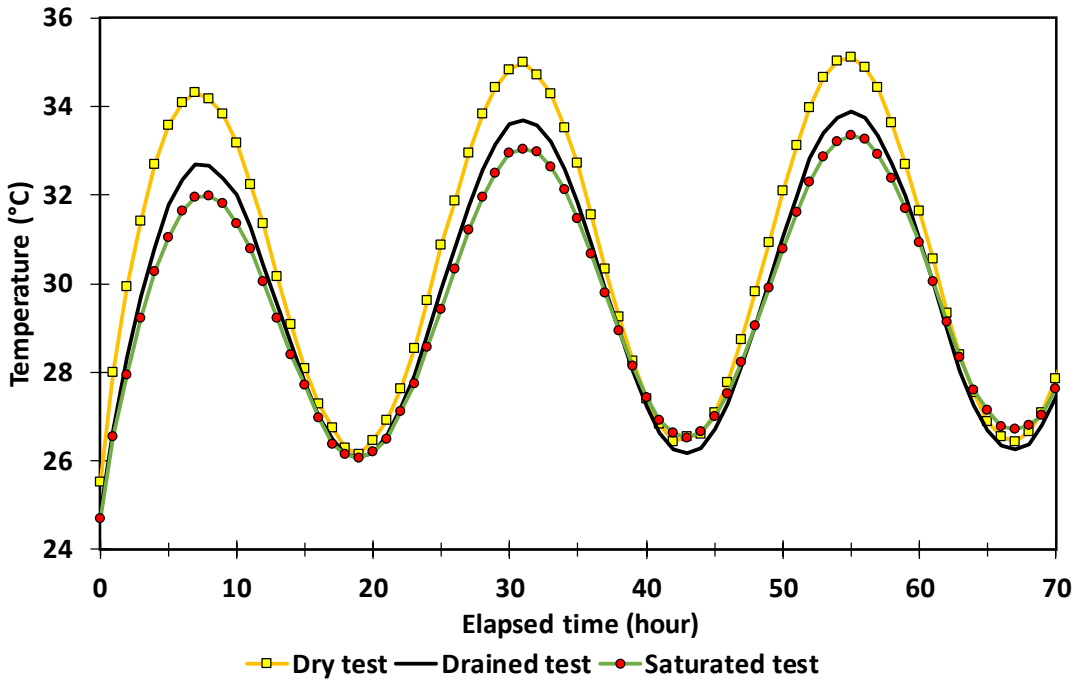

Figure (5.16) Experimental setup comparisons for coated bead

(Immediately above adaptable insulation layer at 90 mm)

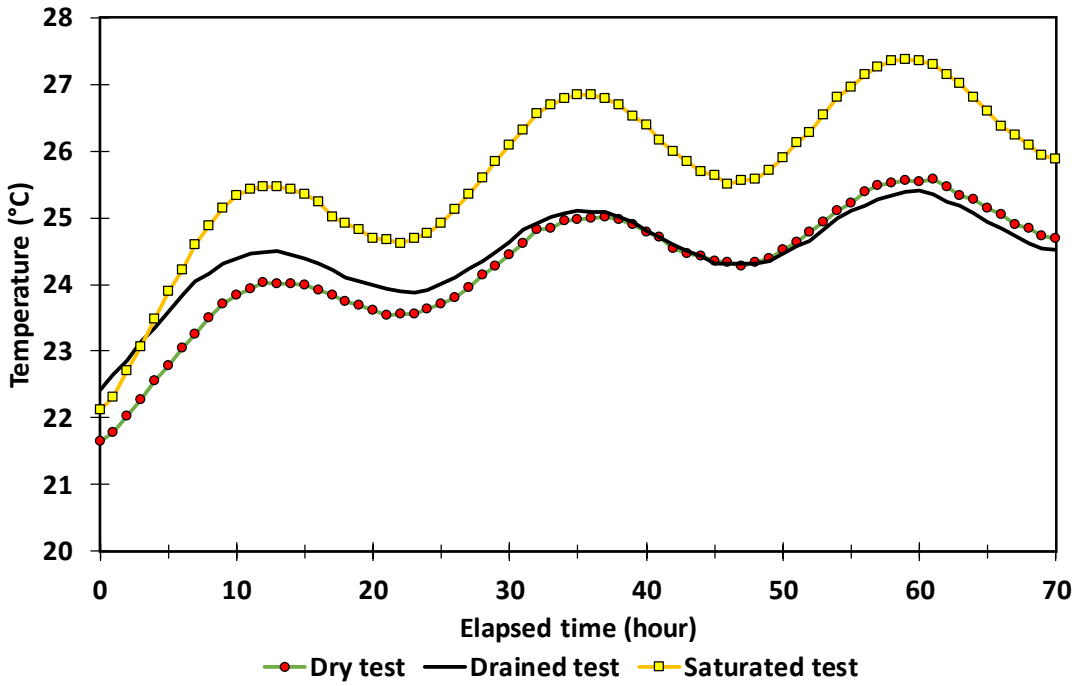

Figure (5.17) Experimental setup comparisons for coated bead

(Immediately below adaptable insulation layer at 160 mm)

5.5.3 Seasonal tests

As mentioned above following the successful conclusion of the trial tests a series of tests design to mimic seasonal conditions were then undertaken. The main differences in the following tests are that they attempt to represent different seasons as well as lasting for a comparatively longer time.

The tests start with a fully saturated adaptable insulation layer representing the summer and autumn seasons (charging period) with the second part of the experiment representing a winter season having a drained layer (discharging period). The tests span over a 28 days (hour 672) and the adaptable insulation layer to be drained on day 14 (hour 336).

The surface temperature variation applied on the first and second seasonal test was an attempt to capture the system behaviour under full periods of collection and storage (i.e. year cycle). However, due to many limitations (i.e. maintenance of the heating/refrigerating circulator, laboratory room maintenance, duration of the overall study, and a lack of an uninterruptable power supply) the compacted season was then introduced and applied over the 28 days of experiments. For the third seasonal test the system was tested under extreme conditions during both charging and extraction periods with a special focus on the zero curtain phenomenon.

All of the seasonal tests were undertaken following the same procedures demonstrated in the trial tests, the bottom layer was kept in fully saturated condition while the top layer varied from field capacity in the first and third tests while both of the layer (top and bottom) were in fully saturated conditions in the second test

5.5.3.1 First seasonal sets: (upper soil degree of saturation=0.5)

In this test, the initial moisture content for the top soil is set to the field capacity (S_r=0.5) while the bottom soil was under fully saturated conditions.

The test lasted for 28 consecutive days, during which the first 14 days the adaptable insulation layer was remain in a fully saturated condition to represent the charging

period, after which the adaptable insulation layer was drained for the other half time of the experiment.

Figure (5.18) shows the results of this test, the adaptable insulation layer was drained in hour 336 and the test was finalized on hour 672 and then left to restore its initial condition which is related to the room temperature of the laboratory.

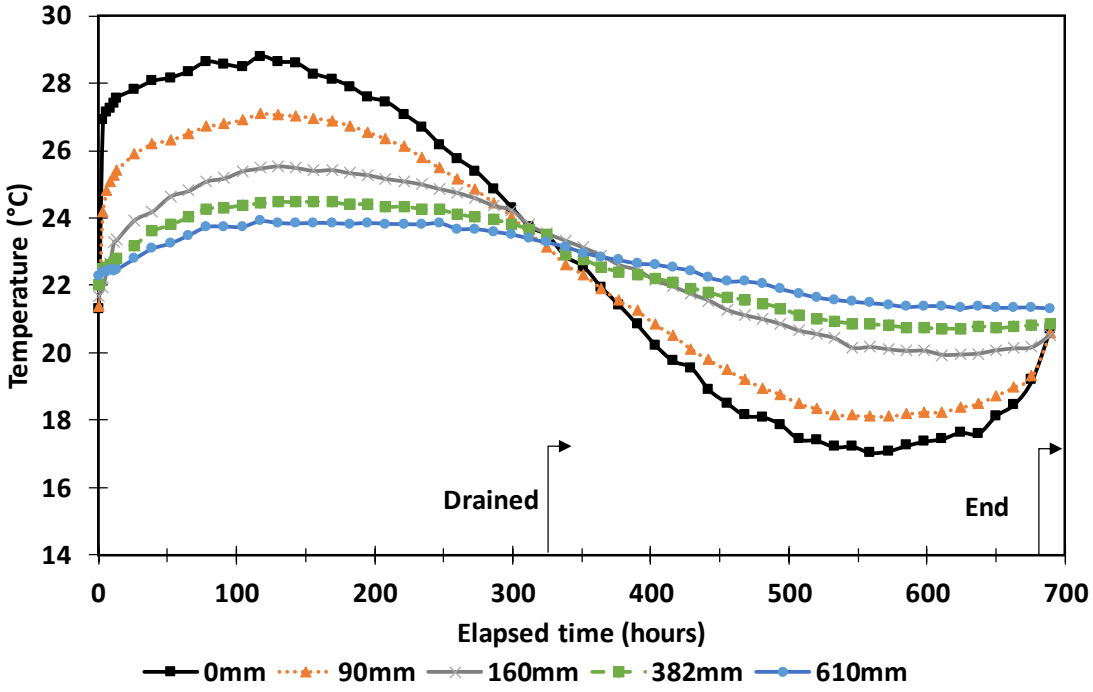

Figure (5.18) First experimental seasonal test

5.5.3.2 Second seasonal sets: (upper soil degree of saturation=1)

The difference in this test is in the initial moisture content of the soil as both layers of soil were fully saturated.

The reason for this change (as discussed before) is to provide a solid ground for comparisons between the experimental and numerical results through overcoming the uncertainties in thermal conductivity's measurement. Figure (5.19) shows the results of this test.

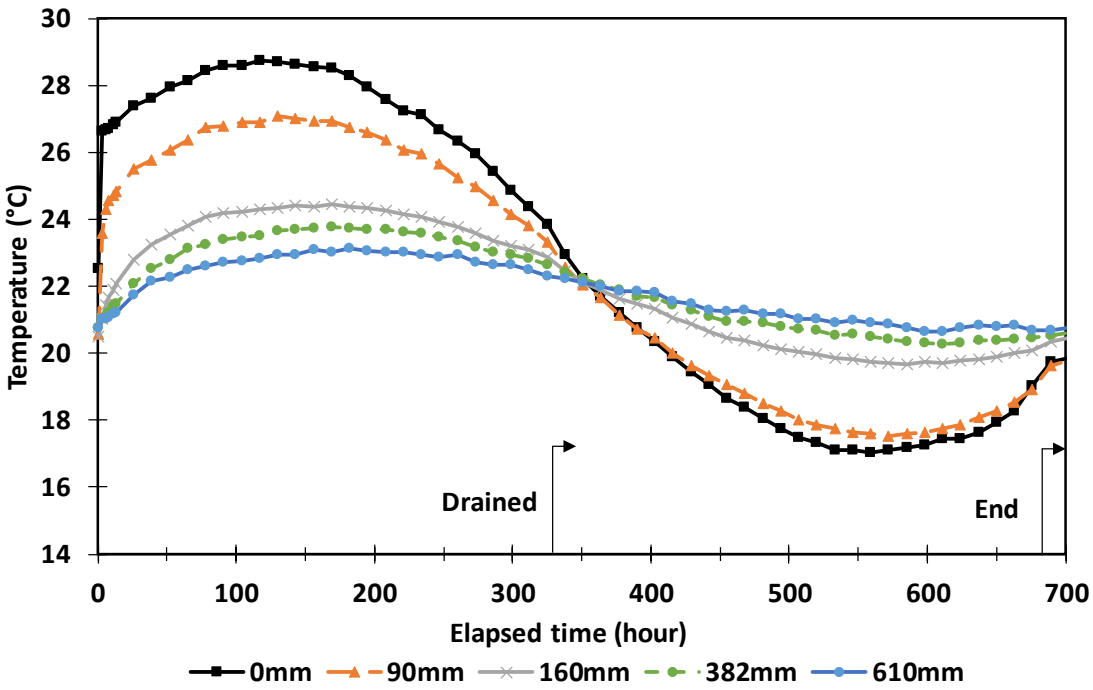

Figure (5.19) Second experimental seasonal test

5.5.3.3 Third sets: seasonal behaviour test including freezing

The surface temperature applied at the soil surface is completely different in this test as the charging period is fixed at a relatively high temperature (35.2 ˚C) for the charging period and a relatively low temperature (-8.0 ˚C) discharging period.

The objective of this test was to study the effect of latent heat and freezing on shallow geothermal systems and to test the whole system under a more extreme temperature range for the discharging period.

Figure (5.20) presents the applied surface temperature (0 mm) and measured temperature at a series of depths. As expected it can be seen that the soil propagate the temperature gradually and smoothly to lower layers of soil.

Also it can be noted that the differences between the thermocouples reading at 45 mm and 90 mm is higher on the charging period (up to 5 ˚C) while it is much lower on the usage period (up to 12.5 ˚C). This is clearly shows that the adaptable insulation layer is working as expected.

Figure (5.21) shows in more detail the temperature variation as the sample freezes in the upper layers. It can be seen that there is limited evidence of so called zero curtain (Thomas *et al.* 2009).

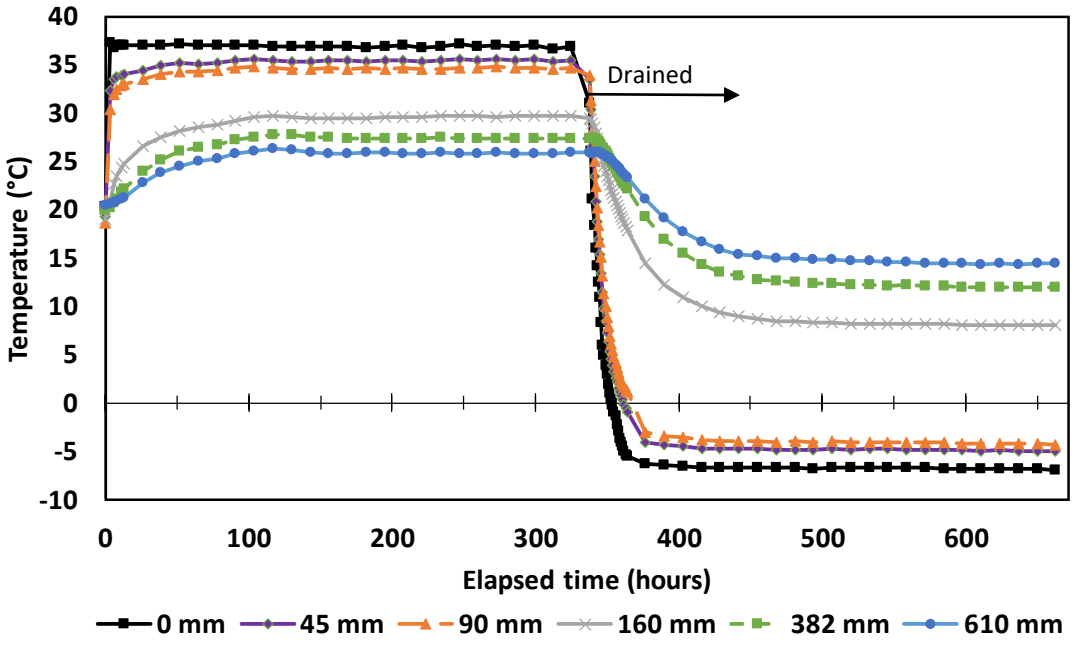

Figure (5.20) Third experimental seasonal test

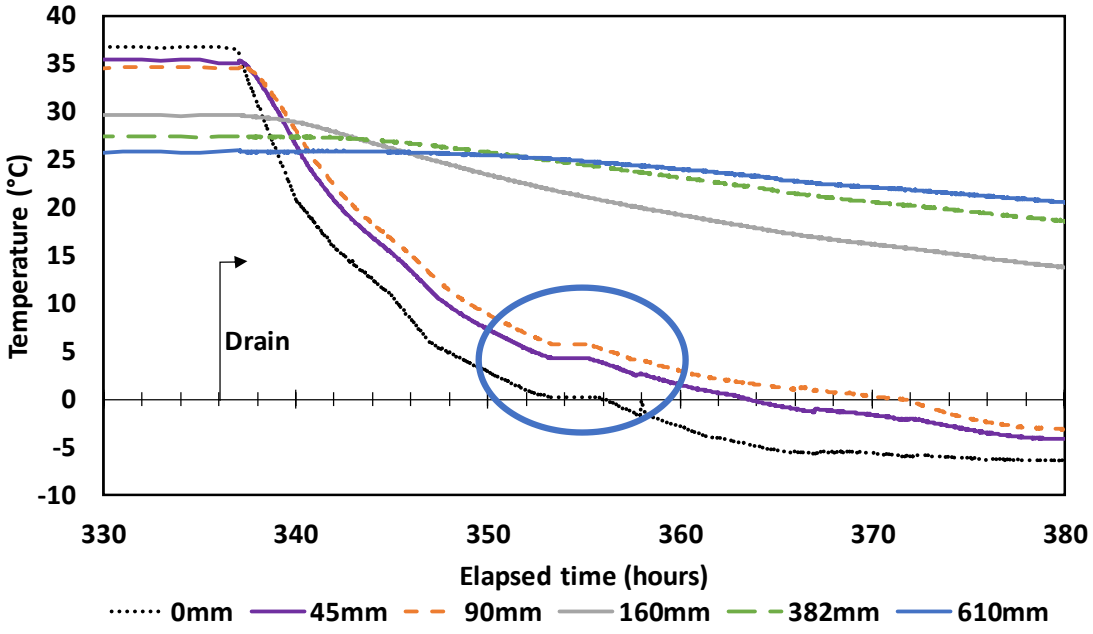

Figure (5.21) Zero curtain in the third experimental seasonal test

The limitation could possibly be related to the fast rate of temperature gradient dropping from the higher extremes or to the low moisture content values at that stage of the experiment.

Moreover, Figure (5.22) shows a comparisons for the reading differences between the central and radial thermocouples, the comparisons would take place over thermocouples installed directly above (90 mm) and below (160 mm) the adaptable insulation layer. It can be seen that there is a radial heat loss towards the side of the acrylic tube with a difference of almost 1 °C between the central and the radial readings for the high temperature while for low temperature the differences goes down to 0.5 °C. On the other hand, for the thermocouples lays beneath the adaptable insulation layer the difference is quiet minimal ~ 0.2 °C.

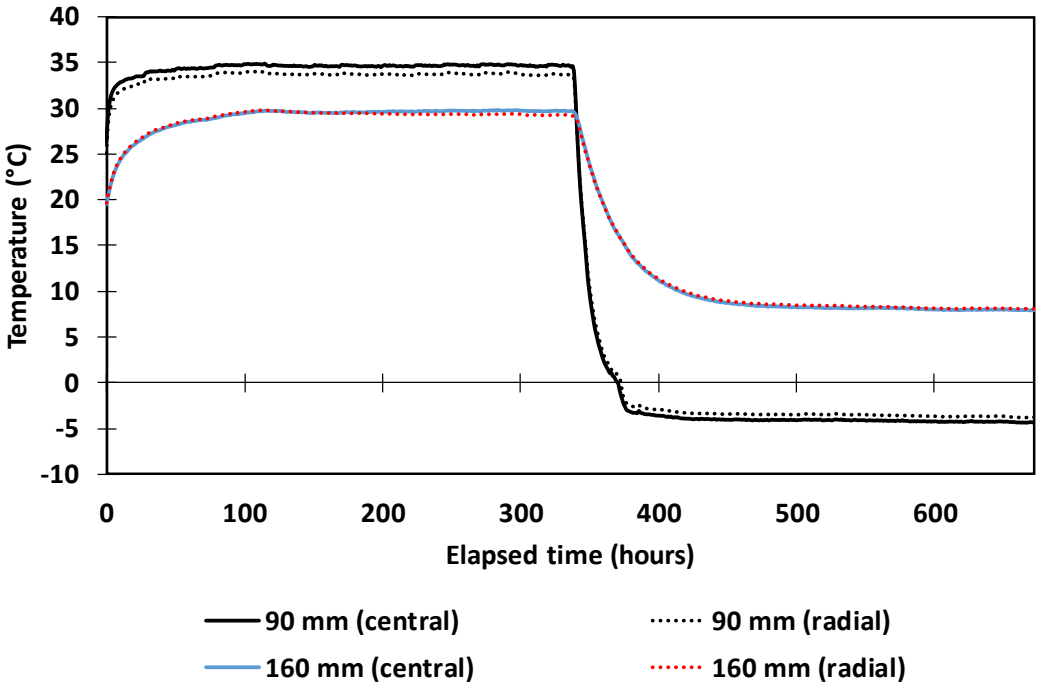

Figure (5.22) Radial heat loss for third experimental seasonal test

Finally, Figure (5.23) shows the experimental temperature profiles with depth of this test with the position of the adaptable insulation layer shown for reference. The effect of the adaptable insulation layer is to allow higher temperatures (and thus more thermal energy) in the charging period compared to the drained conditions. Two days

were chosen to demonstrate the effectiveness of the adaptable insulation layer, the first day (day 14) refers to a fully saturated adaptable insulation layer while the second day (day 17) represent the drained adaptable insulation layer (i.e. three days for the adaptable insulation layer to work under extreme condition). It can be observed that the difference between the top and bottom soil layer while the adaptable insulation layer in saturated condition is 5 °C while even after three days of draining the adaptable insulation layer and applying a freezing temperature at the surface the differences is 14.1 °C, this clearly shows the effectiveness of the adaptable insulation layer. The first and last day (dotted lines) of the experiment is shown for reference.

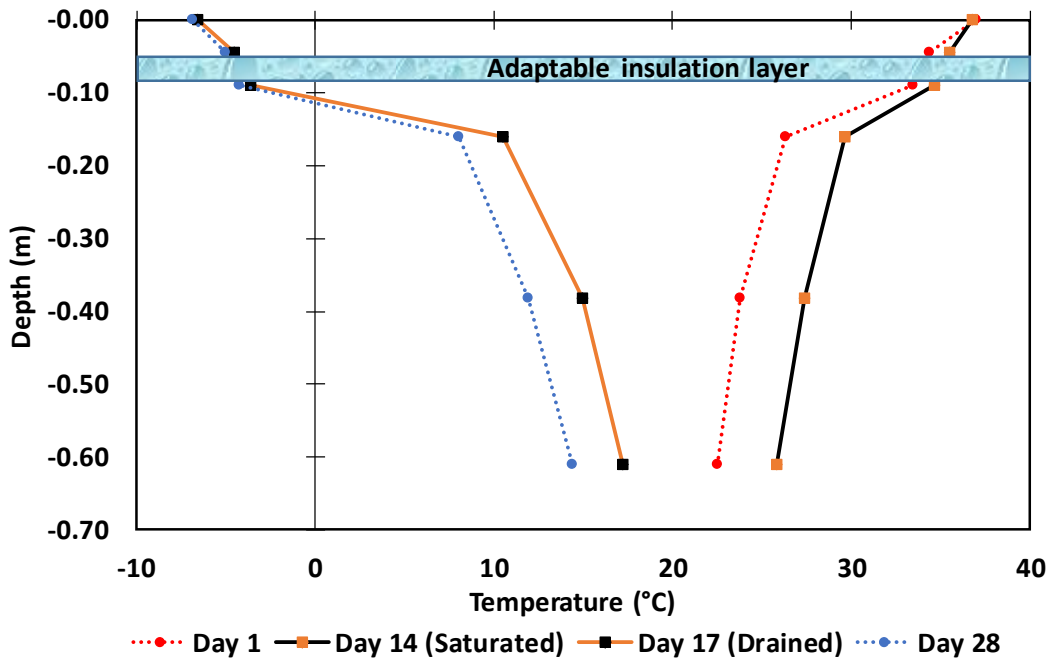

Figure (5.23) Experimental temperature profiles with depth on day 14 and 17 for third seasonal test

5.6 Model validation

In this section, the numerical model presented in Chapter 3 and 4 and selected material parameters are validated using the previously described laboratory experiments. The experimental results used for the model validation are presented earlier in the second trial test and the third seasonal test sections, the former set

include the coated trial test under dry and saturated adaptable insulation layer conditions while the latter set consider the most extreme temperature variations and allow consideration of ground soil freezing.

Material parameters are presented in Table (5.3, 5.4 and 5.5). Where possible properties are prescribed measured or reported values. However, the thermal conductivity of soil and bead was estimated using Equation (3.13) and Equation (3.14) respectively (Haigh 2012 ; Donazzi 1977). In all simulations, a one-dimensional numerical domain was used.

A homogeneous domain discretization of 1024 elements and an hourly time steps has been found to yield converged results. The boundary condition at the soil surface is assumed to be of the first kind varying in time and is based on the temperature applied via the heating/cooling plate.

The bottom of the domain is assumed to be adiabatic (zero thermal flux), representing the presence of the Rockwool insulation at the base of the apparatus.
The domain of the problem replicates the experimental setup presented earlier and is assumed to be composed of five materials (including the two plastic lids used to define the boundaries of the adaptable insulation layer). The initial temperature of the soil column is linearly interpolated from column observations at the beginning of each experiment setup.
As discussed and shown earlier in Figure (5.15) there is a difference in the peak temperature applied at the sample surface in dry and saturated sets of more than 2 °C with the higher temperatures applied under dry conditions.

Parameter	Value	Units	Remarks
$\lambda_{s,beads}$	1.102	(W/mK)	
$\rho_{s,beads}$	2500	(kg/m^3)	
$c_{s,beads}$	1175	(J/kgK)	
n_{beads}	0.343	Dimensionless	measured

Table (5.3) Values of the adaptable insulation layer parameters used in the model (Cospheric 2018)

Parameter	Value	Units	Remarks
λ_s	8.79	(W/mK)	
λ_w	0.57	(W/mK)	
λ_a	0.025	(W/mK)	
ρ_s	2600	(kg/m^3)	measured
ρ_w	1000	(kg/m^3)	
ρ_a	1.25	(kg/m^3)	
c_s	2010	(J/kgK)	
c_w	4186	(J/kgK)	
c_a	1000	(J/kgK)	
n	0.37	Dimensionless	measured

Table (5.4) Soil parameters used in the model (de Vries 1952)

Parameter	Value	Units
$\lambda_{acrylic}$	0.2	(W/mK)
λ_{lid1}	0.22	(W/mK)
λ_{lid2}	0.16	(W/mK)
ρ_{lid1}	1200	(kg/m^3)
ρ_{lid2}	1440	(kg/m^3)
c_{lid1}	1200	(J/kgK)
c_{lid2}	900	(J/kgK)

Table (5.5) Values of the other parameters used in the model

(Engineering tool box 2018)

5.6.1 Initial simulation of trial tests

Figure (5.24) presents the results obtained from the numerical model assuming zero heat losses and using thermal properties presented earlier in the previous tables, the top boundary condition used in the model was extracted from the experimental result.

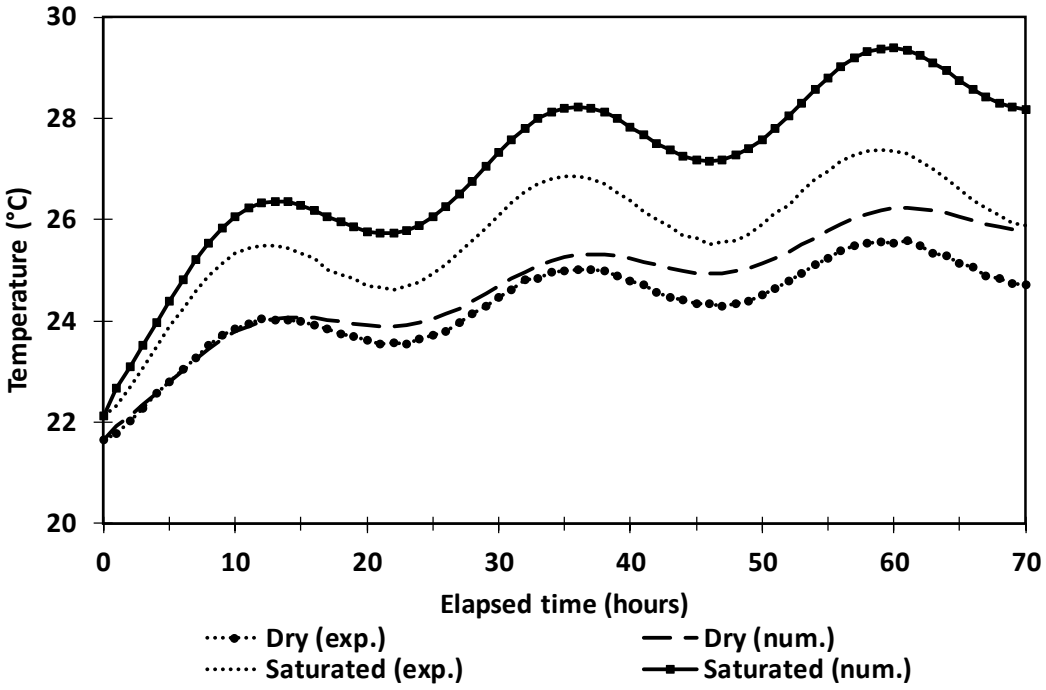

Figure (5.24) Comparisons of experimental and numerical temperature variation (without applying heat loss at 160 mm depth)

It can be seen that in general the model is able to capture the observed behaviour of the experimental system under the adaptable insulation layer. However, under dry conditions the model overestimates temperatures by up to 1.17 °C while under saturated conditions the results overestimate the observations by up to 2.29 °C. Two possible explanations for these differences are: the equations used to obtain thermal properties for the soil and bead are idealized and not completely representative of the experimental system and/or there are heat losses through the column wall that are not accounted for in the numerical model. To consider this latter explanation further heat losses are examined in more detail in the following section.

5.6.2 Heat losses

The need to include heat losses within the numerical analysis identified in the previous section is addressed here to explore the possibility of radial heat loss. The inclusion of radial heat loss in the numerical analyses is achieved via a radial heat flux term defined as:

$$q = h\,(T - T_{room}) \tag{5.1}$$

where h (W/m^2°C) is a volumetric heat transfer coefficient related with the radial soil heat conductivity and convective heat transfer coefficient at the column wall, T_{room} (°C) is room temperature (an average of 21.8 °C was used for the temperature controlled laboratory – more details will follow).

In order to derive the volumetric heat transfer coefficient for a cylinder with a very large length compared to diameter Figure (5.25), the heat flow is assumed to be only in a radial direction. Fourier's law is used by inserting the proper area relation for heat flow in the cylindrical system as follows:

$$A_r = 2\pi\, rL \tag{5.2}$$

so that Fourier's law is written:

$$q_r = -\lambda A_r \frac{dT}{dr} \tag{5.3}$$

or

$$q_r = -2\pi\, rL\lambda \frac{dT}{dr} \tag{5.4}$$

with the boundary conditions of $T = T_i$ or T_e and $r = r_i$ or r_e; the solution to Equation (5.4) is given by:

$$q = 2\pi\, \lambda L \frac{T_i - T_e}{\ln(r_e/r_i)} \tag{5.5}$$

where r_e (m), and r_i (m) are the column exterior and interior radii respectively, T_e (°C) and T_i (°C) are the exterior and interior temperatures.

and the thermal resistance in this case is equal to

$$R_{th} = \frac{\ln(r_e/r_i)}{2\pi\, \lambda L} \tag{5.6}$$

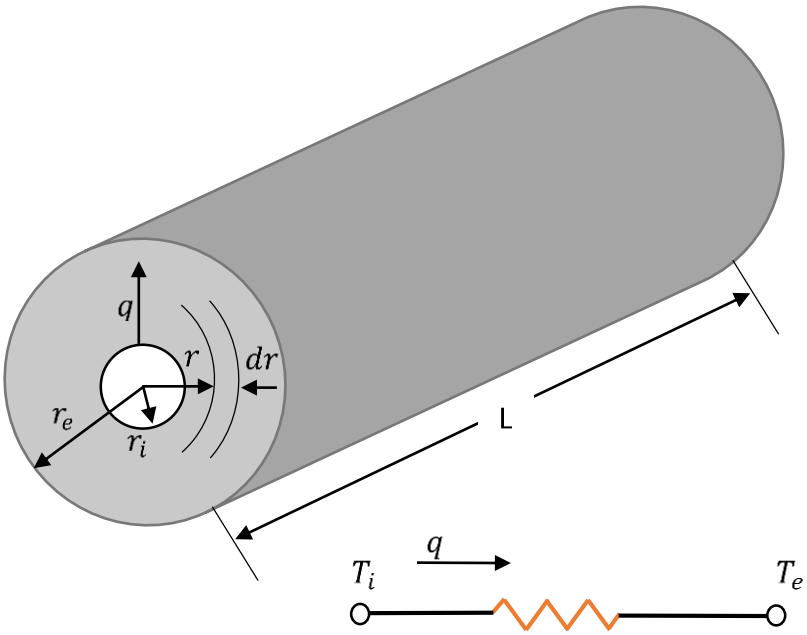

Figure (5.25) Heat flow through a hollow cylinder and electrical analog

The thermal-resistance concept may be used for multiple-layer cylindrical walls (e.g. the experimental setup) just as it was used for plane walls. For the two-layer system shown in Figure (5.26) the value of h equal to 7.64 W/m^2°C was used, which was obtained through adding the thermal resistance of the surfaces covering the soil column volume (i.e. acrylic and Rockwool as shown in Figure (5.26), the obtained equation shown in (5.7):

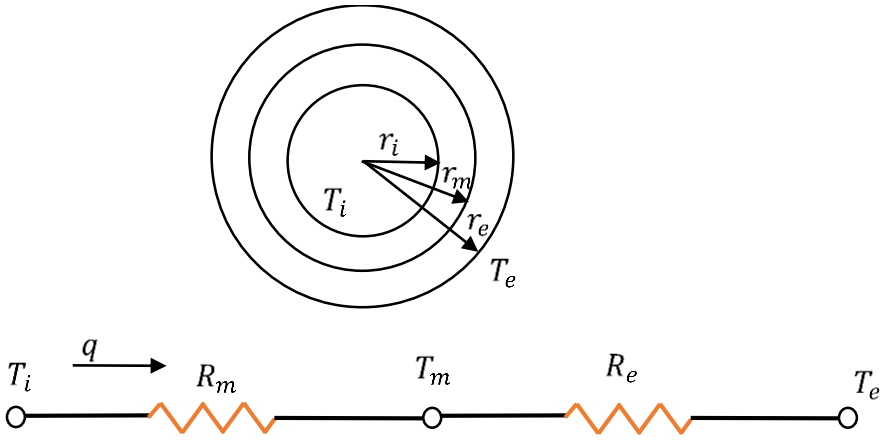

Figure (5.26) heat flow through a multiple cylindrical sections and electrical analog

$$h = \frac{2\pi}{A\left[\frac{\ln\left(\frac{r_e}{r_m}\right)}{\lambda_{rockwool}} + \frac{ln\left(\frac{r_m}{r_i}\right)}{\lambda_{acrylic}}\right]} \tag{5.7}$$

where A (m^2) is the cross-sectional area of the soil column (no radial insulation), r_m (m) is the column middle radius, $\lambda_{rockwool}$ (W/mK) is the Rockwool insulation thermal conductivity and $\lambda_{acrylic}$ (W/mK) is the acrylic tube (containing the sand column) thermal conductivity.

Equation (5.1) is used to estimate the thermal heat losses of the soil column which are then applied as an internal heat generation/loss term in the 1D heat transfer equation.

Equation (5.7) implicitly assumes a maximum heat transfer coefficient between the column surface and the room air thus giving maximum heat losses for the considered case. The results of the analyses including heat losses are presented in Figure (5.27).

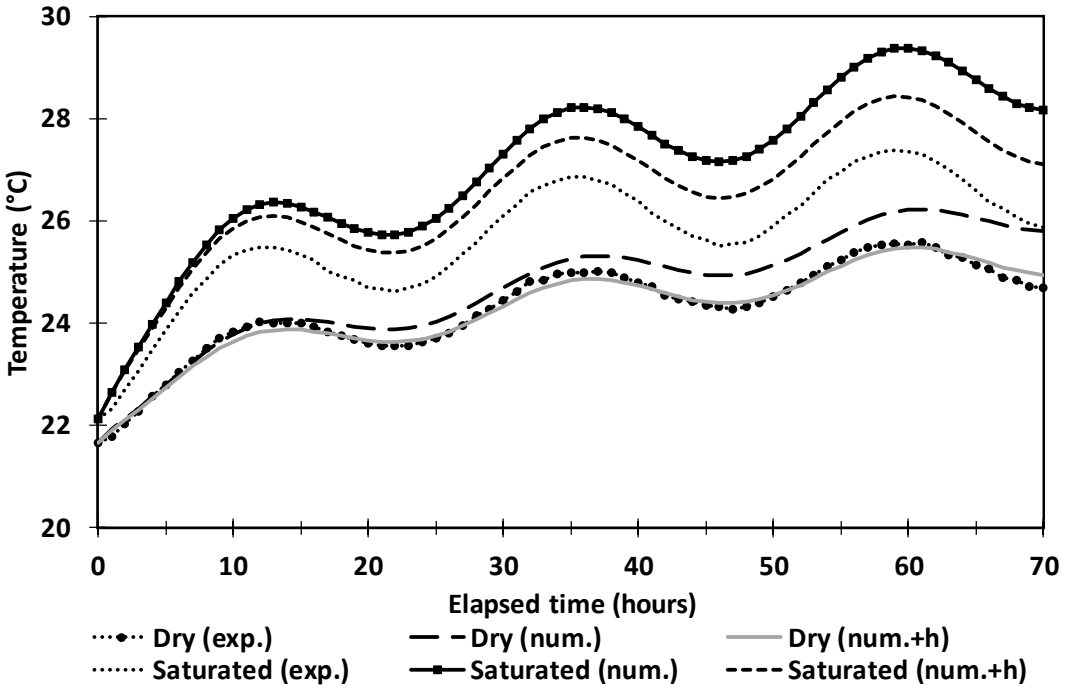

Figure (5.27) Comparisons of experimental and numerical temperature variation (with the application of heat loss effect at 160 mm depth)

It can be seen that the changes due to heat losses estimated in this way in the numerical results successfully capture the behaviour in the dry case and significantly improved the saturated as it reduces the difference to 0.9 °C. Based on these results the heat loss was chosen for all subsequent analyses.

On the other hand, Figure (5.28) shows numerical and experimental temperature profiles with depth at the peak of the second experiment cycle (30 hours). The position of the adaptable insulation layer is shown for reference.

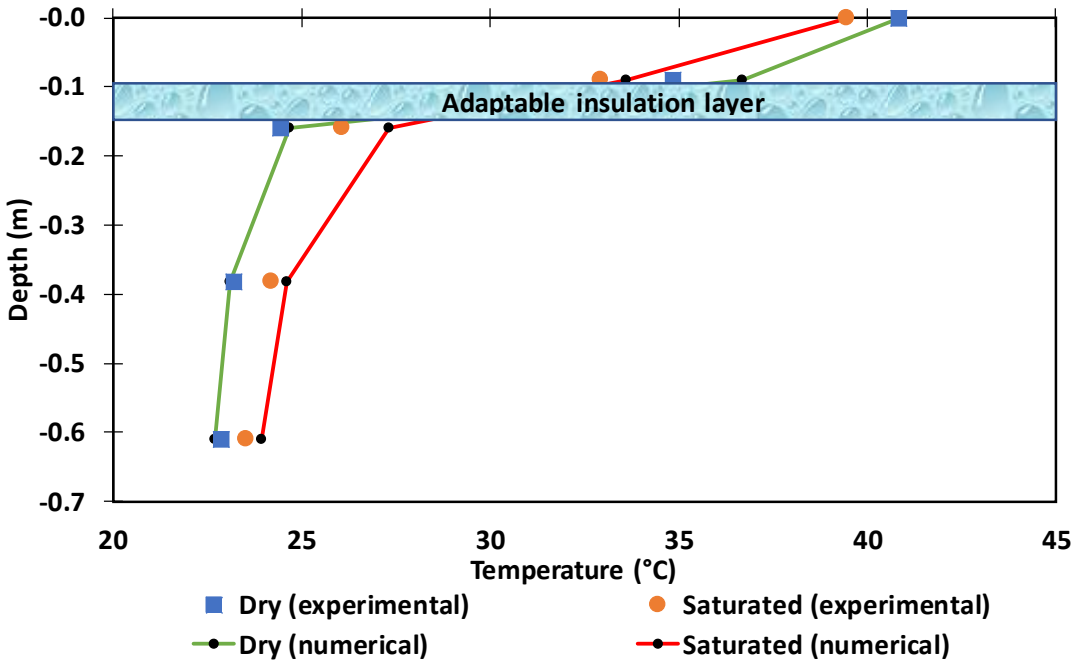

Figure (5.28) Numerical and experimental temperature profiles with depth at the peak of the second experiment cycle (hour 30) (2nd preliminary trial sets)

It can be seen the effect of the adaptable insulation layer on the experimental observations is to allow higher temperatures (and thus more thermal energy) in the saturated case compared with dry conditions.

The numerical results capture this behaviour slightly underestimating the temperatures under dry conditions (a maximum difference of 1.59 °C with experimental observations at 90 mm, 0.2 °C in the rest of the column) and in general offering a good match under saturated conditions (a maximum difference of 0.7 °C

with experimental observations at 160 mm). This could mean that the model offers an idealized representation of the experiment, especially for the thermal properties of the different layers present in the column. However, these analyses sufficiently validate the model for use as a tool to explore hypothetical situations.

It is important to note that all of the experiments are conducted in a temperature controlled room, however the temperature was not always fixed as shown in Figure (5.29) which presents a sample of the laboratory temperature during the first seasonal test, generally speaking the temperature varies between 20 to 22 °C).

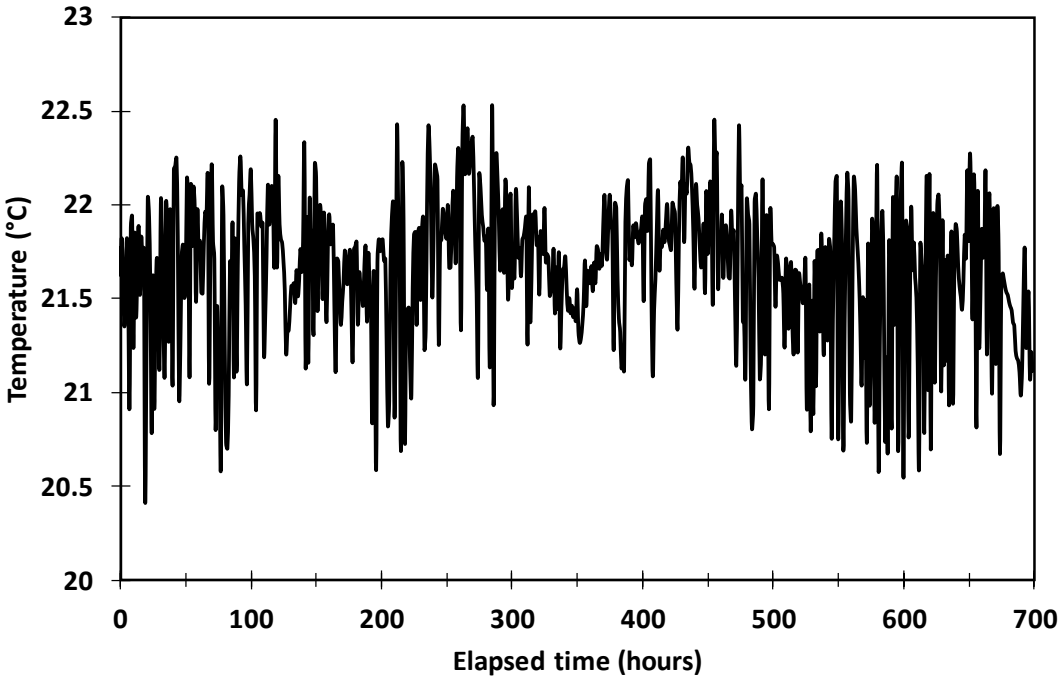

Figure (5.29) Sample of recorded room temperature variation (1st seasonal test)

In order to overcome this issue, the recorded experimental room temperatures were included in the numerical analyses via equation (5.1) for all conducted tests. A further simulation has been undertaken to check the validity of the approach by considering the first seasonal test. Figure (5.30) presents results of a comparison for first seasonal test against the numerical model with the application of heat loss.

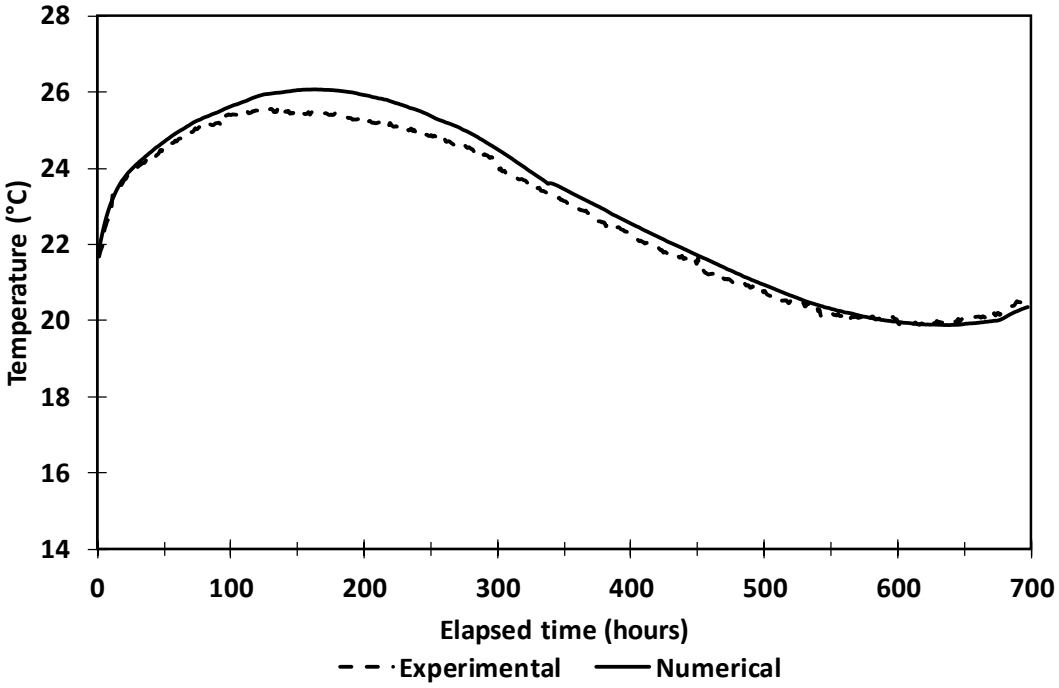

Figure (5.30) Comparisons of experimental and numerical temperature variation (with the application of heat loss effect at 160 mm depth)

5.6.3 Simulation of third seasonal test and consideration of latent heat effects

When the temperature of a soil sample drops below the freezing point of liquid water, a change of phase will occur and sufficiently heat energy if lost all the liquid water will change phase and ice will be present throughout the soil pores.

As this process takes place, a considerable amount of energy is released before the temperature in the sample continues to drop. This energy is known as the latent heat of fusion. Consideration of latent heat has been presented in the theoretical framework earlier in Sections 3.5 and to verify that it had been correctly implemented in the model a hypothetical flux value of -100 W/m^2 was applied at the soil surface. The reason for choosing this specific value was to mimic the surface fluxes on snow surfaces which is usually subjected to those values (Marco and Jacyra 2016).

All other detail of the simulations including remaining boundary conditions, domain dimensions and thermal properties used in the other simulations presented in this

chapter were used in this comparison. Spatial and temporal discretisation were obtained after a thorough investigation to ensure converged results were obtained.

Comparison of changes is total heat energy in the computational domain (obtained by integrating temperature and heat capacity over the total domain) and the extractive heat flux confirmed that latent heat effect were correctly represented. Figure (5.31) shows the comparisons between the results obtained from the third test and the numerical program.

It is clear that between 360 and 375 hours the presence of the so called 'zero curtain' where the latent heat of fusion is being removed with little or no change in temperature of the system.

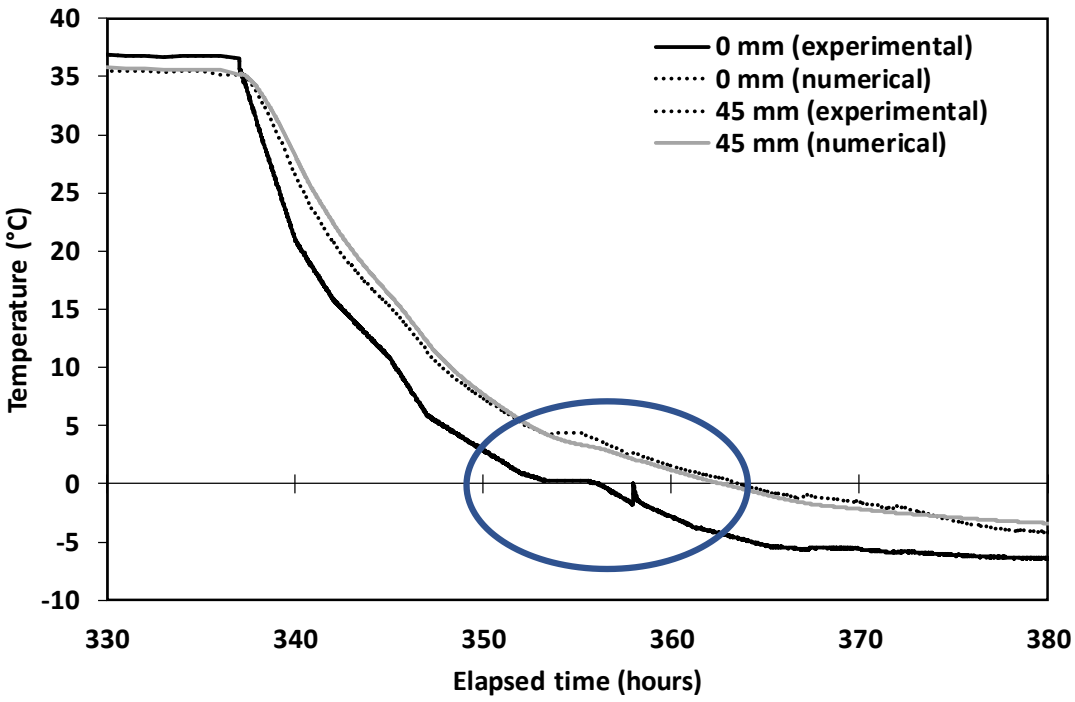

Figure (5.31) Zero curtain in model validation

The good correlation between the experimental and simulated temperatures achieved in this exercise confirm the ability of the numerical model to account for the latent heat of fusion associated with freezing in the soil systems.

Finally, Figure (5.32) shows the experimental and numerical results for this test for the first and last day of the experiment. Easily seen that even with an extreme temperature applied at the soil surface for quiet an extensive period (14 days), the base of the apparatus maintains a temperature of almost 15 °C.

Moreover, the temperature difference on the two sides of the adaptable insulation layer is almost 12 °C and it can be noticed that even when the temperature at 90 mm (immediately above the adaptable insulation layer) is almost -4.5 °C, the temperature at 160 mm (immediately below the adaptable insulation layer) was 8 °C. This behaviour over the two sides of the adaptable insulation layer clearly shows that the layer is working as it is expected to be.

These analyses sufficiently validate the model for use as a tool to explore other different case scenarios.

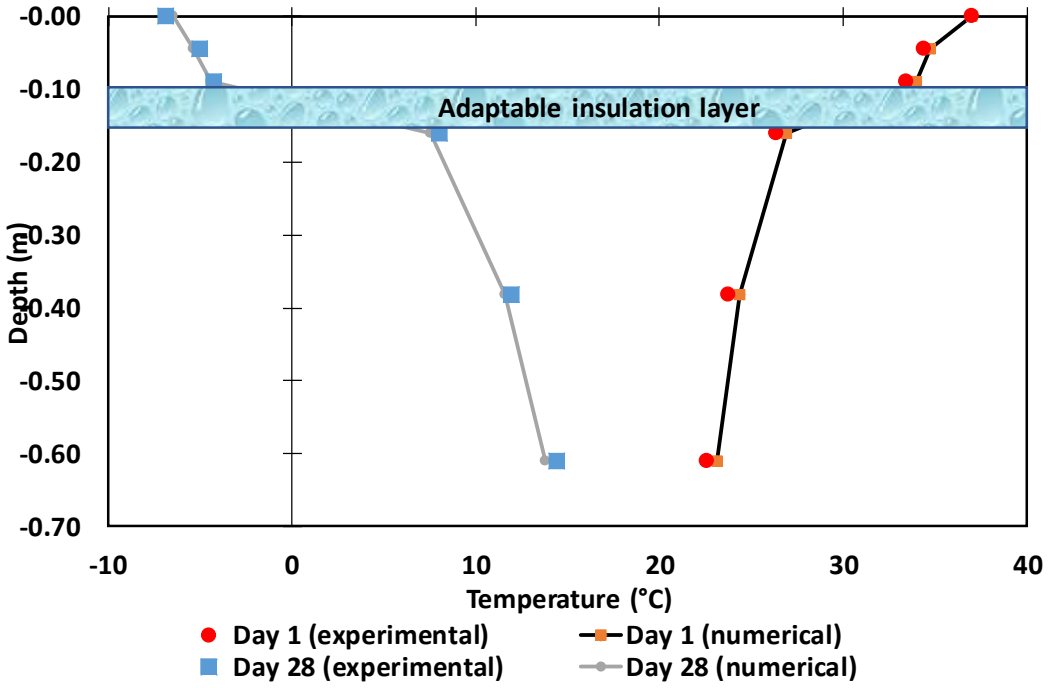

Figure (5.32) Numerical and experimental temperature profiles with depth for the first and last day of experiment for the 3rd seasonal test

5.7 Conclusions

This chapter reported the successful design, fabrication and calibration of the new experimental test setup with each of the defined design criteria met. Furthermore, the accessories and sensors work perfectly fine in conjunction with the new setup. The new setup shows the possibility of creating a much simpler form of heat storage systems other than the typical ones.

The experimental approach and methodology was developed and defined which includes the soil preparation, assembling and dismantling to perform the thermal tests. Five different main test results were introduced and differences between each test and the rationale behind each individual one has been also highlighted. The early two set of tests includes a trial tests which will provide basis for forecoming ones while the other three seasonal tests were performed later to observe the system behaviour over long and extreme conditions. The experimental results clearly shows the potential of the proposed system and its ability.

In this chapter, the experimental results obtained has been presented. The differences between each test and the rationale behind each individual one has been also highlighted. The proposed numerical model predictions have been validated against the experimental results. A very good approximations was achieved and the model proved to be able to capture the experimental results correctly.

A very important aspect of this chapter was to observe the latent heat of fusion numerically and experimentally. It is clear that between 360 and 375 hours the presence of the so called ‘zero curtain’, where the latent heat of fusion is being removed with little or no change in temperature of the system. The good correlation between the experimental and simulated temperatures achieved in this exercise confirm the ability of the numerical model to account for the latent heat of fusion associated with the ground freezing in the soil systems.

The model ability to capture the 'zero curtain', where the latent heat of fusion is being removed with little or no change in temperature of the system has been validated as well.

5.8 References

Cospheric. 2018. *Microspheres, spheres, and nanospheres - World wide* [Online]. Available at: http://www.cospheric.com/Solid-Soda-Lime-Glass-Polished-Spheres-2-5g-cc-Prcision-Grades-0_7mm-to-5mm.htm [Accessed: 26/01/2018].

de Vries, D. A. 1952. The thermal conductivity of soil. *Mededelingen van de Landbouwhogeschool te Wageningen.* 52(1), pp. 1952:1951-1973. DOI.

Donazzi, F. ed. 1977. *Soil thermal and hydrological characteristics in designing underground cables*. Proceedings of the Institution of Electrical Engineers.

Engineering tool box. 2018. *Resources, Tools and Basic Information for Engineering and Design of Technical Applications* [Online]. Available at: https://www.engineeringtoolbox.com/ [Accessed: 26/01/2018].

Haigh, S. K. 2012. Thermal conductivity of sands. *Géotechnique.* 62(7), pp. 617-625. DOI: 10.1680/geot.11.P.043.

Marco, A. and Jacyra, S. 2016. Diurnal variation of soil heat flux at an antarctic local area during warmer months. *Applied and Environmental Soil Science*. 2016(2016), p. 9. DOI: 10.1155/2016/1769203.

Thomas, H. R., Cleall, P. J., Li, Y.-C., Harris, C. and Kern-Luetschg, M. 2009. Modelling of cryogenic processes in permafrost and seasonally frozen soils. *Géotechnique.* 59(3), pp. 173-184. DOI: 10.1680/geot.2009.59.3.173.

Chapter 6: Large-Scale Application - Including Modelling Surface Snow Condition

6.1 Introduction

This chapter presents results obtained using the model presented in Chapter 3 and 4, that can represent and solve the transient heat transfer processes in relation to geoenvironmental energy storage system. In particular, it investigates the presence of different factors that can affect the behaviour of such systems including surface snow and ground freezing. The process of heat collection from external sources and the storage in the soil mass and its reverse cycle were simulated following the work of Muñoz-Criollo (2014) who propose a 2D model that can represent the pipe heat exchangers, however, the model was found to be incapable of dealing with freezing, snow and the correct representation of the soil materials. The proposed model applied in this chapter includes features important key additions to take into account layered systems with all of its elements (solids, water and air) and the availability of freezing or snow in the system.

The proposed numerical model is validated against observed behaviour of an experimental case study carried out by TRL (Carder *et al.* 2008). The objective of the TRL experimental study was to check the feasibility of implementing an inter-seasonal heat storage system beneath a road surface. The benefit of which is the prevention of snow formation on the road surface. The system can also provide clean energy for nearby buildings.

The main objectives of this chapter are:

- To demonstrate a 2D application of the numerical model that can represents the process of heat collection and storage in soil via operational geoenvironmental buried devices composed of pipe heat exchangers.
- To assess the impact surface snow cover has on the thermal performance of a ground storage device.

- To assess the impact of soil freezing has on the thermal performance of a ground storage device
- To assess the combined impact of surface snow and ground freezing on the coefficient of performance of the system.

Furthermore, the chapter will be divided into the following sections:

i. Section 6.2 presents a summary of details and description for the TRL experiment.
ii. Section 6.3 describes how the numerical model is applied and is subdivided as: (i) the material properties used; (ii) description of the domain under consideration with its discretized representation; and (iii) the initial and boundary conditions used to solve the numerical problem.
iii. Section 6.4 presents comparisons of the results of the numerical simulations against the experimental results for selected periods that had been extracted from the full-scale case study.
iv. Section 6.5 provides a conclusion summary for this chapter.
v. Section 6.6 summarized the references used in the chapter.

6.2 Large-scale experiment description (TRL)

The experimental site is located on an access road near Toddington's motorway service station (51.952° North, 0.508° West) over the M1 highway between Junctions 11 and 12 in England, UK (shown in Figure (6.1)). The experimental setup was composed of two configurations each comprising two sets of pipe arrays that works as a collector and storage pipes respectively. Each pipe array was composed of 10 pipes placed near the surface of the ground that act like heat exchangers and were arranged in a U-loop as shown in Figure (6.2), the length of which was of 30 m long by 5 m wide (i.e. road width). In the context of this study, the pipe arrays are referred to either “collector pipes” or “storage pipes” which reflects the depth and use of each.

The collector pipes are those installed close to the surface at 0.12 m depth, directly below the road surface while storage pipes are the ones installed at 0.875 m. The pipes

are made of cross-linked polyethylene with 0.025 m diameter with a spacing of 0.25 m between each adjacent longitudinal run.

The heat carrier fluid that runs in the pipes was a mixture of ethylene glycol and water mixed at a ratio of 1:10. A polystyrene insulation layer with a thickness of 0.2 m was placed on top of the storage pipes to minimize heat losses from the storing banks to the soil surface.

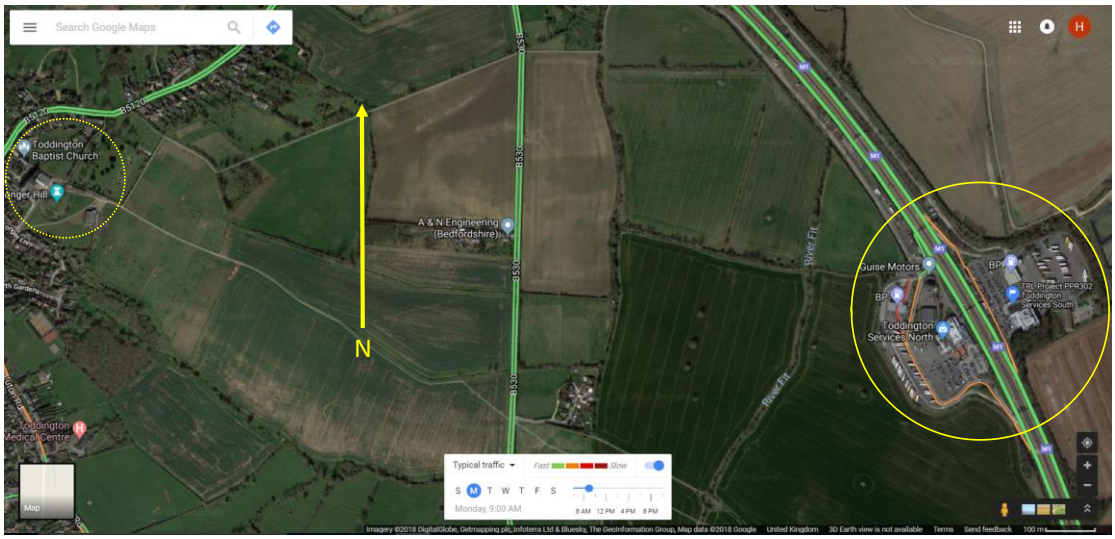

Figure (6.1) Location of Toddington service station (solid line circle), Motorway M1 (highlighted in green) and the location of Toddington (dashed circle) are also shown for reference (Google Maps 2017)

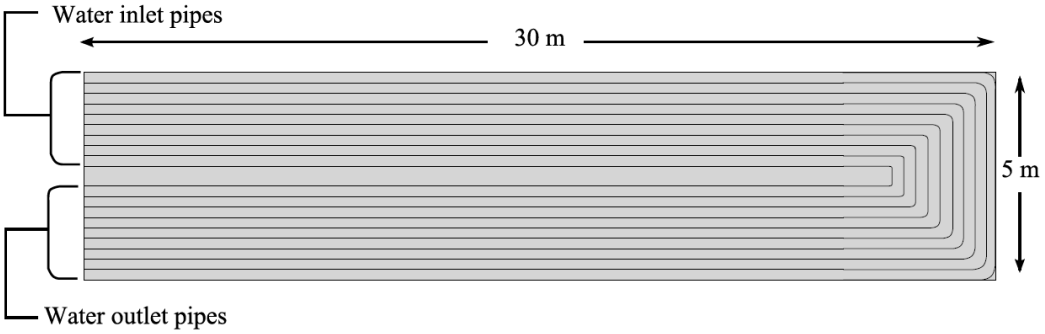

Figure (6.2) Schematic distribution of pipes in the collector and storage arrays, the exchanger arrays are 30 m long by 5 m wide (figure not to scale) (Carder *et al.* 2008)

Furthermore, the experiment consists of two different systems that relate to the storage pipe location. One system has both the storage pipes and the insulation layer placed directly under the collector pipes (i.e. all system elements were placed under the road surface), while the other have them placed at the same depth, but located next to the road. The reason for such installation was to explore the different feasibility of installing the inter-seasonal system. The former (referred to as "System 2") is thought to be useful for newly constructed roads because it is relatively easy to layer the whole system under the road. The latter (referred to as "System 1") is more suitable for already built roads where it is relatively cheaper to remove only the upper most road layers (e.g. maintaining the road) to install the collector pipes and excavate next to the road to install the storage pipes.

Figure (6.3) shows the general layout of the experimental systems while Figure (6.4) and Figure (6.5) presents transverse sections of each system showing the distribution and thickness of the different material layers present in each configuration. The used material layers are defined as follows:

1. Thick wearing course (35 mm).
2. Thick binder course (70 mm).
3. Thick concrete screed (55 mm).
4. Collector pipe array.
5. (a) Thick new lean concrete base (165 mm).
5. (b) Thick type 1 granular material (200 mm).
5. (c) Thick existing cement bound material (240 mm).
6. Thick polystyrene insulation (200 mm).
7. Thick sand overlying pipework (150 mm).
8. Store pipe array.
9. Backfill from original excavation.

Although not shown in Figure (6.4), a slope existed to the west of the road and the insulation layer of System 2 needed to be adjusted properly to overcome this issue.

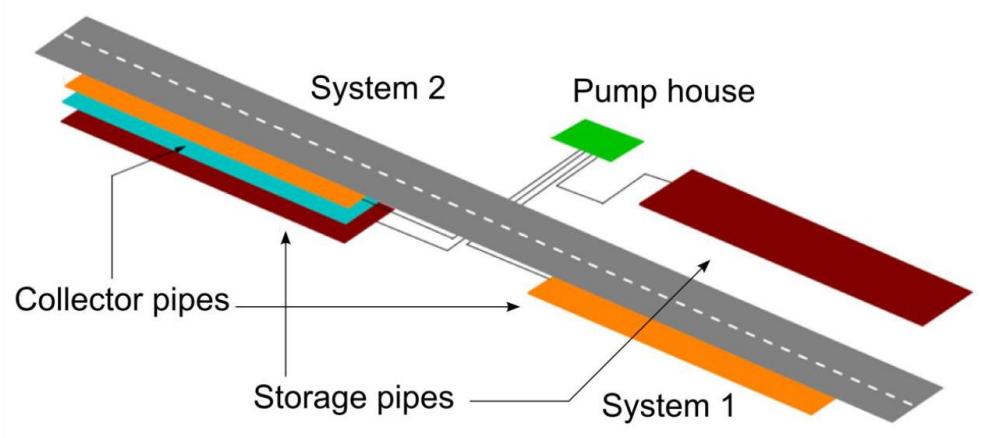

Figure (6.3) 3D schematic distribution of pipes showing the layout of the trial (Carder *et al.* 2008)

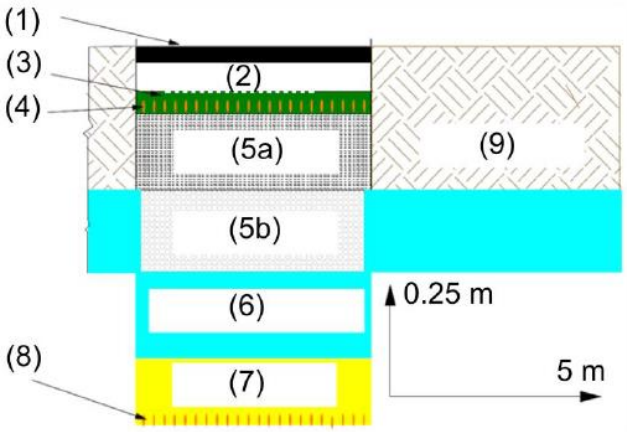

Figure (6.4) Distribution of layers in experimental System 2 (Carder *et al.* 2008)

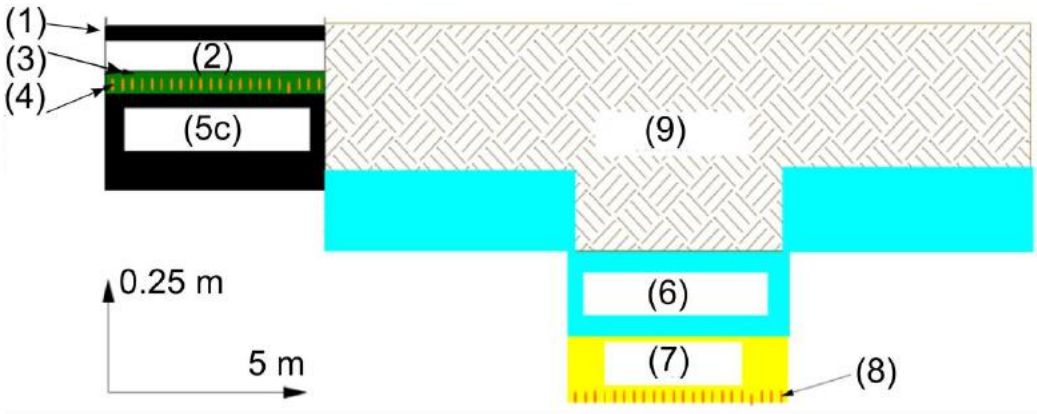

Figure (6.5) Distribution of layers in experimental System 1 (Carder *et al.* 2008)

6.2.1 Site layout and instrumentation

Many temperature sensors were installed at the experimental site in order to record data related to the system performance. Two control boreholes labelled 'A' and 'B' were drilled to the north and south of the construction zone so as to record the soil temperature profile. In each of these boreholes a set of temperature sensors were installed at different depths namely: 0.025, 0.125, 0.825, 0.875, 1.025, 1.175, 1.375, 1.875, 3.875, 7.875 and 12.875 m. Another additional control borehole was drilled half way between the experimental systems to record the undisturbed temperature variations under the road surface (labelled as borehole 'F'). In this borehole, the temperature sensors were installed at the following depths: 0.875, 0.925, 0.975, 1.025, 1.175, 1.375, 1.875, 2.875, 3.875, 7.875 and 12.875 m. With the same distribution of sensors, six additional boreholes were drilled under the locations of the experimental systems, three for each one. The location of these boreholes, labelled C, D, E, G, H, I, and of the control boreholes are shown in Figure (6.6).

Additionally, temperature sensors were placed near the surface of boreholes G and F and at centre of collector 1 at depths of 0.01, 0.025, 0.075 and 0.1 m. These sensors recorded the temperature of the road surface during the execution of the experiment at the centre of each system and at a control zone. Additional flow meters, temperature sensors and strain gauges were distributed; however, data from these measurements were not used for the purposes of this work.

6.2.2 Data summary

As discussed earlier, TRL placed several temperature sensors through the experimental site in order to monitor the transient behaviour of the experimental systems modes of operation in summer and winter. In addition, their report (Carder *et al.* 2008) includes the main thermal properties of the soil (based on literature) which summarized in the following sections. Furthermore, a meteorological station was installed on the site to record weather data during the time of experiment.

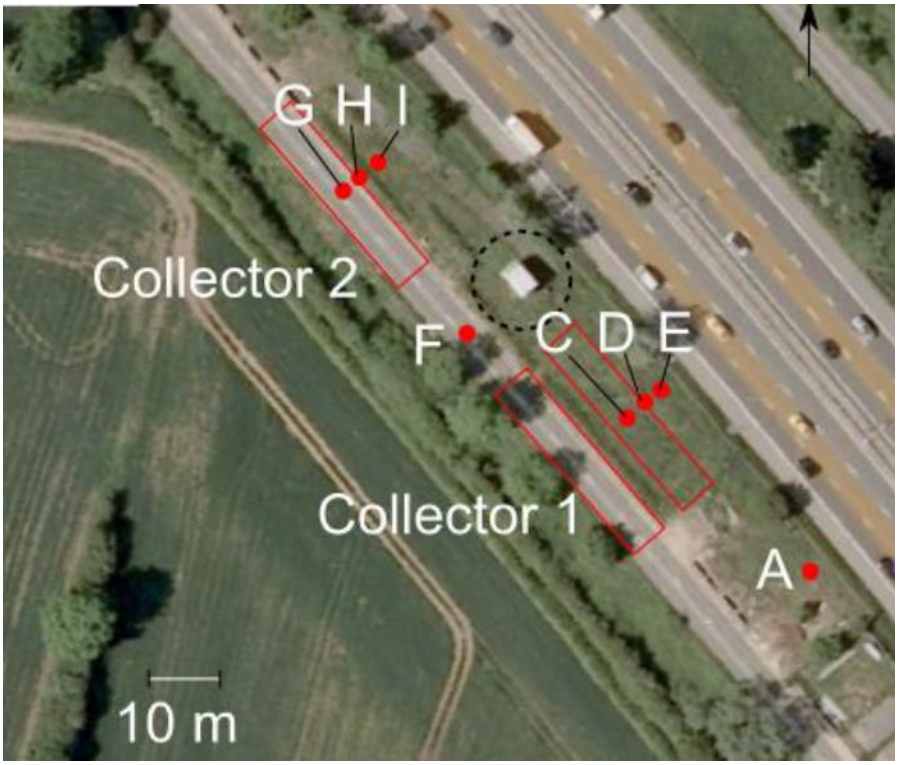

Figure (6.6) Positions of boreholes with temperature sensors on the experimental site (borehole B is not shown)

6.2.2.1 Material properties

Carder *et al.* (2008) describe the composition of the site as a stiff grey clay soil from 3 m to 25 m depth while on both road sides, the gault clay is overlain by a layer of firm silty clay, although a final layer of reworked gault clay of 0.8 m is existed at the west side of the road.

Table (6.1) shows the material properties provided by TRL (Carder *et al.* 2008). The material properties were derived from: (i) suppliers (in the case of the polystyrene insulation), (ii) calculations based on constituents (in the case of the asphalt), (iii) obtained from Phoenics 3.5.1 package (in the case of concrete) and (iv) the literatures (for others).

Table (6.2) on the other hand, summarizes the relevant geometrical and material data of the pipe systems and thermal properties of the fluid used as a heat carrier.

Code	Material type	Density (kg/m^3)	Specific heat (J/kgK)	Thermal conductivity (W/mK)
1	Wearing course	2400	850	0.85
2	Binder course	2400	850	0.85
3	Concrete screed	2100	840	1.4
5a	New lean concrete base	2100	840	1.4
5b	Type 1 granular material	2100	840	1.4
6	Polystyrene insulation	30	1130	0.034
8	Sand	2240	840	0.33
9	Clay	1960	1227	1.21

Table (6.1) Material parameters used in this study (Carder *et al.* 2008)

Internal pipe diameter (m)	0.0227
External pipe diameter (m)	0.0250
Thickness of pipe wall (m)	0.0023
Length of pipes (straight sections) (m)	60
Number of pipes per heat exchanger	10
Pipe thermal conductivity (W/mK)	0.4
Flow rate (l/s)	1.41
Fluid composition	90 % water, 10 % ethylene glycol

Table (6.2) Pipe system data provided by TRL report (Carder *et al.* 2008)

6.2.2.2 Meteorological data

As stated in Section 6.2.2 a weather station was installed on the experimental site to monitor the weather variations. The benefits of having such a system is to relate the recorded weather data to the overall transient behaviour of the experimental systems. This station recorded the main meteorological variables data: air temperature, relative humidity, wind speed (including wind direction and standard deviation of wind direction), solar radiation and rainfall.

The station was recording data every five minutes starting from August 2005 until September 2007. During which the system kept logging except December 2016 and during 2007 where it seems that it has been stopped or failed as there are no data available for such periods. Nevertheless, data for most of the relevant periods when the systems were active are available and used as input data in the numerical model proposed in this study.

6.2.2.3 Temperature data

Similarly, soil temperature data were recorded for the boreholes stated on Figure (6.6). Each borehole is 100 mm in diameter and about 13 m depth with control sensors distributed at various previously presented depths. The sensors were positioned in the boreholes using bentonite pellets with the appropriate addition of water. The available data covers the period starting from August 2005 to September 2007 for all boreholes with a recorded time step of 15 minutes during the whole experiment except for a month during the spring of 2006 when the log system seemed to be stopped or failed. As mentioned before, two temperature sensors at control borehole F (road control borehole) were damaged during installation and data are not available for them. The soil and road temperature data recorded by TRL are used in this work for validation of the numerical model proposed.

6.2.3 System operation

Two operational modes were used to operate the system which related to the different seasons. 'Mode 1' represent the summer mode when the transferred heat was moving from the road surface to the collector pipes carrying out the fluid to the storage pipes to warm the soil surrounding them and use them as a thermal energy deposit. 'Mode 2', on the other hand, represents the winter mode where the cycle was reversed, and the thermal energy stored in the soil was transferred to the storage pipes, carried to the collector pipes, and then used for intended purposes (e.g. heating up the road surface and prevent the formation of snow on its surface). In order to prevent or minimize the heat losses from the thermal energy storage banks, an insulation layer of 0.2 m thick of expanded polyethylene was placed over the storage pipes. The experimental project contains two periods of heat collection and storage during which happens during the late summers of 2005 and 2006, and, another two periods of road heating during the corresponding winters.

The heat carrying fluid was moved through the pipes using control pumps that were connected to temperature sensors located at the centre of each heat exchangers. Whenever the temperature difference between the control sensors located at the

collector and storage was approximately 1.4˚C the pumps were activated while it was turned off when the differences dropped to approximately 0.3˚C.

6.3 Numerical approach

As mentioned earlier the work presented in this chapter is based on the theoretical framework discussed in chapter three and the work of Muñoz-Criollo (2014). Outcomes and recommendations of previous work has been taken into considerations where necessary during the development of the model in an attempt to overcome limitations of the previous work. It is important to note that a coupled analysis of heat and moisture transfer or a 3D model was deemed to be unnecessary for the performance representations of the inter-seasonal system in hand (Muñoz-Criollo 2014). These recommendations were reinforced with the fact that the current analysis is focused on a part of soil that has a nearly impermeable insulation layer near the surface (pavement) and an impermeable one within it (insulation layer), also, that the 3D model provides unnecessary needed accuracy. Following that, an uncoupled 2D numerical analysis using the heat transfer equation has been performed.

"System 2" was chosen as an experimental case study due to its complexity as all of the system components located under the road which offers a more challenging problem in terms of model validation. Muñoz-Criollo (2014) performed a soil laboratory experiments on a sample collected from "System 2" and found that the soil compositions surrounding it was a silty clay. The material properties of the soil were assumed to be homogeneous and are presented (along with those of the different layers composing "System 2") in Table (6.1). The code numbering in the table is related to the numbers shown in Figure (6.4).

6.3.1 Model summary

The model was compared against the measured performance of the inter-seasonal heat transfer system. As noted in Chapter 4 the numerical solution of the 2D model in the context of this study has been developed using the Galerkin weighted residual finite element method to solve the transient heat transfer equation. Time

discretisation is achieved following Rothe's method via a Crank–Nicholson scheme. A publicly available open source finite element library Deal.ii was used to implement the numerical method and solve the system of equations (Bangerth *et al.* 2013).

In order to calculate the surface heat flux in each time step, the implementations of the heat balance equations presented earlier in Section 3.8 was used. Depending on the surface type (whether it was bare soil, pavement, vegetation canopy or snow) the related equation and its subsequent parameters were used accordingly. The equations were solved using Newton's method, as suggested by Deardorff (1978) due to its non-linearity because of the longwave and latent heat transfer fluxes.

For the purpose of modelling, pipes in collector and storage arrays are idealized in 3D as shown in Figure (6.7) with each consisting of a flow and return sections. For collector pipes $T_{cf,i}$ (K), $T_{cf,o}$ (K) corresponds to inlet and outlet temperatures in the flow section while $T_{cr,i}$ (K), $T_{cr,o}$ (K) corresponds to inlet and outlet temperatures in the return section. The heat flux rate from the flow and return sections of collector and storage pipes are referred to as q_{cf} (W/m^2) q_{cr} (W/m^2) q_{sf} (W/m^2) and q_{sr} (W/m^2) respectively.

In order to solve the 2D numerical problem, suitable values for the heat fluxes on the flow and return sections of the pipes need to be estimated. The algorithm used in this practice is based on the work of Muñoz-Criollo (2014) with the following assumptions:

- There are two possible states for the system: ON and OFF in each time step which depends on activation criteria defined in Section 6.3.4.
- The soil-pipe boundaries q_{cf}, q_{cr}, q_{sf} and q_{sr} is set to zero when the system is OFF.
- If the system is ON, q_{cf}, q_{cr}, q_{sf} and q_{sr} would be estimated using the following algorithm, however, an additional assumptions needs to be made: (i) the soil in direct contact with the pipes is considered to be at constant temperature $T_{s,av}$, during the time step (equal to the average between the previous time step and the current estimation of the time step), (ii) The fluid flowing through the pipes is considered to complete a certain number of flow

cycles, F_c, in the system (collector and storage pipes) in each time step defined by the flow velocity and the length of the pipes. (iii) No heat losses are considered in the transit section between collector and storage arrays.

The 2D algorithm to represent the system under ON conditions is describe as follows:

1. For initial state: If the system was OFF during the previous time step, then $T_{cf,i}$, $T_{cf,o}$, $T_{cr,i}$, $T_{cr,o}$, $T_{sf,i}$, $T_{sf,o}$ $T_{sr,i}$ and $T_{sr,o}$ are assumed to be equal to $T_{s,av}$. If the system was ON then $T_{cf,i}$, $T_{cf,o}$, $T_{cr,i}$, $T_{cr,o}$, $T_{sf,i}$, $T_{sf,o}$ $T_{sr,i}$ and $T_{sr,o}$ are assumed to be equal to the corresponding values for the previous time step. In both cases q_{cf}, q_{cr}, q_{sf} and q_{sr} are initialized to 0.
2. For pipe outlet temperatures: $T_{cf,o}$, $T_{cr,o}$, $T_{sf,o}$and $T_{sr,o}$ are calculated using the overall pipe heat transfer coefficient U_p presented in Equation (3.30).
3. For pipe inlet temperatures: from the geometry shown in Figure (Added later), the following consideration to be made: $T_{cr,i} = T_{cf,o}$ and $T_{sr,i} = T_{sf,o}$. On the other hand, for $T_{cf,i}$ and $T_{sf,i}$ these are equal to $T_{cr,o}$ and $T_{sr,o}$ or to the averages of the corresponding temperatures in a pipe arrangement (i.e. the fluid is mixed at the inlet of the heat exchanger).
4. For pipe heat fluxes: q_{cf}, q_{cr}, q_{sf} and q_{sr} are calculated using the pipe effectiveness ε_p presented earlier in Equation (3.39).
5. Steps 1-4 are repeated until the required number of flow cycles F_C is achieved. Corresponding pipe heat fluxes are added to q_{cf}, q_{cr}, q_{sf} and q_{sr}.

When the required number of flow cycles F_C is completed, the heat fluxes are averaged by F_C. Averaged values for q_{cf}, q_{cr}, q_{sf} and q_{sr} are used as boundary conditions at the soil-pipes boundaries and the numerical problem is solved and a new estimation for $T_{s,av}$ is obtained.

The previous algorithm is repeated until the difference between the current and previous estimation for $T_{s,av}$ is less that a suitable convergence criteria δ.

Figure (6.8) presents a flow diagram of the proposed algorithm to calculate surface heat fluxes.

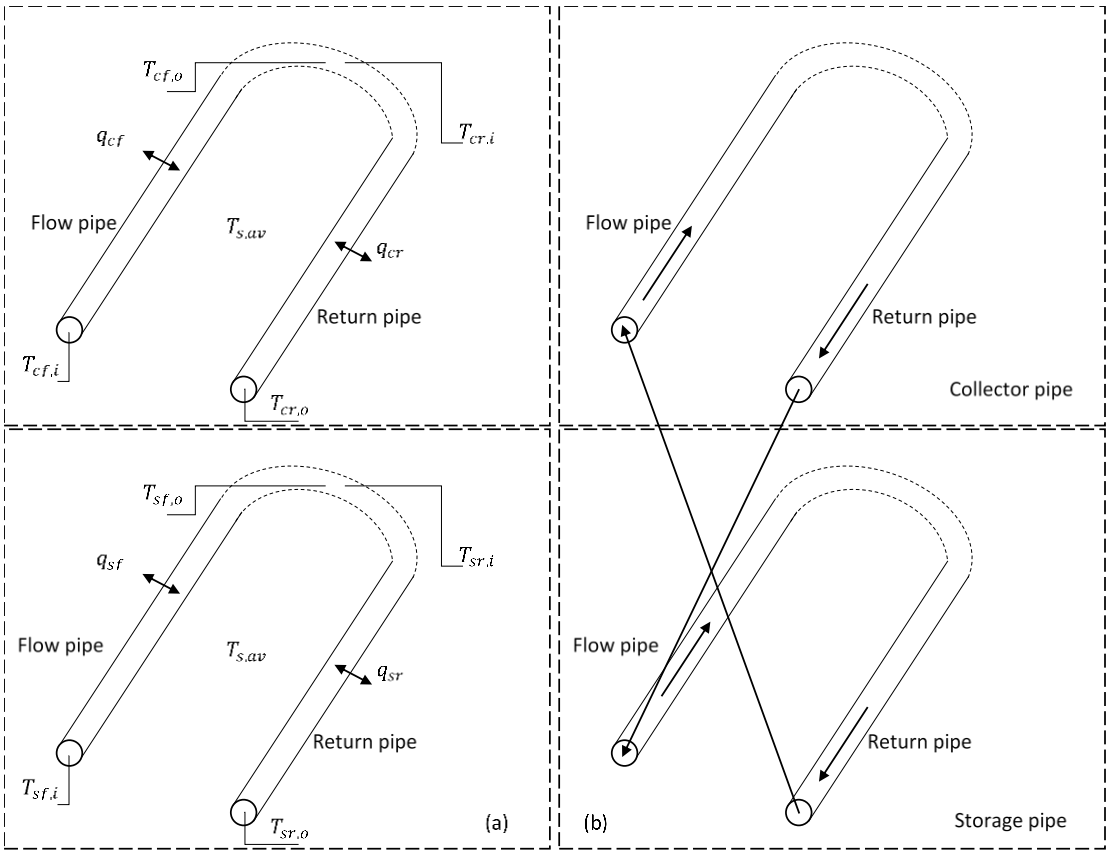

Figure (6.7) (a) Idealized of 3D pipe for 2D modelling and (b) flow direction

Following are main outcomes extracted from the previous study conducted by Muñoz-Criollo (2014) which would be used in the context of this study in order to bypass time consuming and unnecessary repetitious analyses:

- The presence of nearby objects (e.g. vegetation shadow) highly affects the collection surfaces of the system through minimizing the solar radiation reaching it which would be reflected on the thermal potential of the system.
- A pre-system activation analysis consisting of eight yearly cycles using meteorological data provided by Carder *et al.* (2008) proved to be satisfactory for the problem convergence check before the simulation of the system activation period.

Finally, Table (6.3) summarizes the used values for the proposed snow layer, the values were derived from the encyclopaedia work presented by Singh *et al.* (2011) for fresh snow.

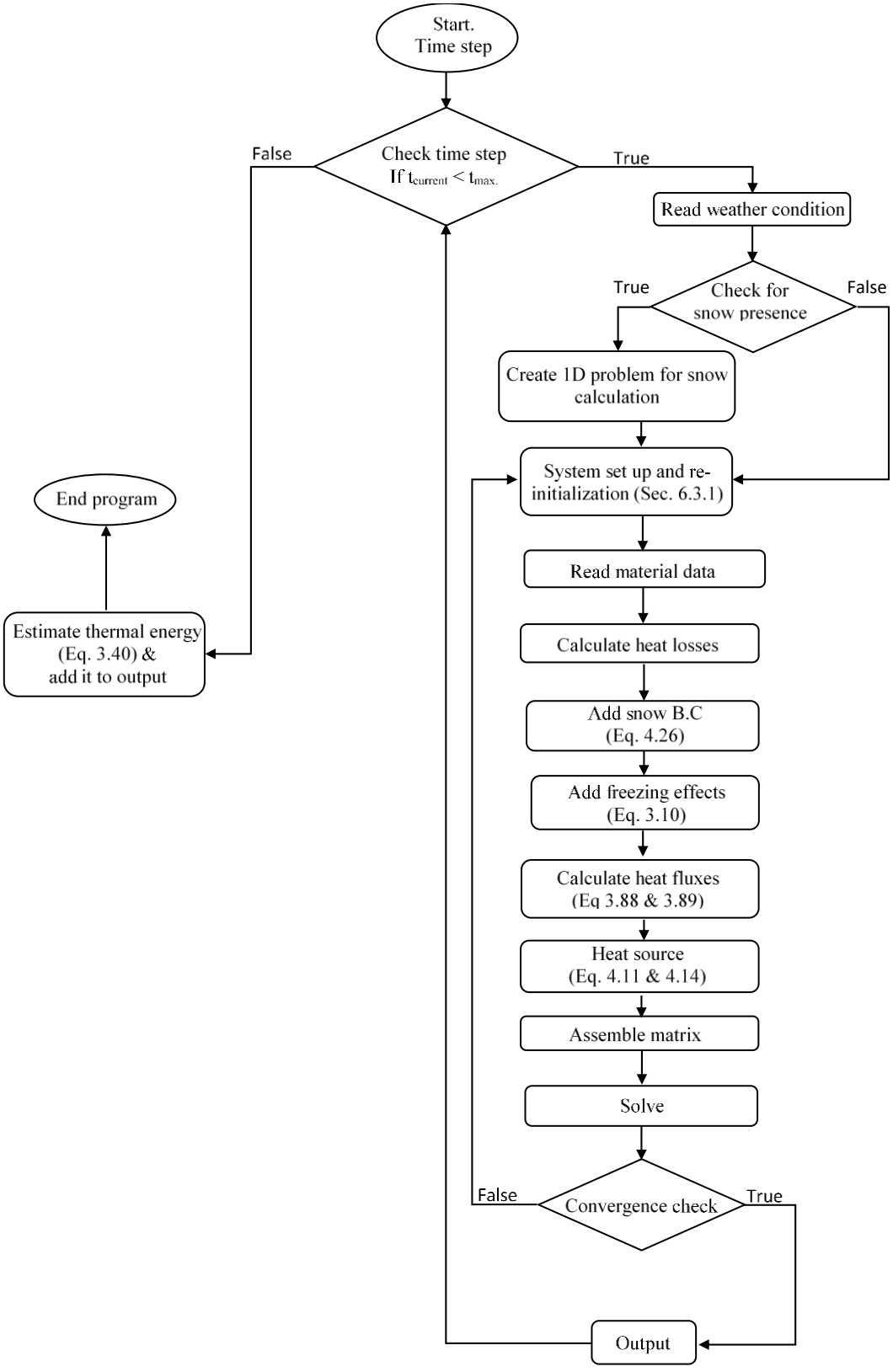

Figure (6.8) Flow diagram of proposed algorithm to calculate surface fluxes

Thermal conductivity (W/mK)	0.12
Density (kg/m^3)	100
Specific heat capacity (J/kgK)	2100
Emissivity (dimensionless)	0.95
Absorptivity (dimensionless)	0.15

Table (6.3) Snow parameters used in the context of this study (Singh *et al.* 2011)

6.3.2 Domain and discretization

The mesh was constructed using 2452 four-node isoparametric linear elements (four temperature degrees of freedom per element) which was found to be a suitable level of discretisation after spatial convergence tests. A pavement surface layer built on top of a concrete layer was located at the middle of the domain and surrounded by a homogeneous clay soil. The overall size of the domain (in particular the position of the vertical and lower horizontal domain boundaries) was chosen based on the recommendations provided by Muñoz-Criollo (2014) to ensure that the far-field boundary conditions do not impact the results.

Figure (6.9) shows the 2D domain under consideration that represents a 2D section of soil 14 m deep by 27.6 m wide which contains both the road layers materials and heat exchangers near its centre. The boreholes position 'G' is marked for reference. The slope next to the road is considered in the domain as well to correctly represent the heat flow for the layers beneath the insulation layer.

6.3.3 Initial and boundary conditions

The initial and boundary conditions of the problem are set as:

- For pavement surface boundary condition, the non-turbulent formulation presented in (3.7.6.ii) was proved to be more suitable for representing the thermal boundary formulation (Muñoz-Criollo 2014).
- For soil surface boundary condition, the canopy layer formulation presented in (3.8) was chosen to the represent the thermal fluxes at the soil surface.

- For a snow surface boundary condition, a 10 cm thick of snow was presented on a predefined periods that were extracted from the experimental reports. The snow thermal properties were assumed to be constant during snow existence.
- The boundary condition at the bottom and sides of the domain has a minimal impact in the prediction of the temperature profile of the soil (Muñoz-Criollo 2014), thus a free boundary condition is thought to be able to represents the active shallow engineering thermal devices thermal behaviour, this is applied for the lower and sides boundaries of the domain.

The initial condition of the domain was set to a uniform value of 10 ˚C. This value was calculated from the average air temperature measured on the experimental site by TRL (Carder *et al.* 2008) for the period of analysis.

6.3.4 Analysis periods

The numerical simulation was undertaken in a series of sequential steps and could be divided to certain periods that was mainly based on the experimental description provided by (Carder *et al.* 2008) plus the pre-system activation period. All periods are summarized as follows:

- The pre-system activation period: a period of eight yearly cycles was considered enough for performing a preliminary simulation (Muñoz-Criollo 2014) which was necessary to establish suitable initial conditions for the model. The meteorological data from August 2005 to August 2006 was used as an input to cover the analysis period. The original soil type provided by Carder *et al.* (2008) was used during this simulation instead of the inter-seasonal system layout.
- First insulation period: the TRL experimental system was operated in early May 2005 without any specified date (assumed here to be starting on 1st May 2005). This activation only related to the insulation layer and it started from 1st May 2005 until 22nd August 2005, because of that the soil under insulation layer was prevented from normally heating up due to the presence of the active

insulation layer. It is important to note that the distribution of material layers for this and the following period was as described by the TRL experiment (Carder *et al.* 2008), and also, that there were only two experimental data points available for it listed as follows: (i) 9th May 2005 at 12:30 h and (ii) 15th July 2005 at 14:00 h.

- First activation period: In this period, the experimental system was activated under the collection mode starting from the 23rd August 2005 until the 13th November 2005. The pump system was activated to transfer the fluid between the heat exchangers based on the temperature difference between the temperature sensor located at the middle of the collection or storage pipes. If the difference between the exchangers exceed 1.4 ˚C the system would be active and turned off when the temperature difference dropped to approximately 0.3 ˚C.
- Second activation period: In this period, the experimental system was activated under the usage mode starting from 14th November 2005 until 20th February 2006. The pumps were activated when the road surface went below 2 ˚C for more than 15 minutes and turned off when it went above 2 ˚C for more than 15 min.
- Second insulation period: For this period, the experimental system was activated one more time under hibernation mode starting from 21st February 2006 until 26th April 2006.
- Third activation period: In this period, the experimental system was activated on the collection mode again starting from 27th April 2006 until 31st October 2006.
- Fourth activation period: For this period, the experimental system was activated on a usage mode starting from 1st November 2006 until 1st March 2007.

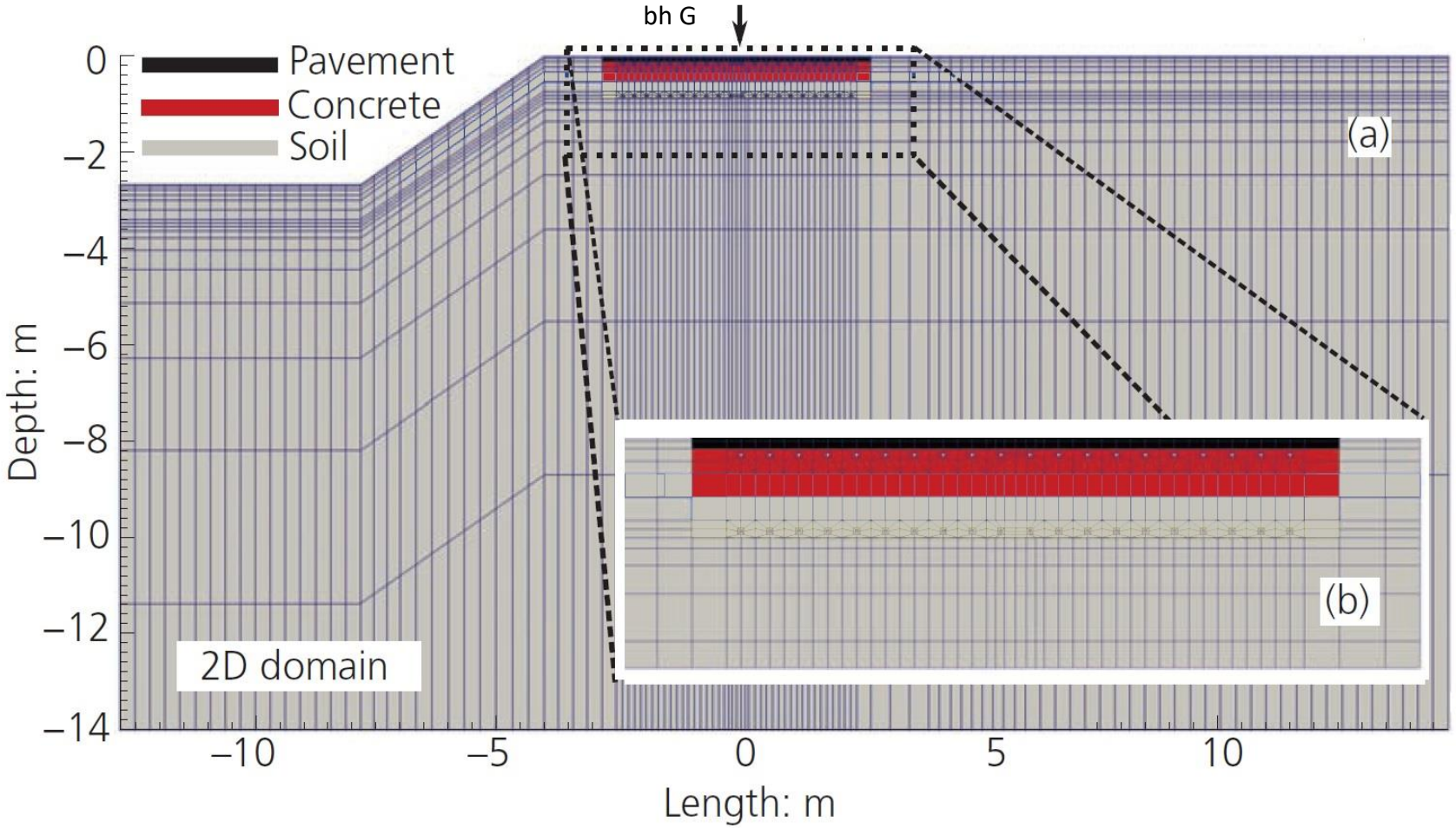

Figure (6.9) Domains considered in this study: (a) full 2D domain; (b) zoom-in section

6.4 Results

The results of this chapter are presented in series of subsections and relate to the second operating year of the TRL experiment. The reason for considering the second year was due to the relatively lower amount of missing data during it, and also, because it abides the correct designing timing criteria unlike the first year (i.e. it runs for almost five months in collection periods / full summer). These sub-sections present comparisons between experimental and numerical transient variations of temperature corresponding to borehole G at two selected depths, 0.1325 m (collector depth) and at 0.8475 m (storage depth) for the following selected periods of tests: (i) the second insulation periods, (ii) third and (iii) fourth activation periods.

Before considering the results, it was important to quantify the shadowing effects presented on site in order for the approach chosen to be used for the whole period of analysis to be justified. Figure (6.10) shows a comparison of the first insulation period of the transient variations of temperature of the soil at the pipe storage depth for borehole 'G' for three levels of shading (0 %, 50 % and 100 %).

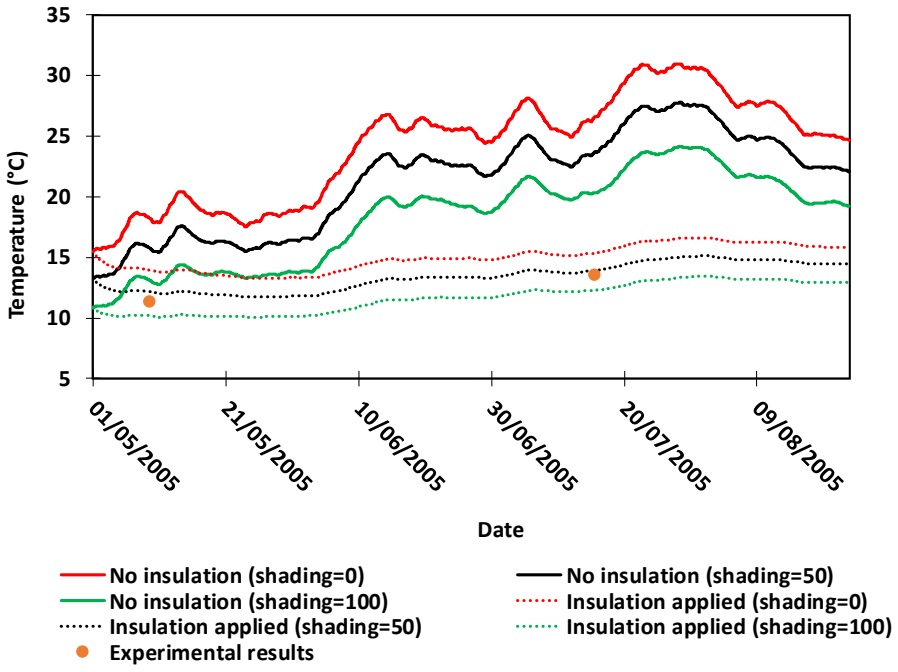

Figure (6.10) Comparison of numerical predictions under different levels of shading for the pre-activation (No insulation) and 1st insulation periods at storage depth

The available experimental measurements during this period as mentioned before was only available for 9th May 2005 at 12:30 h and 15th July 2005 at 14:00 h. The corresponding profiles for the previous pre-system activation yearly cycle are shown for reference (as 'No insulation').

The results shown in this figure demonstrate the impact of the insulation layer and its effectiveness as the temperature variations at this depth were significantly damped for equivalent periods. Compared to the soil heating results before placing of the insulation layer (solid lines) the temperature variations results for this period (dotted lines) had only a small increment (of approximately 2 ˚C) by the end of July and then slowly decreasing towards the end of August. This behaviour mainly due to the soil at this depth being insulated from the atmospheric interactions at its surface (i.e. pavements). The numerical results for 0 % and 100 % shading lie either side of the experimental values which indicates that the use of 50 % shading effects is appropriate.

6.4.1 Second insulation period

This period starts from the 21rd February until the 26th April 2006, during which time the system was manually turned off (i.e. neither collection nor usage were carried out). Figure (6.11) shows the experiment and numerical result of soil temperature at borehole G at collector depth while Figure (6.12) shows the results at the storage depth. As seen clearly in the aforementioned figures the numerical results deviate from the experimental ones until the end of March 2007 where they start to converge. These differences are due to the usage of meteorological data that corresponds to late February and March of 2007 into the corresponding months of 2006 because of the absences of these periods on the experimental weather data. During this period the numerical results are in very good agreement with the experimental measurements.

It can be seen that when the system was turned off the temperatures at collector depth slowly goes above 10 ˚C while at storage depth it shows a slow increase of about 4 ˚C. This discrepancy could be partly related to the presence of insulation layer and its effect as it would prevent the soil underneath from naturally heating up. The

experimentally odd behaviour around 23rd March 2006 was believed to be due to a glitch in the experimental system (Muñoz-Criollo 2014).

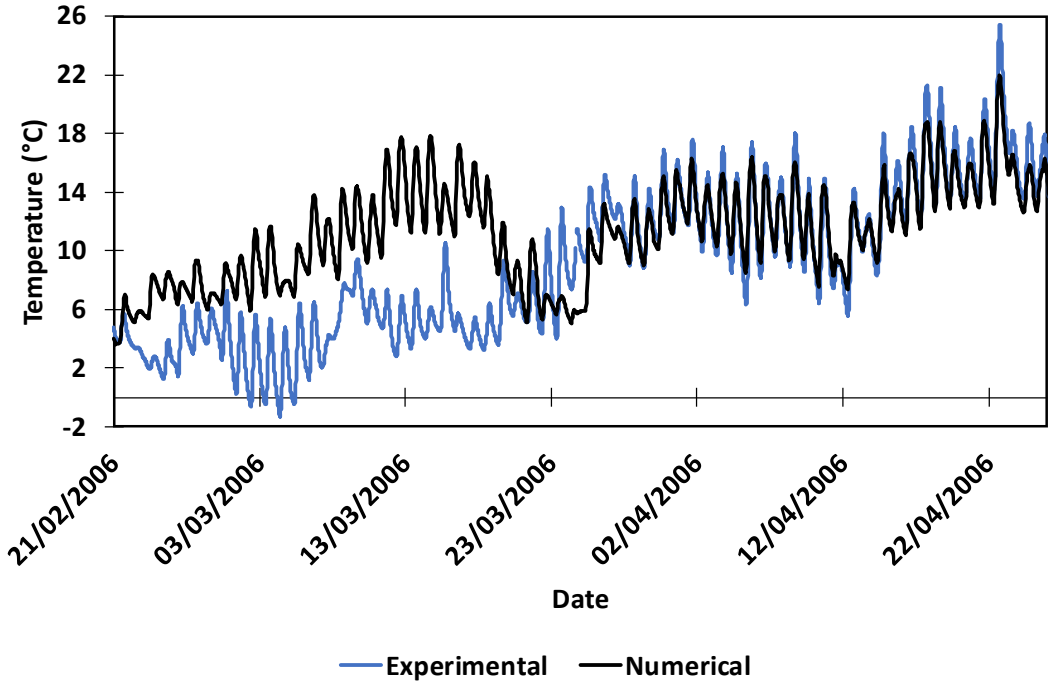

Figure (6.11) Soil temperature at collector depth (0.1325 m) for borehole G

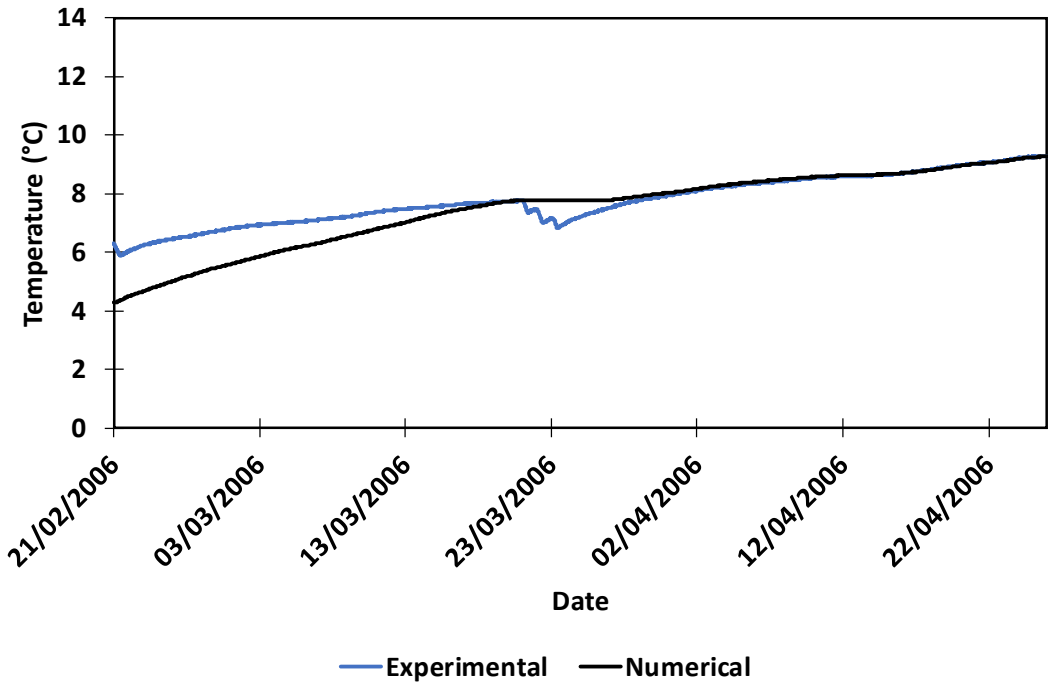

Figure (6.12) Soil temperature at storage depth (0.8475 m) for borehole G

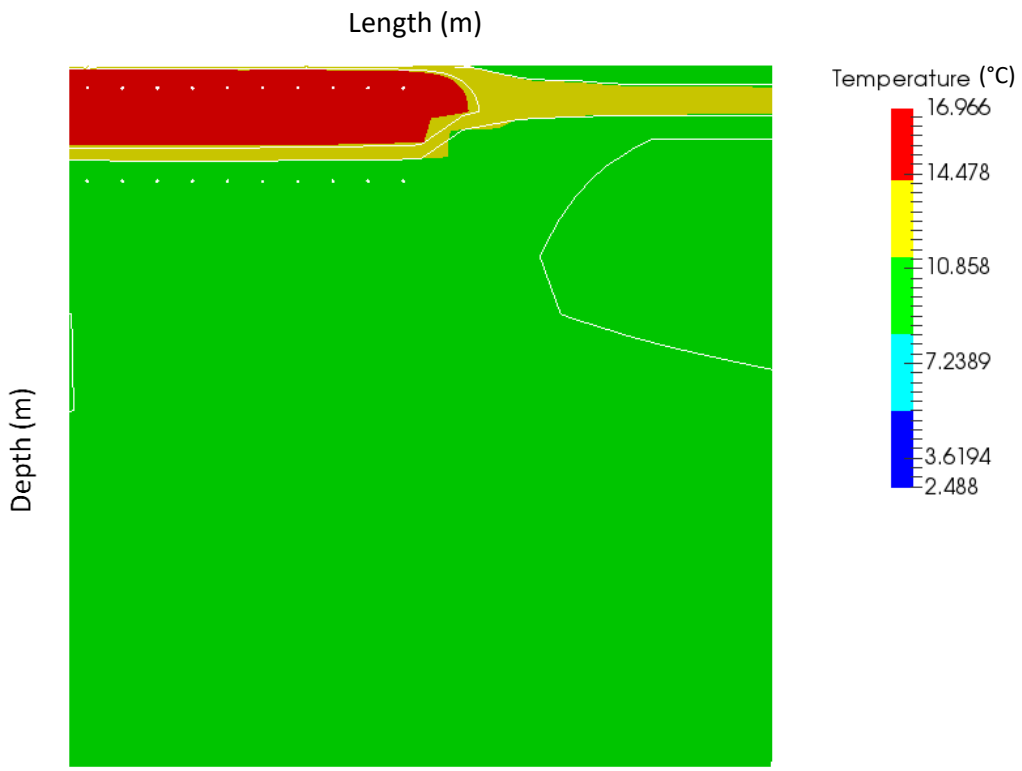

Figure (6.13) Contour temperature profile on 26th April 2006

Finally, Figure (6.13) shows the temperature contour profile at the end of this period near the road surface. It can be seen that the temperature under the insulation layer is almost homogeneous and has almost the same temperature of 9.5 ˚C that had been showed in Figure (6.12) which confirms that the soil has reached a thermal equilibrium.

6.4.2 Third activation period (2nd Collection)

This period starts from the 27th April 2006 and lasts until 31st October 2006. The first indication on the temperature collected during this period that it is higher than the first activation period.

This is related to the commencing activation time as the third activation period lasted for a full summer (approximately five months) while the first activation period

commenced for approximately month and a half. The second indication on this period that it ended on 6th September 2006.

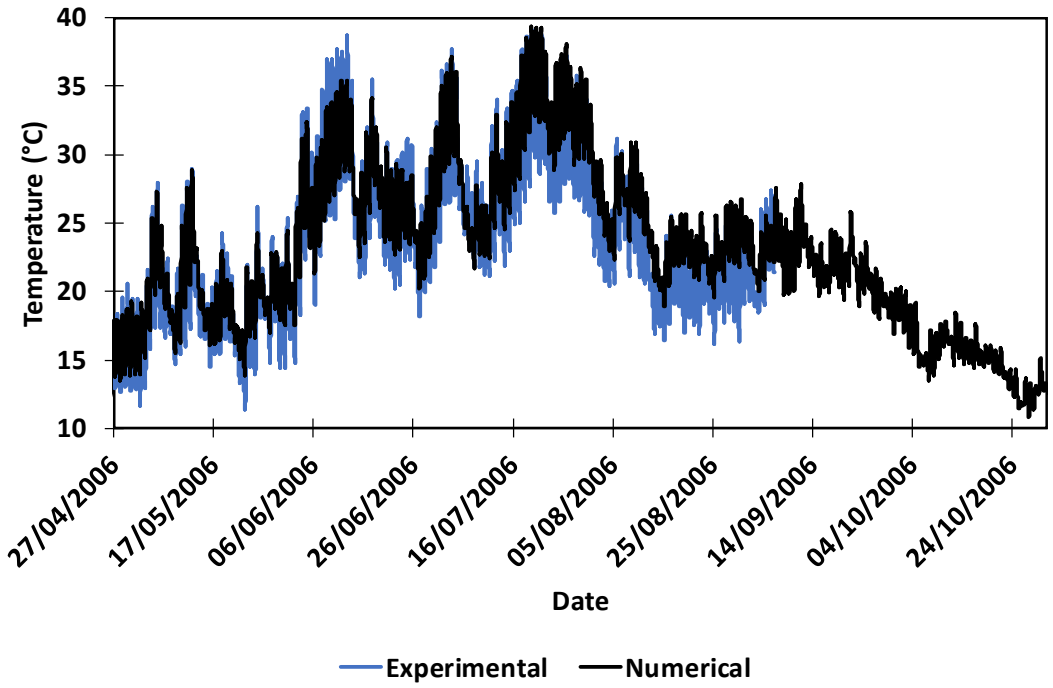

Figure (6.14) Soil temperature at collector depth (0.1325 m) for borehole G

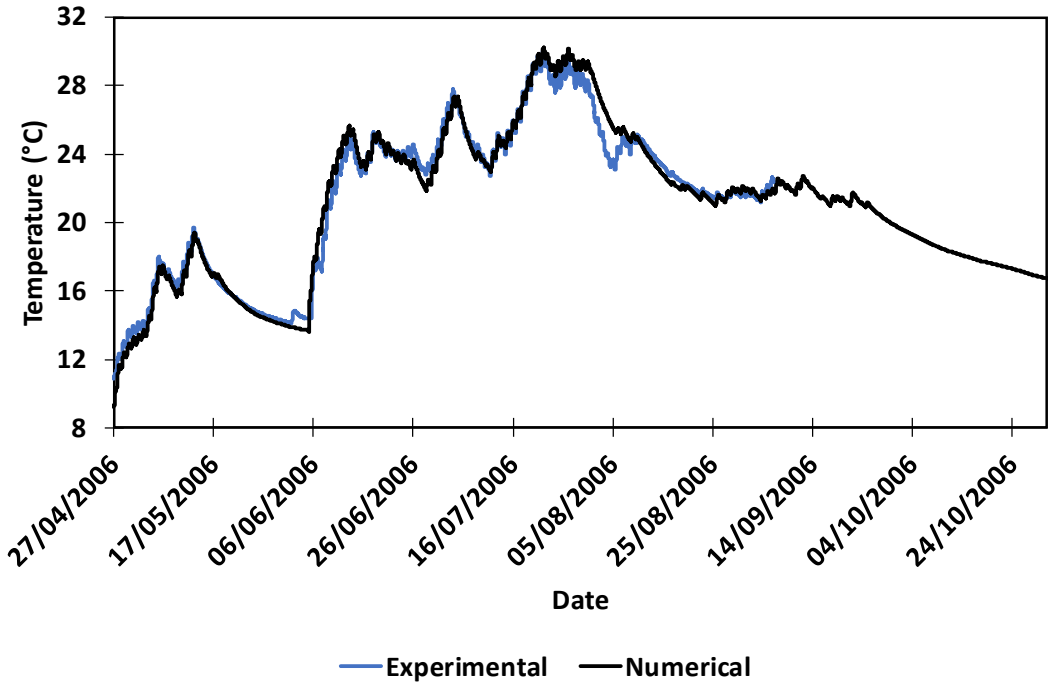

Figure (6.15) Soil temperature at storage depth (0.8475 m) for borehole G

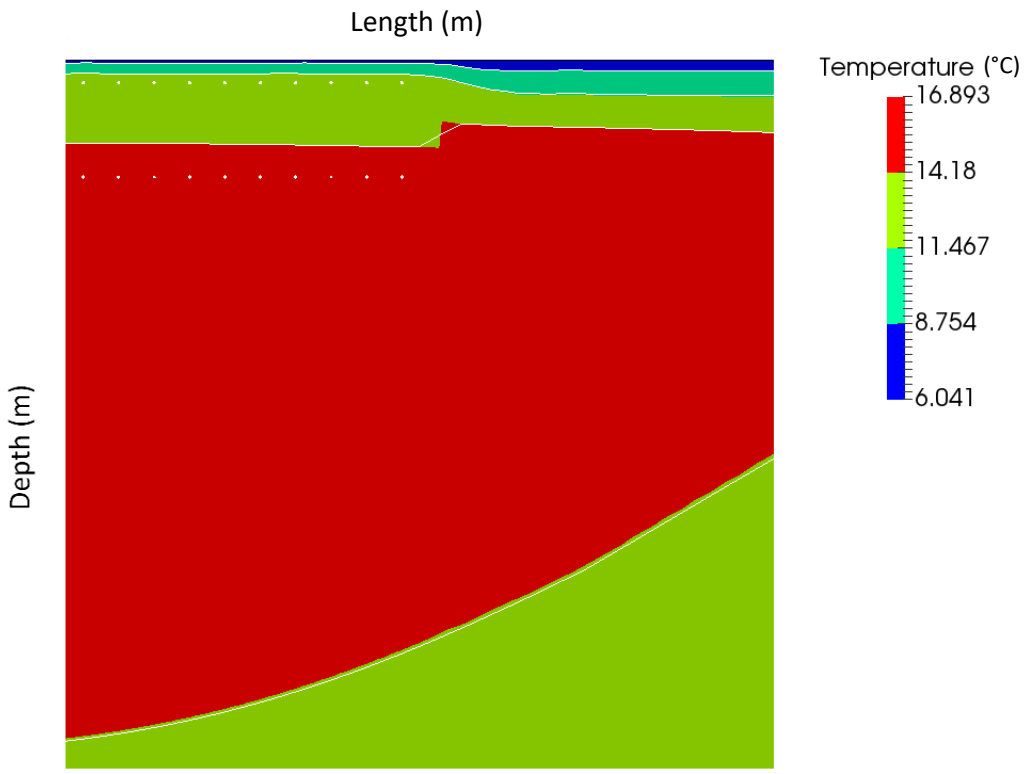

Figure (6.16) Contour temperature profile on 31st October 2006

Figure (6.14) and Figure (6.15) shows the experimental and numerical result of soil temperature at borehole G at the collector and storage depths respectively. In general, a very good agreement between experimental measurements and numerical predictions for both depths can be observed. Furthermore, the higher temperature achieve during this activation period agrees well with the temperature profile shown in Figure (6.16) where a marked increment in temperature can be clearly observed beneath the insulation layer.

6.4.3 Fourth activation period (2nd Usage)

This period started from the 1st November 2006 and lasted until 1st March 2007. Due to the presence of snow during this period and to demonstrates the effectiveness of the model, four analysis of result sets would be presented to facilitate the comparisons and are summarized as follows:

- Analysis 1: would provide a comparison between the experimental and numerical behaviour where neither surface snow nor ground freezing were activated.
- Analysis 2: would present the results for the activations of the ground freezing.
- Analysis 3: presents the results for the surface snow layer activations.
- Analysis 4: shows the results for the storage pipes when a forced correction was applied to the system.

Figure (6.19) to Figure (6.26) show the experimental results and numerical predictions of soil temperature at borehole 'G' at the collector and storage depths respectively for this period.

☐ The numerical results shown in Figure (6.18) and Figure (6.19) were generated based on an analysis that followed the approach presented by Muñoz-Criollo (2014) and neither freezing nor snow cover were considered.

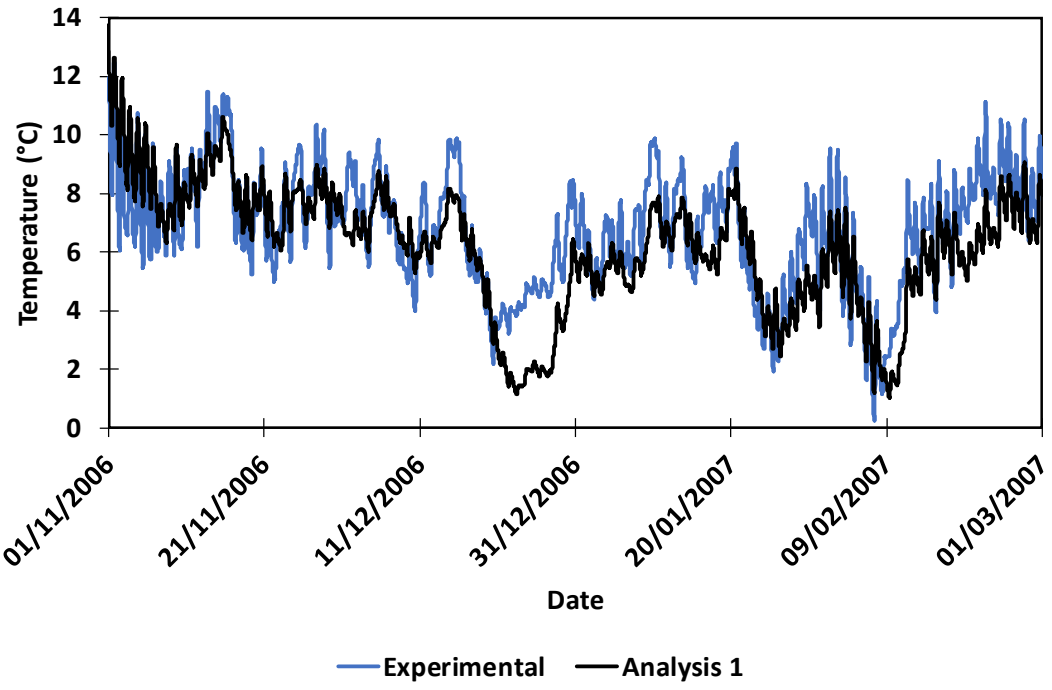

Figure (6.17) Soil temperature at collector depth (0.1325 m) for borehole G (neither freeze nor surface snow considered)

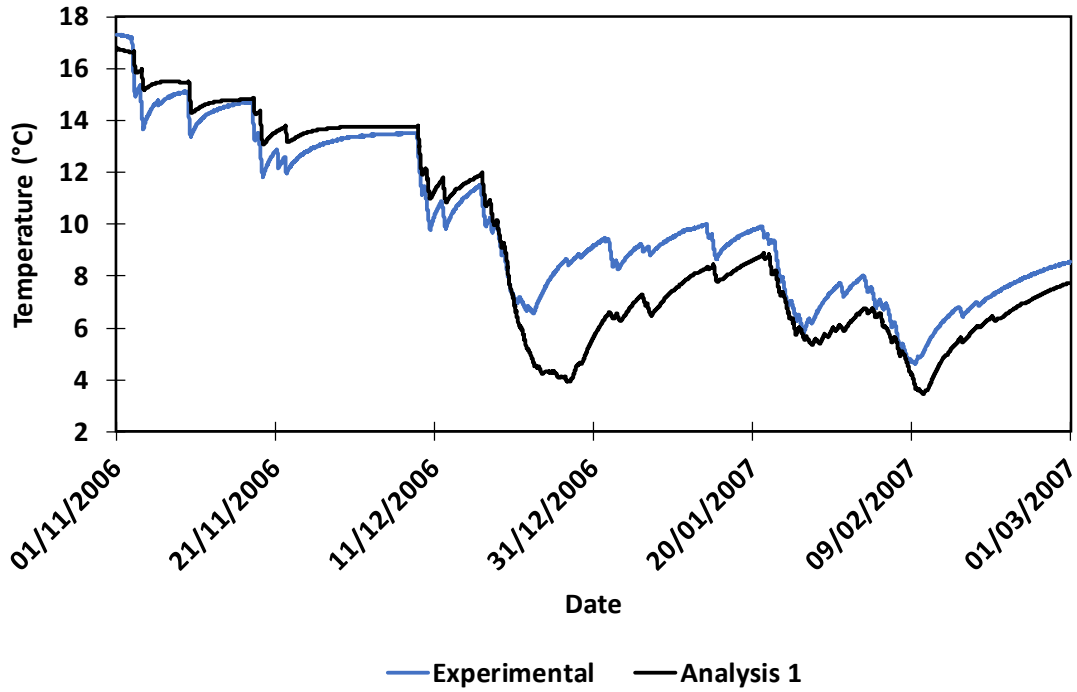

Figure (6.18) Soil temperature at storage depth (0.8475 m) for borehole G (neither freeze nor surface snow considered)

It can be seen that the numerical solution was underestimating the experimentally measured temperatures for more than 5 ˚C in the third week of December and for almost 2 ˚C in first week of February 2007.

This behaviour is noticeable at both depths (collector and storage) for the same periods. Overall, except in these periods the experimental results trend was captured successfully.

☐ The next set of results considers the effects of soil freezing on the system performance. The main difference here beside the ground freezing consideration is the relatively more accurate representation for the porous layer thermal properties of a multi layered system through considering its components (i.e. air, water and solids particles). Figure (6.21) and Figure (6.22) shows the results using this modification.

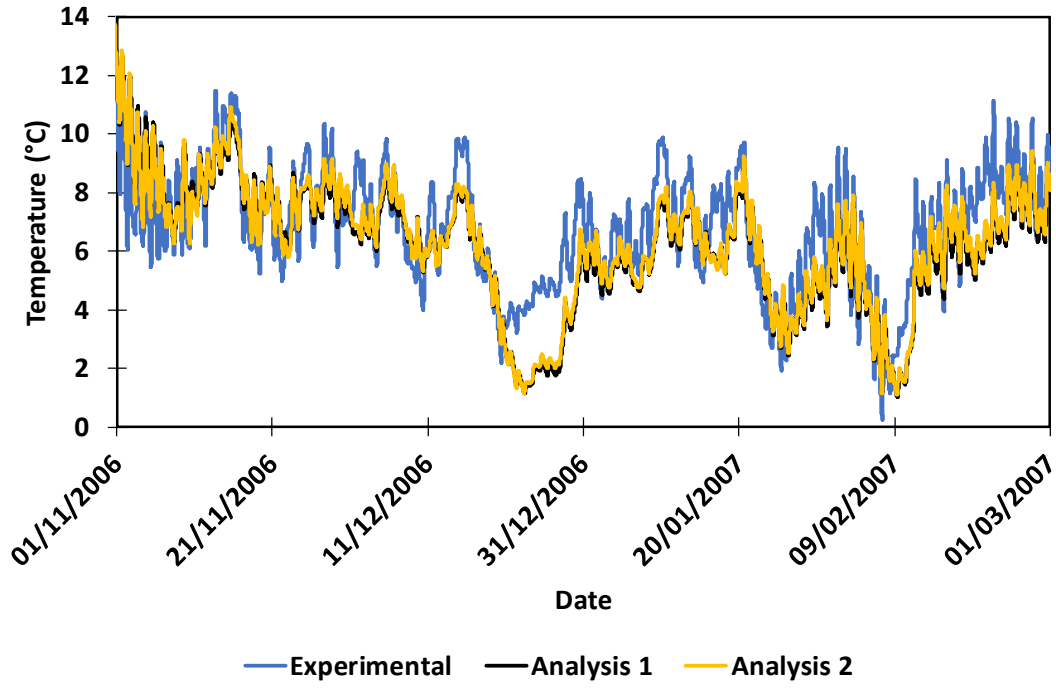

Figure (6.19) Experimental temperature at collector depth for borehole G (0.1325 m) (ground freezing activated)

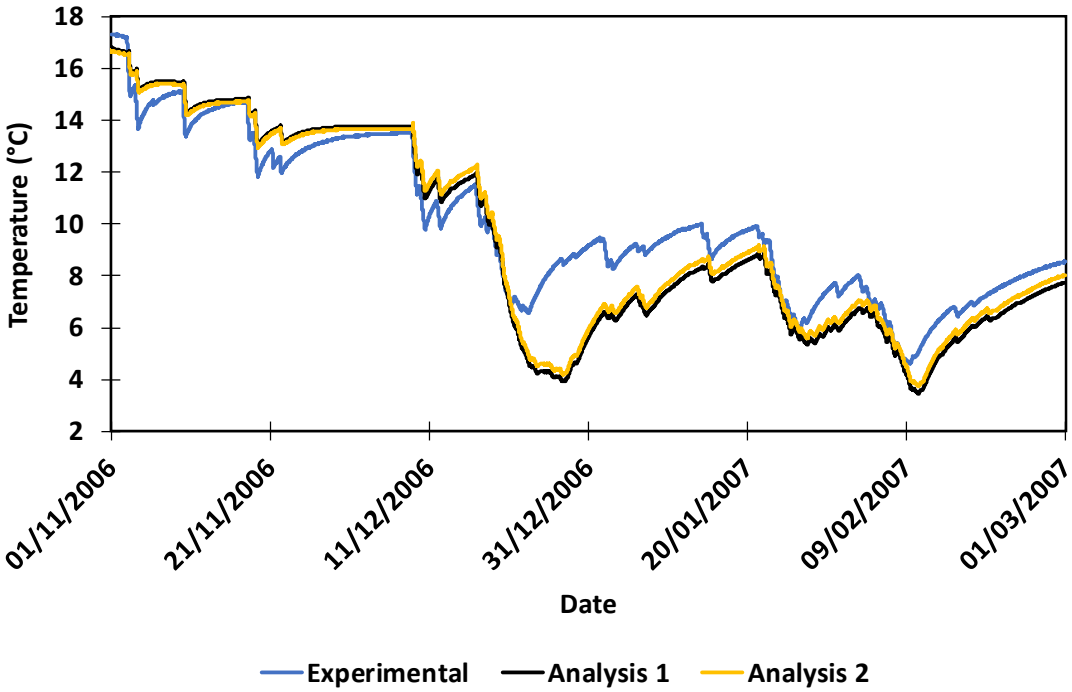

Figure (6.20) Experimental temperature at storage depth for borehole G (0.8745 m) (ground freezing activated)

It can be observed that when soil ground freezing is considered the results were slightly affected, however, the implementation did marginally improve the results. It is thought that the freezing did not affect the system significantly as the snow events did not last for long and the freezing would not penetrate deeply into the soil in such short periods.

☐ Additionally, an analysis where soil ground freezing was considered and combined with the component of the model to represent snow cover presence on the surface was undertaken.

The presence of a snow layer was based on a reported salt spreading events that took place at the nearby highway (M1) (Carder *et al.* 2008). The reported periods listed as follows: (i) starting from the 19th December 2006 (hour 17:00) to 21th December 2006 (hour 12:00); (ii) starting from 23rd January 2007 (hour 18) to 25th January 2007 (hour 13:00) and (iii) starting from 7th February 2007 (hour 18) to 9th February 2007 (hour 13:00). During these specific periods, the previous numerical results notably deviated from the experimental ones.

Figure (6.21) and Figure (6.22) shows that the developed model was capable of capturing the trend of the experimental results with the differences on the snow periods that its maximum difference is almost (3 ˚C) for the storage depths, however, near after mid-February the numerical predictions successfully capture the experimental results.

Although, the results of the numerical solution which incorporate the surface snow and ground freezing is significantly better from the predecessor results, it still however, cannot capture the exact behaviour of the system in one certain period.

These differences in results could be attributed to the fact that (i) the model assumes ideal situation for the material in hand, (ii) the snow layer is assumed of constant thickness for a pre-defined period of time with a constant properties and (iii) uncertainties in the thermal properties values for all the system components.

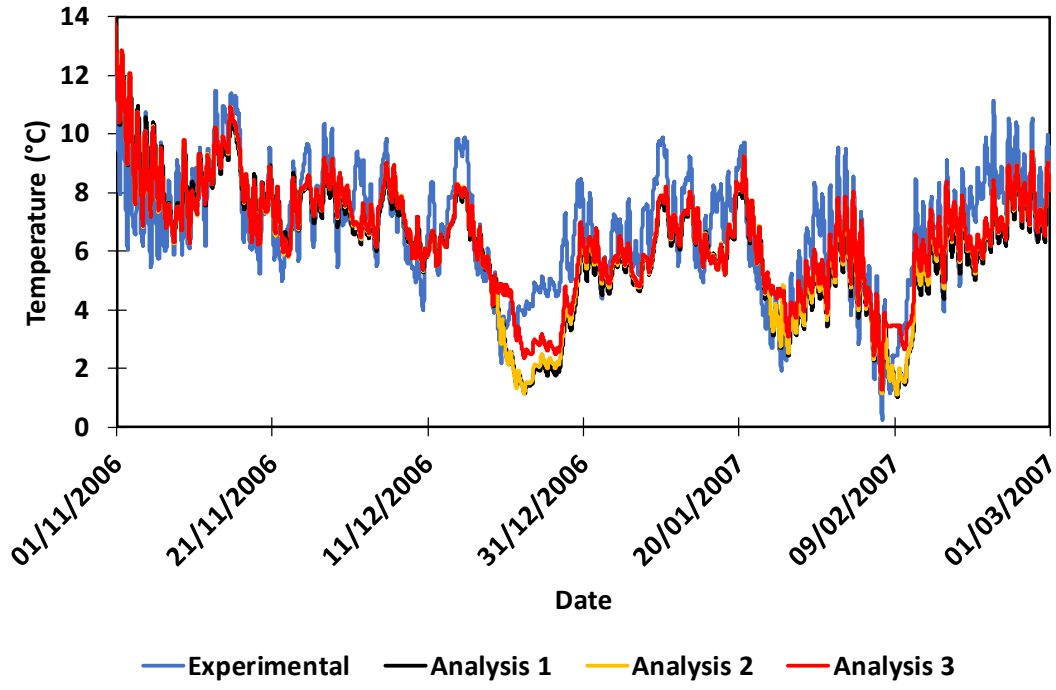

Figure (6.21) Experimental temperature at collector depth for borehole G (0.1325 m) (ground freezing and surface snow were activated)

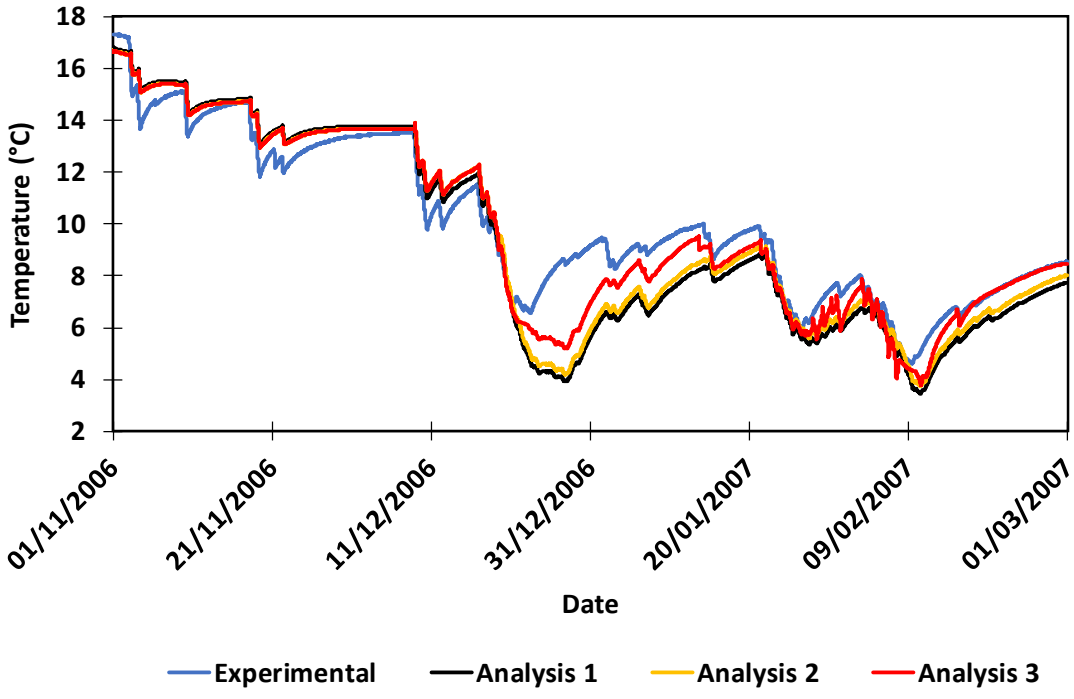

Figure (6.22) Experimental temperature at storage depth for borehole G (0.8745 m) (ground freezing and surface snow were activated)

☐ Finally, it can be clearly seen that in the period from 23rd to 27th December 2006 (Figure (6.18, 6.19 and 6.20)) the numerical model does not follow the general trend of behaviour and underestimates the temperature in comparison to the experimental results. This is due, in part, to the fact that while experimentally the system is not active and the temperature of the soil in the store is recovering and increasing, the numerical model is still triggering system activation. It is not clear why the system did not run in this period, however, Carder *et al.* (2008) reported that the system was off during certain periods especially around the last ten days of December which can be summarized as follows:

1) Starting from 23rd December 2006 (hour 12:30) and forward until 27th December 2006 (hour 17:15).
2) Starting from 27th December 2006 (hour 19:45) until 29th December 2006 (hour 06:45).
3) Starting from 29th December 2006 (hour 08:15) until 1st January 2007 (hour 10:00).
4) Starting from 01st January 2007 (hour 10:45) until 1st January 2007 (hour 22:30).

In order to remove uncertainty related to the representation of the system activation during this period a further analysis has been undertaken with the system manually switched off during the aforementioned periods to align to the actual experiment conditions. For the sake of comparisons, Figure (6.23) shows the results being created using this modification.

It can be seen that during the period under consideration (23rd - 27th December) the correlation between the numerical simulations and the experimental results significantly improved and the differences reaches almost ~1.4 °C, also, due to this implied correction the results following these periods captured the experimental system behaviour more accurately. The results confirms the effect of the snow presence onto the system and that the new model captures the snow processes which would prevent overestimation of the heat losses at the surface, and, consequently the thermal energy required to maintain the surface above 2 ˚C.

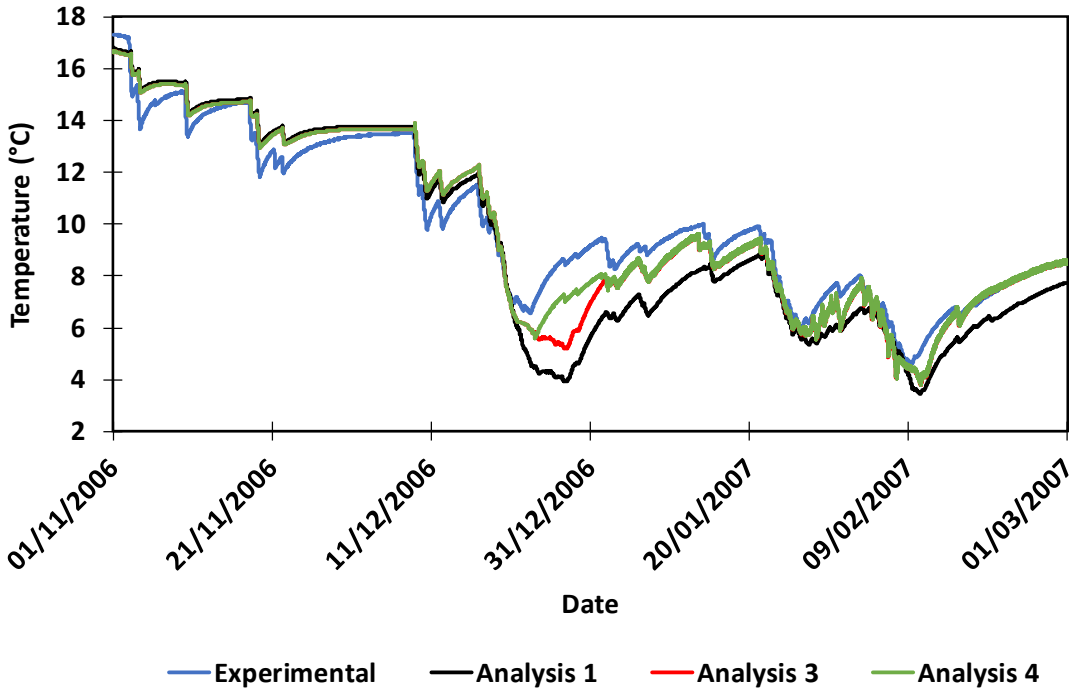

Figure (6.23) Experimental temperature at storage depth for borehole G (0.8745 m) (ground freezing and surface snow were activated with system corrections applied)

Finally, Figure (6.24) shows the temperature profile near the road surface at the end of this period.

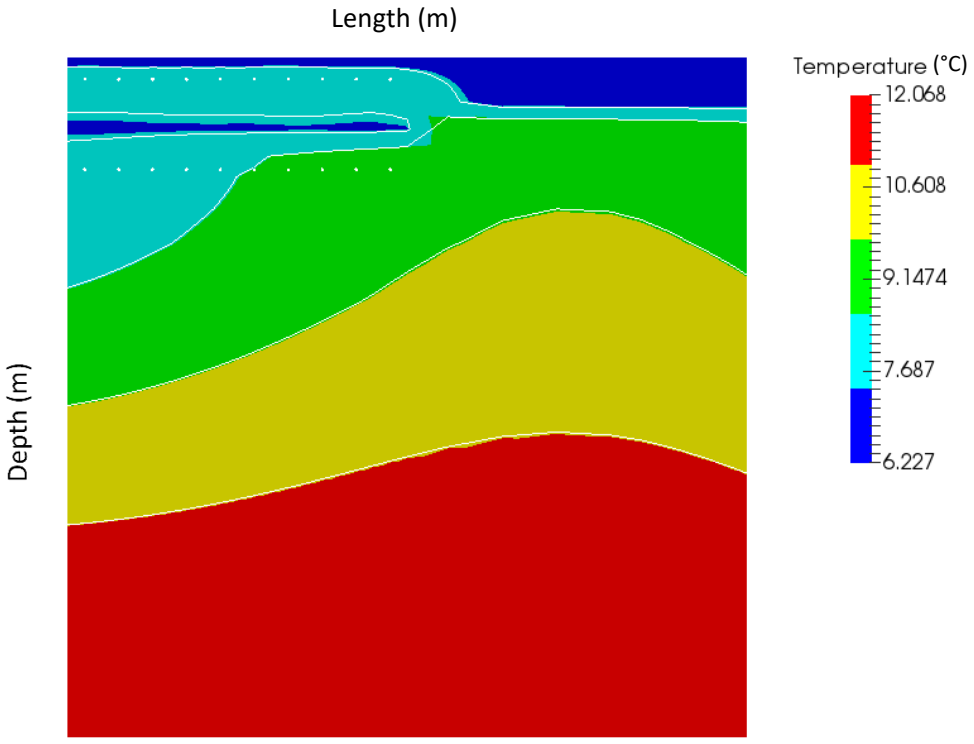

Figure (6.24) Contour temperature profile on 1st March 2007

The temperature reduction effect can be clearly observed due to the extraction process happened during this period beneath the insulation layer. In addition, the temperature profile implies that not all the available thermal energy being used for road maintenance during this period as the average soil temperature beneath the adaptable insulation layer still high. That excess temperature could possibly be used on other applications (e.g. residential heating).

6.4.4 System thermal energy

In order to estimate the coefficient of performance for the system, the numerical results were used to calculate thermal energy recovered during the third and fourth activation period and compared against the experimental measurements of electrical energy used in the pumping system. Figure (6.25) and Figure (6.26) presents the aforementioned comparisons. It can be observed from Figure (6.25) that the recovered energy during summer reaches almost 14000 MJ while the electrical energy required to activate the pumping system during the same period was approximately only 800 MJ.

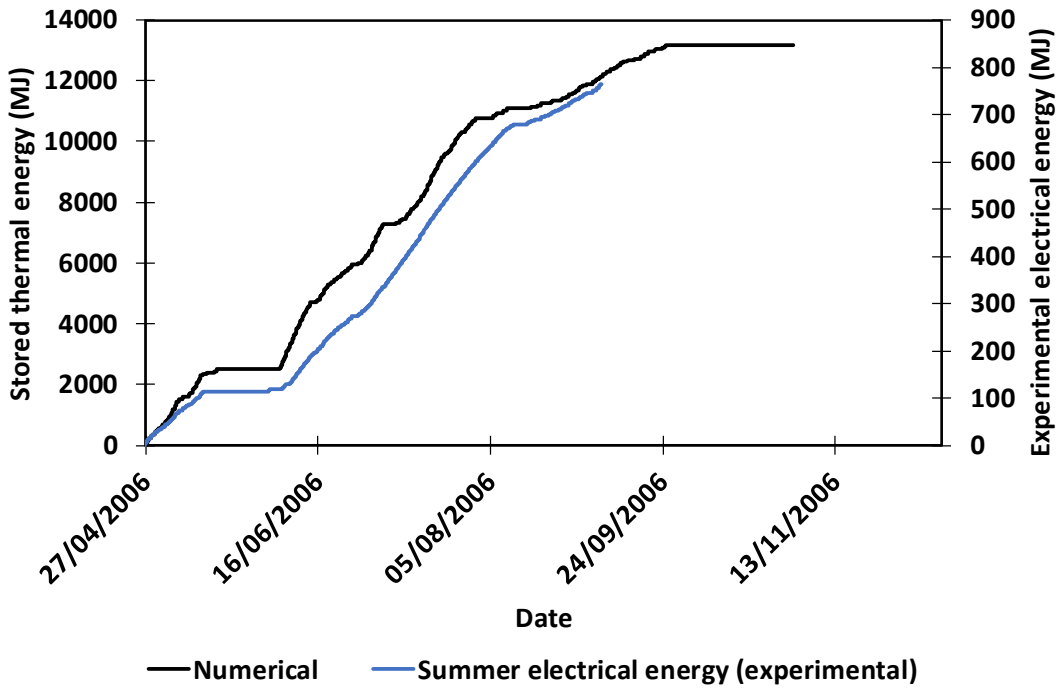

Figure (6.25) Thermal energy available in the system during the 3rd activation period (summer 2006)

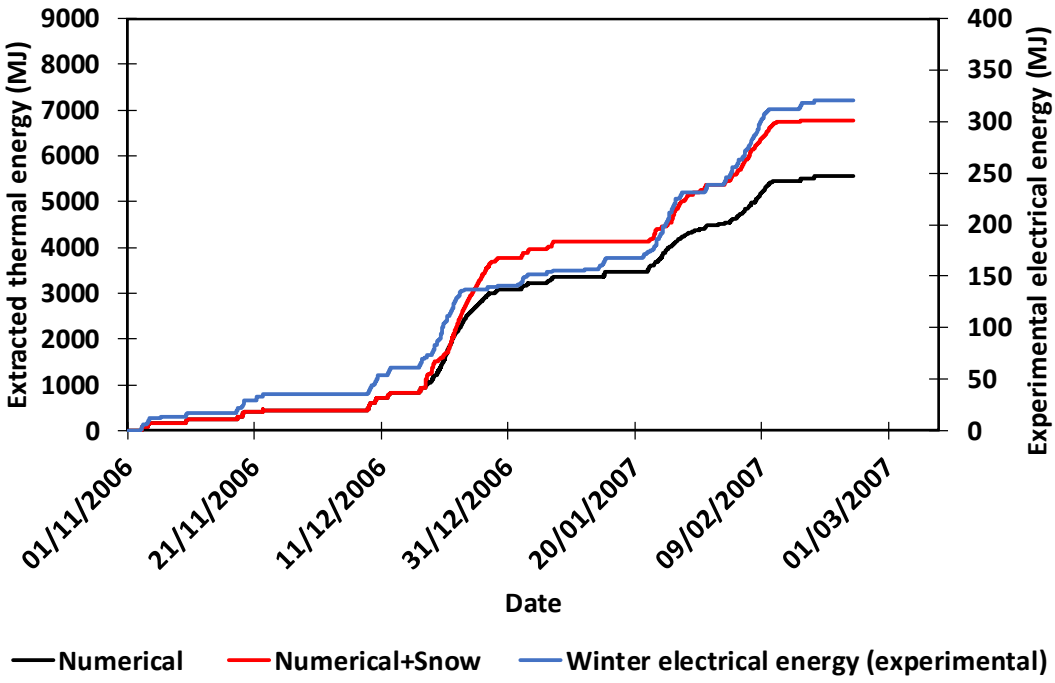

Figure (6.26) Thermal energy available in the system during the 4th activation period (winter 2006-2007)

On the other hand, Figure (6.26) shows that the recovered energy in winter reaches up to 7000 MJ while the required experimental electrical energy was 330 MJ. It can be seen that almost half of the thermal energy collected during summer was used in winter for thermal maintenance of the road; this confirms the previous findings that the system is delivering more energy that might be useful in other applications (e.g. residential heating).

In summary, the total system requirements to operate the pumping system during collection and storage period was almost 1130 MJ while the useful extracted energy in winter is about 6700 MJ which leads to a coefficient of performance that equals to 5.9. The periods where the system was off are clearly seen in the graph (no change).

It is important to note that the system electrical measurements indicates that it was active for few times in winter which might be related to the snow cover presence on its surface and its insulative properties. This in turns implies that the numerical model to some extent overestimate the coefficient of performance presented before

because it is predicting higher levels of thermal extraction. However, the current results provides more reliable results for the thermal energy due to the addition of the snow cover in the system.

6.5 Conclusions

This chapter has presented the successful development of a 2D numerical model which is capable of representing the process of ground thermal energy storage using buried shallow engineering geoenvironmental devices equipped with heat exchangers.

The proposed numerical model has been compared against the case study of TRL (Carder *et al.* 2008). The experimental system runs for a consecutive period of two years that is subdivided into: (i) two periods of insulation, (ii) two periods of energy collections (summer 2005, summer 2006) and (iii) two periods of energy extractions (winter 2005-2006, winter 2006-2007).

The newly development parts in the numerical model has been proven to enhance the results by many aspects. The accurate representations of the thermal properties of the layered system alongside the possibility of taking into considerations the freezing and snow events on its surface provide significant improvements to the results.

The proposed 2D numerical model has proved that it is able to estimate the amount of thermal energy being collected and extracted from the ground by this kind of geoenvironmental devices under different scenarios on the surfaces.

The limitations on the current development that the current numerical development assumes constant thickness and properties for the snow during a predefined time, however, it is not that crucial on a little snowing events countries.

Finally, it was found that the thermal energy required to provide thermal maintenance to the road surface is lower than the amount of thermal energy that was collected. This difference could be used in other applications that require thermal energy in winters (e.g. residential heating).

6.6 References

Bangerth, B., Heister, T., Heltai, L., Kanschat, G., Kronbichler, M., Maier, M., Turcksin, B. and Young, T. D. 2013. The deal.II Library, Version 8.1. doi.

Carder, D. R., Barker, K. J., Hewitt, M. G., Ritter, D. and Kiff, A. 2008. Performance of an interseasonal heat transfer facility for collection, storage, and re-use of solar heat from the road surface. Transport Research Laboratory.

Deardorff, J. W. 1978. Efficient prediction of ground surface temperature and moisture, with inclusion of a layer of vegetation. Journal of Geophysical Research: Oceans. 83(C4), pp. 1889-1903. doi: 10.1029/JC083iC04p01889.

Muñoz-Criollo, J. J. 2014. An investigation of inter-seasonal near-surface ground heat transfer and storage. Ph.D. thesis, Cardiff University, http://orca.cf.ac.uk/73226/.

Singh, V. P., Singh, P., Bishop, M. P., Björnsson, H., Haritashya, U. K., Haeberli, W., Oerlemans, J., Shroder, J. F. and Tranter, M. 2011. Encyclopedia of snow, ice and glaciers. Springer Netherlands.

Chapter 7: Impact of Adaptable Insulation Layer on Thermal System Performance

7.1 Introduction

The main objective of this chapter is to explore the impact of the use of an adaptable insulation layer on thermal performance, in terms of heat storage, in shallow geothermal systems. This chapter explores three different examples in order to demonstrate the potential of using the adaptable insulation layer within them and are presented in the following sections:

- Section 7.2 considers a simple vertical storage system, similar to the system investigated at bench-scale in Chapter 5, but with field-scale dimensions and longer periods of operation, this analysis was performed using the developed and validated 1D numerical model.
- Section 7.3 presents an analysis of using an adaptable insulation layer in a full-scale inter-seasonal heat storage system and compares performance to that of a system which incorporates the use of pipes to transfer heat into the storage banks. The TRL experiment presented in Chapter 6 provides the basis of this comparison, the analysis in this example was generated using the developed and validated 2D numerical model.
- Section 7.4 considers a hypothetical U-tube problem to explore the possible benefits gained from using the adaptable insulation layer in such systems. The analysis performed in this example was done using a general-purpose platform software for modelling engineering applications. COMSOL Multiphysics® is a well-known software package that can be used for simulating designs and processes based on electromagnetics, structural mechanics, acoustics, fluid flow, heat transfer, and chemical engineering behaviour (Comsol Multiphysics® 2015). Since the developed and validated numerical 1D and 2D models already been used, it was a good practice to explore the use of the adaptable insulation layer in a different working platform and observe the

overall system behaviour alongside the fact that it takes relatively shorter time to build, process and analyse the model.

- Section 7.5 summarize the conclusions of the chapter.
- Section 7.6 summarizes the chapter references.

7.2 Simple vertical column storage

In this case study, the numerical model is used to investigate the potential of using adaptable insulation layer in the accumulation of thermal energy in a soil column. For this purpose, an up-scaled hypothetical soil column (shown in Figure (7.1)) subjected to a process of seasonal thermal charge and discharge has been analysed. Thermal properties required by the numerical model for both adaptable insulation layer and sand are as defined previously in Chapter 5 and presented in Table (5.3, 5.4 and 5.4). The validated numerical model, presented in Chapter 3 and 4, is used to study a hypothetical scenario of thermal charge and discharge for the case of a 10 m depth soil column that is subjected to a soil surface temperature variation as shown in Figure (7.2). The surface temperature variation represents seasonal periods of high and low thermal energy availability in a typical temperature weather environment.

The soil column is composed of three layers:

- ☐ Top soil: from 0 m to 0.5 m depth, 0.5 m thickness.
- ☐ Adaptable insulation layer: from 0.5 m to 1 m depth, 0.5 m thickness.
- ☐ Bottom soil: from 1 m to 10 m depth, 9 m thickness.

The simulation period spans over 270 days. The degree of saturation of the adaptable insulation layer was varied in order to allow thermal energy to reach the region under the adaptable insulation layer during the period of high-energy availability and to reduce thermal losses during the low availability period. Two situations were analysed:

- Analysis 1: The adaptable insulation layer was assumed to be saturated from day 1 to day 270 (end of numerical experiment).

- Analysis 2: The adaptable insulation layer was assumed to be saturated from day 1 to day 125 and then dry from day 125 to day 270.

The bottom boundary condition was assumed as adiabatic (zero thermal flux). The top boundary condition (at 0 m) was shown in Figure (7.2). The initial temperature of the soil column is set at 22 °C, which was equal to the average applied surface temperature. Following appropriate convergence checks the domain was discretised with 1024 equally sized linear elements and the time step is set at 3600 seconds. Importantly, Figure (7.2) shows the temperature variation under the adaptable insulation layer (at 1.1 m depth) compared for both situations.

As expected, it can be seen that the variation was identical before day 125 (before the adaptable insulation layer being drained). After day 125 the temperature in the saturated case steadily decreases towards the end of the simulation period while for the drained conditions the temperature drop is comparatively lower with a difference of up to 2.1 °C by the end of the simulation period. The difference in temperature between both cases is correlated to the difference in thermal energy contained in the area below the adaptable insulation layer (from 1 m to 10 m depth).

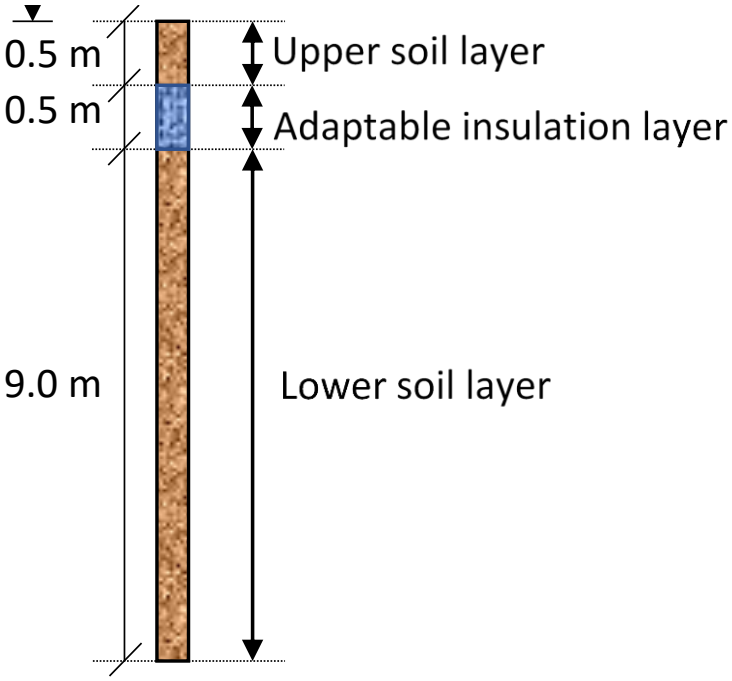

Figure (7.1) Simple schematic representation of the problem domain

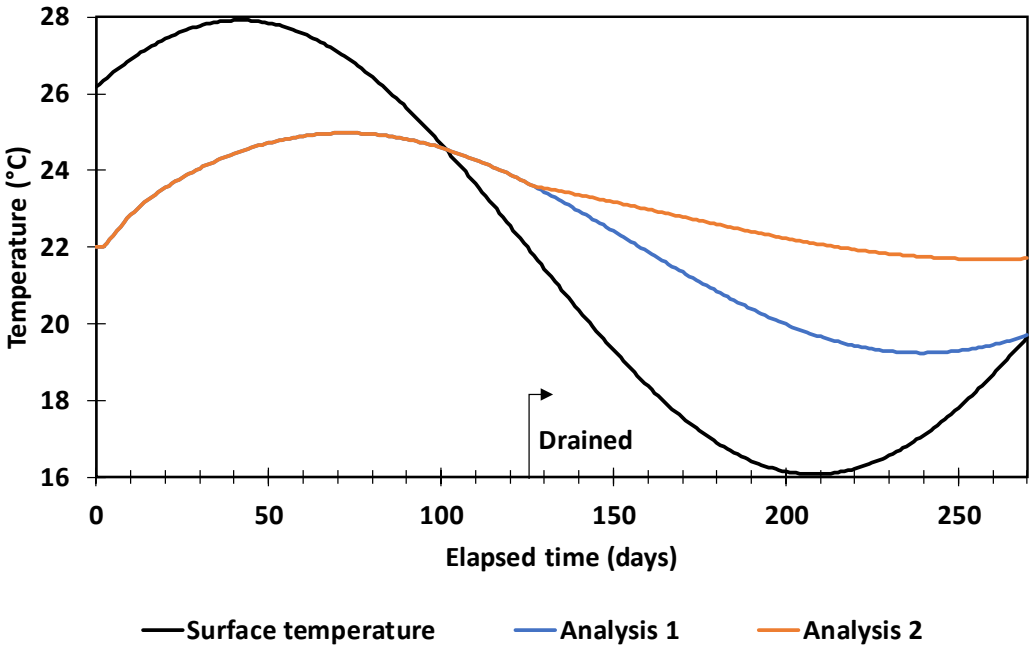

Figure (7.2) Temperature variation at 1.1 m depth for saturated and adaptable insulation layer

On the other hand, Figure (7.3) shows the difference in total thermal energy in the region under the adaptable insulation layer (from 1 m to 10 m depth) between the two analyses.

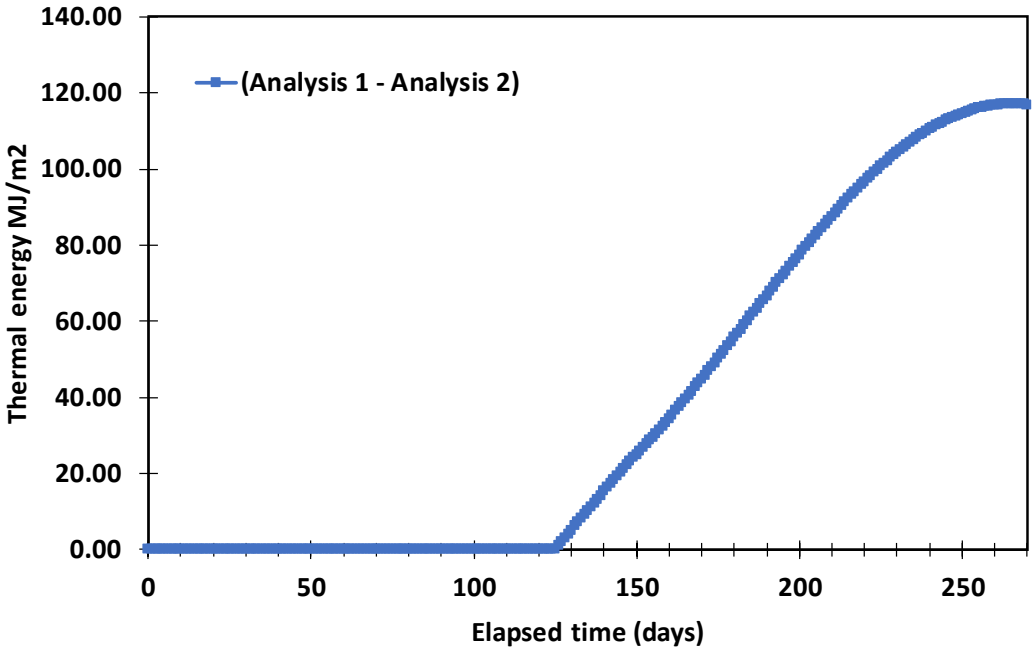

Figure (7.3) Numerical estimation of the difference in the contained thermal energy

It can be seen that before day 125 the differences between the values of thermal energy is equal to zero which is expected since both cases have the same temperature profiles but from day 125 onwards the energy difference steadily increases reaching a maximum of 120 MJ/m^2 towards the end of the simulation period.

Additionally, it is of use to also study and explore the influence of varying the degree of saturation of the drained adaptable insulation layer via a simple parametric study. These variations could arise in practice as a result of the process of installation of the system or from incomplete drainage of the adaptable insulation layer. Additional two cases were introduced to observe the effects as follows:

- Analysis 3: The adaptable insulation layer was assumed to be saturated from day 1 to day 125 and then drained, with degree of saturations of 0.25 from day 125 to day 270.
- Analysis 4: The adaptable insulation layer was assumed to be saturated from day 1 to day 125 and then drained, with a degree of saturation of 0.5 from day 125 to day 270.

The same initial conditions and parameters had been used in each simulation in order to simplify the comparisons between the analyses. Figure (7.4) shows the results obtained from these analyses.

As might be expected the different values of the adaptable insulation layer degree of saturation affects the amount of heat transferred into the soil which in turn is reflected in the amount of energy available for the system. The higher the value of degree of saturation, the higher the amount of heat that is transferred into the lower soil layer. By the end of the analysis, the temperature differences between the fully saturated and half saturated layer reaching almost 0.2 °C (i.e. no thermal benefits gained from using the adaptable insulation layer).

On the other hand, Figure (7.5) shows the difference in total amount of thermal energy available in the region below the adaptable insulation layer (from 1 m to 10 m depth) between the analyses.

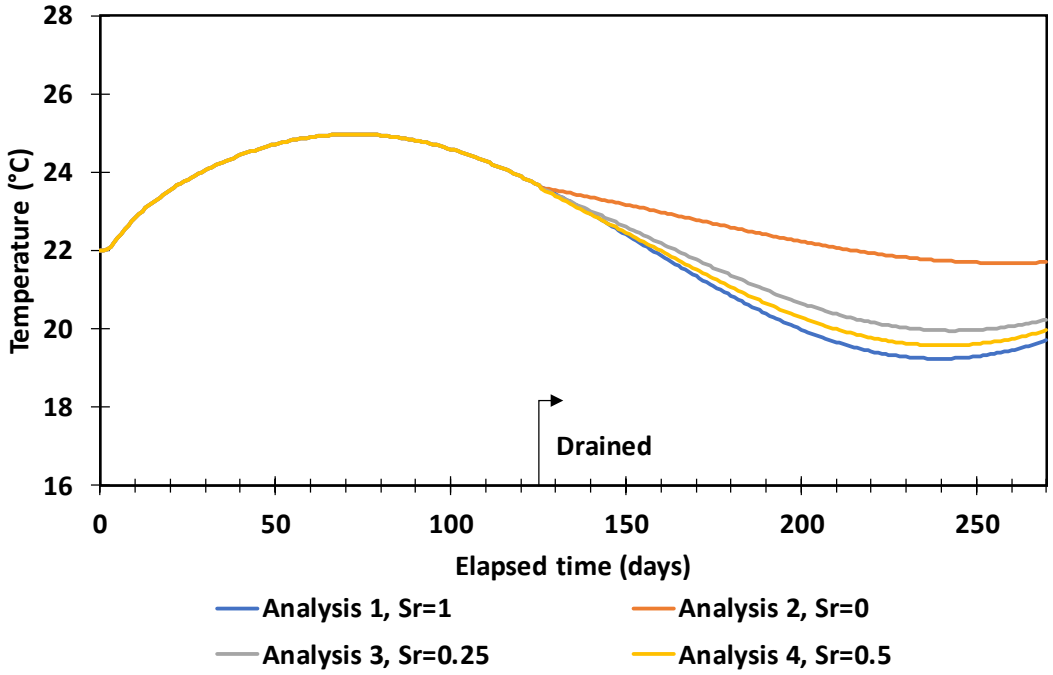

Figure (7.4) Temperature variation at 1.1 m depth for all analysis

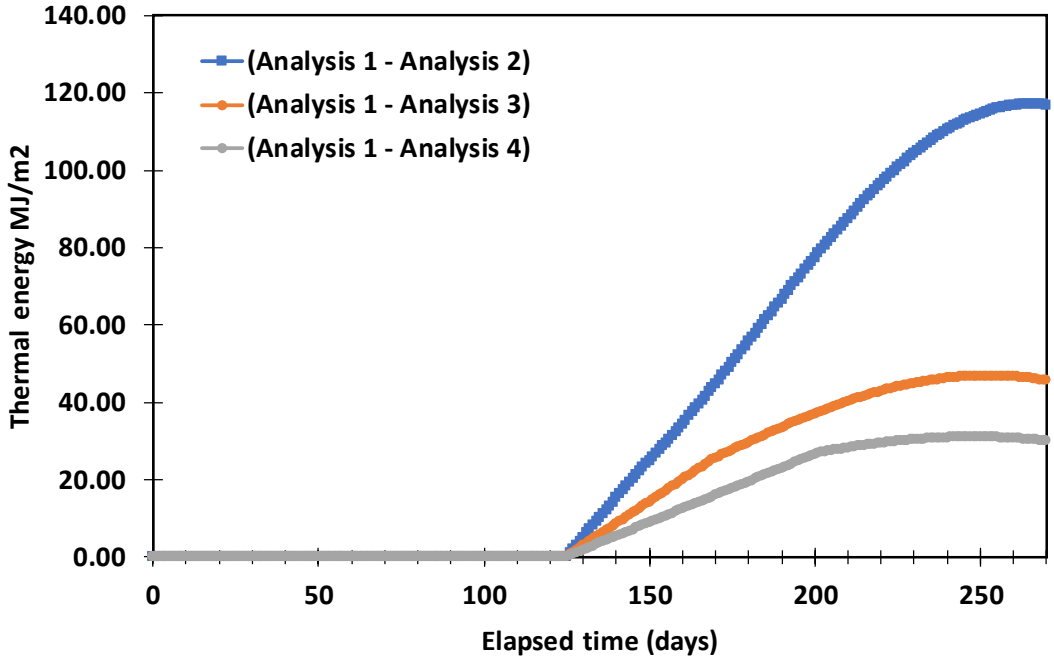

Figure (7.5) Numerical estimation of the difference in the contained thermal energy

As expected, the highest difference is achieved between the two extremes of degree of saturation. Moreover, when a drained layer of S_r = 0.25 was introduced and compared the first analysis, the difference significantly changed from 120 MJ/m^2 to almost 40 MJ/m^2 (i.e. a total loss of 80 MJ/m^2) and the difference became even more when S_r = 0.5. These thermal losses clearly diminish the system behaviour and stability and suggest the importance of carefully selecting and installing the materials used inside the adaptable insulation layer and more importantly for the methods used to drain it.

7.3 Inter-seasonal heat storage system

In this section, a case study that considers the potential inclusion of an adaptable insulation layer in an inter-seasonal heat storage system (based on the TRL system considered in Chapter 6) is presented. In particular a numerical approach based on the theoretical framework model and solution presented previously in Chapter 3 and 4 for the transient heat conduction equation in a soil domain that includes the adaptable insulation layer was applied to the case study of TRL problem used in the previous chapter (shown in Figure (7.6).

In order to facilitate the comparison, the same periods of simulation, initial and boundary conditions of the TRL experiment were used as described in Section 6.3.3. Also, same material parameters of the TRL experiment were used except for the adaptable insulation layer which are based on the values of the glass bead layer presented earlier in Table (5.3) during saturation/dry periods (i.e. 1.35 W/mK and 0.19 W/mK respectively). Two analyses were performed in this study:

- Analysis 1: An analysis that will involve the using of conventional typical system of ISHT that uses buried shallow engineering geoenvironmental devices equipped with heat exchangers.
- Analysis 2: An analysis, with all details as analysis 1 except for the insulation layer which is replaced by the proposed adaptable insulation layer.

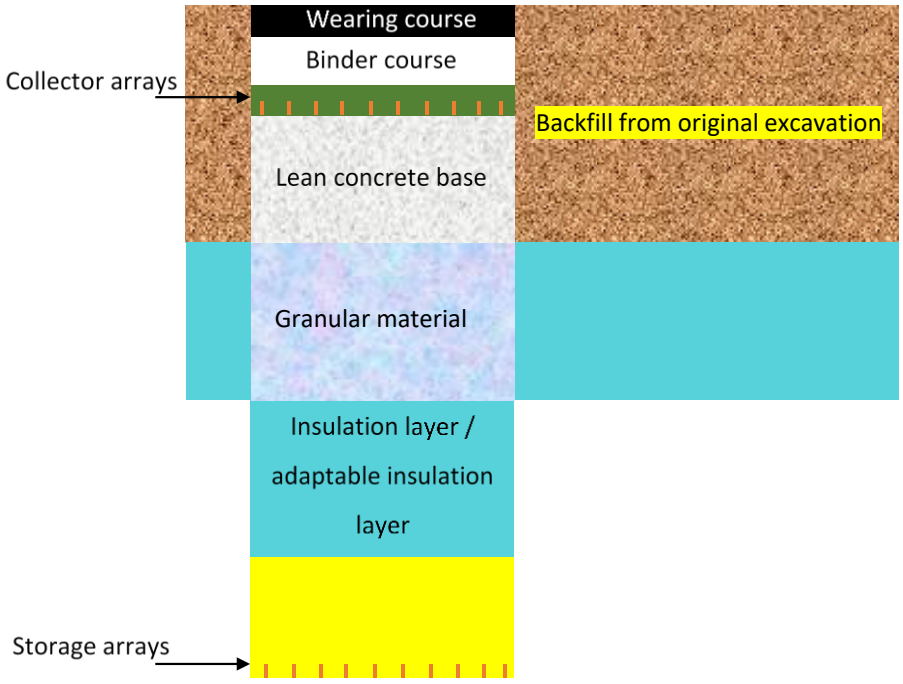

Figure (7.6) Layer distributions in experimental System 2, figure not to scale (Carder *et al.* 2008)

For this purpose, the model presented in Chapter 3 and 4 was used to explore the use of this layer in a more complicated and large-scale problem. Comparisons are made via consideration of the amount of thermal energy available in the system within a 5 m deep section that lies beneath the adaptable insulation layer with a total width size of 8 m (centred on the road centreline).

Figure (7.7) presents the results of this comparison with reference to the typical system (i.e. results obtained from analysis of TRL experiment, previously presented in Section 6.4.2) while Figure (7.8) and Figure (7.9) provide a comparisons between the temperature contours of the same section for the two systems on 31st October 2006 for 10 m depth (i.e. at the end of the 2nd collection period).

It can be seen from Figure (7.7) that the use of the adaptable insulation layer in the system works efficiently and produces slightly greater amounts of energy in the storage area of the system compared to the typical one.

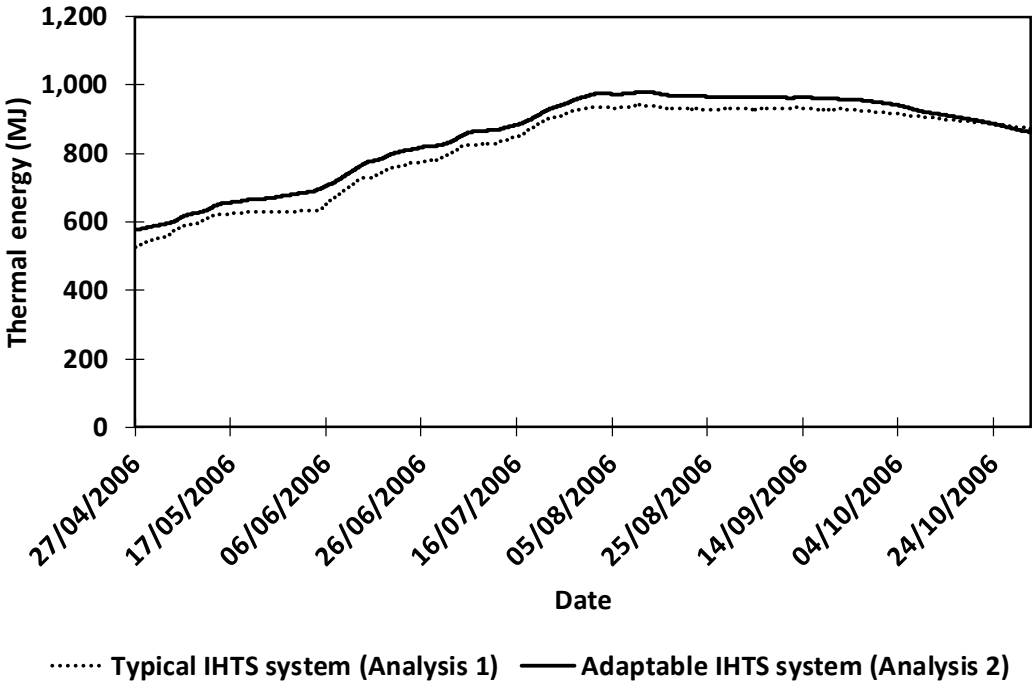

Figure (7.7) Thermal energy comparison between the two systems
(i.e. adaptable insulation layer system and the conventional typical one)

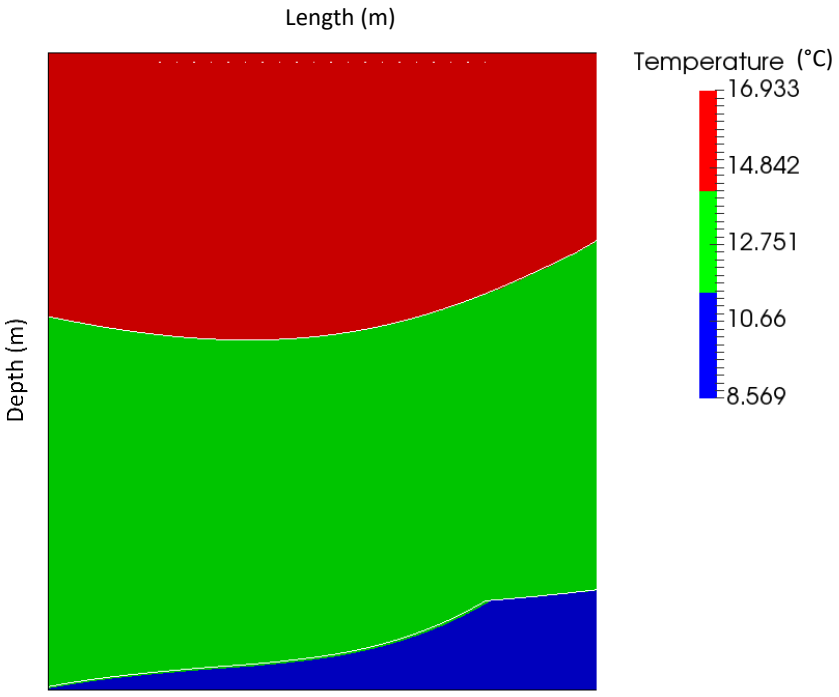

Figure (7.8) Contour temperature of TRL typical system setup (Analysis 1) on 31st October 2006

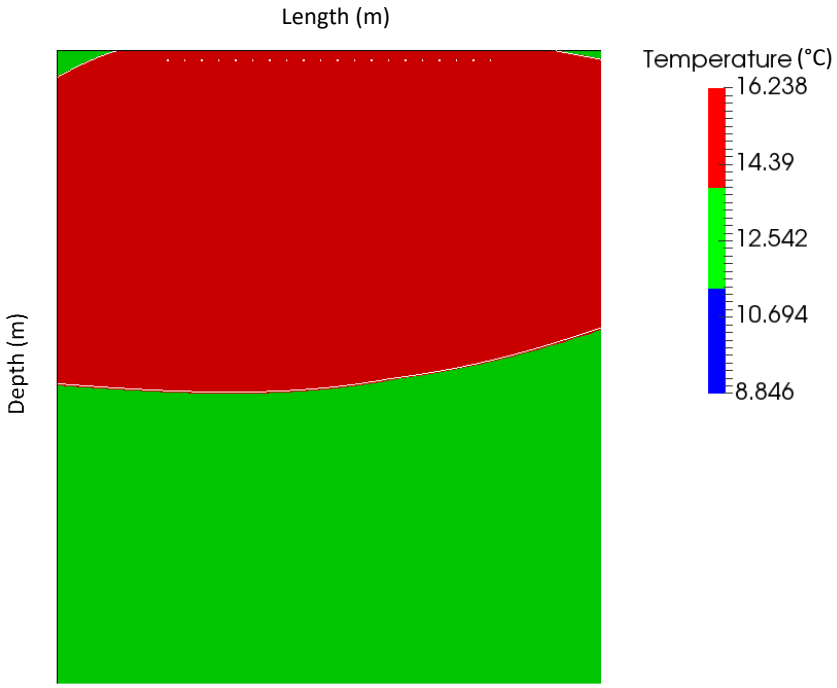

Figure (7.9) Contour temperature of TRL system with adaptable insulation layer (Analysis 2) on 31st October 2006

The ease of heat transfer movement into the soil shows that the proposed system would be able to provide a behaviour that is more efficient. An added benefit is that this increase is achieved without any use of electrical power (required to circulate the water in the typical system). This means that by using the adaptable insulation layer the system efficiency would also be increased as there would be no pumping to be used to circulate the water. Of course, it should be noted that this study focuses on the charging potentials of the adaptable insulation layer and not for the usage of the stored energy. However, there are two possibilities to handle the usage periods, one of the possibilities would be via making use of the conductive properties of the adaptable insulation layer and allow it to transfer heat back to the surface on the usage season through equilibrium, which would be potentially limited as it would be relatively slow. Unfortunately this was beyond the scope of the study and it is carried forward to the suggestions for further work. The second possibility would be via making use of the pumping system only during the usage season, in order to ensure use of system energy at time of need rather than depending on the thermal equilibrium heat movements. Additionally, the behaviour of the adaptable insulation

layer system could be improved via certain aspects such as choosing different soil type or insulation layer properties that will boost the amount of available energy (e.g. enhancing the fluid conductivity used in the adaptable insulation layer).

7.4 Vertical U-tube borehole system

In this section, the use of an adaptable insulation layer to address unbalanced vertical U-tube borehole system is considered. For reasons of expediency, a numerical model was developed using Comsol Multiphysics software. Comsol is a cross-platform finite element analysis solver and Multiphysics simulation software which allows conventional physics-based user interfaces and coupled systems of partial differential equations (PDEs) (Comsol Multiphysics® 2015). The objective of this example is to explore the potential effectiveness of using an adaptable insulation layer to counterbalance the effects of net inter-seasonal injection or extraction of heat energy into a geothermal system. In the following analyses a vertical U-tube borehole system with a 1 m thick adaptable insulation layer placed on top of the underling soil surface with a domain size equal to 70 x 10 X 10 m (the domain of the problem is shown in Figure (7.10)) is considered. An hourly time step with a mesh of a total 101766 4-noded tetrahedral elements was found suitable to represent the system (a fine mesh was required due to the steep temperature gradients developed during operation). In this section, two loading situations are compared (i.e. with net extractions or with net injections) and two system designs considered (i.e. one with adaptable insulation layer and the other without the adaptable insulation layer). This results in four distinct analyses which can be summarised as follows:

- Analysis 1: was not involve using the adaptable insulation layer on a vertical U-tube borehole system subjected to net extractions.
- Analysis 2: was involve using the adaptable insulation layer on a vertical U-tube borehole system subjected to net extractions.
- Analysis 3: was not involve using the adaptable insulation layer on a vertical U-tube borehole system subjected to net injections.

- Analysis 4: was involve using the adaptable insulation layer on a vertical U-tube borehole system subjected to net injections.

It is expected that a geothermal system that is subjected to net thermal extraction or injection will exhibit a gradual decrease or increase in temperature of its soil mass, resulting in progressive long-term deterioration of system efficiency and performance. In order to overcome the limitation associated with net thermal extraction, an adaptable insulation layer is used to provide a high thermal conductivity in the summer and a low thermal conductivity in the winter. On the other hand, for a system with net thermal injection, the adaptable insulation layer is used to provide a high thermal conductivity in winter to increase heat loss and a low thermal conductivity in the summer season to reduce recharge from surface fluxes.

The test spans 5 years of system operation and the values of adaptable thermal conductivity layer used in this problem are based on the glass bead layer properties presented earlier in Table (5.3). The function of the layer would be reflected on the values of the implemented thermal conductivity where it was changed according to the use and needs of the layer/season (i.e. for insulative/drained purposes it was 0.19 W/mK while for conductive/flooded purposes the value is 1.35 W/mK). For net extraction analyses, the high thermal properties would be used in summer (1.35 W/mK) while the low thermal values would be applied in winter (0.19 W/mK). On the other hand, for net injection analyses, the high thermal properties would be used in winter (1.35 W/mK) while the low thermal values would be applied in summer (0.19 W/mK). Initial conditions of the ground and circulating fluid are regarded as being in equilibrium:

$$T_g(x,y,z,t)\big|_{t=0} = T_f(x,y,z,t)_{t=0} \tag{7.1}$$

where T_g (°C) is the ground temperature and T_f (°C) is the circulating fluid temperature. The temperature are defined by the following relationship for the background soil temperature profile $T(z,t)$ at time t=0:

$$T(z,t) = T_{mean} - T_{amp}\, exp\left(z\sqrt{\frac{\pi}{t_0 \alpha_{eff}}}\right)\cos\left(\frac{2\pi t}{t_0} - \varphi + z\sqrt{\frac{\pi}{t_0 \alpha_{eff}}}\right) \quad (7.2)$$

where T_{mean} (°C) is the average annual temperature, T_{amp} (°C) is the amplitude of the annual temperature, t_0 is the period of one year, φ_{eff} is ground thermal diffusivity and φ (m^2/s) is the phase angle.

Far field boundaries of the computational domain are fixed at the background soil temperature profile:

$$T_g(x,y,z,t) = T(z,t) \quad (7.3)$$

The working load for the borehole is represented in a simplified way by a regular sinusoidal load with a period of one year using the following equation:

$$Q_{bh} = \frac{1}{2}A_0 \sin\left(\frac{2\pi}{t_0}t - \varphi'\right) + \frac{1}{2}A_0 \left|\sin\left(\frac{2\pi}{t_0}t - \varphi'\right)\right| \quad (7.4)$$

where A_0 (W) is the highest magnitude of the load in each year and is taken as -3000 for extraction analysis and 3000 for injection, φ' is phase angle to control the beginning time of the system operation and is taken as zero here.

Figure (7.11 and 7.12) shows the applied load for the extraction and injection analyses respectively while Table (7.1) provides parameters values used in the numerical model.

The temperature variation applied at the soil surface is represented as a simplified regular sinusoidal shape with a period of one year as shown in Figure (7.13 and 7.14) refers to the surface temperature variation applied during the net extraction and injection analysis respectively.

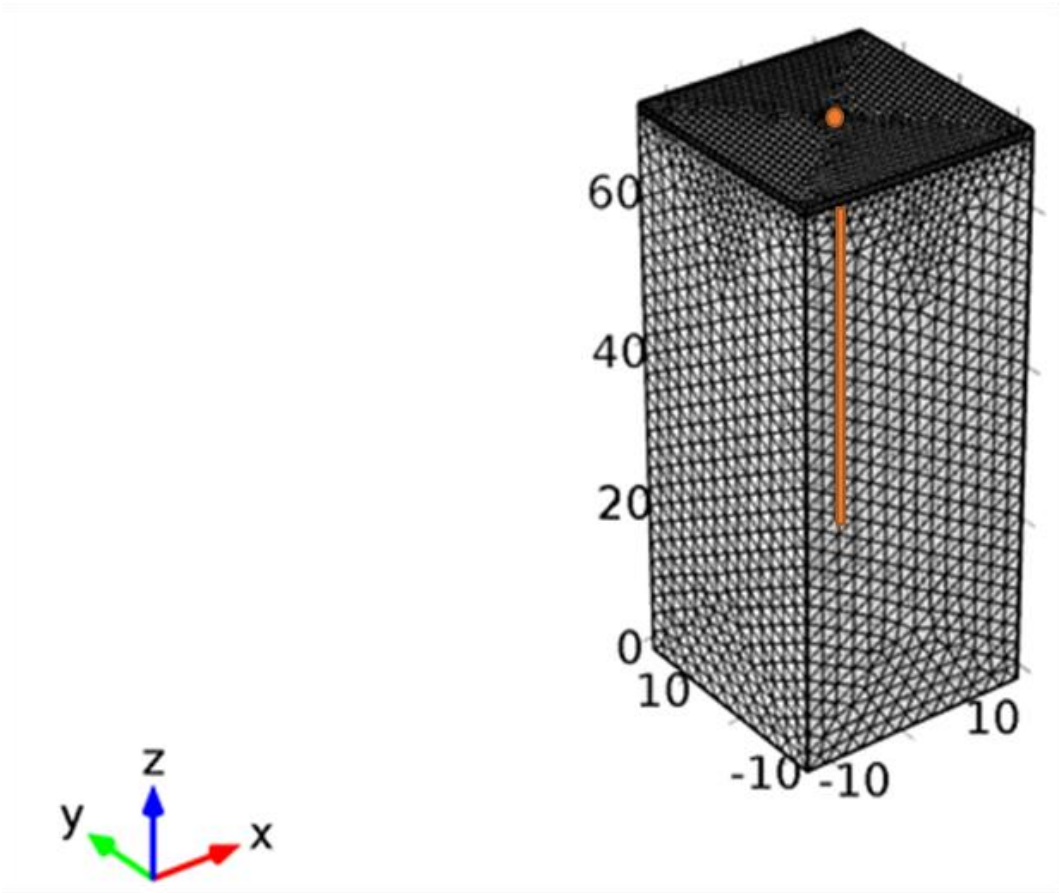

Figure (7.10) Computational domain of U-tube problem (70 x 10 X 10 m)

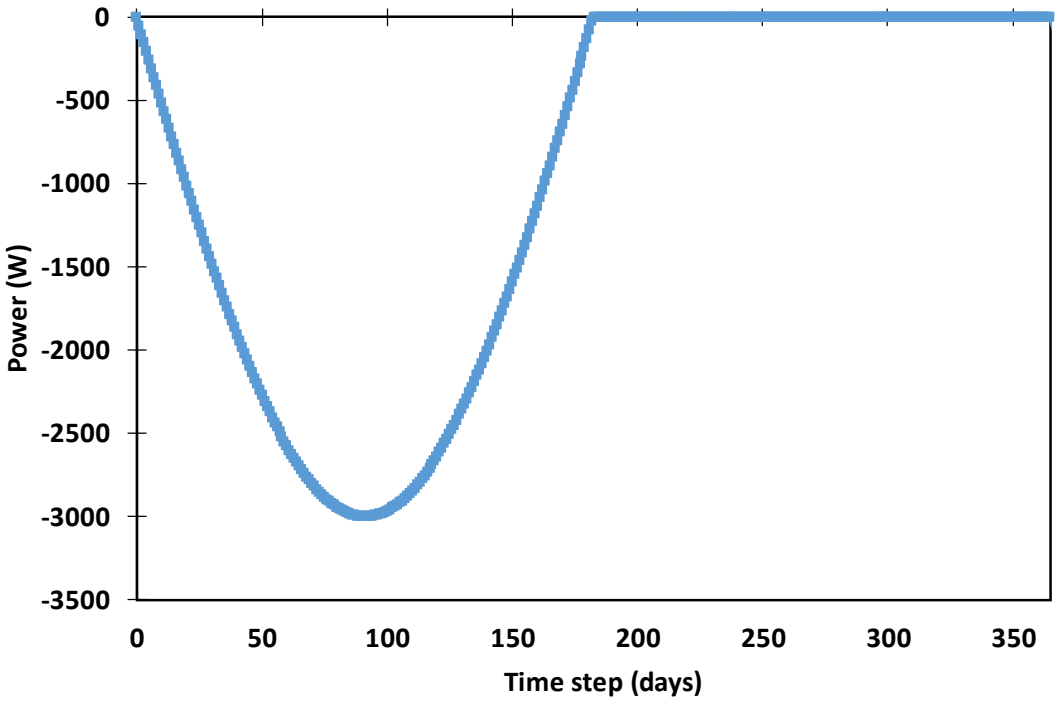

Figure (7.11) Yearly applied load for net extraction analyses (Analysis 1 and 2)

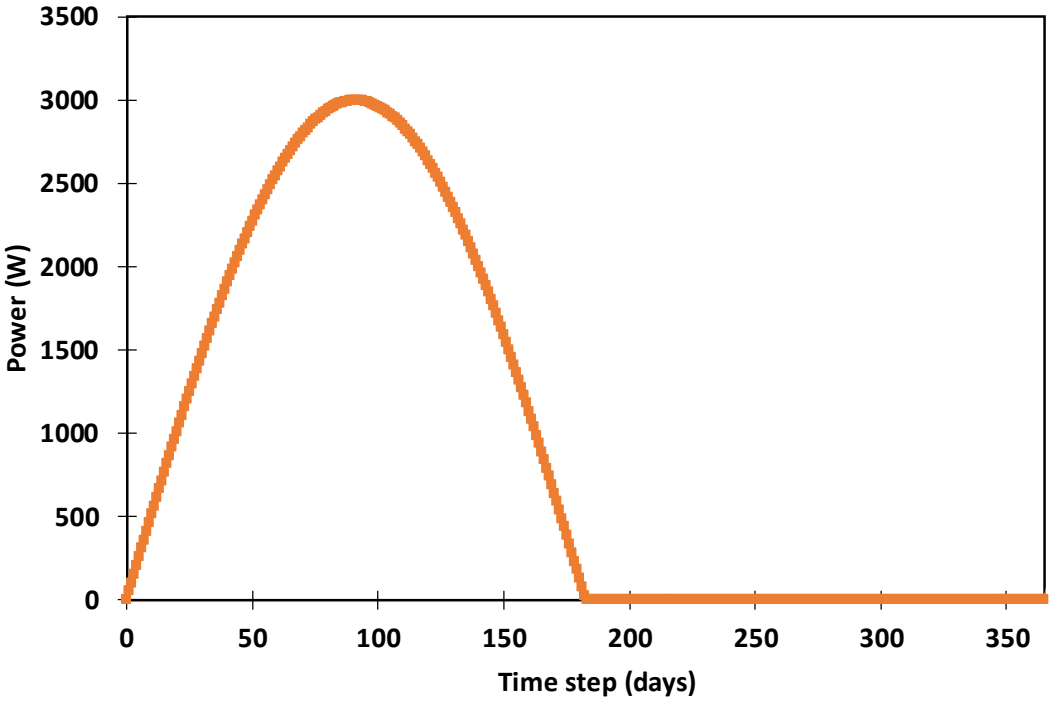

Figure (7.12) Yearly applied load for net injection analyses (Analysis 3 and 4)

Parameters	Value
Ground thermal conductivity	2.38 W/m°C
Ground thermal capacity/conductive	1.9 MJ/m^3 °C
Ground thermal capacity/insulative	0.9 MJ/m^3 °C
Length of pipe	50 m
Internal pipe radius	0.014 m
External pipe radius	0.016 m
Pipe shank spacing	0.06 m
Thermal conductivity of pipe wall	0.6 W/m°C
Fluid velocity inside the pipe	0.4 m/s
Annual average temperature,	18.2 °C
Amplitude of annual temperature,	22.8 °C

Table (7.1) Parameters used in the numerical model

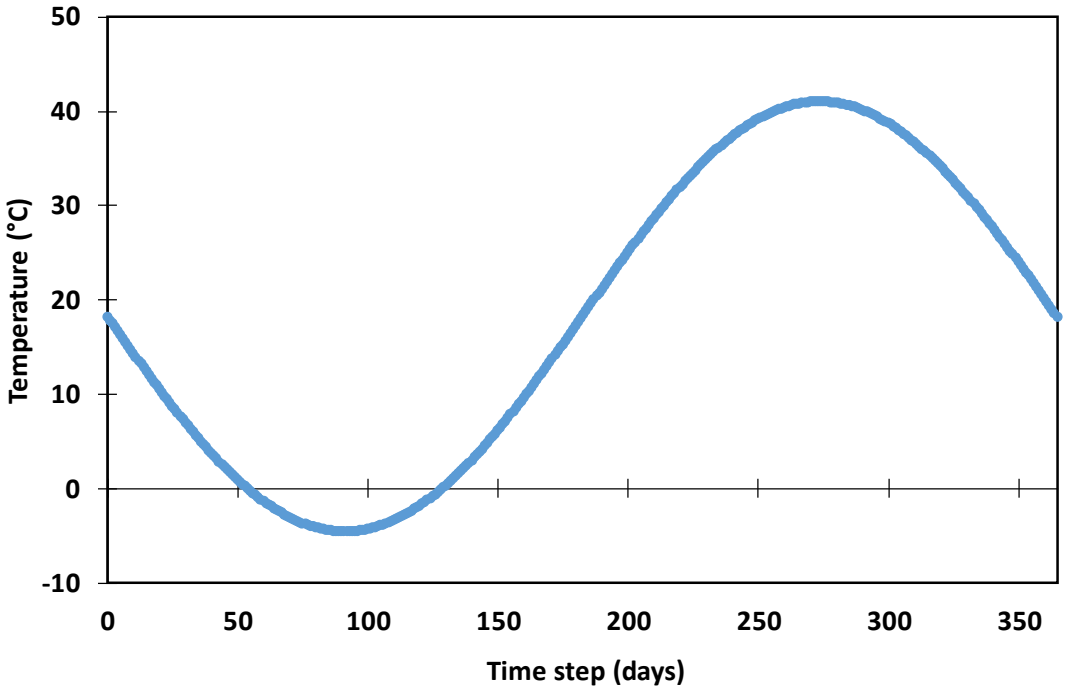

Figure (7.13) Surface temperature variation applied in net extraction analyses (Analysis 1 and 2)

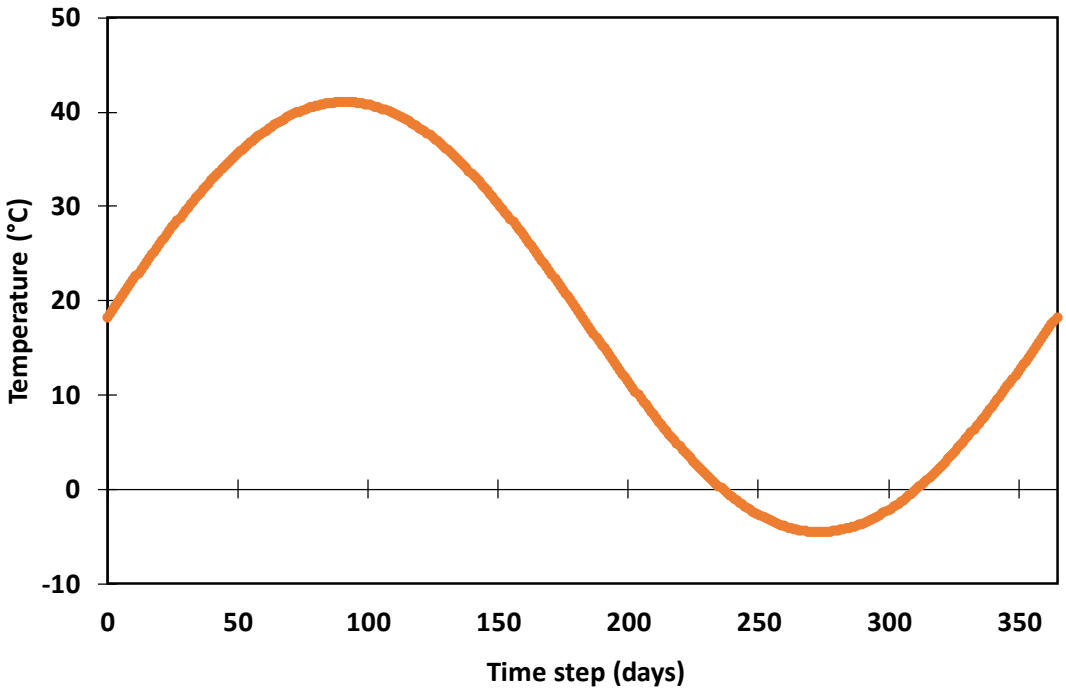

Figure (7.14) Surface temperature variation applied on net injection analyses (Analysis 3 and 4)

Figure (7.15) shows the results obtained for the net thermal extraction case (Analysis 1 and 2) while Figure (7.16) focuses on the maximum and minimal temperature points of each year in order to facilitate and ease the comparison. On the other hand, Figure (7.17) presents the results for net injection analysis (Analysis 3 and 4) with Figure (7.18) shows the maximum and minimum temperature variation with time during the analysis. It can be seen form Figure (7.15 and 7.16) that when a system that was not equipped with an adaptable insulation layer is subjected to net heat extractions it experiences peak temperature decreases over each year, also, it can be noted that the differences between the first two years of operation is higher compared to the rest of the analysis period.

The difference between the first two years of operations was 0.6 °C and kept on decreasing over each year with a rate of ~0.25 °C. On the other hand when the proposed system of adaptable insulation layer was used the system became more stable and the differences between the first two years of operation was as low as 0.19 °C and for the rest period of operation the differences was as low as 0.05 °C.

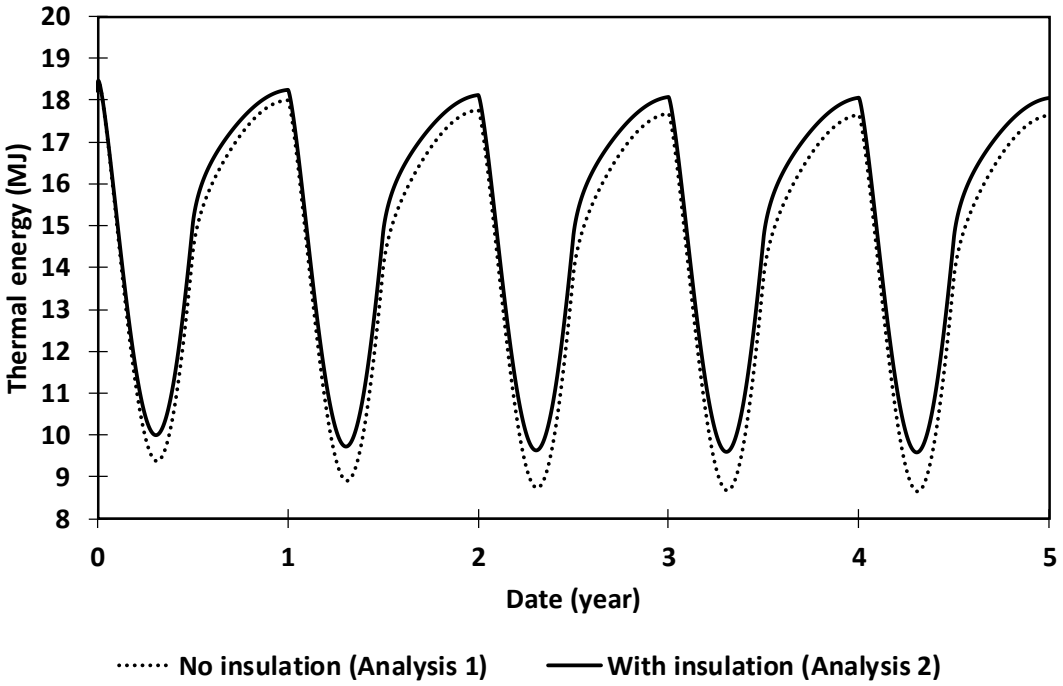

Figure (7.15) Comparisons of two systems subjected to over extractions of heat

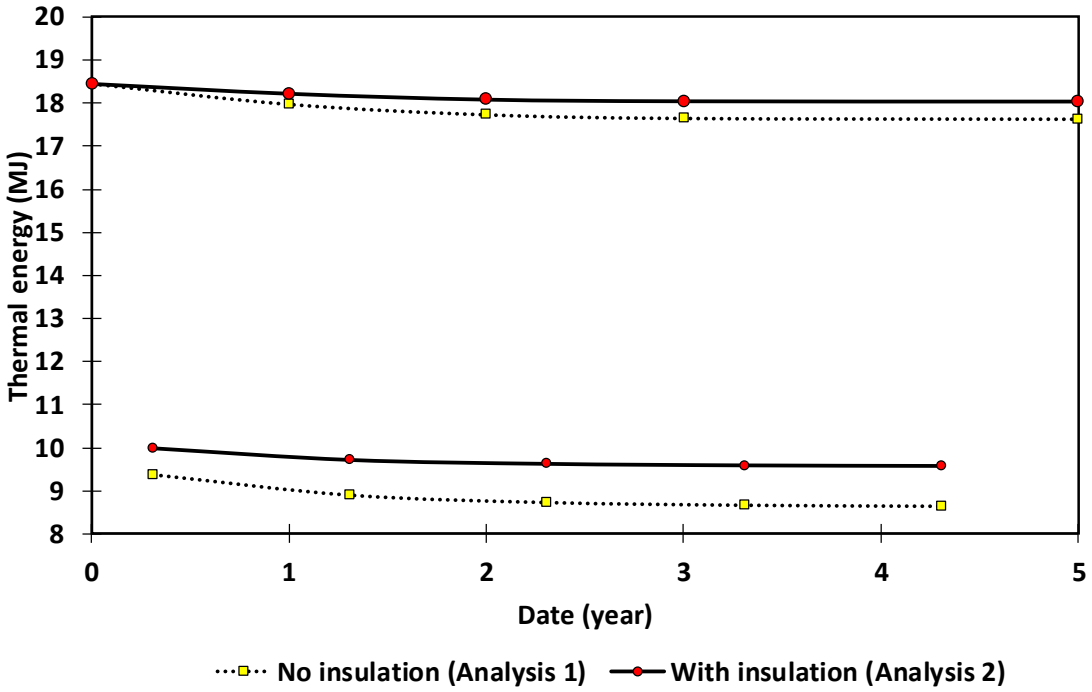

Figure (7.16) Comparisons of maximum and minimum temperature variation with time for net heat extractions analysis

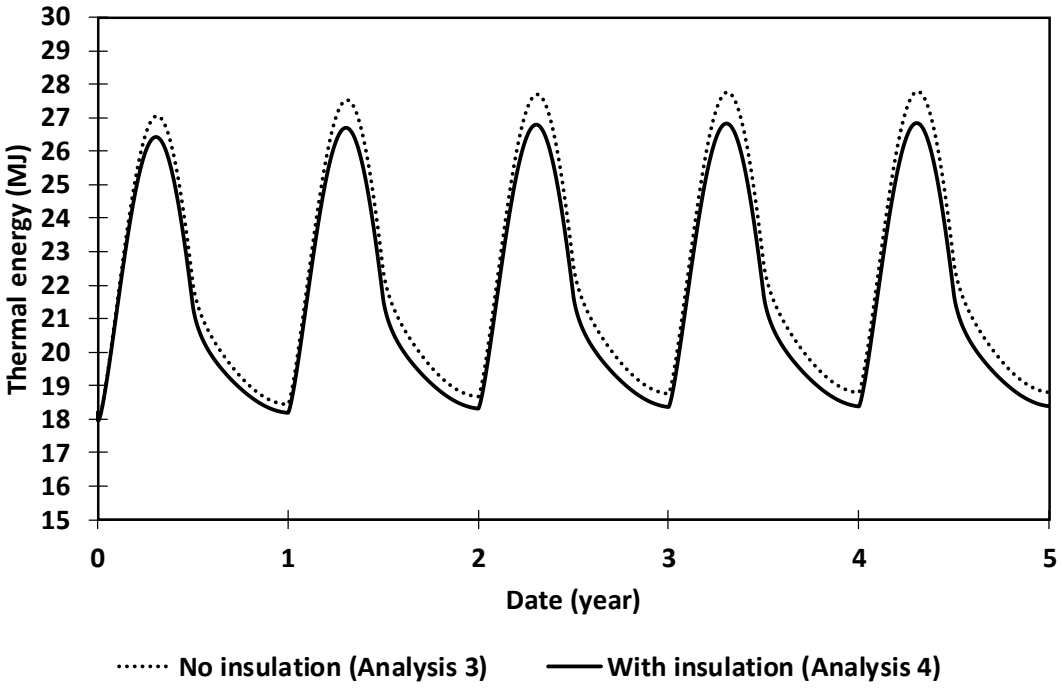

Figure (7.17) Comparisons of two systems subjected to over injection of heat

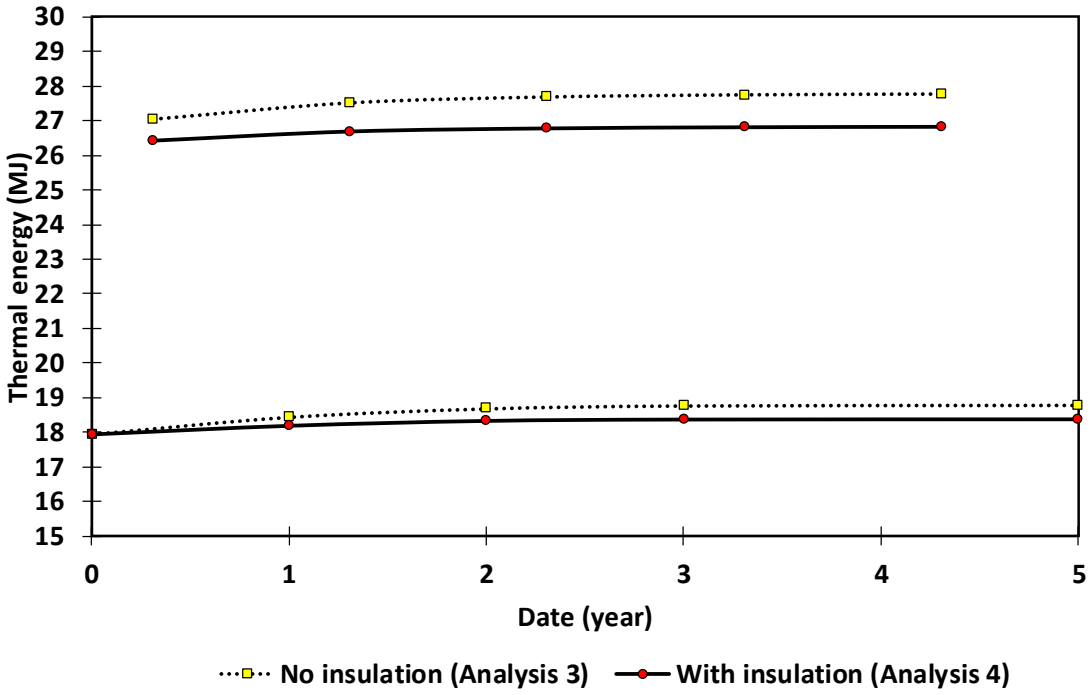

Figure (7.18) Comparisons of maximum and minimum temperature variation with time for net heat injections analysis

In contrast Figure (7.17 and 7.18) show that when a system that is not equipped with an adaptable insulation layer is subjected to net heat injections it experiences an increasing temperature over each year of use.

The notable difference related as well to the first two years of use where a difference of 0.55 °C was observed while for the rest of the simulation period the difference was ~0.16°C. In comparisons, the use of the adaptable insulation layer allow the system to recover from the continuous heat injection as the difference between the first two years was as low as 0.28 °C while for the rest of the simulation period the difference rate was 0.01 °C.

In summary, the analyses clearly shows the benefits of utilizing the adaptable insulation layer to balance such type of systems. It is clear that a system subjected to a long term load imbalance will suffer from decreasing efficiency during each year of use, while introduction of an adaptable insulation layer could compensate for the this issue.

7.5 Conclusions

This chapter presented the results obtained from the use of the developed numerical models to investigate the potential impact of adaptable insulation layer on thermal system performance. A 1D numerical model has been used to describe an up-scaled hypothetical soil column subjected to a process of seasonal thermal charge and discharge. Results show that the use of the adaptable insulation layer could allow the soil to keep a temperature up to 2.4 °C higher compared with a layer of constant thermal conductivity that translates in 120 MJ/m^2 of additional thermal energy in the storage region. Also, a simple parametric study was performed to explore the effect of degree of saturation on the adaptable insulation layer behaviour. The results shows the critical importance of preventing excess thermal bridges availability in the layer that would results because of unsuccessful drainage of the layer for example.

Moreover, the use of the adaptable insulation layer in a large-sale experiment was introduced in this chapter and it provides promising results. The results show that use of the adaptable insulation layer on a collection period would enhanced the amount of harvested energy due to the relatively easier heat transfer method between the system layers.

Additionally, consideration of the use an adaptable insulation layer in a U-tube thermal system subjected to an imbalance load was made. Comparisons of two system performance shows that the use of the adaptable insulation layer can result in improved system efficiency and long term sustainability.

In summary, it has been shown that by controlling the thermal properties of an adaptable insulation layer, it is possible to influence the thermal energy transferred to or from selected regions in the ground. The proposed adaptable insulation layer could potentially reduce costs associated with the placement of active thermal energy storage systems (e.g. heat exchangers) and increase the efficiency of existing ground source heat pump systems, promote the development of new ground heat storage devices and mitigate environmental impacts associated with thermal disequilibrium due to thermal exploitation of the ground.

7.6 References

Carder, D. R., Barker, K. J., Hewitt, M. G., Ritter, D. and Kiff, A. 2008. *Performance of an interseasonal heat transfer facility for collection, storage, and re-use of solar heat from the road surface*. Transport Research Laboratory.

Comsol Multiphysics®. 2015. *COMSOL Multiphysics Reference Manual*. version "5.2". Available at: https://www.comsol.com/

Chapter 8: Conclusions, Suggestions for Future Work and Recommendations

8.1 Objectives summary

Thermal energy storage is one of the technologies that may contribute to energy conservation through peak energy load alleviation and shifting energy demand. In the context of this thesis, thermal energy storage solutions with their categories, characteristics and certain applications have been briefly described. One of the objectives has been completed via providing an overview of the scientific literature available related to the storage of thermal energy in soils using shallow heat exchangers. The topics covered by literature review included: (i) heat transfer in soil and factors affecting it, (ii) the main physical properties governing heat transfer in the ground, (iii) the description of three main formulations describing the energy interactions at the soil surface for different soil covers, (iv) analytical methods for the estimation of the soil temperature profiles and, (v) a brief overview of some scientific works regarding the numerical treatment of buried thermal devices. This understanding is essential in building the necessary knowledge related to such systems.

A theoretical framework and solution has been introduced that defines governing equations for heat transfer within soil, heat advection within pipe systems and derived the equations defining the relation between soil and pipes. Energy balance equations have been used to define the boundary conditions for selected soil surface cases (bare soil, fully or partially covered by a layer of vegetation and surface snow). The implications of ground freezing effects inside the soil and how to capture them were also covered which helped address limitations associated with previous models.

One of the main objectives of this thesis was to provide a numerical and experimental study of near surface ground energy systems including the use of an innovative adaptable insulation layer. The aforementioned combinations considered are unique, as they will enhance the fundamental understanding of thermal systems and explore

possibilities of improving it. The main objective of the proposed new system was to show the possibility of creating a much simpler form of heat storage system than the other more conventional ones that use buried shallow devices equipped with heat exchangers. Five different set of experimental test results were presented, where the early two sets were trial tests which provided the basis for the subsequent three seasonal tests which were perform later to observe the system behaviour over long and extreme conditions. The experimental results showed the potential of the proposed system. The bench-scale experiment was also able to capture the so-called zero curtain behaviour (where the latent heat of fusion is being removed with little or no change in temperature of the system).

A 1D and 2D numerical model based on the theoretical framework has been introduced and validated against the laboratory and large-scale experimental studies respectively. The 1D model proved to be able to successfully capture the system behaviour via consideration of the amount of thermal energy available in the system. Relatively more accurate representations of the porous material were made considering its components (air, water and solids) and the latent heat and the 'zero curtain' phenomena (where the latent heat of fusion is being removed with little or no change in temperature of the system). The developed 2D model was used to represent the process of ground thermal energy storage using buried shallow devices equipped with heat exchangers. The model was applied to estimate soil temperature variations of a large-scale demonstration project on inter-seasonal heat storage beneath a paved highway. In particular, the research focused on the representation of surface snow and ground freezing presence in the system which previous studies fail to capture.

Finally, the developed and validated numerical models were used to investigate the potential impact of the proposed adaptable insulation layer on different thermal system performance. The 1D numerical model has been used to describe a hypothetical soil column subjected to a process of seasonal thermal charge and discharge on large-sale numerical experiment. Moreover, the use of the adaptable insulation layer was incorporated into the 2D model and compared against large-sale

experimental study (TRL experiment). Both results prove that the use of the adaptable insulation layer on a collection period would enhanced and increased the amount of harvested energy due to the relatively easier heat transfer method between the system layers. In addition, the use of the adaptable insulation layer was proposed to overcome problems often associated with a U-tube thermal and how to avoid it using the proposed layer.

In summary, the use of the adaptable insulation layer has shown that by controlling the thermal properties of an adaptable insulation layer, it is possible to influence the thermal energy transferred to or from selected regions in the ground. The proposed layer could potentially reduce costs associated with the placement of active thermal energy storage systems (e.g. heat exchangers) and increase the efficiency of existing ground source heat pump systems, promote the development of new ground heat storage devices and mitigate environmental impacts associated with thermal disequilibrium due to thermal exploitation of the ground.

8.2 Main findings

The main findings presented in this thesis are summarized as follows:

- The overall objective of this thesis has been to shed light and provide novel knowledge in the field of thermal energy systems especially the ones that incorporates thermal buried shallow engineering geoenvironmental devices equipped with heat exchangers (inter-seasonal heat transfer system) in terms of overall collection and storage performance with a special attention being given to certain factors that affect the system behaviour (i.e. surface snow and ground freezing), and investigating the system coefficient of performance.
- In the context of this thesis, new knowledge is brought forward on many levels that includes the material, the components, and on the system level of ISHS system integration to the built environment via proposing a novel design to enhance its behaviour. The use of the innovative system was found to be effective and shows promising results suggesting that it should be applied to different types of energy

system. The cheap and readily available material proves the effectiveness of creating such system instead of the conventional typical ones that uses pipes heat exchangers.

- The 1D numerical model for the transient heat transfer equation proved to be able to successfully capture the system behaviour and would be used to explore the impact of different scenarios had on the seasonal variations of thermal energy stored in the ground. In addition, the model was capable of representing different boundary conditions, multi-layered domain (each holds its own characteristics thermal properties), ground freezing availability and the amount of thermal energy available in the system. In general, the model will provide a significant decision-making tool for analysing such systems.
- The 2D numerical model proved to be capable of successfully capturing and representing the process of ground thermal energy storage carried out by buried engineering geoenvironmental devices. The proposed model provides more accurate results than the previous model and more importantly it incorporates the snow surface and ground freezing effect on the system performance.
- The use of the adaptable insulation layer on different scenarios proves that the layer would enhance the thermal energy storage and increase the efficiency of existing ground source heat pump systems, promote the development of new ground heat storage devices and mitigate environmental impacts associated with thermal disequilibrium due to thermal exploitation of the ground.

8.3 Limitations

The limitations associated with the proposed study could be summarized in the following points:

- No mechanical deformations or chemical reactions were considered in the development of the theoretical framework.
- The temperature and thermal properties of the snow were consider constant during the commencing periods in the simulation analysis.
- The study only considers isotropic properties of soil.

- The scope of the study explores the benefits gained from using the adaptable insulation layer in the collection period.
- Uncertainties associated with the thermal properties of used materials.
- The study did not explore the use of different soil types in the bench-scale experiment.
- The bench-scale study considers compressed seasonal tests which lasts for only 28 consecutive days.
- A limited number of bench-scale experimental tests are performed.
- The bench-scale experimental study focuses on one-dimensional heat transfer in soil.

8.4 Future work and recommendations

8.4.1 General recommendations:

Based on the results obtained in this thesis the following general recommendations are suggested:

- In order to meet the targeted goal for renewable sources set by the UK government, there is a clear merit in continued research and development on this topic looking for new ideas due to its low carbon footprint and the fact that it is likely to become dominant over depleted sources.
- Assessment of the proposed adaptable insulation layer concept within a large-scale-case study is needed. This could help extending the application to reach motorways, airport runways or near-building heat source.
- The presence of snow cover on the surface would insulate the layer underneath and affects the shallow geoenvironmental heat storage system installed beneath the surface. Further study is required to investigate this effect.
- It is worth testing the installation of heat pipe array at a shallower depth as that could improve the efficiency of both the heat collection and winter maintenance procedure.

8.4.2 Recommendations related to the modelling process

The proposed future work related to the numerical work is in part related to the limitations listed previously and could be summarized as follows:

- Improving the prediction of heat energy transfer interactions under extreme weather conditions (snow events) via using more complex representations of snow.
- Explore the use of the proposed adaptable insulation layer for other different types of thermal systems.
- Test the effects of different parameters on the amount of thermal energy available for the system (i.e. different soil types, different insulation layer components or testing the thickness or position of the insulation layer).
- Expand the developed numerical model to include more heat transfer systems.

8.4.3 Recommendations related to the experimental work

The recommendations associated with the experimental work of this thesis is also in part related to the limitations listed previously and could be summarized as follows:

- Explore the use of the proposed adaptable insulation layer for different types of thermal energy systems both on laboratory and field-scale experiments.
- Test the effect of different parameters has on the amount of thermal energy available for the system (i.e. different soil types, different insulation layer components).
- Test the effect of adaptable insulation layer thickness or position on the overall system behaviour.
- Explore and design possible methods to facilitate the use the harvested energy in usage periods.
- Expand the laboratory experiments to include different boundary conditions applied to the surface for longer periods (full seasonal experiments).
- Study the thermal soil behaviour in the lateral direction.

- Experimentally measure the thermal properties of any used materials.
- Conduct a large-scale experiment to test the use of the adaptable novel layer.

Appendix A: Thermal Properties of Water-Ethylene-Glycol Mixtures

This appendix presents thermal properties of a fluid that is commonly used in thermal engineering applications: water-ethylene-glycol mixtures. The equations and coefficients used are based on the product description provided by MEGlobal (2008).

A.1 Thermal conductivity

The thermal conductivity λ_{eg} (W/mK) of an aqueous ethylene glycol solution is given by the equation:

$$\lambda_{eg} = A + BT + CT^2 \qquad \text{(A.1)}$$

where all the coefficients depend on the percentage of ethylene glycol present on the solution and are available on the cited reference.

Table (A.1) shows the variation of the thermal conductivity of an ethylene-glycol mixture at representative temperatures. The thermal conductivity of the solution decreases with the percentage of ethylene glycol present in it for the same temperature and increases with temperature for the same content of ethylene glycol.

	Thermal conductivity (W/mK)		
Temperature (°C)	10 %	20 %	30 %
5	0.5343	0.5022	0.4717
15	0.5485	0.5127	0.4787
25	0.5616	0.5221	0.4849

Table (A.1) Values of thermal conductivities of aqueous ethylene glycol solutions for different percentages of ethylene glycol and different temperatures

A.2 Specific heat capacity

The specific heat capacity c_{eg} (J/kgK) of an aqueous ethylene glycol solution is given by:

$$c_{eg} = A + BT + CT^2 \quad \text{(A.2)}$$

where all the coefficients depend on the percentage of ethylene glycol present on the solution and are taken from the same reference. Table (A.2) shows the variation of specific heat capacity of an ethylene-glycol mixture at representative temperatures. The specific heat capacity of the solution decreases with the percentage of ethylene glycol present in it for the same temperature and increases with temperature for the same content of ethylene glycol.

	Specific heat capacity (J/kgK)		
Temperature (°C)	10 %	20 %	30 %
5	4074.90	3926.20	3774.26
15	4082.92	3942.93	3795.85
25	4091.41	3959.66	3817.43

Table (A.2) Values of specific heat capacities of aqueous ethylene glycol solutions for different percentages of ethylene glycol and different temperatures

A.3 Density and specific gravity

The specific gravity γ_{eg} of the fluid is given by the equation:

$$\gamma_{eg}\left(\frac{T}{15.5\ C}\right) = A + Bx + Cx^2 \quad \text{(A.3)}$$

where x is the percentage of ethylene glycol present in the solution where all the coefficients depend on the temperature and are taken from the same reference.

Table (A.3) and Table (A.4) shows the variation of specific gravity and density of an ethylene-glycol mixture at representative temperatures. The specific gravity and density of the solution increase with the percentage of ethylene glycol present in it for the same temperature while the behaviour is non-linear with temperature.

	Specific gravity		
Temperature (°C)	10 %	20 %	30 %
5	1.013	1.029	1.045
15	1.042	1.028	1.042
25	1.010	1.024	1.037

Table (A.3) Values of specific gravity of aqueous ethylene glycol solutions for different percentages of ethylene glycol and different temperatures

	Density (kg/m^3)		
Temperature (°C)	10 %	20 %	30 %
5	1011.79	1027.76	1043.74
15	1012.04	1026.76	1040.75
25	1008.80	1022.77	1035.75

Table (A.4) Values of density of aqueous ethylene glycol solutions for different percentages of ethylene glycol and different temperatures

A.4 Dynamic viscosity

The dynamic viscosity μ_{eg} (kg/ms) for an aqueous ethylene glycol solution is given by:

$$\log_{10}(\mu_{eg}, cP) = A - B/(x + C) \quad \text{(A.4)}$$

where x is the percentage of ethylene glycol present in the solution where all the coefficients depend on the temperature and are taken from the same reference.

Table (A.5) shows the variation of viscosity of an ethylene-glycol mixture at representative temperatures. The viscosity of the solution increases with the percentage of ethylene glycol present in it for the same temperature and decreases with temperature for the same content of ethylene glycol.

	Dynamic viscosity $x10^3$ (kg/ms)		
Temperature (°C)	10 %	20 %	30 %
5	2.060	2.704	3.604
15	1.450	1.882	2.476
25	1.140	1.456	1.883

Table (A.5) Values of density of aqueous ethylene glycol solutions for different percentages of ethylene glycol and different temperatures

A.5 References

MEGlobal (2008). *Ethylene Glycol - Product Guide [Brochure]*.

Appendix B: Convective Heat Transfer Coefficient Inside a Pipe

This appendix explores the impact of varying fluid temperature and mean velocities on the convective heat transfer coefficient between the pipe wall and the fluid. For the purpose of this study, representative mean velocities (0.10 m/s, 0.14 m/s and 0.20 m/s) and temperatures (5 ˚C, 15 ˚C and 25 ˚C), thermal properties of ethylene glycol solutions presented in Appendix A and assumed values of 0.0125 m and 0.002 m for the external pipe radius and pipe wall thickness are used in the theoretical formulation introduced in Section 3.6.1.

B.1 Reynolds number

Table (B.1), Table (B.2) and Table (B.3) show values for Reynolds number calculated using equation (3.33) at different mean velocities and percentages of ethylene glycol present in the aqueous solution inside the pipe. Many of the values for the Reynolds number are expected to be in the range defined as transitional flow ($2000 < Re < 4000$).

	Reynolds number - (10%)		
Mean Velocity (l/s)	5°C	15°C	25°C
0.10	3,067.09	4,354.58	5,522.11
0.14	4,293.92	6,096.42	7,730.95
0.20	6,134.17	8,709.17	11,044.21

Table (B.1) Values of Reynolds number at different temperatures and mean velocities corresponding to some aqueous solutions with 10% ethylene glycol.

	Reynolds number - (20%)		
Mean Velocity (l/s)	5°C	15°C	25°C
0.10	2,373.53	3,403.94	4,383.92
0.14	3,322.95	4,765.52	6,137.49
0.20	4,747.06	6,807.88	8,767.85

Table (B.2) Values of Reynolds number at different temperatures and mean velocities corresponding to some aqueous solutions with 20% ethylene glycol.

	Reynolds number - (30%)		
Mean Velocity (l/s)	5°C	15°C	25°C
0.10	1,807.68	2,623.21	3,434.16
0.14	2,530.75	3,672.50	4,807.83
0.20	3,615.36	5,246.42	6,868.32

Table (B.3) Values of Reynolds number at different temperatures and mean velocities corresponding to some aqueous solutions with 30% ethylene glycol.

B.2 Prandtl number

Table (B.4) show results for Prandtl number calculated using equation (3.35) for different percentages of ethylene glycol present in the solution and for different temperatures.

	Prandtl number		
Temperature (°C)	Ethylene Glycol (10%)	Ethylene Glycol (20%)	Ethylene Glycol (30%)
5	15.70	21.14	28.83
15	10.80	14.48	19.64
25	8.31	11.05	14.83

Table (B.4) Values of Reynolds number at different temperatures and mean velocities corresponding to some aqueous solutions with 30% ethylene glycol

B.3 Friction factor

Table (B.5), Table (B.6) and Table (B.7) show results for the friction factor calculated using equations (3.36), (3.37) and (3.38), and the Reynolds values presented in Section B.1.

	Friction factor f - (10%)		
Mean Velocity (l/s)	5°C	15°C	25°C
0.10	0.033861	0.040332	0.037455
0.14	0.040512	0.036347	0.033880
0.20	0.036280	0.032736	0.030621

Table (B.5) Values of friction factor at different temperatures and mean velocities corresponding to some aqueous solutions with 10% ethylene glycol.

	Friction factor *f* - (20%)		
Mean Velocity (l/s)	5°C	15°C	25°C
0.10	0.03115	0.03626	0.04025
0.14	0.03564	0.03920	0.03627
0.20	0.03925	0.03517	0.03267

Table (B.6) Values of friction factor at different temperatures and mean velocities corresponding to some aqueous solutions with 20% ethylene glycol.

	Friction factor *f* - (30%)		
Mean Velocity (l/s)	5°C	15°C	25°C
0.10	0.03540	0.03166	0.03650
0.14	0.03139	0.03848	0.03909
0.20	0.03799	0.03805	0.03508

Table (B.7) Values of friction factor at different temperatures and mean velocities corresponding to some aqueous solutions with 30% ethylene glycol.

B.4 Nusselt number

Table (B.8), Table (B.9) and Table (B.10) show results for the Nusselt number obtained using equation (3.34) and the results for presented in previous sections for Reynolds number, Prandtl number and friction factor. Note that the relations for laminar flows are not required since the assumed conditions for the fluid put it in transitional and turbulent states.

	Nusselt number *Nu* - (10%)		
Mean Velocity (l/s)	5°C	15°C	25°C
0.10	25.66	40.55	47.60
0.14	45.45	57.79	66.46
0.20	66.38	81.95	92.93

Table (B.8) Values of Nusselt number at different temperatures and mean velocities corresponding to some aqueous solutions with 10% ethylene glycol.

	Nusselt number *Nu* - (20%)		
Mean Velocity (l/s)	5°C	15°C	25°C
0.10	18.04	30.20	41.17
0.14	32.98	49.55	58.66
0.20	56.23	71.64	83.16

Table (B.9) Values of Nusselt number at different temperatures and mean velocities corresponding to some aqueous solutions with 20% ethylene glycol.

	Nusselt number *Nu* - (30%)		
Mean Velocity (l/s)	5°C	15°C	25°C
0.10	12.73	20.97	30.96
0.14	22.54	38.66	50.44
0.20	42.87	61.02	72.89

Table (B.10) Values of Nusselt number at different temperatures and mean velocities corresponding to some aqueous solutions with 30% ethylene glycol.

B.5 Pipe convection heat transfer coefficient

Finally, Table (B.11), Table (B.12) and Table (B.13) summarize the results of convective heat transfer coefficients calculated using equation (3.32) and the results presented in the previous sections for the Nusselt number.

In general, h_f decreases when the percentage of ethylene glycol in the solution increases. For a given content of ethylene glycol, the higher values for h_f are obtained with increasing the mean velocity in the tubes and the temperature of the solution. This can be appreciated more easily in Figure (B.1), Figure (B.2) and Figure (B.3), where the convective heat transfer coefficient, for different percentages of ethylene glycol, has been plotted against temperature for three fluid mean velocities.

	h_f - (10%)		
Mean Velocity (l/s)	5°C	15°C	25°C
0.10	672.00	1,090.36	1,310.40
0.14	1,190.35	1,554.15	1,829.58
0.20	1,738.69	2,203.69	2,558.33

Table (B.11) Values of convective heat transfer coefficient, h_f, at different temperatures and mean velocities corresponding to some aqueous solutions with 10% ethylene glycol

	h_f - (20%)		
Mean Velocity (l/s)	5°C	15°C	25°C
0.10	444.22	759.07	1,053.98
0.14	812.06	1,245.32	1,501.61
0.20	1,384.40	1,800.64	2,128.74

Table (B.12) Values of convective heat transfer coefficient, h_f, at different temperatures and mean velocities corresponding to some aqueous solutions with 20% ethylene glycol

	h_f - (30%)		
Mean Velocity (l/s)	5°C	15°C	25°C
0.10	294.27	492.04	735.95
0.14	521.17	907.19	1,199.03
0.20	991.30	1,432.11	1,732.69

Table (B.13) Values of convective heat transfer coefficient, h_f, at different temperatures and mean velocities corresponding to some aqueous solutions with 30% ethylene glycol

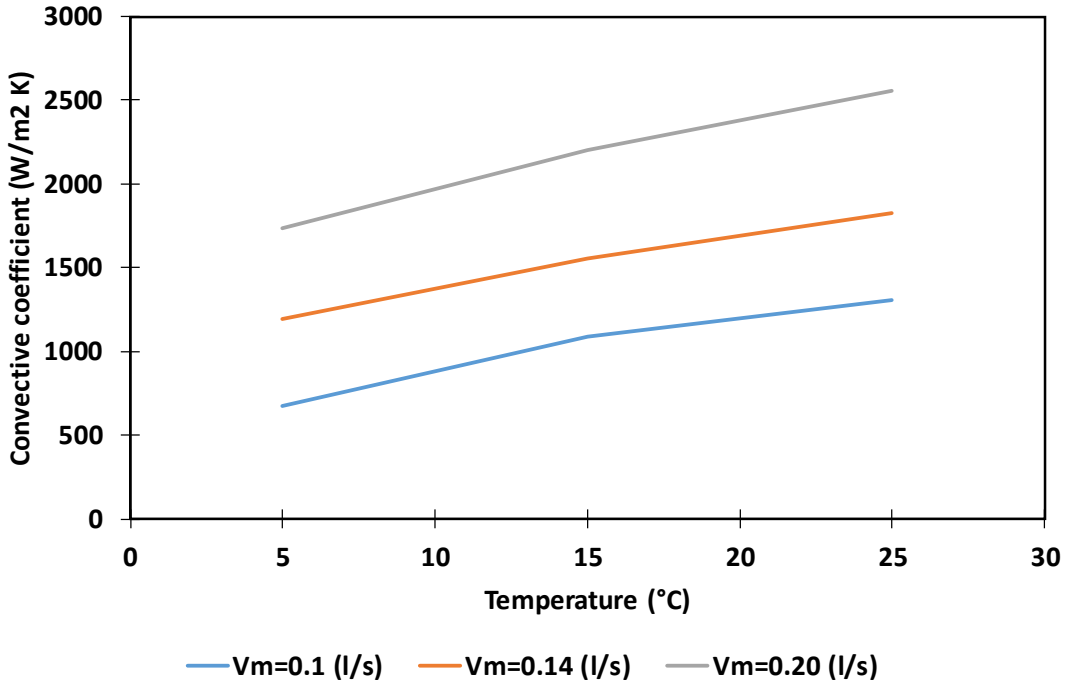

Figure (B.1) Variation of the convective heat transfer coefficient with temperature at three fluid mean velocities for an aqueous solution of ethylene glycol at 10%.

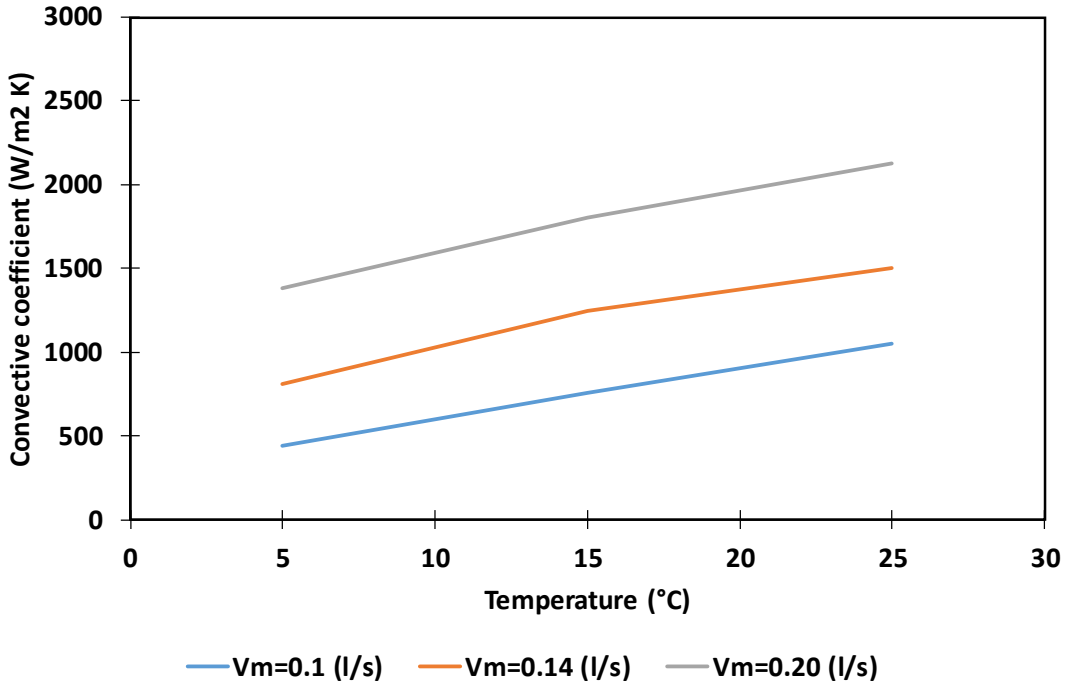

Figure (B.2) Variation of the convective heat transfer coefficient with temperature at three fluid mean velocities for an aqueous solution of ethylene glycol at 20%.

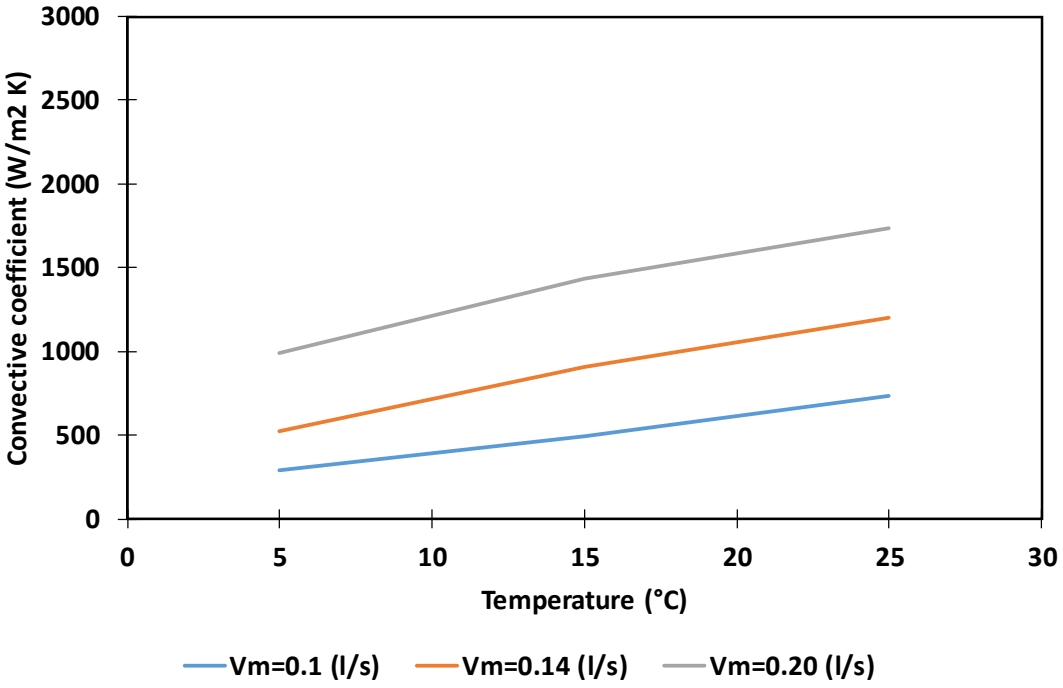

Figure (B.3) Variation of the convective heat transfer coefficient with temperature at three fluid mean velocities for an aqueous solution of ethylene glycol at 30%